Doctoral Dissertation

Development and On-sky Demonstration of Atmospheric Turbulence Profiler for Future Adaptive Optics with Multiple Laser Guide Stars

(次世代の複数レーザーガイド星補償光学に向けた
大気ゆらぎ測定装置の開発と観測実証)

TOHOKU
UNIVERSITY

Hajime Ogane

Astronomical Institute, Graduate School of Science
Tohoku University

This dissertation is submitted for the degree of
Doctor of Philosophy

August 2023

Abstract

In ground-based astronomy in optical and near-infrared wavelength, turbulence in the Earth's atmosphere causes wavefront distortion, which results in poorer angular resolution or worse sensitivity compared to the intrinsic performance of large telescopes. One of the solutions is using an adaptive optics (AO) system, which controls the wavefront distortion with a loop speed faster than the atmosphere changes. Recently, AO using multiple laser guide stars (LGS) and atmospheric tomography techniques have been developed and demonstrated for AO working with a wider field of view, at shorter wavelength, and over larger sky coverage, compared to the classical AO. The AO with multiple LGS is also important in terms of the technique being a standard observation mode in the era of extremely large telescopes.

This thesis focuses on two topics related to the development of AO with multiple LGS in the context of the ULTIMATE project at the Subaru telescope. The first topic, measuring atmospheric turbulence profiles at the Subaru telescope, is crucial for designing AO parameters, optimizing the tomographic wavefront reconstruction matrix, and evaluating AO performance. In order to investigate free atmospheric turbulence with a high altitude range and ground layer turbulence with a fine altitude resolution at the same time, we develop a novel atmospheric turbulence profiler comprising two Shack-Hartmann (SH) sensors with a fine pupil sampling of 2 cm. Through several engineering observations at the Subaru telescope, we obtain free atmospheric turbulence profiles with a range of 1-20 km and a resolution of a few km and ground layer turbulence profiles with a range of up to 400 m and a resolution of 10-20 m, which is applicable to tomography and performance simulation for the ULTIMATE AO systems. Besides, we measure total seeing and wind speed/direction profile based on the slope and scintillation measurements by a single SH sensor.

The second topic, evaluating the performance of detectors with rolling shutter mode as AO wavefront sensors, is important considering that recent commercially-available CMOS detectors have many attractive features such as faster frame rate, lower readout noise, and larger format size, compared to conventional CCD detectors. In this study, we model the behaviors of wavefront sensors with rolling shutter mode and perform AO simulations to evaluate their performance. The result suggests that additional wavefront error induced by the rolling shutter is sufficiently small for GLAO, though not negligible for LTAO.

Table of contents

List of figures ix

List of tables xiii

Nomenclature xv

1 General Introduction 1

1.1 Ground-based astronomy under Earth's atmosphere . . . 1

1.2 Atmospheric turbulence . . . 3

1.2.1 Theoretical model of turbulent field . . . 3

1.2.2 Correlation function and structure function . . . 5

1.2.3 Vertical structure of atmospheric turbulence . . . 6

1.2.4 Wavefront distortion . . . 8

1.2.5 Parameters characterizing atmospheric turbulence . . . 11

1.3 Single conjugate adaptive optics . . . 12

1.3.1 Principle of the system . . . 12

1.3.2 Performance metrics . . . 15

1.3.3 Fundamental limitation . . . 15

1.4 Adaptive optics with multiple laser guide stars . . . 17

1.4.1 Classification of the systems . . . 17

1.4.2 Tomographic wavefront reconstruction . . . 19

1.4.3 ULTIMATE project . . . 21

1.4.4 Structure formation of star-forming galaxies . . . 22

1.5 Scope of the thesis . . . 23

2 Atmospheric Turbulence Profiling at Subaru Telescope 25

2.1 Introduction . . . 25

2.1.1 Atmospheric turbulence effect on propagating light . . . 25

2.1.2 Reviewing measurement methods of atmospheric turbulence . . . 27

2.1.3 Principles of methods considered in this study . . . 31
2.2 Instrumentation . . . 39
2.2.1 Design concept . . . 39
2.2.2 Optical design . . . 40
2.2.3 Mechanical design . . . 44
2.2.4 Data acquisition software . . . 45
2.2.5 Laboratory assembly and performance check . . . 47
2.2.6 Installation to the Subaru telescope . . . 49
2.3 Observation . . . 56
2.3.1 Observation target . . . 56
2.3.2 Engineering observation . . . 56
2.4 Analysis . . . 61
2.4.1 Timing and synchronicity of data acquisition . . . 61
2.4.2 Shack-Hartmann sensor spot detection . . . 61
2.4.3 Slope auto-covariance . . . 62
2.4.4 SH-MASS . . . 67
2.4.5 Scintillation temporal auto-covariance . . . 70
2.4.6 Pupil matching . . . 71
2.4.7 SLODAR . . . 72
2.5 Results . . . 73
2.5.1 Total seeing . . . 73
2.5.2 Free atmospheric turbulence profile . . . 77
2.5.3 Wind profile . . . 79
2.5.4 Ground layer turbulence profile . . . 83
2.6 Discussion . . . 86
2.6.1 Comparison with CFHT MASS-DIMM . . . 86
2.6.2 Consistency between scintillation auto-covariance map and SH-MASS 87
2.7 Conclusion . . . 87

3 Rolling Shutter Effect on Wavefront Sensing 91
3.1 Introduction . . . 91
3.2 Analytical evaluation . . . 93
3.2.1 Modeling the shutter modes . . . 93
3.2.2 Simplified simulation of wavefront measurement . . . 95
3.2.3 Laboratory verification . . . 102
3.3 End-to-end simulation . . . 103
3.3.1 Sources of wavefront distortion . . . 103

3.3.2 Simulation setup . . . 105
3.3.3 Results . . . 106
3.4 Conclusion . . . 108

4 Summary and Future Prospects **111**
4.1 Summary of the thesis . . . 111
4.2 Future prospects . . . 113
4.2.1 Additional observations with the turbulence profiler . . . 113
4.2.2 Mitigation of the rolling shutter effect for LTAO . . . 114

References **117**

Appendix A Correlation function, structure function, and power spectrum of wavefront distortion by a thin turbulent layer **123**

Appendix B Power spectrum of amplitude fluctuation and wavefront distortion after Fresnel propagation **125**

Appendix C Slope auto-covariance analysis **127**

Appendix D SH-MASS analysis **153**

Appendix E Scintillation auto-covariance analysis **159**

Appendix F SLODAR analysis **169**

List of figures

1.1 Atmospheric effect on observed PSF size 2
1.2 Example of the vertical structure of the Earth's atmosphere 7
1.3 Example of atmospheric turbulence profile 9
1.4 Schematic illustration of SCAO system 13

2.1 Aperture pattern comparison between MASS and SH-MASS 34
2.2 Response function comparison between MASS and SH-MASS 36
2.3 Conceptual drawing of the turbulence profiler 41
2.4 Optical design of the turbulence profiler 43
2.5 Mechanical layout of the turbulence profiler 46
2.6 Laboratory setup for the turbulence profiler alignment 48
2.7 Optical alignment using alignment cones and positioning jigs 49
2.8 Comparison of images expected in optical simulation and obtained in the laboratory 50
2.9 Auto-Guider and Shack-Hartmann module 51
2.10 Base plate of the turbulence profiler 52
2.11 Turbulence profiler installed on the AG-SH module 54
2.12 Pictures of the turbulence profiler 55
2.13 Histogram of detected CoG position of spots 63
2.14 Histogram of detected brightness of spots 64
2.15 Example of slope auto-covariance analysis 66
2.16 Example of measured scintillation indices 68
2.17 Weighting function matrix 69
2.18 Example of scintillation auto-covariance map 71
2.19 Example of scintillation auto-covariance analysis 72
2.20 Part of the Subaru telescope pupil measured by the turbulence profiler . . . 73
2.21 Pupil matching between two SH sensors with datasets on Nov.12, 2022 . . 74
2.22 Pupil matching between two SH sensors with datasets on Mar.14, 2023 . . . 75

2.23 Example of slope cross-covariance analysis . . . 76
2.24 Total seeing measured by slope auto-covariance analysis . . . 78
2.25 Free atmospheric turbulence profile . . . 80
2.26 Free atmospheric seeing . . . 81
2.27 Wind speed/direction profile . . . 82
2.28 Ground layer turbulence profile . . . 84
2.29 Ground layer seeing . . . 85
2.30 Comparison of free atmospheric turbulence measurement with CFHT MASS 88
2.31 Comparison of profiles obtained by scintillation auto-covariance analysis and SH-MASS . . . 89

3.1 Conceptual diagram of shutter modes considered in this study . . . 94
3.2 Response of each shutter mode to tip or tilt oscillation . . . 97
3.3 Response of each shutter mode to defocus or spherical oscillation . . . 98
3.4 Response of each shutter mode to astigmatism oscillation . . . 99
3.5 Response of each shutter mode to coma oscillation . . . 100
3.6 Response of each shutter mode to trefoil oscillation . . . 101
3.7 Orthonormality of 32×32 Zernike modes and slope expansion modes in Zhao & Burge 2007 . . . 101
3.8 Result of aliasing measurement in lab experiment . . . 103
3.9 Power spectrum of telescope vibration . . . 104
3.10 Power spectrum of LGS jitter . . . 105
3.11 Schematic description of the end-to-end simulation . . . 107
3.12 Time series and power spectrum models of telescope vibration and LGS jitter used in the end-to-end simulation . . . 107
3.13 Histogram of wavefront error in end-to-end simulation . . . 109

C.1 Fitting slope auto-covariance map obtained at 23:17, Nov.12 by SH-1 . . . 128
C.2 Fitting slope auto-covariance map obtained at 23:17, Nov.12 by SH-2 . . . 129
C.3 Fitting slope auto-covariance map obtained at 23:37, Nov.12 by SH-1 . . . 130
C.4 Fitting slope auto-covariance map obtained at 23:37, Nov.12 by SH-2 . . . 131
C.5 Fitting slope auto-covariance map obtained at 23:42, Nov.12 by SH-1 . . . 132
C.6 Fitting slope auto-covariance map obtained at 23:42, Nov.12 by SH-2 . . . 133
C.7 Fitting slope auto-covariance map obtained at 23:45, Nov.12 by SH-1 . . . 134
C.8 Fitting slope auto-covariance map obtained at 23:45, Nov.12 by SH-2 . . . 135
C.9 Fitting slope auto-covariance map obtained at 23:49, Nov.12 by SH-1 . . . 136
C.10 Fitting slope auto-covariance map obtained at 23:49, Nov.12 by SH-2 . . . 137

C.11 Fitting slope auto-covariance map obtained at 2:42, Mar.14 by SH-1 138
C.12 Fitting slope auto-covariance map obtained at 2:45, Mar.14 by SH-1 139
C.13 Fitting slope auto-covariance map obtained at 3:30, Mar.14 by SH-2 140
C.14 Fitting slope auto-covariance map obtained at 3:34, Mar.14 by SH-2 141
C.15 Fitting slope auto-covariance map obtained at 3:37, Mar.14 by SH-2 142
C.16 Fitting slope auto-covariance map obtained at 4:44, Mar.14 by SH-1 143
C.17 Fitting slope auto-covariance map obtained at 4:44, Mar.14 by SH-2 144
C.18 Fitting slope auto-covariance map obtained at 5:07, Mar.14 by SH-1 145
C.19 Fitting slope auto-covariance map obtained at 5:07, Mar.14 by SH-2 146
C.20 Fitting slope auto-covariance map obtained at 5:13, Mar.14 by SH-1 147
C.21 Fitting slope auto-covariance map obtained at 5:13, Mar.14 by SH-2 148
C.22 Fitting slope auto-covariance map obtained at 5:16, Mar.14 by SH-1 149
C.23 Fitting slope auto-covariance map obtained at 5:16, Mar.14 by SH-2 150
C.24 Fitting slope auto-covariance map obtained at 5:20, Mar.14 by SH-1 151
C.25 Fitting slope auto-covariance map obtained at 5:20, Mar.14 by SH-2 152

D.1 Scintillation indices obtained at 23:17, Nov.12 154
D.2 Scintillation indices obtained at 23:37, Nov.12 154
D.3 Scintillation indices obtained at 23:42, Nov.12 154
D.4 Scintillation indices obtained at 23:45, Nov.12 155
D.5 Scintillation indices obtained at 23:49, Nov.12 155
D.6 Scintillation indices obtained at 2:42, Mar.14 155
D.7 Scintillation indices obtained at 2:45, Mar.14 156
D.8 Scintillation indices obtained at 3:30, Mar.14 156
D.9 Scintillation indices obtained at 3:34, Mar.14 156
D.10 Scintillation indices obtained at 3:37, Mar.14 157
D.11 Scintillation indices obtained at 4:44, Mar.14 157
D.12 Scintillation indices obtained at 5:07, Mar.14 157
D.13 Scintillation indices obtained at 5:13, Mar.14 158
D.14 Scintillation indices obtained at 5:16, Mar.14 158
D.15 Scintillation indices obtained at 5:20, Mar.14 158

E.1 Scintillation auto-covariance map obtained at 23:17, Nov.12 by SH-1 160
E.2 Scintillation auto-covariance map obtained at 23:17, Nov.12 by SH-2 160
E.3 Scintillation auto-covariance map obtained at 23:37, Nov.12 by SH-1 160
E.4 Scintillation auto-covariance map obtained at 23:37, Nov.12 by SH-2 161
E.5 Scintillation auto-covariance map obtained at 23:42, Nov.12 by SH-1 161

E.6 Scintillation auto-covariance map obtained at 23:42, Nov.12 by SH-2 161
E.7 Scintillation auto-covariance map obtained at 23:45, Nov.12 by SH-1 162
E.8 Scintillation auto-covariance map obtained at 23:45, Nov.12 by SH-2 162
E.9 Scintillation auto-covariance map obtained at 23:49, Nov.12 by SH-1 162
E.10 Scintillation auto-covariance map obtained at 23:49, Nov.12 by SH-2 163
E.11 Scintillation auto-covariance map obtained at 2:42, Mar.14 by SH-1 163
E.12 Scintillation auto-covariance map obtained at 2:45, Mar.14 by SH-1 163
E.13 Scintillation auto-covariance map obtained at 3:30, Mar.14 by SH-2 164
E.14 Scintillation auto-covariance map obtained at 3:34, Mar.14 by SH-2 164
E.15 Scintillation auto-covariance map obtained at 3:37, Mar.14 by SH-2 164
E.16 Scintillation auto-covariance map obtained at 4:44, Mar.14 by SH-1 165
E.17 Scintillation auto-covariance map obtained at 4:44, Mar.14 by SH-2 165
E.18 Scintillation auto-covariance map obtained at 5:07, Mar.14 by SH-1 165
E.19 Scintillation auto-covariance map obtained at 5:07, Mar.14 by SH-2 166
E.20 Scintillation auto-covariance map obtained at 5:13, Mar.14 by SH-1 166
E.21 Scintillation auto-covariance map obtained at 5:13, Mar.14 by SH-2 166
E.22 Scintillation auto-covariance map obtained at 5:16, Mar.14 by SH-1 167
E.23 Scintillation auto-covariance map obtained at 5:16, Mar.14 by SH-2 167
E.24 Scintillation auto-covariance map obtained at 5:20, Mar.14 by SH-1 167
E.25 Scintillation auto-covariance map obtained at 5:20, Mar.14 by SH-2 168

F.1 Fitting slope cross-covariance map obtained at 23:17, Nov.12 170
F.2 Fitting slope cross-covariance map obtained at 23:37, Nov.12 170
F.3 Fitting slope cross-covariance map obtained at 23:42, Nov.12 171
F.4 Fitting slope cross-covariance map obtained at 23:45, Nov.12 171
F.5 Fitting slope cross-covariance map obtained at 23:49, Nov.12 172
F.6 Fitting slope cross-covariance map obtained at 4:44, Mar.14 172
F.7 Fitting slope cross-covariance map obtained at 5:07, Mar.14 173
F.8 Fitting slope cross-covariance map obtained at 5:13, Mar.14 173
F.9 Fitting slope cross-covariance map obtained at 5:16, Mar.14 174
F.10 Fitting slope cross-covariance map obtained at 5:20, Mar.14 174

List of tables

2.1 Summary of atmospheric turbulence measurement methods 30
2.2 Specification of the turbulence profiler 40
2.3 Specification of the Shack-Hartmann sensor 42
2.4 Transmissive optics on the turbulence profiler 44
2.5 Reflective optics on the turbulence profiler 44
2.6 Detectors on the turbulence profiler 45
2.7 Target list of turbulence profiler observation 58
2.8 Data of astronomical objects obtained by the turbulence profiler 59
2.9 Data of non-astronomical objects obtained by the turbulence profiler 60

Nomenclature

Acronyms / Abbreviations

AO Adaptive Optics

CCD Charge Coupled Device

CMOS Complementary Metal Oxide Semiconductor

CoG Center of Gravity

DM Deformable Mirror

DSI Differential Scintillation Index

EMCCD Electron Multiplying Charge Coupled Device

FWHM Full Width at Half Maximum

GLAO Ground Layer Adaptive Optics

HST Hawaiian Standard Time

LGS Laser Guide Star

LTAO Laser Tomography Adaptive Optics

MCAO Multi Conjugate Adaptive Optics

MLA Microlens Array

MMSE Minimum Mean Square Error

MOAO Multi Object Adaptive Optics

NCPA Non Common Path Aberration

NGS Natural Guide Star

NSI Normal Scintillation Index

PSF Point Spread Function

RMS Root Mean Square

SCAO Single Conjugate Adaptive Optics

SFG Star-Forming Galaxy

SH Shack-Hartmann

SH-WFS Shack-Hartmann Wavefront Sensor

WFS Wavefront Sensor

Chapter 1

General Introduction

1.1 Ground-based astronomy under Earth's atmosphere

Angular resolution is one of the most important parameters in astronomical observations. Higher angular resolution improves the accuracy of astrometry and the sensitivity of photometry. Spatially-resolved observations of extended sources such as galaxies, nebulae, and star clusters, reveal morphological or kinematical structures of the objects.

The theoretical angular resolution of telescopes is determined by the aperture diameter of the telescope D and observed wavelength λ as the diffraction limit $\sim \lambda/D$, and human beings have devoted their technology to developing telescopes with larger apertures. Since the invention of the world's first telescope in the 17th century, telescope aperture has been increasing, and today we have various 8-10 m class telescopes all over the world. There are even plans for 30-40 m class telescopes within a few decades.

However, in practice, the angular resolution of ground-based telescopes is limited by the Earth's atmosphere. The Earth's atmosphere has various effects on light coming from astronomical objects, such as reflection, absorption, scattering, emission, and refraction. The atmospheric refraction, especially, is responsible for the angular resolution of the observation. A non-uniform refractive index originating from turbulence in the atmosphere makes the phase or wavefront of light distorted, resulting in a blurred image.

Figure 1.1 shows a comparison of angular resolution between diffraction-limited and atmosphere-limited cases. The size of the point spread function (PSF) is shown as a function of the observed wavelength. Cyan and blue lines represent diffraction-limited cases for 8 m and 30 m telescopes, respectively, and the red and magenta lines represent atmosphere-limited PSF size known as "seeing" at a typical and good astronomical site, respectively. The limitation imposed by the atmosphere is a major obstacle in the visible or near-infrared wavelength range.

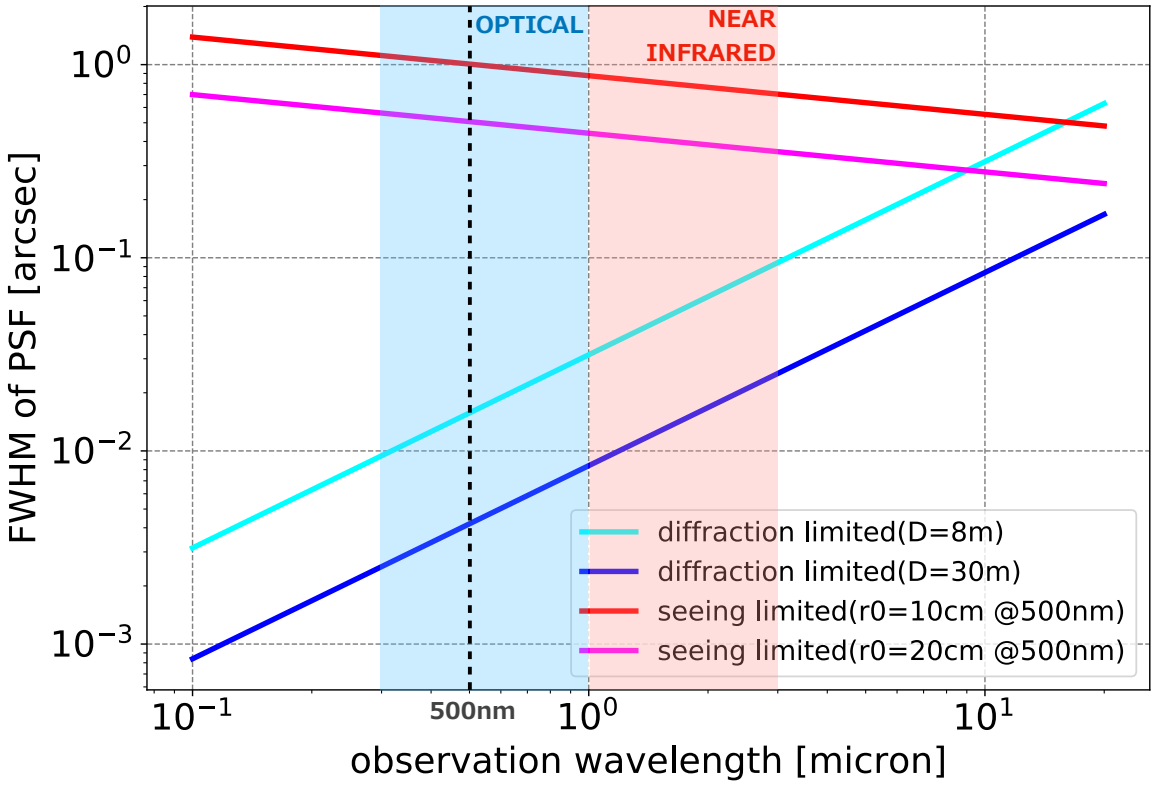

Fig. 1.1 Atmospheric effect on observed PSF size. The cyan and blue lines show diffraction-limited PSF sizes for 8 m and 30 m telescopes, respectively. The red and magenta lines show seeing limited PSF sizes for the atmosphere with the Fried parameter at 500 nm wavelength of 10 cm and 20 cm, respectively.

One of the solutions for the atmospheric effects is using space telescopes. By launching telescopes out of the atmosphere, not only the effect on angular resolution but also the effects on transmittance or sensitivity imposed by absorption or emission are resolved. However, space telescopes have several disadvantages compared to ground-based telescopes such as the need to be compact in size, difficulty of replacing and maintaining, taking much more costs, and the need to use technology that is available at the time of planning.

Adaptive optics (AO) provides another solution. AO is a control system that measures and corrects wavefront distortion at a control speed faster than atmospheric changes. By combining observation sites with stable atmospheric conditions and AO systems, image performance close to the diffraction limit is achieved while taking advantage of the light-gathering power of large ground-based telescopes. However, conventional AO has disadvantages such as lower performance in the optical wavelength range and a narrow field of view that is corrected at once. To overcome these problems, new systems using multiple laser guide stars have been developed and demonstrated in recent years.

1.2 Atmospheric turbulence

This section describes the basic theory of turbulence in the Earth's atmosphere and its optical effects with reference to Hardy (1998) and Tyson and Frazier (2022).

1.2.1 Theoretical model of turbulent field

The Earth's atmosphere is constantly turbulent due to wind shear, friction with the ground surface, and global circulation caused by solar heating. This is understood by considering the Reynolds number, which is a measure of the flow state of fluids, including the atmosphere. The Reynolds number R_e is defined using the flow velocity V, the spatial scale characterizing the flow L, and the kinematic viscosity coefficient of the fluid ν as follows,

$$R_e = \frac{VL}{\nu}. \tag{1.1}$$

It is known that when this value exceeds a certain threshold determined by the geometry of the flow, the flow changes from laminar to turbulent. In the case of the Earth's atmosphere, $V \sim 1\ \mathrm{m \cdot s^{-1}}, L \sim 15\ \mathrm{m}, \nu \sim 1.5 \times 10^{-5}\ \mathrm{m^2 \cdot s^{-1}}$ and $R_e \sim 10^6$. Generally, this Reynolds number corresponds to well-developed turbulence, indicating that the Earth's atmosphere is turbulent.

The general theory of turbulence involving the Earth's atmosphere has been examined by Kolmogorov (1941). Kolmogorov's model considers that the energy of turbulence is

injected at the largest spatial scale of turbulence, called the outer scale L_0. Then, the energy is transferred to smaller scales to produce turbulence at various spatial scales, called energy cascade. The spatial scale at which the Reynolds number is the threshold separating turbulent and laminar flows is called inner scale l_0, which is the smallest spatial scale of turbulence. The range of spatial scales between the outer scale and inner scales is called the inertial region. In the case of the Earth's atmosphere, the source of turbulence energy that creates the outer scale is the temperature difference due to solar heating, and the energy cascade is caused by mixing with wind shear. The typical outer scale is $L_0 \sim 30$ m and the inner scale is $l_0 \sim 1$ mm.

Considering steady turbulence and focusing on a turbulent component of a certain spatial scale l, the rate of energy injection into the component and rate of energy transfer from that component are equal and are written as ϵ. Then, a representative velocity v of the component is written from dimensional analysis as $v \propto \epsilon^{1/3} l^{1/3}$. Therefore, energy spectrum Φ of turbulence in one-dimensional space is a function of turbulence wavenumber $\kappa = 2\pi/l$ as

$$\Phi(\kappa) d\kappa \propto v^2 \propto \kappa^{-2/3}, \tag{1.2}$$

that is

$$\Phi(\kappa) \propto \kappa^{-5/3}. \tag{1.3}$$

Thus, the energy spectrum of turbulence is proportional to the power of $-5/3$.

In the Earth's atmosphere, turbulence causes spatial differences in temperature or temperature fluctuations. Furthermore, atmospheres with different temperatures have different refractive indices, resulting in refractive index fluctuations. It has been shown by Obukhov (1949) and Yaglom (1949) that temperature and refractive index fluctuations follow the same form of spatial power spectrum as turbulence itself, as long as these additional physical quantities do not affect the dynamics or chemical composition of the turbulence. Since the actual atmospheric turbulence is a three-dimensional structure, the energy spectrum of the turbulence in three-dimensional space is necessary. According to Tatarski (1971), the spatial power spectrum of the refractive index fluctuations in three-dimensional space Φ_n is written as follows,

$$\Phi_n(\boldsymbol{\kappa}) = \frac{\Gamma(8/3)\sin(\pi/3)}{4\pi^2} C_n^2 |\boldsymbol{\kappa}|^{-11/3} \sim 0.033 C_n^2 |\boldsymbol{\kappa}|^{-11/3}, \tag{1.4}$$

where $\boldsymbol{\kappa}$ is a three-dimensional wavenumber vector, $\Gamma(\cdot)$ is the gamma function, and C_n^2 is a measure of the magnitude of fluctuations called refractive index structure constant. The definition of the refractive index structure constant is explained later in this section.

1.2.2 Correlation function and structure function

The correlation function and structure function of a turbulent field are quantities that characterize the spatial structure of the turbulence. The correlation function B_A of a certain physical quantity A (e.g., fluid velocity, density, temperature, etc.) in a turbulent field is defined as follows,

$$B_A(\boldsymbol{x}) =< A(\boldsymbol{r})A(\boldsymbol{r}+\boldsymbol{x}) >, \tag{1.5}$$

where $\boldsymbol{x}$ and $\boldsymbol{r}$ are position vectors in space. $< \cdot >$ is ensemble mean, which represents mean with respect to the position $\boldsymbol{r}$ and mean with respect to the time of the turbulent field, which temporally changes. Therefore, the correlation function $B_A(\boldsymbol{x})$ represents the statistical correlation of the physical quantity A at two points separated by a distance vector $\boldsymbol{x}$.

On the other hand, the structure function D_A of a physical quantity A is defined as follows.

$$D_A(\boldsymbol{x}) =< \{A(\boldsymbol{r}) - A(\boldsymbol{r}+\boldsymbol{x})\}^2 > . \tag{1.6}$$

Similar to the correlation function, the structure function is also a quantity that expresses the degree of correlation between physical quantities at two points in a turbulent field. In fact, these functions are related as follows.

$$\begin{aligned} D_A(\boldsymbol{x}) &=< \{A(\boldsymbol{r}) - A(\boldsymbol{r}+\boldsymbol{x})\}^2 > \\ &=< A(\boldsymbol{r})^2 > + < A(\boldsymbol{r}+\boldsymbol{x})^2 > -2 < A(\boldsymbol{r})A(\boldsymbol{r}+\boldsymbol{x}) > \\ &= 2\{< A(\boldsymbol{r})^2 > - < A(\boldsymbol{r})A(\boldsymbol{r}+\boldsymbol{x}) >\} \\ &= 2\{B_A(\boldsymbol{0}) - B_A(\boldsymbol{x})\}. \end{aligned} \tag{1.7}$$

The use of structure functions is more appropriate when discussing the spatial structure of physical quantities such as temperature, humidity, and refractive index in atmospheric turbulence. Many of these meteorological quantities change more slowly in time as the spatial scale increases, hence their time series consist of quick, small variations superimposed on slow, large variations. Since the structure function does not depend on the average value

of the physical quantity, it provides a valid evaluation of fluctuation when the time scale of interest is not long enough.

It has been shown by Kolmogorov (1941) that the structure function in Kolmogorov turbulence has the form of

$$D_v(\boldsymbol{x}) \propto |\boldsymbol{x}|^{2/3} \tag{1.8}$$

in terms of the velocity field in the turbulence. Furthermore, it has been shown by Obukhov (1949) and Yaglom (1949) that temperature and refractive index fluctuations in turbulence have the same spatial structure,

$$D_T(\boldsymbol{x}) = C_T^2 |\boldsymbol{x}|^{2/3} \tag{1.9}$$

$$D_n(\boldsymbol{x}) = C_n^2 |\boldsymbol{x}|^{2/3}. \tag{1.10}$$

The coefficients C_T^2 and C_n^2 for the distance to the 2/3 power are called the temperature structure constant and refractive index structure constant, respectively. C_T^2 has a unit of $\mathrm{K}^2 \cdot \mathrm{m}^{-2/3}$ and C_n^2 has a unit of $\mathrm{m}^{-2/3}$, and both are measures of the intensity of Kolmogorov turbulence.

1.2.3 Vertical structure of atmospheric turbulence

In the previous section, the discussion is based on the assumption that turbulence is uniform in one-dimensional or three-dimensional space. However, the actual Earth's atmosphere has a spatial structure that is non-uniform in the height direction. An example of the vertical structure of the Earth's atmosphere is shown in figure 1.2. The figure shows the vertical structure of temperature, wind speed, and wind direction measured at Hilo, Hawaii, by a rawinsonde, which is a direct measurement method using a balloon. Each line shows the structure averaged every three months in 2022: January to February with a solid line, March to May with a dashed line, June to August with a dotted line, and September to November with a dash-dotted line. Measurement in December 2022 is removed because the data contains many missing values. There are two different temperature gradient regions. In the troposphere below an altitude of $\sim$ 15 km, temperature decreases with altitude, and in the stratosphere above $\sim$ 15 km, there is an opposite temperature gradient. In addition to the temperature gradient, velocity structures that change with seasons also exist.

Although temperature and velocity structures exist in height range which is not shown in figure 1.2, i.e. above 35 km, the range is not considered in this study because the pressure and density are low and turbulence is unlikely to occur in the height range. When modeling

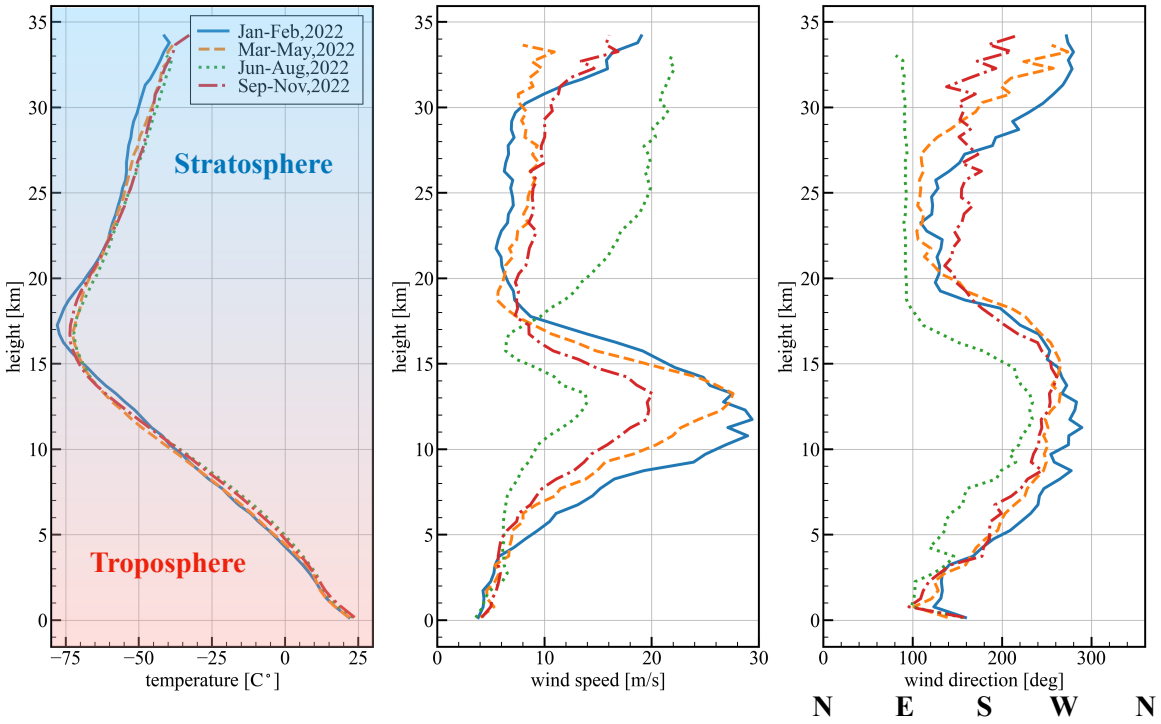

Fig. 1.2 Example of the vertical structure of the Earth's atmosphere. The data are taken from rawinsonde measurements at Hilo, Hawaii, which is provided by Maunakea Weather Center (http://mkwc.ifa.hawaii.edu/). Vertical structures of temperature, wind speed, and wind direction are shown in the left, center, and right panels, respectively. Solid, dashed, dotted, and dash-dotted lines show average structure in Jan-Feb, Mar-May, Jun-Aug, and Sep-Nov in 2022, respectively. Measurement data in December 2022 is removed since it contains many missing values.

turbulence in the Earth's atmosphere, it is common to assume a layered structure to account for this non-uniformity in the height direction. In other words, the Kolmogorov turbulence model is valid at a certain height, but the intensity of turbulence differs depending on the height. Since the typical thickness of each layer is a few 100 m to km scale and much larger than the typical outer scale of ~ 30 m, we still use the three-dimensional form of Kolmogorov turbulence. Rewriting equation (1.4) with explicit declaration that its intensity measure C_n^2 is a function of height,

$$\Phi_n(\boldsymbol{\kappa}, h) = 0.033 C_n^2(h) |\boldsymbol{\kappa}|^{-11/3}. \tag{1.11}$$

The refractive index structure constant as a function of altitude $C_n^2(h)$ is called atmospheric turbulence profile. Atmospheric turbulence profile has a time-varying feature, which is not only seasonal variations but also day-night variation or variations with a time scale of

a few hours. It also has spatial differences such as geographic features and altitude among observation sites.

Figure 1.3 shows an example of an atmospheric turbulence profile measured by launching a meteorological balloon at the Canary Island (Coulman et al., 1995). Some measurements by equipped sensors are performed from an altitude of 2200 m and valid data is obtained from 2400 m. The sensors measure local pressure $p(h)$, temperature $T(h)$, and temperature structure constant $C_T^2(h)$ as functions of altitude h with an altitude resolution of 6 m, to calculate the refractive index structure constant by

$$C_n^2(h) = C_T^2(h) \left[\frac{8 \times 10^{-5} p(h)}{T(h)^2} \right]^2 \tag{1.12}$$

(Roddier, 1981). The measured atmospheric turbulence profile is not smooth with altitude and has several peaks, indicating the turbulence has a layered structure. Since altitudes of the layers change as time goes on, it is important to measure atmospheric turbulence profile on site and in real time, or to handle profile as stochastic variables following statistical data obtained by long-term measurements on site.

1.2.4 Wavefront distortion

Since atmospheric turbulence has a layered structure in the height direction, we first consider the situation where there is one turbulent layer with a thickness of Δh_0 at height h_0. The wavefront of the light from an astronomical object is regarded as a plane because the object is at infinity. Let $n(\boldsymbol{x}, h)$ be a fluctuation of the refractive index inside the turbulent layer. $\boldsymbol{x}$ is a two-dimensional position vector in the plane along the turbulent layer, and h is the altitude. The spatial power spectrum of the refractive index fluctuations is represented by equation (1.4). Here, we use the spatial frequency $\boldsymbol{f} = \boldsymbol{\kappa}/(2\pi)$ instead of the wavenumber $\boldsymbol{\kappa}$ of the refractive index fluctuation to distinguish it from the wavenumber of light k. Power spectrum of refractive index fluctuation in equation (1.11) is rewritten as

$$\Phi_n(\boldsymbol{f}, h_0) = 9.7 \times 10^{-3} C_n^2(h_0) |\boldsymbol{f}|^{-11/3}. \tag{1.13}$$

Wavefront distortion of the light just after passing through the turbulent layer is,

$$\phi(\boldsymbol{x}) = k \int_{h_0}^{h_0 + \Delta h_0} n(\boldsymbol{x}, h) dh. \tag{1.14}$$

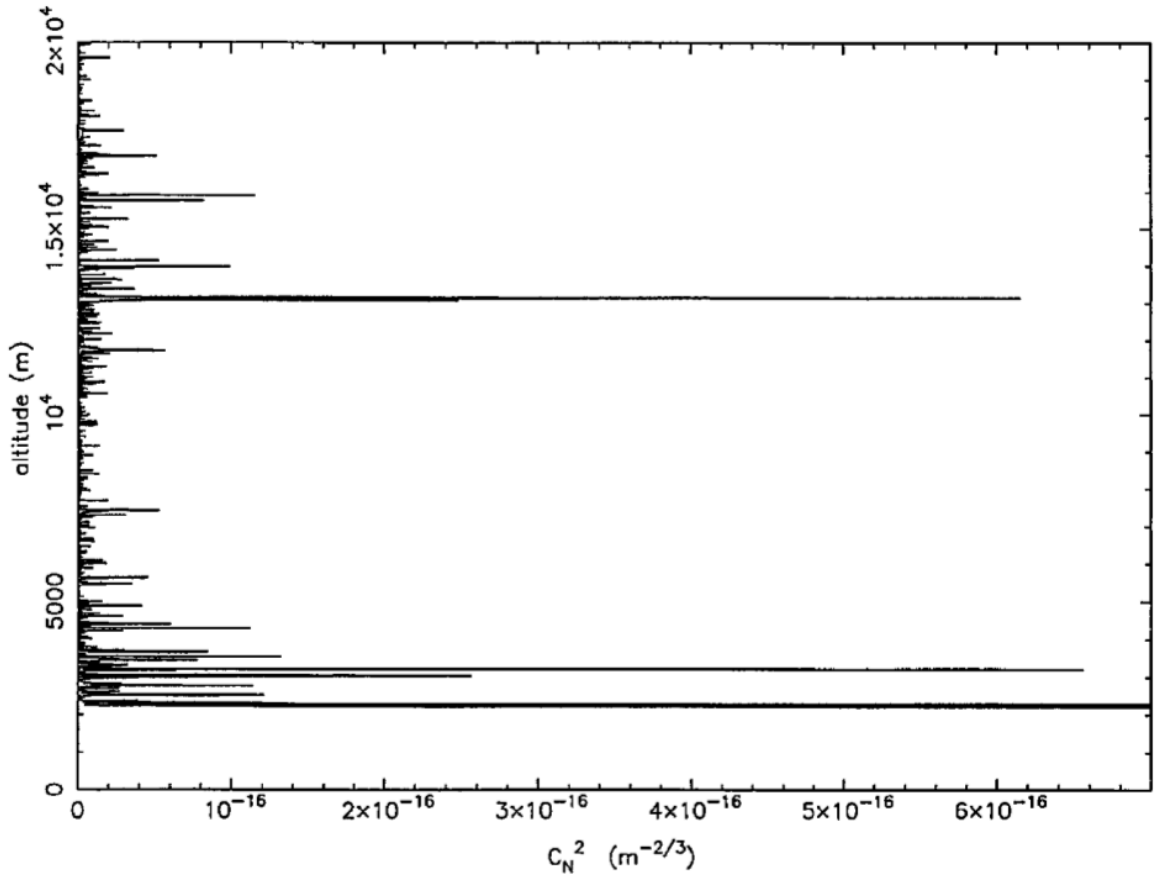

Fig. 1.3 An example of atmospheric turbulence profile measured by Coulman et al. (1995) using a balloon-borne sensor at the Canary Island. The height resolution of the measurement is 6 m, which is determined by a duty cycle of 1.5 s and an ascent speed of the order of 4 $\mathrm{m} \cdot \mathrm{s}^{-1}$.

The unit is radian. k is the wavenumber of the light from the astronomical object, $k = 2\pi/\lambda$, using the wavelength λ. The correlation function B_ϕ of the wavefront distortions just after passing through the turbulent layer is from its definition,

$$B_\phi(\boldsymbol{x}) =< \phi(\boldsymbol{r})\phi(\boldsymbol{r}+\boldsymbol{x}) > . \tag{1.15}$$

By substituting equation (1.14) into equation (1.15),

$$B_\phi(\boldsymbol{x}) = k^2 \Delta h_0 \int_{-\infty}^{\infty} B_n(\boldsymbol{x}, h) dh \tag{1.16}$$

is obtained (Roddier, 1981, see appendix A for the details). B_n is the correlation function of the refractive index fluctuation. In addition, the structure function of the wavefront distortion is from equation (1.7),

$$D_\phi(\boldsymbol{x}) = 2\{B_\phi(\boldsymbol{0}) - B_\phi(\boldsymbol{x})\}. \tag{1.17}$$

By using equation (1.16), we get

$$D_\phi(\boldsymbol{x}) = 2.91 k^2 C_n^2(h_0) \Delta h_0 |\boldsymbol{x}|^{5/3} \tag{1.18}$$

(Roddier, 1981; Obukhov, 1970; see appendix A for the details). The power spectrum of the wavefront distortion is obtained by Fourier transforming the correlation function B_ϕ from the Wiener-Khinchin theorem (see appendix A for the details),

$$\Phi_\phi(\boldsymbol{f}) = 9.7 \times 10^{-3} k^2 |\boldsymbol{f}|^{-11/3} C_n^2(h_0) \Delta h_0. \tag{1.19}$$

Thus, the power spectrum of the wavefront distortion is obtained by multiplying the power spectrum of the refractive index fluctuation by the square of the wavenumber k^2 and the thickness of the turbulent layer Δh_0.

When there are multiple turbulent layers, the total power spectrum is approximated as a sum of the power spectra of each layer,

$$\Phi_\phi(\boldsymbol{f}) = 9.7 \times 10^{-3} k^2 |\boldsymbol{f}|^{-11/3} \int C_n^2(h) dh. \tag{1.20}$$

The approximation is valid when the turbulence spatial scale of interest is large enough as $|\boldsymbol{f}| \ll \sqrt{\lambda h}$, where λ is observed wavelength, and the effect of scintillation is ignored.

1.2.5 Parameters characterizing atmospheric turbulence

While atmospheric turbulence affects astronomical observations via image degradation with wavefront distortion, it also has temporal variations and spatial variations from site to site. Here, we introduce some parameters to quantitatively characterize atmospheric turbulence.

Fried parameter r_0, which is introduced by Fried (1965) is defined as

$$r_0 = \left[0.423k^2 \int C_n^2(z)dz\right]^{-3/5}, \tag{1.21}$$

where k is the wavenumber of light observed and z is propagation distance from the turbulence layer, which is written as $z = h/\cos(\beta)$ using the height of the turbulence layer h and the zenith angle in the observing direction β. The $\int C_n^2(z)dz$ is the integrated turbulence amounts along the observing direction. Using the Fried parameter, the structure function of the wavefront distortion is written as,

$$D_\phi(\boldsymbol{x}) = 6.88\left(\frac{|\boldsymbol{x}|}{r_0}\right)^{5/3}. \tag{1.22}$$

The Fried parameter is a quantity that corresponds to a spatial scale where the root-mean-square (RMS) of the wavefront distortions of the light is ~ 1 rad and has a dimension of length.

Seeing ϵ is defined as the FWHM of the point image distribution function, which is written using the Fried parameter r_0 and the observed wavelength λ as follows,

$$\epsilon = \frac{0.98\lambda}{r_0}. \tag{1.23}$$

Isoplanatic angle θ_0 corresponds to the angular scale where the RMS of the difference between wavefront distortions in two directions is ~ 1 rad. Isoplanatic angle is defined as

$$\theta_0 = \left[2.91k^2 \int C_n^2(z)z^{5/3}dz\right]^{-3/5}. \tag{1.24}$$

Coherence time τ_0 corresponds to the time scale in which the RMS of the difference between wavefront distortions in two times is ~ 1 rad. Similarly, Greenwood frequency f_G (Greenwood, 1977) gives a characteristic temporal frequency of the wavefront distortion. The coherence time and the Greenwood frequency are calculated by

$$\tau_0 = \frac{0.31r_0}{V_0} = \frac{0.13}{f_G}. \tag{1.25}$$

V_0 is the wind speed $v(h)$ weighted by the atmospheric turbulence intensity, defined as follows,

$$V_0 = \left[\frac{\int C_n^2(z) v(z)^{5/3} dz}{\int C_n^2(z) dz} \right]^{3/5} . \tag{1.26}$$

1.3 Single conjugate adaptive optics

1.3.1 Principle of the system

Adaptive optics (AO) is a technique proposed by Babcock (1953) to measure and correct wavefront distortions of incident light from astronomical objects in real time. It has become one of the standard observation modes in large telescopes in modern times. The configuration of the standard system, single conjugate adaptive optics (SCAO), is shown in figure 1.4. It generally consists of four components: a guide star, a wavefront sensor, a control system, and a deformable mirror. The system consists of three processes: (1) the shape of the incident wavefront is sensed by measuring the light from the guide star with the wavefront sensor, (2) the wavefront is reconstructed in the control system and the voltage command required to drive the deformable mirror is calculated, and (3) the wavefront distortion is mitigated by reflecting the light onto the deformable mirror. This process is repeated as a single loop at a rate faster than the time variation of atmospheric turbulence, allowing correction over a long time period.

The wavefront sensor (WFS) has the ability to measure the shape of the incident wavefront as an image. There are several principles of measurement, and the most commonly used Shack-Hartmann WFS (SH-WFS; Hartmann, 1900; Platt and Shack, 1971) is outlined here. SH-WFS consists of a microlens array (MLA), which is an array of small transmissive lenses and a photon detector. An MLA is placed at a position conjugated to the telescope pupil to effectively divide the pupil into many subapertures. The light is focused by each microlens and makes an array of spots on the detector. By examining the spot position displacement, the local wavefront tilt at each subaperture is measured. The shape of the incident wavefront is obtained by integrating the local wavefront tilt.

In addition to the SH-WFS, there are other sensors such as curvature WFS (Roddier et al., 1988), which measures the wavefront curvature by examining the brightness at a position slightly off the focal plane, and pyramid sensor (Ragazzoni, 1996), which measures the wavefront tilt by dividing light into four beams at the focal plane and examining the difference of each pupil image. By modeling the sensing as a linear process, the wavefront

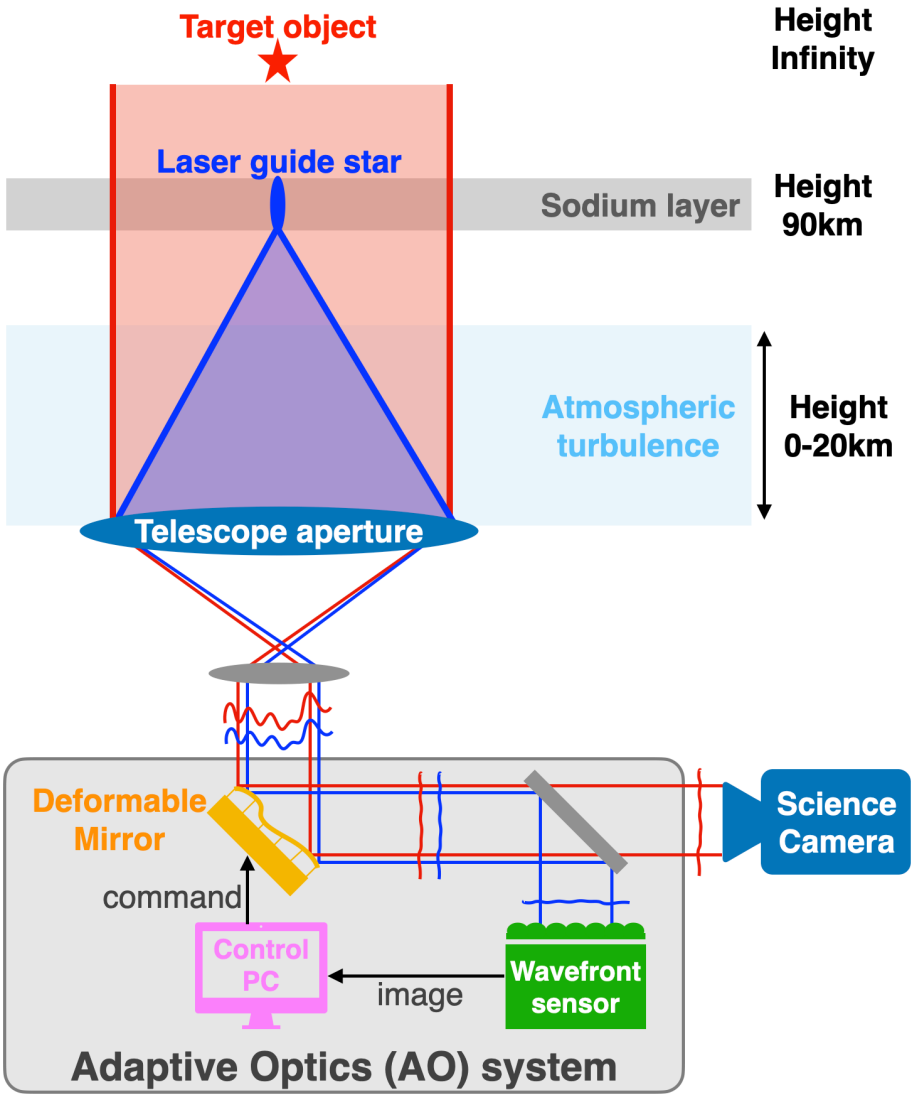

Fig. 1.4 Schematic illustration of SCAO system.

sensing is expressed as a matrix operation;

$$\boldsymbol{s} = \boldsymbol{G}\boldsymbol{\phi} + \boldsymbol{n}, \tag{1.27}$$

where $\boldsymbol{s}$ is a vector of WFS measurements, $\boldsymbol{\phi}$ is a vector of the discrete wavefront, $\boldsymbol{G}$ is a geometry matrix, which represents a wavefront sensing model. There are many geometries such as Fried geometry, Hudgin geometry, Southwell geometry, etc. $\boldsymbol{n}$ is a vector of sensing noise.

A guide star is a light source for measuring the wavefront. Due to the requirement for wavefront sensing with several hundred Hz, the guide star must be bright enough. Because targets of observation by large telescopes are generally faint, a bright star in the vicinity of the target should be used as a guide star. Such a guide star is called a natural guide star (NGS). In exoplanet observations, the main star is used as an NGS to observe faint planets around the bright main star. If there are no available stars, a reference source is artificially generated. Such a guide star is called a laser guide star (LGS). There are several methods of creating LGS, but the best known is the sodium LGS (Foy and Labeyrie, 1985; Thompson and Gardner, 1987), which is created by exciting sodium atoms at 90 km above the ground with a 589 nm laser.

A deformable mirror (DM) generally consists of a continuous membrane mirror and an array of piezoelectric actuators behind it. By driving the actuators, the surface mirror shape is changed. The mirror surface shape with invoking one actuator is called the influence function. There are many typical models of the influence function, such as Gaussian or cubic polynomials as a function of distance from the actuator position. The number of actuators is often comparable to the number of subapertures of a WFS.

The control system analyzes the spot image measured by the WFS and reconstructs the wavefront to determine commands to be given to the DM. The computation of wavefront reconstruction is expressed as a matrix operation;

$$\boldsymbol{d} = \boldsymbol{C}\boldsymbol{R}\boldsymbol{s}, \tag{1.28}$$

where $\boldsymbol{s}$ is a vector of WFS measurements and $\boldsymbol{d}$ is a vector of DM voltage commands. $\boldsymbol{R}$ is the wavefront reconstruction matrix, which reproduces wavefront from WFS measurement and is basically an inverse matrix of the geometry matrix. $\boldsymbol{C}$ is the control matrix, which computes the DM voltage command from the incident wavefront shape and is calculated using the influence function. Alternatively, in more practice, the relationship between DM voltage and WFS measurement is investigated by examining WFS response when poking

DM actuators one by one. By this procedure, the inverse matrix of the product of the control matrix and the wavefront reconstruction matrix, $(\boldsymbol{CR})^{-1}$, is obtained.

1.3.2 Performance metrics

There are a number of metrics that are used to assess the performance of AO systems.

The first is the full width at half maximum (FWHM) of the PSF. This is one of the easiest metrics to measure. In a general analysis in imaging observation, the FWHM is obtained by fitting a star image with a PSF model such as Gaussian or Moffat function. It should be noted, however, that the PSF after correction by the AO is not fitted by a single component. The actual PSF is represented by the superposition of a diffraction-limited component called a core and a seeing-limited component called a halo. The performance of the correction is evaluated by examining the energy ratio of the core and halo.

The second is wavefront error. Wavefront error is defined as the RMS of the corrected wavefront and is the most fundamental performance metric considering that the AO system corrects wavefront distortion. When the corrected wavefront is $\phi(\boldsymbol{x})$, the wavefront error σ_ϕ is written as,

$$\sigma_\phi = \sqrt{\frac{\int\int \{\phi(\boldsymbol{x}) - \overline{\phi}\}^2 d\boldsymbol{x}}{\int\int d\boldsymbol{x}}}, \tag{1.29}$$

where $\overline{\phi}$ represents mean wavefront over the considered area.

The third is the Strehl ratio. The Strehl ratio is defined as the ratio of the measured peak intensity of the PSF to the peak intensity of the PSF at the diffraction limit. It is also called normalized intensity. Considering that PSF after AO correction has core and halo components, the Strehl ratio is approximated to the energy ratio included in the core component. As a useful approximated form for cases where the wavefront error is sufficiently smaller than $\lambda/2\pi$, the Strehl ratio is written as a function of the wavefront error as follows,

$$S = 1 - \left(\frac{2\pi}{\lambda}\right)^2 \sigma_\phi^2 \sim \exp\left[-\left(\frac{2\pi}{\lambda}\right)^2 \sigma_\phi^2\right]. \tag{1.30}$$

1.3.3 Fundamental limitation

The SCAO system has been implemented in many AO instruments as a basic observing mode and has realized high-resolution observations in ground-based telescopes. However, SCAO does not always achieve a perfect diffraction-limited image and its performance is limited by

a number of factors. In this section, we consider several basic factors of wavefront error that limit the performance of SCAO.

Fitting error is an error component resulting from the fact that the wavefront distortion is not completely canceled out due to the mechanical constraints of the DM. Because of the limited number of actuators, it is not possible to reproduce structures finer than actuator spacing. Hudgin (1977) obtained the following expression for the fitting error by least-squares fitting of Kolmogorov wavefront with the DM surface shape created by a finite number of actuators.

$$\sigma_{\text{fit}}^2 = \kappa \left(\frac{r_s}{r_0} \right)^{5/3} \tag{1.31}$$

where r_s is the actuator spacing, r_0 is the Fried parameter, and κ is a coefficient that depends on the influence function, which is the DM surface shape created by driving a single actuator. For example, $\kappa = 0.23$ if the influence function is Gaussian, $\kappa = 0.28$ for pyramidal shape, and $\kappa = 1.26$ for piston shape.

Temporal error is an error component originating from the fact that the wavefront may change during the time delay between measuring and correcting the wavefront. When cutoff frequency of the AO system is $f_{3\text{dB}}$, wavefront error due to the temporal constraints is

$$\sigma_{\text{temp}}^2 = \left(\frac{f_G}{f_{3\text{dB}}} \right)^{5/3}. \tag{1.32}$$

Anisoplanatic error is caused by the fact that the wavefront is different in between the direction of the target and the guide star. When the angle between the target and the guide star is θ, the anisoplanatic error is written as

$$\sigma_{\text{iso}}^2 = \left(\frac{\theta}{\theta_0} \right)^{5/3}. \tag{1.33}$$

When LGS is used instead of NGS, there is an additional error source called focal anisoplanatic error or cone effect (Tallon and Foy, 1990). This error is caused by the different altitudes between the target and the guide star. The volume through which light from the LGS passes is conical, whereas that of the target is cylindrical. The cone effect is expressed as

$$\sigma_{\text{cone}}^2 = \left(\frac{D}{d_0} \right)^{5/3}. \tag{1.34}$$

D is the telescope aperture diameter and d_0 is the mean of the diameter of the conic shape weighted by the atmospheric turbulence profile;

$$d_0 = \lambda^{6/5} \left[19.77 \int \left(\frac{z}{z_{\mathrm{LGS}}} \right)^{5/3} C_n^2(z) dz \right]^{-3/5}, \tag{1.35}$$

where λ is observed wavelength and z_{LGS} is distance to the LGS.

WFS noise also imposes a limitation on the AO performance. Based on the wavefront sensing error expression in Kern et al. (1989), the measurement error in the case of NGS sensing with SH-WFS is

$$\sigma^2_{\mathrm{wfs}} = \frac{3\pi^2}{8} \left[\frac{N}{N + n_{\mathrm{pix}}(\sigma_{\mathrm{r}}^2 + \sigma_{\mathrm{bg}}^2)} \right]^{-1}, \tag{1.36}$$

where N is the number of signal electrons and n_{pix} is the number of pixels used in each subaperture. σ_{r} and σ_{bg} are readout and background noise in electrons per pixel, respectively.

Non common path aberration (NCPA), which is expressed as σ^2_{ncpa} is also considered as one of the main error components. This is caused by some misalignments in the science instruments. AO systems are not able to measure NCPA due to differences in optical paths between the science instruments and the AO systems. Although NCPA is a temporally static error, it is necessary to make a measurement in advance, for example, by using a camera inside the science instrument.

By assuming the above wavefront errors are independent, the combined wavefront error is estimated as

$$\sigma^2_{\phi} = \sigma^2_{\mathrm{fit}} + \sigma^2_{\mathrm{temp}} + \sigma^2_{\mathrm{iso}} + \sigma^2_{\mathrm{cone}} + \sigma^2_{\mathrm{wfs}} + \sigma^2_{\mathrm{ncpa}} \tag{1.37}$$

When an AO system is designed or evaluated, analytical calculation or numerical simulation is used to estimate the total wavefront error and Strehl ratio.

1.4 Adaptive optics with multiple laser guide stars

1.4.1 Classification of the systems

In order to overcome some of the error components of SCAO systems, AO systems using multiple LGS have been developed and demonstrated.

Laser tomography adaptive optics (LTAO) is a system for overcoming the cone effect and anisoplanatic error through atmospheric tomography. In this system, multiple LGS are arranged around the target object. Multiple WFS are also prepared for measuring the wavefront in several directions of the LGS. The measurement of each WFS includes turbulence information in the conic volume integrated in the direction of each LGS. By using tomographic wavefront estimation explained in the next section, the wavefront in the target direction is estimated and anisoplanatic error is overcome. Since several conic volumes cover turbulence at high altitudes, the cone effect is mitigated or resolved. Correction field of view is, however, still limited by anisoplanatism. In recent years, VLT/GALACSI using 4 LGS has been developed. Subaru/ULTIMATE-START system also uses 4 LGS and is under development. In the future 30-40 m class telescope, ELT/HARMONI, and GMT are planning to have LTAO systems.

Multi conjugate adaptive optics (MCAO; Beckers, 1988) is a system for overcoming a narrow field of view constrained by the anisoplanatic error. In MCAO, several DM conjugated to several heights are used for the purpose. Usually, the conjugation height is determined by considering the typical turbulence profile at the site. By correcting several turbulence layers with dedicated DM, field of view $\sim 1-2$ arcmin, which is wider than SCAO and LTAO is achieved. For modern 8-10 m telescopes, Gemini-South/GeMS and LBT/LINC-NIRVANA are existing systems, and VLT-MAVIS and Gemini-North/GNAO are under development. TMT/NFIRAOS and ELT/MORFEO are planned for future 30-40 m telescopes.

Multi object adaptive optics (MOAO; Hammer et al., 2004; Vidal et al., 2010) is a system that enables simultaneous correction in several target directions. In the MOAO system, several DM are used the same as MCAO. However, each of these DM is dedicated to each astronomical target. Using wavefront measurements in several lines of sight and the tomographic wavefront estimation, the optimum wavefront in the directions of the targets is computed. The correction is performed by the corresponding DM, basically with open-loop control. MOAO is regarded as a parallelized version of the LTAO system. The first on-sky demonstration of the MOAO system has been achieved by Subaru/RAVEN. Gemini-South/GIRMOS is currently developed and ELT/MOSAIC is planned.

Ground layer adaptive optics (GLAO; Rigaut, 2002; Tokovinin, 2004) is a system for achieving a very wide field of view of $\sim 10-20$ arcmin instead of the moderate performance of correction. Ground layer turbulence affects over wide field of view because it is close to the telescope. In the GLAO system, only the wavefront affected by ground layer turbulence is extracted and corrected. For the extraction of the ground layer component, the tomographic wavefront reconstruction or just taking a mean of the several wavefront measurements of the LGS is conducted. Recently, VLT/GRAAL has been using GLAO for imaging of 7.5×7.5

arcmin field of view. ULTIMATE-Subaru is a planned system for an 8-m Subaru telescope, which enables imaging of 14×14 arcmin field of view with an angular resolution of two times higher than the seeing limit. GMT is also planning a GLAO system.

1.4.2 Tomographic wavefront reconstruction

In AO with multiple LGS, the wavefront reconstruction process becomes more complicated than the SCAO case, which is introduced in section 1.3.1. The tomographic wavefront reconstruction is a process of estimating the optimum wavefront in the direction of targets using measurements of multiple WFS. The optimization strategy may differ depending on the AO systems. Here we consider one of the basic tomographic reconstruction matrices called the minimum mean square error (MMSE) reconstructor (Ellerbroek, 2002).

Let's consider N turbulence layers at altitude $h_1, h_2, h_3, \ldots, h_N$ with turbulence strength of $J_1, J_2, J_3, \ldots, J_N$, respectively. Here, turbulence strength is defined as C_n^2 multiplied by the thickness of the turbulence layer, i.e. $J_i = C_n^2(h_i)\Delta h_i$. We also assume wavefront of each turbulence layer is $\boldsymbol{\phi_1}, \boldsymbol{\phi_2}, \boldsymbol{\phi_3}, \ldots, \boldsymbol{\phi_N}$, respectively. We have multiple LGS and corresponding WFS. The wavefront sensing by all the WFS is modeled by modifying equation (1.27);

$$\boldsymbol{s} = \boldsymbol{G}\boldsymbol{P}\boldsymbol{\varphi} + \boldsymbol{n}, \tag{1.38}$$

where $\boldsymbol{s}$ and $\boldsymbol{n}$ are the measurement and its error vector of all the WFS. $\boldsymbol{G}$ is the geometry matrix. $\boldsymbol{P}$ is called the projection matrix, which cuts out the observed wavefront vector from each turbulence layer in the direction of all the LGS. $\boldsymbol{\varphi}$ is the wavefront vector in all the measured turbulence volume, i.e. $\boldsymbol{\varphi} = [\boldsymbol{\phi_1^T}, \boldsymbol{\phi_2^T}, \boldsymbol{\phi_3^T}, \ldots, \boldsymbol{\phi_N^T}]^T$. If we have tomographic wavefront reconstruction matrix $\boldsymbol{R}_{\mathbf{tomo}}$, wavefront in target direction is estimated as

$$\boldsymbol{\varphi}_{\mathbf{tomo}} = \boldsymbol{R}_{\mathbf{tomo}}\boldsymbol{s}. \tag{1.39}$$

Here, we assume that the tomography process is also modeled as a linear transformation. This assumption is valid when the turbulence spatial scale of interest is large enough as $|\boldsymbol{f}| \ll \sqrt{\lambda h}$, where λ is observed wavelength, and the effect of scintillation is ignored. Tomographic error, which is defined as wavefront error from the actual target wavefront $\boldsymbol{\varphi}$ is

$$\sigma^2_{\text{tomo}} = |\boldsymbol{\varphi} - \boldsymbol{\varphi}_{\mathbf{tomo}}|^2 = |\boldsymbol{\varphi} - \boldsymbol{R}_{\mathbf{tomo}}\boldsymbol{s}|^2. \tag{1.40}$$

By minimizing the tomographic error statistically, the optimal tomographic reconstruction matrix $\boldsymbol{R}_{\mathbf{tomo}}$ is written as

$$\boldsymbol{R}_{\mathbf{tomo}} = \left(\boldsymbol{P}^{\boldsymbol{T}}\boldsymbol{G}^{\boldsymbol{T}}\boldsymbol{G}\boldsymbol{P} + \sigma_n^{-2}\boldsymbol{C}_{\boldsymbol{\varphi}}{}^{-1}\right)^{-1}\boldsymbol{P}^{\boldsymbol{T}}\boldsymbol{G}^{\boldsymbol{T}}. \tag{1.41}$$

$\boldsymbol{C}_{\boldsymbol{\varphi}} =< \boldsymbol{\varphi}\boldsymbol{\varphi}^{-1} >$, where $<>$ is statistical mean, denotes statistical covariance of the turbulence layers. The matrix has statistical covariance matrix of each turbulence layer $\boldsymbol{C}_{\boldsymbol{\phi_1}}, \boldsymbol{C}_{\boldsymbol{\phi_2}}, \boldsymbol{C}_{\boldsymbol{\phi_3}}, ..., \boldsymbol{C}_{\boldsymbol{\phi}_N}$ in its diagonal components. Since we know the formalism of spatial power spectrum of Kolmogorov turbulence as equation (1.20), $\boldsymbol{C}_{\boldsymbol{\phi}}$, the statistical covariance matrix of model turbulence with a strength of unity, is computed by Fourier transforming the power spectrum. Finally, we obtain the following,

$$\boldsymbol{C}_{\boldsymbol{\varphi}} = \begin{pmatrix} \boldsymbol{C}_{\boldsymbol{\phi_1}} & 0 & \cdots & 0 \\ 0 & \boldsymbol{C}_{\boldsymbol{\phi_2}} & \cdots & 0 \\ \vdots & \vdots & \ddots & \vdots \\ 0 & 0 & \cdots & \boldsymbol{C}_{\boldsymbol{\phi}_N} \end{pmatrix} = \begin{pmatrix} J_1\boldsymbol{C}_{\boldsymbol{\phi}} & 0 & \cdots & 0 \\ 0 & J_2\boldsymbol{C}_{\boldsymbol{\phi}} & \cdots & 0 \\ \vdots & \vdots & \ddots & \vdots \\ 0 & 0 & \cdots & J_N\boldsymbol{C}_{\boldsymbol{\phi}} \end{pmatrix}. \tag{1.42}$$

σ_n^2 denotes variance of WFS noise. We here assume that the noise is common in all the WFS and $\boldsymbol{C}_{\boldsymbol{n}} =< \boldsymbol{n}\boldsymbol{n}^{-1} >= \sigma_n^2\boldsymbol{I}$, where $\boldsymbol{I}$ is an identity matrix.

By using the MMSE reconstructor, we estimate the three-dimensional structure of atmospheric turbulence by equation (1.39), but we need the information of $\boldsymbol{P}, \boldsymbol{G}, \boldsymbol{\sigma_n^2}, \boldsymbol{C}_{\boldsymbol{\varphi}}$ in advance. The projection matrix is obtained from the heights of turbulence layers and directions of targets and LGS. The geometry matrix is modeled in many ways, as done in SCAO. The WFS noise characteristic is measured in laboratory experiments. Therefore, the most important and uncertain information is turbulence strength at each height, i.e. turbulence profile.

After obtaining the wavefront of turbulence layers, the optimum wavefront in the target direction is estimated. The optimization process is different depending on the kinds of AO systems. In LTAO, the integrated wavefront in the direction of the target is calculated using a projection matrix for the target. Then, the DM command is computed using the control matrix same as the SCAO case. In MCAO, the integrated wavefront in the direction of the target is calculated in the same way as the LTAO case. Since there are multiple DM in MCAO, wavefront distortion made by the multiple DM is integrated using a projection matrix in DM space. By minimizing the integrated DM phase compared to the integrated wavefront, optimum commands for DM are obtained. In MOAO, integrated wavefronts for the multiple targets are calculated using corresponding projection matrices, and DM commands are computed using the control matrices of each DM. In GLAO, only the ground layer wavefront is extracted from the reconstructed wavefront structure, and the DM command is obtained by

multiplying the control matrix. However, in practice, the ground layer wavefront is estimated as the mean wavefront measured by the multiple WFS. This approach is computationally much easier.

1.4.3 ULTIMATE project

Ultra-wide Laser Tomographic Imager and MOS with AO for Transcendent Exploration (ULTIMATE) project is an upgrading project of the Subaru telescope using two types of next-generation AO with multiple LGS.

One is ULTIMATE-START (Akiyama et al., 2020; Terao et al., 2020), LTAO development project. A powerful 20W TOPTICA laser is used for generating four LGS which make asterism with 10-40 arcsec in diameter on the sky. To measure wavefronts from the LGS, a WFS system which consists of four SH-WFS with 32×32 subapertures is placed after AO188, the current AO facility of the Subaru telescope. The wavefront correction is done by a 188-element DM of the AO188 as the first step. Then the DM is to be upgraded to 3228-element DM to make fitting errors much smaller than the current system. The AO loop speed is as fast as 800 Hz. This equipment reduces mainly fitting error and cone effect to make the total wavefront error be $\sim$ 150 nm, which corresponds to a Strehl ratio of 10% at a visible wavelength of $\sim$ 600 nm.

As for recent development status, the bright LGS launching system was developed in 2022. WFS system with four SH-WFS has been developed in Tohoku University and is going to be shipped to Hawaii in 2023. In a few years, the single laser is planned to be divided into four beams to create four LGS. The 3228-element DM is also planned to be installed in place of the current 188-element DM.

Corrected light by the LTAO is planned to be fed to three different science instruments including IRCS; a near infrared imager and spectrograph, Kyoto3DII; a visible integral field spectrograph, and NINJA; a visible to near infrared simultaneous spectrograph.

The other is ULTIMATE-Subaru (Hayano et al., 2014; Minowa et al., 2017; Minowa et al., 2022), GLAO development project. Four LGS generated by two 20W bright lasers are arranged in asterism with 20 arcmin in diameter. The corresponding WFS are 32×32 SH-WFS. The wide field correction is performed using an adaptive secondary mirror, which is a DM placed at the position of the telescope secondary mirror. Since the GLAO system only corrects ground layer components, the typical total wavefront error of the system is $\sim$ 500 nm. The corrected wavefront is fed to a wide field imager making it possible to observe 14×14 arcmin field of view at the same time. The wide field of view and sensitivity by GLAO enables efficient narrow band search of galaxies at very high redshift around >7 such as Lyman alpha emitters or Lyman break galaxies.

1.4.4 Structure formation of star-forming galaxies

One of the scientific objectives of the ULTIMATE project is understanding the structure formation process of star-forming galaxies (SFGs). In the universe at $1 < z < 3$, known as the period of cosmic noon, SFGs are known to have a disk with a predominant turbulent component and massive star-forming clumps. Guo et al. (2015) examined how the fraction of SFGs with clumps varies with respect to a cosmological time of $0.5 < z < 3$ for different galaxy masses. They found that the fraction of SFGs with clamps stay constant at 55% for low-mass galaxies with $\log(M_*/M_\odot) < 9.8$, while it decreases with cosmological time for more massive galaxies. More specifically, for intermediate-mass galaxies with $9.8 < \log(M_*/M_\odot) < 10.6$, the fraction is constant at 45% for $1.5 < z < 3$ but gradually decreases to $\sim 30\%$ for $z \sim 0.5$. For massive galaxies of $10.6 < \log(M_*/M_\odot)$, the value is constant at 45% for $2 < z < 3$ but drops rapidly to $\sim 15\%$ for $z \sim 0.5$. Thus, while it is suggested that disks with predominant turbulent components and giant star-forming clumps have evolved at a rate dependent on galaxy mass into disks with predominant rotational components and bulges seen in SFGs in the local universe, it is still unclear what physical processes are responsible for this evolution.

To answer this question, it is important to study the distribution and kinematics of star-forming clumps and stars in distant SFGs at $z < 3$ with a high spatial resolution that resolves the size of the clumps. Guo et al. (2018) showed that the typical scale of the star-forming clump is on the order of kpc and that the typical mass is a few $10^9 M_\odot$. These scales are consistent with the Toomre scale, which describes the stability of gas disks, and the mass scale, which causes gravitational instability in disks with a gas-rich predominantly turbulent component. However, the study of the distant SFG structures with a spatial resolution of up to 30 pc using gravitational lensing magnification pointed out that the size of star-forming clumps may not have been fully resolved at the spatial resolution of previous instruments and may have been overestimated (Cava et al., 2018).

In order to resolve the scale of clumps in distant SFGs and investigate their distribution and kinematics, narrow-band imaging or integral field spectroscopy (IFS) over a wide spectral range becomes a powerful tool. For SFGs at $z < 3$, Hα emission lines are captured by narrow-band imaging to study the distribution of star-forming clumps in the galaxy. Such observations in the wide near-infrared field of view provided by GLAO capture many galaxies in several redshift ranges at once, making it possible to construct a statistical sample of SFGs. The combination of IFS and LTAO, which achieves diffraction limit over a wide range of wavelengths down to visible wavelength allows us to study the distribution and kinematics of both star-forming clumps and evolved stellar components for a single galaxy by capturing Hα emission line and 4000 Å break at once. In particular, the diffraction limit in the visible

wavelength range explored by LTAO provides important information, since it is difficult to achieve even by the James Webb Space Telescope (JWST) due to its lack of spectral sensitivity.

1.5 Scope of the thesis

This thesis plays an important role in the development of the next-generation AO system with multiple LGS at the Subaru telescope through the following two studies.

Atmospheric turbulence profiling at Subaru telescope

The first study is a measurement of the atmospheric turbulence profile at the Subaru telescope. Information on atmospheric turbulence profile is important for the design and operation of AO with multiple LGS and WFS.

First, in the context of LTAO, the atmospheric turbulence profile is prior information needed to construct the tomographic wavefront reconstruction matrix, as described in section 1.4.2. The structure of atmospheric turbulence changes over a variety of time scales: seasonal, day/night, and hourly to minute scales. Therefore, it is ideal to measure the atmospheric turbulence profile in quasi-real time and update the tomographic wavefront reconstruction matrix. For example, Gendron et al. (2014) and Farley et al. (2020) performed analytical simulations using atmospheric turbulence profile measured at La Palma and Paranal, respectively, and found that it is optimal to update tomographic wavefront reconstruction matrix using averaged profile over a timescale of 10-20 minutes. As for the altitude resolution of the profile measurement, a relatively coarse resolution of a few layers is sufficient for LTAOs with narrow LGS separation angles. In fact, for example, VLT/GALACSI constructs the wavefront reconstruction matrix using an MMSE-based method that assumes two layers, a surface layer and a higher layer.

For GLAO performance simulation, the ground layer turbulence profile is the largest uncertainty, and it is important to reflect the actual measurement results. Because ground layer turbulence, especially dome seeing, may vary depending on the telescope and dome structure, on-site measurements are essential. In addition, a fine altitude resolution of about 20 m is needed to measure the profile that resolves the dome structure.

In this study, a new atmospheric turbulence profiler consisting of two SH sensors is developed and directly mounted on the Subaru telescope to demonstrate methods for real-time measurement of free atmospheric turbulence above 1 km with a resolution of several kilometers and ground layer turbulence below 400 m with a resolution of approximately 20

m, at the same time. In Chapter 2, we review atmospheric turbulence profiling methods used in previous studies as an introduction, describe the instrumentation of the new atmospheric turbulence profiler, and then describe observations at the Subaru telescope, data analysis, results, discussion, and conclusions.

Rolling shutter effect on wavefront sensing

The second study is the evaluation of the effect of the rolling shutter mode of detectors on wavefront sensing. Conventionally, charge coupled devices (CCD) have been mostly used as detectors in AO WFS. On the other hand, recent advances in detector development have led to the emergence of complementary metal oxide semiconductors (CMOS) that are superior to conventional CCD in terms of readout speed, readout noise, quantum efficiency, and format size. For AO systems, improvements in readout speed, readout noise, and quantum efficiency of WFS improve temporal errors. In addition, future AO systems of 30-40 m class telescopes require large-format detectors because the number of WFS spots and the number of pixels needed to sample the spots increase compared to those of 8-10 m class telescopes. Therefore, there is significant worth in considering CMOS as detectors for WFS. However, the rolling shutter mode used in many CMOS has a disadvantage in that each pixel row that makes up the detector is exposed at a different time, resulting in distorted images of fast-moving objects. To date, there has been little quantitative evaluation of the impact of image distortion on wavefront measurements.

In this study, assuming detectors with two common rolling shutter modes, we verify that a simple model reproduces their behavior as WFS, and then run AO simulations to evaluate their impact on wavefront measurement error. In Chapter 3, we summarize the general characteristics of detectors and requirements for AO WFS as an introduction, then describe the rolling shutter modeling, followed by the results of the AO simulation and conclusions.

Finally, in Chapter 4, we summarize the conclusions of this thesis and discuss future perspectives.

Chapter 2

Atmospheric Turbulence Profiling at Subaru Telescope

2.1 Introduction

2.1.1 Atmospheric turbulence effect on propagating light

In ground-based astronomical observations in visible and near-infrared wavelength, light from astronomical objects is collected by telescopes and guided to instruments for imaging or spectroscopy. As the light passes through the fluctuating refractive index field created by atmospheric turbulence, the phase of the light fluctuates, affecting the performance of the image when it is focused. This section provides a theoretical explanation of these effects based on Roddier (1981) and Tatarski (1971).

The propagation of light with wavefront distortions to the ground is described by Fresnel diffraction. Because the amplitude or brightness of light differs from object to object, we normalize the amplitude of light that passes through a turbulent layer to 1. Then complex amplitude of light before propagation is expressed as $\exp[i\phi(\boldsymbol{x})]$, where i is the imaginary unit. Complex amplitude $\Psi(\boldsymbol{x})$ of the light after propagation to the ground by Fresnel diffraction is,

$$\Psi(\boldsymbol{x}) = \exp[i\phi(\boldsymbol{x})] * \left[\frac{1}{i\lambda z}\exp\left(i\pi\frac{|\boldsymbol{x}|^2}{\lambda z}\right)\right], \tag{2.1}$$

where z is the propagation distance, λ is the wavelength of the light, and $*$ means convolution. We further assume here that the weak turbulence approximation, $\phi(\boldsymbol{x}) \ll 1$. It has been shown by Young (1970) that the approximation is valid for observations in directions where

the zenith angle does not exceed 60 degrees. Therefore,

$$\Psi(\boldsymbol{x}) \sim (1 + i\phi(\boldsymbol{x})) * \left[\frac{1}{i\lambda z}\exp\left(i\pi\frac{|\boldsymbol{x}|^2}{\lambda z}\right)\right]. \tag{2.2}$$

The amplitude fluctuations $\chi(\boldsymbol{x})$ and wavefront distortions $\psi(\boldsymbol{x})$ of the light after propagation is expressed by taking absolute and argument for equation (2.2) as follows,

$$\chi(\boldsymbol{x}) = 1 + \phi * \frac{1}{\lambda z}\cos\left(\pi\frac{|\boldsymbol{x}|^2}{\lambda z}\right), \tag{2.3}$$

$$\psi(\boldsymbol{x}) = \phi * \frac{1}{\lambda z}\sin\left(\pi\frac{|\boldsymbol{x}|^2}{\lambda z}\right). \tag{2.4}$$

Also, the power spectrum of amplitude fluctuations Φ_χ and wavefront distortions Φ_ψ are,

$$\Phi_\chi(\boldsymbol{f}) = \Phi_\phi \sin^2(\pi\lambda z|\boldsymbol{f}|^2) = 9.7\times10^{-3}k^2|\boldsymbol{f}|^{-11/3}\sin^2(\pi\lambda z|\boldsymbol{f}|^2)C_n^2(z)\Delta z, \tag{2.5}$$

$$\Phi_\psi(\boldsymbol{f}) = \Phi_\phi \cos^2(\pi\lambda z|\boldsymbol{f}|^2) = 9.7\times10^{-3}k^2|\boldsymbol{f}|^{-11/3}\cos^2(\pi\lambda z|\boldsymbol{f}|^2)C_n^2(z)\Delta z. \tag{2.6}$$

The details of this part of the calculation are given in the appendix B. The fact that

$$\Phi_\phi(\boldsymbol{f}) = \Phi_\chi(\boldsymbol{f}) + \Phi_\psi(\boldsymbol{f}) \tag{2.7}$$

means that the wavefront distortion energy injected by the atmospheric turbulence is distributed between amplitude and wavefront distortions as it propagates to the ground.

Due to the amplitude fluctuation of light, the measured flux of an astronomical object changes in time and space. This is known as scintillation, a phenomenon observable as the twinkling of a star. Since the energy of light is proportional to the square of its amplitude, the flux fluctuation $I(\boldsymbol{x})$ is expressed, by using the weak turbulence approximation, as follows,

$$I(\boldsymbol{x}) = \chi(\boldsymbol{x})^2 \sim 1 + 2\phi * \frac{1}{\lambda z}\cos\left(\pi\frac{|\boldsymbol{x}|^2}{\lambda z}\right). \tag{2.8}$$

Therefore, power spectrum of scintillation Φ_I is

$$\Phi_I(\boldsymbol{f}) = 4\Phi_\chi(\boldsymbol{f}) = 1.53|\boldsymbol{f}|^{-11/3}\left[\frac{\sin(\pi\lambda z|\boldsymbol{f}|^2)}{\lambda}\right]^2 C_n^2(z)\Delta z \tag{2.9}$$

Also, due to the wavefront distortion of light, the local tilt of the beam changes in time and space. This is called beam wander or tip-tilt and corresponds to the effect of the position of the object image changing from time to time. When α and β are local slopes of wavefront

measured in x and y directions, respectively,

$$\alpha(\boldsymbol{x}) = -\frac{\partial\psi(\boldsymbol{x})}{\partial x}, \tag{2.10}$$

$$\beta(\boldsymbol{x}) = -\frac{\partial\psi(\boldsymbol{x})}{\partial y}. \tag{2.11}$$

Thus, the power spectra of the fluctuations of local slopes are,

$$\Phi_\alpha(\boldsymbol{f}) = (2\pi f_x)^2\Phi_\psi(\boldsymbol{f}) = 15.1 f_x^2|\boldsymbol{f}|^{-11/3}\left[\frac{\cos(\pi\lambda z|\boldsymbol{f}|^2)}{\lambda}\right]^2 C_n^2(z)\Delta z, \tag{2.12}$$

$$\Phi_\beta(\boldsymbol{f}) = (2\pi f_y)^2\Phi_\psi(\boldsymbol{f}) = 15.1 f_y^2|\boldsymbol{f}|^{-11/3}\left[\frac{\cos(\pi\lambda z|\boldsymbol{f}|^2)}{\lambda}\right]^2 C_n^2(z)\Delta z. \tag{2.13}$$

For actual atmospheric turbulence, which consists of multiple turbulent layers, we neglect terms that are more than the second order of the fluctuations based on the weak turbulence approximation. Therefore, effects from multiple turbulence layers are represented as the sum of the contributions from each of the turbulence layers, that is,

$$\Phi_I(\boldsymbol{f}) = \int_0^\infty 1.53|\boldsymbol{f}|^{-11/3}\left[\frac{\sin(\pi\lambda z|\boldsymbol{f}|^2)}{\lambda}\right]^2 C_n^2(z)dz, \tag{2.14}$$

$$\Phi_\alpha(\boldsymbol{f}) = \int_0^\infty 15.1 f_x^2|\boldsymbol{f}|^{-11/3}\left[\frac{\cos(\pi\lambda z|\boldsymbol{f}|^2)}{\lambda}\right]^2 C_n^2(z)dz, \tag{2.15}$$

$$\Phi_\beta(\boldsymbol{f}) = \int_0^\infty 15.1 f_y^2|\boldsymbol{f}|^{-11/3}\left[\frac{\cos(\pi\lambda z|\boldsymbol{f}|^2)}{\lambda}\right]^2 C_n^2(z)dz. \tag{2.16}$$

2.1.2 Reviewing measurement methods of atmospheric turbulence

To date, a number of methods have been proposed and demonstrated to measure atmospheric turbulence in real time by observing stars. Differential Image Motion Monitor (DIMM) proposed by Sarazin and Roddier (1990) is a method to measure seeing by measuring the positional variation of two star images produced by each of two separate apertures in a single telescope. On a telescope with an aperture of about ~ 30 cm, two stellar images are observed simultaneously by attaching a DIMM plate that divides the aperture into two circular sub-apertures with a diameter of ~ 6 cm. Using the differential motion of the two star images, seeing is calculated without being affected by telescope system vibration.

In order to obtain atmospheric turbulence profiles in real time, many methods have been proposed and demonstrated using triangulation with two separate stars. Scintillation detection and ranging (SCIDAR; Rocca et al., 1974) is a method for obtaining atmospheric

turbulence profiles from covariance maps of scintillation in two directions separated by a few arcseconds. SCIDAR has since been applied in many ways including Generalized-SCIDAR (Avila et al., 1997), which enables near-ground profiling by making the detection plane optically conjugate to the negative altitude, and Stereo-SCIDAR (Shepherd et al., 2014), which improves the signal-to-noise ratio by using separate detectors for each of the two directions. Slope detection and ranging (SLODAR; Wilson, 2002; Butterley et al., 2006) is similar in principle to SCIDAR, but it uses covariance maps of wavefront slopes measured with a SH-WFS instead of scintillation. Similarly, a method to measure both scintillation and wavefront slope using a SH sensor is known as Coupled slodar and scidar (CO-SLIDAR; Védrenne et al., 2007). In these methods, there is a tradeoff between the altitude resolution and the highest measurable altitude. For example, the surface layer SLODAR (Osborn et al., 2010) measures ground layer turbulence profile with a resolution of $\sim$ 10 m by observing a widely-separated star pair, but is sensitive only up to $\sim$ 100 m.

Atmospheric turbulence profile is estimated even with a single star from temporal correlation or scintillation spatial scale dependence on the propagation distance. Such single-star methods are realized with a small-aperture telescope, while a large-aperture telescope with a diameter larger than $\sim$ 1 m is required in the measurements with two stars to measure turbulence at high altitudes. Single-star-SCIDAR (Habib et al., 2006) is based on the principle of SCIDAR, but measures the correlation of scintillation at different times in a single direction by using the assumption of frozen flow. Multi aperture scintillation sensor (MASS; Tokovinin and Kornilov, 2007) is a widely-used method that reconstructs a 6-layer turbulence profile from scintillation measured by multiple annular apertures with different radii. Since the spatial scale of scintillation depends on the altitude of turbulence, the intensity of the measured scintillation by each annular aperture is converted to an atmospheric turbulence profile. The scintillation-based technique of MASS is not sensitive to ground layer turbulence and is often combined with DIMM to estimate the ground layer turbulence strength with the difference between the MASS and DIMM measurements.

Recently, several new approaches have been proposed to improve the altitude resolution of MASS. SH-MASS (Ogane et al., 2021) is an applied method that allows MASS to be implemented with SH-WFS. Thanks to a large number of spatial frequencies extracted from combinations of spots, SH-MASS achieves higher altitude resolution than classical MASS. Similarly, full aperture scintillation sensor (FASS; Guesalaga et al., 2021) and ring-image next generation scintillation sensor (RINGSS; Tokovinin, 2021) improve altitude resolution by using full aperture image instead of several annular apertures.

Some methods with single-star measurements combine scintillation and wavefront slope from a SH sensor. Single CO-SLIDAR (SCO-SLIDAR; Védrenne et al., 2007) is a method

that fits the measured scintillation and wavefront slope correlations to a theoretical power spectrum. Shack Hartmann image motion monitor (SHIMM; Perera et al., 2023) is a similar procedure, but uses a larger 4.1 cm subaperture. The scintillation-based approach generally has a wide altitude range for the turbulence profiling, while its altitude resolution is determined by the pupil sampling size and is typically limited down to a few hundred meters considering the signal-to-noise ratio for reliable estimation.

Features of the above methods are summarized in table 2.1.

Table 2.1 Summary of atmospheric turbulence measurement methods

Name	Principle	Target	Separation	Largest baseline	Smallest baseline	Scintillation	Slope	Year
SCIDAR	triangulation	binary	2 arcsec	0.1 m	3 cm	Yes	No	1974
DIMM	image motion	single	-	0.2 m	4 cm	No	Yes	1990
G-SCIDAR	triangulation	binary	8 arcsec	2.5-4.2 m	3-4 cm	Yes	No	1997
SLODAR	triangulation	binary	28 arcsec	4.2 m	52 cm	No	Yes	2002
SS-SCIDAR	temporal cov.	single	-	1.5 m	2 cm	Yes	No	2006
MASS	Fresnel's radius	single	-	0.13 m	2 cm	Yes	No	2007
CO-SLIDAR	triangulation	binary	6 arcsec	1.5 m	15 cm	Yes	Yes	2007
SCO-SLIDAR	temporal cov.	single	-	0.35 m	7 cm	Yes	Yes	2007
Stereo-SCIDAR	triangulation	binary	10 arcsec	1.0 m	1.25 cm	Yes	No	2014
FASS	Fresnel's radius	single	-	0.25 m	0.67 cm	Yes	No	2020
SH-MASS	Fresnel's radius	single	-	0.5-1.4 m	2 cm	Yes	Yes	2021
RINGSS	Fresnel's radius	single	-	0.13 m	NA	Yes	Yes	2021
SHIMM	image motion	single	-	0.5 m	4 cm	Yes	Yes	2023

SCIDAR: Rocca et al. (1974), DIMM: Sarazin and Roddier (1990)

Generalized SCIDAR: Avila et al. (1997), SLODAR: Wilson (2002)

Single star SCIDAR: Habib et al. (2006), MASS: Tokovinin and Kornilov (2007)

CO-SLIDAR: Védrenne et al. (2007), SCO-SLIDAR: Védrenne et al. (2007)

Stereo-SCIDAR: Shepherd et al. (2014), FASS: Guesalaga et al. (2020)

SH-MASS: Ogane et al. (2021), RINGSS: Tokovinin (2021)

SHIMM: Perera et al. (2023)

2.1.3 Principles of methods considered in this study

We explain detailed principles of DIMM, MASS, SH-MASS, and SLODAR, which are used in this study.

DIMM

DIMM uses two small apertures mounted on a single telescope. Let the direction along the line connecting the two apertures be the x direction and the direction perpendicular to it be the y direction, and let the positions of the two star images be $(x_A, y_A), (x_B, y_B)$, respectively, then the DIMM measurement quantities are as follows,

$$\sigma_x^2 =< (x_A - x_B)^2 >, \tag{2.17}$$

$$\sigma_y^2 =< (y_A - y_B)^2 > . \tag{2.18}$$

On the other hand, the position of the two star images is regarded as measuring the average slope of the phase on each aperture. Thus, DIMM measures the structure function of the slope of the ray at the distance between the two apertures. The structure function of the slope fluctuation of a ray is obtained theoretically by Fourier transforming the power spectrum expressed by equation (2.13) to obtain the correlation function, and then transforming it to the structure function by equation (1.7). As a result,

$$\sigma_x^2 = 0.358\lambda^2 r_0^{-5/3} D^{-1/3} \left[1 - 0.541 \left(\frac{d}{D} \right)^{1/3} \right], \tag{2.19}$$

$$\sigma_y^2 = 0.358\lambda^2 r_0^{-5/3} D^{-1/3} \left[1 - 0.810 \left(\frac{d}{D} \right)^{1/3} \right], \tag{2.20}$$

where λ is the observed wavelength, r_0 is the Fried parameter, D is the diameter of the aperture made by the DIMM plate and d is the distance between the two apertures. By fitting the measured quantities with a theoretical equation, r_0 is estimated. One of the features of DIMM is that it can subtract the effect caused by telescope vibration by taking the difference between the two star image positions on a telescope. Also, it is used as a portable atmospheric turbulence measurement system for surveying telescope construction sites because it is implemented on a relatively small telescope.

MASS

MASS estimates turbulence profile based on the fact that the spatial frequency of stellar scintillation depends on the apparent altitude of the turbulence layer.

Let a MASS aperture X. The scintillation measured by aperture X is characterized by the normal scintillation index (NSI) s_{X} defined as

$$s_{\mathrm{X}} = \mathrm{Var}\left[\frac{I_{\mathrm{X}}}{\langle I_{\mathrm{X}}\rangle}\right], \tag{2.21}$$

where I_{X} is the intensity measured by aperture X. The <> denotes the statistical mean and Var denotes the statistical variance. In the same way, let another aperture Y. The correlation between scintillation measured at aperture X and aperture Y is characterized by the differential scintillation index (DSI) s_{XY} defined as,

$$s_{\mathrm{XY}} = \mathrm{Var}\left[\frac{I_{\mathrm{X}}}{\langle I_{\mathrm{X}}\rangle} - \frac{I_{\mathrm{Y}}}{\langle I_{\mathrm{Y}}\rangle}\right] = s_{\mathrm{X}} + s_{\mathrm{Y}} - 2\mathrm{Cov}\left[\frac{I_{\mathrm{X}}}{\langle I_{\mathrm{X}}\rangle}, \frac{I_{\mathrm{Y}}}{\langle I_{\mathrm{Y}}\rangle}\right]. \tag{2.22}$$

On the other hand, these NSI and DSI are expressed analytically, assuming a model of atmospheric turbulence. Scintillation indices in the analytical form are written respectively as

$$s_{\mathrm{X}} = \iint \Phi_I(f_x, f_y)|\mathcal{F}[A_{\mathrm{X}}(x,y)]|^2 df_x df_y, \tag{2.23}$$

$$s_{\mathrm{XY}} = \iint \Phi_I(f_x, f_y)|\mathcal{F}[A_{\mathrm{X}}(x,y) - A_{\mathrm{Y}}(x,y)]|^2 df_x df_y, \tag{2.24}$$

where $\Phi_I(f_x, f_y)$ is the power spectrum of scintillation on the aperture as a function of spatial frequency (f_x, f_y). $A(x,y)$ is the normalized aperture function, which returns 1 divided by the aperture area for (x,y) inside the aperture and 0 for others. $\mathcal{F}$ denotes Fourier transformation. Based on Kolmogorov's turbulence model, weak turbulence approximation, and Fresnel's propagation, the scintillation power spectrum is written as a linear sum of N_{layer} turbulent layers' power spectrum as follows,

$$\Phi_I(\boldsymbol{f}) = \sum_i^{N_{\mathrm{layer}}} 1.53|\boldsymbol{f}|^{-11/3}\left\{\frac{\sin(\pi\lambda z_i|\boldsymbol{f}|^2)}{\lambda}\right\}^2 C_n^2(z_i)\Delta z_i, \tag{2.25}$$

where $\boldsymbol{f}$ is two-dimensional spatial frequency vector, λ is observed wavelength. z_i, $C_n^2(z_i)$, and Δz_i denotes height, strength, and thickness of i-th turbulence layer along the line of sight, respectively.

By substituting equation (2.25) into (2.23) and (2.24), following formula are obtained.

$$s_{\mathrm{X}} = \sum_{i}^{N_{\mathrm{layer}}} W_{\mathrm{X},i} J_i, \tag{2.26}$$

$$s_{\mathrm{XY}} = \sum_{i}^{N_{\mathrm{layer}}} W_{\mathrm{XY},i} J_i, \tag{2.27}$$

where

$$W_{\mathrm{X},i} = \iint 1.53 f^{-11/3} \left\{ \frac{\sin(\pi \lambda z_i f^2)}{\lambda} \right\}^2 |\mathcal{F}[A_{\mathrm{X}}(x,y)]|^2 df_x df_y, \tag{2.28}$$

$$W_{\mathrm{XY},i} = \iint 1.53 f^{-11/3} \left\{ \frac{\sin(\pi \lambda z_i f^2)}{\lambda} \right\}^2 |\mathcal{F}[A_{\mathrm{X}}(x,y) - A_{\mathrm{Y}}(x,y)]|^2 df_x df_y. \tag{2.29}$$

$$J_i = C_n^2(z_i)\Delta z_i. \tag{2.30}$$

$W_{X,i}$ and $W_{XY,i}$ are called normal weighting functions and differential weighting functions, respectively. The weighting functions are calculated from the information of aperture geometry, measurement condition, and turbulence height assumption. By solving equations (2.26) and (2.27), turbulence strengths $J_i = C_n^2(z_i)\Delta z_i$ of multiple layers are estimated.

SH-MASS

SH-MASS is an applied method that allows MASS to be implemented with the SH sensor. While the MASS instrument divides the pupil into several concentric annuli, SH-MASS utilizes combinations of SH sensor subapertures to measure scintillation in the corresponding spatial frequency range. In SH-MASS, an aperture is defined as a combination of two subapertures of the SH sensor shown in figure 2.1. Hence, measured brightness at each aperture becomes the sum of measured brightness at the two subapertures, i.e. $I_X = I_i + I_j$ where I_i and I_j is the brightness of i-th and j-th spot, respectively. By using this aperture

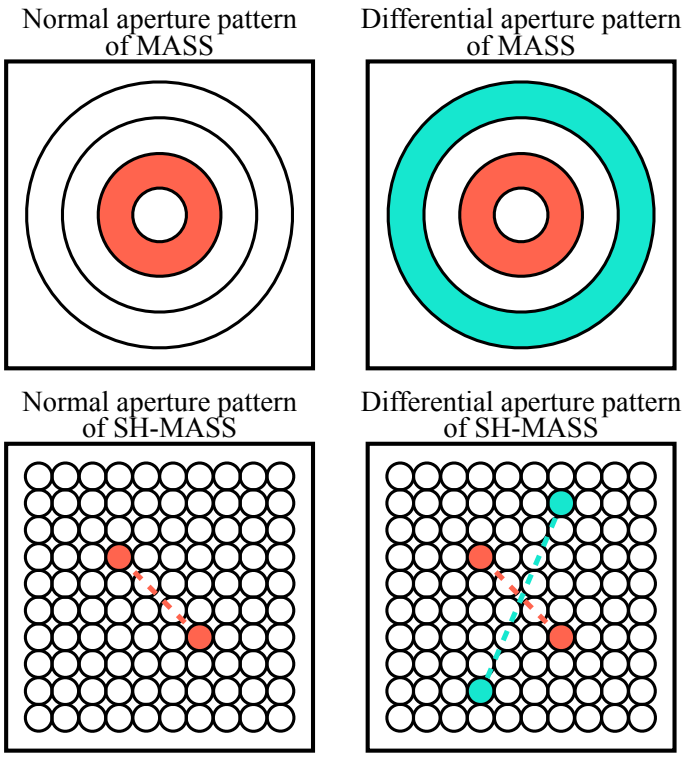

Fig. 2.1 Normal (left) and differential (right) aperture patterns for the traditional MASS (top) and SH-MASS (bottom).

definition, the scintillation indices in equations (2.21) and (2.22) are rewritten as follows,

$$\begin{aligned} s_X &= \mathrm{Var}\left[\frac{I_X}{\langle I_X\rangle}\right] \\ &= \mathrm{Var}\left[\frac{I_i+I_j}{\langle I_i+I_j\rangle}\right] \\ &= \frac{\mathrm{Var}[I_i]+\mathrm{Var}[I_j]+2\mathrm{Cov}[I_i,I_j]}{(\langle I_i\rangle+\langle I_j\rangle)^2}, \end{aligned} \tag{2.31}$$

$$\begin{aligned} s_{XY} &= s_X+s_Y-2\mathrm{Cov}\left[\frac{I_X}{\langle I_X\rangle},\frac{I_Y}{\langle I_Y\rangle}\right] \\ &= s_X+s_Y-2\mathrm{Cov}\left[\frac{I_i+I_j}{\langle I_i+I_j\rangle},\frac{I_k+I_l}{\langle I_k+I_l\rangle}\right] \\ &= s_X+s_Y-2\frac{\mathrm{Cov}[I_i,I_k]+\mathrm{Cov}[I_j,I_k]+\mathrm{Cov}[I_i,I_l]+\mathrm{Cov}[I_j,I_l]}{(\langle I_i\rangle+\langle I_j\rangle)(\langle I_k\rangle+\langle I_l\rangle)}. \end{aligned} \tag{2.32}$$

As seen from the final form of the scintillation indices, scintillation indices in SH-MASS are computed by statistical mean, variance, and covariance of the time series of spot brightness.

The strong point of the SH-MASS method is the large number of spatial frequencies measured by its aperture pattern. In the traditional MASS, the telescope aperture is divided into 4 concentric annular apertures with a diameter of 2.0, 3.7, 7.0, and 13.0 cm. Four NSI and six DSI are measured. On the other hand, in the SH-MASS, the telescope aperture is divided into SH subapertures to make more spatial scales. The number of spatial patterns becomes 15 normal + 28 differential when 5×5 subapertures are used, and 51 normal + 234 differentials when 10×10 subapertures are used. Thanks to the spatial resolution, profiling accuracy or altitude resolution becomes higher than the classical method as shown in figure 2.2. In each panel of the figure, each line shows sensitivity to turbulence at the height shown on the horizontal axis. Different color means the different height of fixed layers to be profiled. The estimation error is propagated from the typical 5% measurement error of scintillation indices. The triangular shape of the sensitivity function means that MASS and SH-MASS have intensity not only at the exact height of the fixed layer but also at turbulence at the surrounding height. As the number of layers to be reconstructed increases, it becomes more difficult to separate the intensity between adjacent layers, which leads to a degradation of estimation accuracy. By comparing the sensitivity function between the traditional MASS and SH-MASS, it is found that the strength estimation accuracy or height resolution of profiling is improved in SH-MASS.

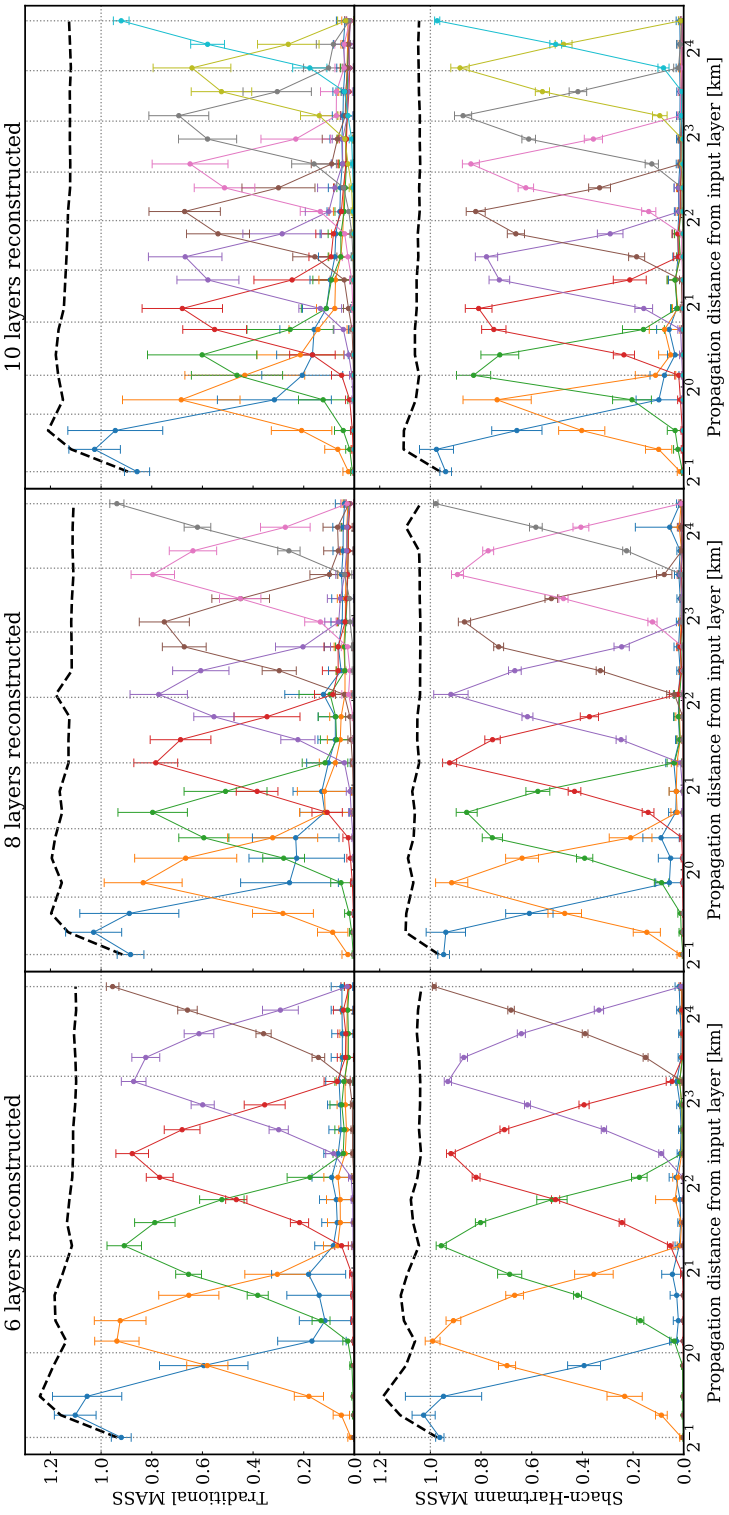

Fig. 2.2 Top panels: The response function for the traditional MASS setup in which turbulence strengths of 6, 8, and 10 layers are reconstructed using scintillation data observed by 4 concentric annular apertures. Bottom panels: The response function for classical SH-MASS setup in which turbulence strengths of 6, 8, and 10 layers are reconstructed using scintillation data observed by 10x10 SH sensor whose subaperture diameter corresponds to 1.3 cm on the primary mirror. In each panel, each triangular line represents the response of each reconstruction layer to the input single turbulence layer. In the cases of 6, 8, and 10 layers are reconstructed, the propagation distances from the reconstruction layers are [0.5, 1.0, 2.2, 4.6, 9.6, 20.0] km, [0.5, 0.8, 1.4, 2.4, 4.1, 7.0, 11.8, 20.0] km, and [0.5, 0.8, 1.1, 1.7, 2.6, 3.9, 5.8, 8.8, 13.3, 20.0] km, respectively. The Black dashed line represents the total sensitivity as a sum of the response of all the reconstruction layers. Gray vertical lines stand for the propagation distance from reconstructed layers, while gray horizontal line stands for the sensitivity when all input turbulence strength is sensed.

SLODAR

Slope Detection And Ranging (SLODAR), proposed by Wilson (2002), is a method for estimating atmospheric turbulence profiles from multiple SH sensor measurements. SLODAR measures the wavefronts of two stars separated by a certain angle θ with corresponding two SH sensors. The paths of light entering the telescope aperture from the two stars have a common volume that overlaps each other at altitudes up to D/θ, where D is the diameter of the aperture. In other words, the wavefront distortion due to the atmosphere at altitudes up to D/θ is commonly measured by the two SH sensors. Furthermore, overlapping light from two stars at a certain altitude $h(< D/\theta)$ has a distance of h/θ on the telescope aperture. Therefore by calculating the cross-correlation of the two SH sensor measurements, turbulence altitude is estimated from the correlation distance and turbulence strength is estimated from the correlation intensity. In reality, the SH sensor measurements are not continuous over the aperture, but discrete in size of the subaperture w, hence the measured altitude is also discrete, and the altitude resolution is w/θ.

Next, we explain how to calculate the turbulence strength from the cross-correlation intensity. The measurement in SLODAR is the cross-correlation of the measurements of the two SH sensors, which is written as follows

$$C_{\mathrm{X}}(\Delta i, \Delta j) = \left\langle \frac{\sum_{i,j}(x^A_{i,j} - \bar{x}^A)(x^B_{i+\Delta i, j+\Delta j} - \bar{x}^B)}{O(\Delta i, \Delta j)} \right\rangle \tag{2.33}$$

$$C_{\mathrm{Y}}(\Delta i, \Delta j) = \left\langle \frac{\sum_{i,j}(y^A_{i,j} - \bar{y}^A)(y^B_{i+\Delta i, j+\Delta j} - \bar{y}^B)}{O(\Delta i, \Delta j)} \right\rangle \tag{2.34}$$

where (i, j) is the index of the subaperture (SH sensor spot) and $x^A_{i,j}$ is the x component of the (i, j)-th spot of the SH sensor corresponding to star A. $\bar{x}^A$ is the value of $x^A_{i,j}$ averaged over all subapertures. $O(\Delta i, \Delta j)$ is the total number of spots separated by $(\Delta i, \Delta j)$ and $< \ldots >$ denotes the statistical mean. Thus, $C_{\mathrm{X}}(\Delta i, \Delta j)$, $C_{\mathrm{Y}}(\Delta i, \Delta j)$ represent the cross-correlation of the SH sensor measurements corresponding to stars A and B. As for statistical averages, they are replaced by temporal averages in the actual analysis. This is because a statistical number of SH sensor measurements are obtained in a single measurement, assuming that SH sensor measurements are generally made at a rate of a few hundred Hz and that the profile of atmospheric turbulence does not change during a few minutes of measurement.

On the other hand, the cross-correlation of SH sensor measurements is expressed analytically, assuming a model of atmospheric turbulence. Assuming that the center position of the subaperture (i, j) on the pupil is $\boldsymbol{r}_{i,j}$ and that the SH sensor measures the phase tilt at the

edge of each subaperture,

$$x^A_{i,j} = \frac{1}{w}\left[\phi(\boldsymbol{r}_{i,j} + \frac{w}{2}\boldsymbol{e}_{\mathrm{X}}) - \phi(\boldsymbol{r}_{i,j} - \frac{w}{2}\boldsymbol{e}_{\mathrm{X}})\right]. \tag{2.35}$$

where $\boldsymbol{e}_{\mathrm{X}}$ is the unit vector in the x direction. Also, assuming that the slope of the entire wavefront is the slope of the phase at the edge of the aperture, we have

$$\bar{x}^A = \frac{1}{Nw}\left[\phi(\boldsymbol{r}_{N,N/2} + \frac{w}{2}\boldsymbol{e}_{\mathrm{X}}) - \phi(\boldsymbol{r}_{1,N/2} - \frac{w}{2}\boldsymbol{e}_{\mathrm{X}})\right] \tag{2.36}$$

assuming that the number of SH sensor elements is $N \times N$. Similarly, let the center position of the subaperture $(i+\Delta i, j+\Delta j)$ be $\boldsymbol{r}_{i,j} + \boldsymbol{\Delta}_{i,j}$ and let the difference in the fields of view of SH sensors A and B be the angle $\boldsymbol{\theta}$. Since both sensors measure the position offset by $h\boldsymbol{\theta}$ on the atmospheric turbulence at the altitude h,

$$x^B_{i+\Delta i,j+\Delta j} = \frac{1}{w}\left[\phi(\boldsymbol{r}_{i,j} + \boldsymbol{\Delta}_{i,j} + h\boldsymbol{\theta} + \frac{w}{2}\boldsymbol{e}_{\mathrm{X}}) - \phi(\boldsymbol{r}_{i,j} + \boldsymbol{\Delta}_{i,j} + h\boldsymbol{\theta} - \frac{w}{2}\boldsymbol{e}_{\mathrm{X}})\right] \tag{2.37}$$

$$\bar{x}^B = \frac{1}{Nw}\left[\phi(\boldsymbol{r}_{N,N/2} + h\boldsymbol{\theta} + \frac{w}{2}\boldsymbol{e}_{\mathrm{X}}) - \phi(\boldsymbol{r}_{1,N/2} + h\boldsymbol{\theta} - \frac{w}{2}\boldsymbol{e}_{\mathrm{X}})\right]. \tag{2.38}$$

Therefore,

$$\begin{aligned} x^A_{i,j}x^B_{i+\Delta i,j+\Delta j} =& -\frac{1}{2w^2}\left[\phi(\boldsymbol{r}_{i,j} + \frac{w}{2}\boldsymbol{e}_{\mathrm{X}}) - \phi(\boldsymbol{r}_{i,j} + \boldsymbol{\Delta}_{i,j} + h\boldsymbol{\theta} + \frac{w}{2}\boldsymbol{e}_{\mathrm{X}})\right]^2 \\ &+ \frac{1}{2w^2}\left[\phi(\boldsymbol{r}_{i,j} + \frac{w}{2}\boldsymbol{e}_{\mathrm{X}}) - \phi(\boldsymbol{r}_{i,j} + \boldsymbol{\Delta}_{i,j} + h\boldsymbol{\theta} - \frac{w}{2}\boldsymbol{e}_{\mathrm{X}})\right]^2 \\ &+ \frac{1}{2w^2}\left[\phi(\boldsymbol{r}_{i,j} - \frac{w}{2}\boldsymbol{e}_{\mathrm{X}}) - \phi(\boldsymbol{r}_{i,j} + \boldsymbol{\Delta}_{i,j} + h\boldsymbol{\theta} + \frac{w}{2}\boldsymbol{e}_{\mathrm{X}})\right]^2 \\ &- \frac{1}{2w^2}\left[\phi(\boldsymbol{r}_{i,j} - \frac{w}{2}\boldsymbol{e}_{\mathrm{X}}) - \phi(\boldsymbol{r}_{i,j} + \boldsymbol{\Delta}_{i,j} + h\boldsymbol{\theta} - \frac{w}{2}\boldsymbol{e}_{\mathrm{X}})\right]^2. \end{aligned} \tag{2.39}$$

Here, the relation $2(a-b)(c-d) = -(a-c)^2 + (a-d)^2 + (b-c)^2 - (b-d)^2$ is used. Also, using the structure function $D_A(\boldsymbol{r}) =< [A(\boldsymbol{x}) - A(\boldsymbol{x}+\boldsymbol{r})]^2 >$ for the physical quantity A, we obtain

$$\begin{aligned} < x^A_{i,j}x^B_{i+\Delta i,j+\Delta j} >=& -\frac{1}{w^2}D_\phi(\boldsymbol{\Delta}_{i,j} + h\boldsymbol{\theta}) \\ &+ \frac{1}{2w^2}D_\phi(\boldsymbol{\Delta}_{i,j} + h\boldsymbol{\theta} + w\boldsymbol{e}_{\mathrm{X}}) + \frac{1}{2w^2}D_\phi(\boldsymbol{\Delta}_{i,j} + h\boldsymbol{\theta} - w\boldsymbol{e}_{\mathrm{X}}). \end{aligned} \tag{2.40}$$

The wavefront phase structure function $D_\phi(\boldsymbol{r})$ is, assuming Kolmogorov turbulence and Fried length of r_0,

$$D_\phi(\boldsymbol{r}) = 6.88\left(\frac{r}{r_0}\right)^{5/3}. \tag{2.41}$$

Similarly, $< x^A_{i,j}\bar{x}^B >, < \bar{x}^A x^B_{i+\Delta i,j+\Delta j} >, < \bar{x}^A\bar{x}^B >$ are written using wavefront phase structure functions. The same procedure described above is applicable to the slope in the y-direction.

Finally, the measured cross-correlations $\boldsymbol{C}^{\mathrm{obs}}_{\mathrm{X}}, \boldsymbol{C}^{\mathrm{obs}}_{\mathrm{Y}}$ are fitted by superposition of the analytically obtained cross-correlations $\boldsymbol{C}^{\mathrm{theo}}_{\mathrm{X}}, \boldsymbol{C}^{\mathrm{theo}}_{\mathrm{Y}}$ to obtain the Fried length for atmospheric turbulence at each altitude.

$$\mathrm{Minimize}\left\|\left(\boldsymbol{C}^{\mathrm{obs}}_{\mathrm{X}} - \sum_k \boldsymbol{C}^{\mathrm{theo}}_{\mathrm{X}}(h_k, r_{0k})\right) + \left(\boldsymbol{C}^{\mathrm{obs}}_{\mathrm{Y}} - \sum_k \boldsymbol{C}^{\mathrm{theo}}_{\mathrm{Y}}(h_k, r_{0k})\right)\right\|^2 \tag{2.42}$$

2.2 Instrumentation

2.2.1 Design concept

The purpose of the system is to measure free atmospheric turbulence profiles with a wide altitude range of up to ~ 20 km using SH-MASS and ground layer turbulence profiles with a high altitude resolution of ~ 20 m using SLODAR technique. To detect scintillation with the SH sensor, the subaperture must be reduced to a few cm scales, as in SCO-SLIDAR (Védrenne et al., 2007) and SHIMM (Perera et al., 2023). According to Ogane et al. (2021), in which the relation between altitude resolution and the lowest measurable altitude of SH-MASS is studied, a subaperture size of 2 cm is optimal for detecting turbulence at higher than ~ 1 km.

The altitude resolution of SLODAR is determined by the subaperture size and angular separation of the observed star pair. A high altitude resolution of ~ 20 m is achieved by observing a star pair with a separation of ~ 3.5 arcmin. Although the field of view at the optical-side Nasmyth focus is 3.5 arcmin in diameter, a larger field of view up to ~ 5 arcmin is achievable by allowing partial vignetting of the pupil. Actually, only a part of the telescope pupil with a size of 1.32×1.32 m is sufficient considering that the typical spatial scale of scintillation is at most ~ 10 cm and that ground layer up to ~ 400 m is measurable by the SLODAR technique. Each star should be brighter than ~ 6 magnitude in the V or R band to achieve a spot signal-to-noise ratio of more than ~ 5 with the 2 cm subaperture. Although the number of targets is very limited due to the angular separation and the brightness, there

Table 2.2 Specification of the turbulence profiler

Parameter	Designed value
Target	
Number of targets	2
Angular separation	180-300 arcsec
Magnitude	<~ 6 at V or R band
Telescope	
Effective aperture size	1.32 × 1.32 m
Turbulence profiler	
Number of Shack-Hartmann sensors	2
Number of subapertures	66 × 66
Subaperture size	2.0 cm
FA profiling method	SH-MASS
FA height resolution	a few km
FA height range	>~ 1 km
GL profiling method	SLODAR
GL height resolution	~ 20 m
GL height range	<~ 400 m

is at least one target that is observable from the Subaru telescope throughout a year. The specification of the turbulence profiler is summarized in Table 2.2.

2.2.2 Optical design

A conceptual drawing of the turbulence profiler attached on the surface of the Auto Guider & Shack Hartmann module (AG-SH module) at the optical-side Nasmyth focus of the Subaru telescope is shown in figure 2.3. The turbulence profiler consists of two symmetric SH sensors. The optical system on the rear side of the telescope is called SH sensor 1 (SH-1) and that on the front side is called SH sensor 2 (SH-2). Light from the object reaches the turbulence profiler as a convergent beam through the telescope's composite focal length of approximately 104 m. The turbulence profiler uses pickoff mirrors to pick up beams from the two stars at 470 mm upstream of the telescope focal plane and introduce the rays into the two SH sensors. To deal with the different separation angles of observation targets, the pickoff mirror moves in a range of 1.5-2.5 arcminutes from the center of the telescope field of view.

Figure 2.4 shows details of one of the SH sensors. The other SH sensor has a symmetric optical design. A trombone mirror system, which consists of two fold mirrors, adjusts optical path length to make the focal plane at the fixed position in the profiler system. After the trombone, the beam is collimated by a collimator lens with a focal length of 750 mm. The MLA consists of 66×66 microlenses with a diameter and pitch of 150 μm and a focal length

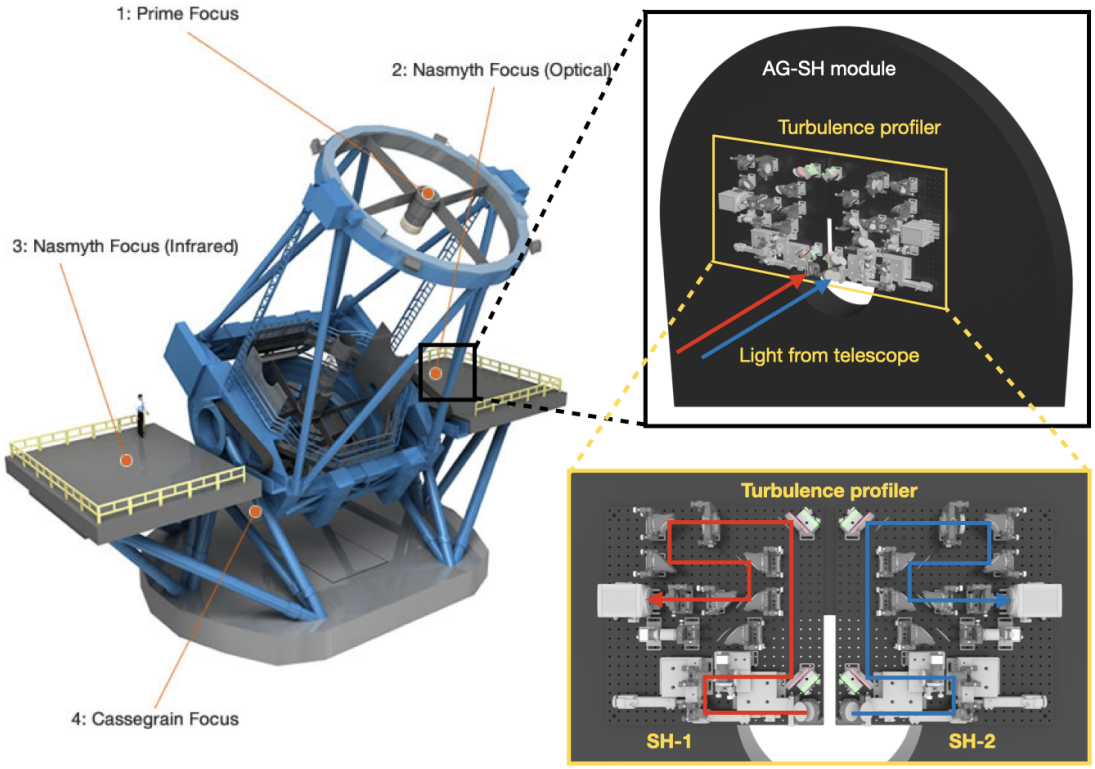

Fig. 2.3 Conceptual drawing of the atmospheric turbulence profiler. The profiler system is installed on the surface of the AG-SH module, which is shown as a black semi-circular object on one of the Nasmyth focus platforms (optical Nasmyth side) of the Subaru telescope. (credit of telescope figure: National Astronomical Observatory of Japan)

Table 2.3 Specification of the Shack-Hartmann sensor

Parameter	Designed value
Number of subapertures	66×66
Subaperture size	2.0 cm
Subaperture FoV	25 arcsec
Number of pixels in a subaperture	10
Pixel scale	2.5 arcsec pix^{-1}
Pixel size	6.5 μm
Readout noise	1.6 electron pix^{-1}
QE	>50% at 420-800 nm
	82% at peak

of 10 mm and is arranged at a position conjugate to the telescope primary mirror. The pitch of the MLA corresponds to a subaperture of 2.0 cm on the primary mirror. Thus, the pupil area covered by the MLA corresponds to a square area of approximately 1.32×1.32 m on the primary mirror, which is a portion of the entire aperture of the 8.2 m telescope. Focused spots by the MLA are then reduced by 60% in F-number and form an image on the SH sensor detector. The diffraction limit of 2 cm subaperture determines the FWHM size of each spot of 7.55 arcsec at 600 nm, which is sampled by ~ 3 pixels of the detector.

We also have telescope focus and pupil cameras to assist object acquisition to the optical axis of each SH sensor and to check the observed pupil position, respectively. The focus camera has a field of view of 10×10 arcsec, which allows us to check the tracking by the telescope, field rotation by the image rotator, acquisition by the pick-off arms, and focusing by the trombone system. The pupil camera monitors the area of 3 m diameter on the primary mirror. The observed areas of the telescope pupil are checked by looking at the shade position by telescope structures, such as spiders, or the secondary mirror, on the pupil camera or the SH sensors. When the observed pupil area is apparently different between the two SH systems, we use two motorized picomotor mirrors to adjust the observed pupil areas to each other. The remaining misregistration between the two areas is precisely matched by SLODAR analysis software using spatial synchronization of spots on the two SH sensors. The optical specification of the SH sensor is summarized in table 2.3.

Also, the transmissive optics, reflective optics, and detectors used in the turbulence profiler are summarized in the table 2.4, 2.5, 2.6, respectively.

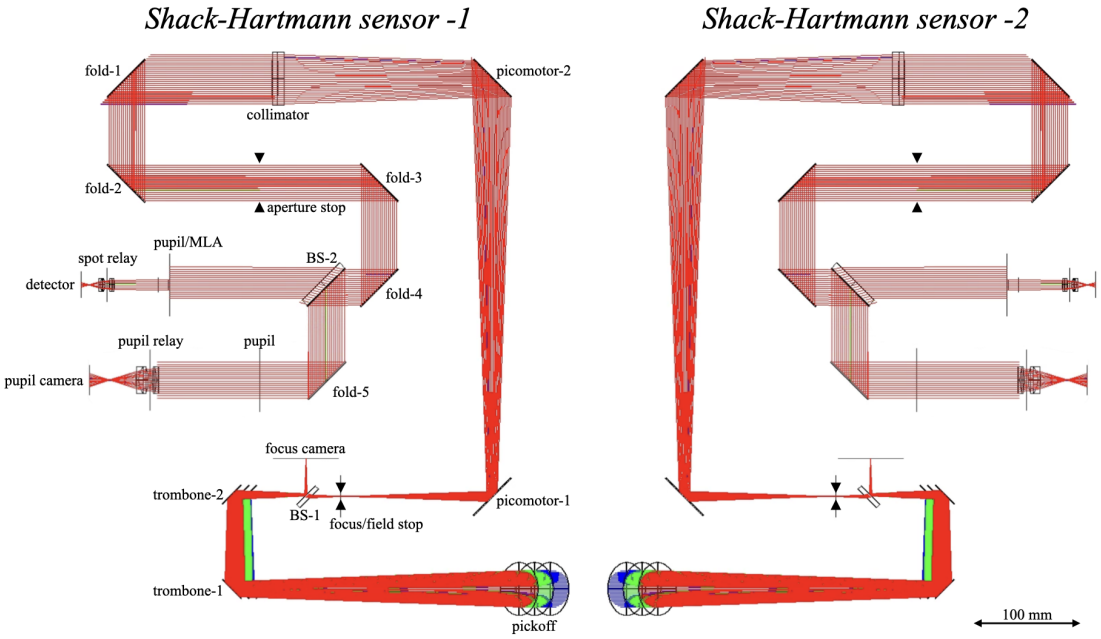

Fig. 2.4 Optical design of the turbulence profiler. The profiler system consists of two symmetrical SH sensors. Rays from the telescope come in the direction from the front to the back of the paper and are introduced into each SH sensor by the pick-off mirrors at the bottom of the figure. Blue, green, and red lines represent rays from two stars with a separation of 3, 4, and 5 arcmin, respectively.

Table 2.4 Transmissive optics on the turbulence profiler

Name	Diameter (mm)	Focal length (mm)	Product name
collimator	50.8	750	ACT508-750-A, Thorlabs
microlens array	0.15×67	10	APO-Q-P150-F10, Okotech
spot relay -1	12.7	50	MAP051950-A, Thorlabs
spot relay -2	12.7	19	MAP051950-A, Thorlabs
pupil relay -1	25.4	100.1	MAP1050100-A, Thorlabs
pupil relay -2	25.4	50.2	MAP1050100-A, Thorlabs

Table 2.5 Reflective optics on the turbulence profiler

Name	Diameter (mm)	Product name
pickoff	50.8	BB2-E02, Thorlabs
trombone 1	25.4	BB1-E02, Thorlabs
trombone 2	25.4	BB1-E02, Thorlabs
beam sampler 1	25.4	BSF10-A, Thorlabs
picomotor 1	50.8	BB2-E02, Thorlabs
picomotor 2	50.8	BB2-E02, Thorlabs
fold 1	50.8	BB2-E02, Thorlabs
fold 2	50.8	BB2-E02, Thorlabs
fold 3	50.8	BB2-E02, Thorlabs
fold 4	50.8	BB2-E02, Thorlabs
beam sampler 2	50.8	BSF20-A, Thorlabs
fold 5	50.8	BB2-E02, Thorlabs

2.2.3 Mechanical design

Figure 2.5 shows a 3D CAD drawing of the completed mechanical design of the SH-1. SH-2 is a symmetrical form of SH-1 and is not shown here.

The most significant constraint in the mechanical design of the turbulence profiler is the limited available space to install it. The entire turbulence profiler optics system must be accommodated in a gap of only 30 cm between the telescope light exit and the AG-SH module on the optical Nasmyth focus. Therefore, it is necessary to design a planar optical system with a thickness sufficiently smaller than 30 cm, as well as to install the entire device in a vertical orientation in the gap. Hence, in this design, all optical components in one SH sensor constitute a two-dimensional optical system on an optical bench of 600×600 mm. Because the height of each component must be kept sufficiently smaller than 30 cm, there is no room to use height adjustment stages. Thus, the height of each component's pedestal

Table 2.6 Detectors on the turbulence profiler

Name	# of pixels (pix^2)	Pixel size (μm)	Product name
focus camera	1280×1024	5.3	UI-1240SE-M-GL, IDS
pupil camera	2048×2048	5.5	UI-3370CP-M-GL Rev.2, IDS
Shack-Hartmann sensor	2048×2048	6.5	ORCA-Flash4.0 v2, Hamamatsu

is designed in advance so that the height of the optical path is 100 mm from the bottom of the optical bench. This reduced the thickness of the optical system to 160 mm, and 200 mm including the cover of the entire optical system. The pedestals were designed to match the shape of each optical component, and machining was performed by cutting using MISUMI-meviy, an automated quotation and manufacturing service for mechanical components by MISUMI. The pedestal is made of aluminum A5052, with a black anodized surface coating. The machining of some parts was done by the machine shop of the Subaru telescope.

The pickoff mirror is mounted on top of the pickoff mirror stage which has a travel range of 50 mm in the x axis direction. The two mirrors of the trombone optics are mounted on a common trombone stage, which also has a travel range of 50 mm in the x axis direction. These mirror stages are motorized stages and are operated remotely by a control PC. This feature allows the telescope's focal image to be fixed at a particular position even if the separation angle of the observed object is changed between 3-5 arcmin. The picomotor mirror 1,2 is mounted on a gimbal mount that is driven electrically by a picomotor. The gimbal mount allows the mirror angle to be adjusted over a range of ±4 deg with an angular resolution of 0.7 μrad. This feature allows the tilt and translation of the rays to be adjusted, and the area on the pupil where each SH sensor measures is changed. The other folding mirrors, beam sampler, and lenses are all held in mounts with 3-axis angular adjustment. Focus and pupil cameras have no adjustment mechanism. The SH sensor detector is on a manual single-axis stage along the optical path which allows position adjustment in the focal direction.

2.2.4 Data acquisition software

We utilize the ORCA-Flash4.0 V2 from Hamamatsu Photonics as detectors for the SH sensors. This detector is a 2048×2048 CMOS sensor with a pixel size of 6.5 μm, a readout noise of 1.6 electron pix^{-1} in RMS and a quantum efficiency of $\sim 80\%$ at 600 nm. The fastest frame rate is 100 Hz when reading the entire region, but an even faster readout is achievable by limiting the number of readout rows. In observation, the turbulence profiler reads out 800 rows at maximum to cover the entire image of the MLA. The fastest frame rate

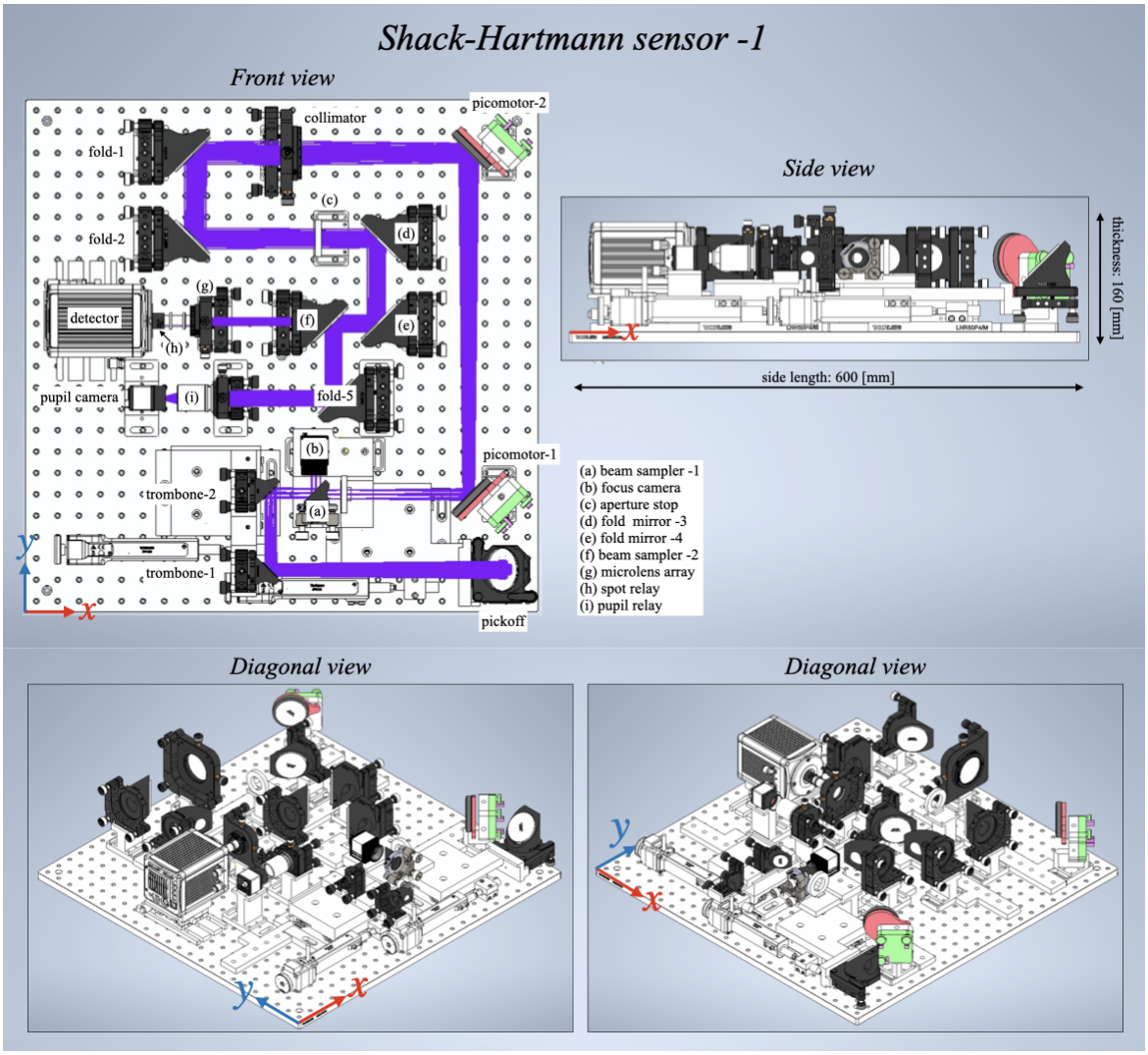

Fig. 2.5 Mechanical layout of the turbulence profiler. Only SH-1 is shown. The other sensor, SH-2, is the symmetrical version of SH-1. The purple lines on the front view show an optical path.

corresponding to the 800-row readout is 230 Hz, but we also use a slower frame rate of 80 Hz for fainter targets. In addition, data with a faster frame rate of 350 Hz and 700 Hz for brighter targets, by limiting the number of readout rows to 512 and 256 respectively, is also obtained to check the impact of exposure time of data acquisition. The turbulence profiler synchronizes the image acquisition timing of the two SH sensors by an external trigger signal from a single function generator to the two detectors.

The detector works in air-cooling mode. We place a partition between the ventilator on the side of the detector and the other optics so that the circulating air does not affect the measurement. Also, we keep covers at the back side of the detectors open to prevent heat accumulation in the system.

Data acquisition by the detector system, driving of the pickoff and trombone mirror stages, and angle adjustment of the picomotor mirror are controlled by a server computer with Ubuntu 20.04 with a real time kernel patch and C-based software.

2.2.5 Laboratory assembly and performance check

Assembly, optical alignment, and performance evaluation of the turbulence profiler are performed at the laboratory of the Subaru telescope. In the laboratory, the optical benches of the two SH sensors are laid down and placed on an optical table, although they should finally be mounted on a vertical surface of the AG-SH module with the entire optical bench in an upright position.

For the assembly, a simulated light source is arranged as shown in figure 2.6. We use a single He-Ne laser, which emits a single wavelength of 632.8 nm, as a light source. The ray is divided into two paths by a beam splitter, one for straight light and the other for a simulated source of the telescope. The beam traveling along the straight path is reflected by a single mirror and enters another beam splitter, where the beam is split into two and enters the SH sensor 1 and 2, respectively. By removing the pickoff mirror, the beam from the simulated source can enter the SH sensor optics in a laid-down position. The beam traveling along the optical path for telescope simulation is reflected by a mirror and then enters the lens system to emit a point source, and is collimated. The aperture stop placed after the collimator corresponds to the primary mirror of the Subaru telescope and narrows the beam to a size corresponding to a region of 3 m in diameter on the primary mirror. The beam is then split into two by the second beam splitter and focused by a lens before entering the SH sensors 1 and 2.

Placement of reflective optics on the optical bench is at first performed using positioning jigs for coarse accuracy. The positioning jigs have corner cuts to indicate the position of each component on the optical bench. Each component is positioned with coarse precision by

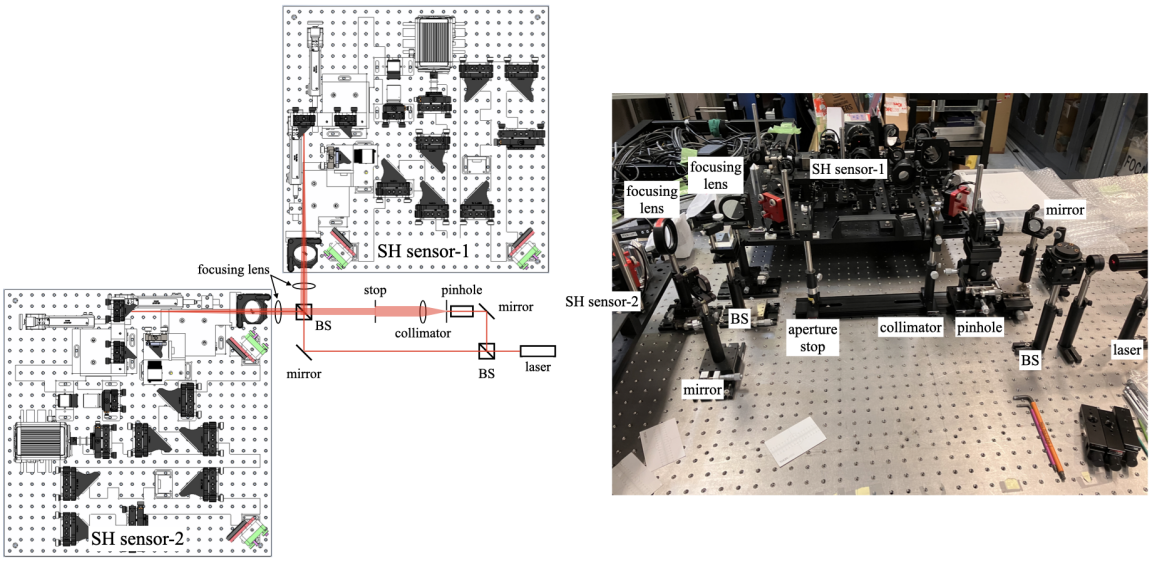

Fig. 2.6 Laboratory setup for the turbulence profiler alignment. Left: Conceptual drawing of the simulated source setting and SH sensors' position. Right: Actual picture of the laboratory setup.

putting its pedestal along the corner cut. Fine-tuning of the placement is performed with a method using an alignment cone. This method is also used for the optical alignment of a prototype WFS of the ULTIMATE-START project. In this method, we use two alignment cones made by machining one end of a cylindrical aluminum material into a conical shape, and a positioning jig that indicates the position where the alignment cones are to be placed. With the two alignment cones placed on the positioning jig, a laser is introduced from the simulated source. The tilt and translation of the reflective optics between the laser and the alignment cones are adjusted so that the laser passes through the top of the alignment cones. The height and eccentricity of the alignment cone are, in advance, measured and confirmed to be as designed.

As for the transmission optics, coarse adjustment is conducted by looking at the reflected light when a straight laser beam is introduced after placement using the positioning jig. The collimator is fine-tuned by checking the collimation of the emitted light when the simulation source is introduced. For the MLA and spot relay lens, the relative position between them was mechanically determined by fixing them to a common mount. After that, fine adjustments are performed by viewing the detector spot image. When the angle of the mount is not aligned with the beam, ghosts caused by the relay lens appear on the detector. A slight deviation of the translation of the mount with respect to the beam is not a problem in this design because the MLA itself is an aperture stop. Conjugation of the MLA position to the telescope pupil

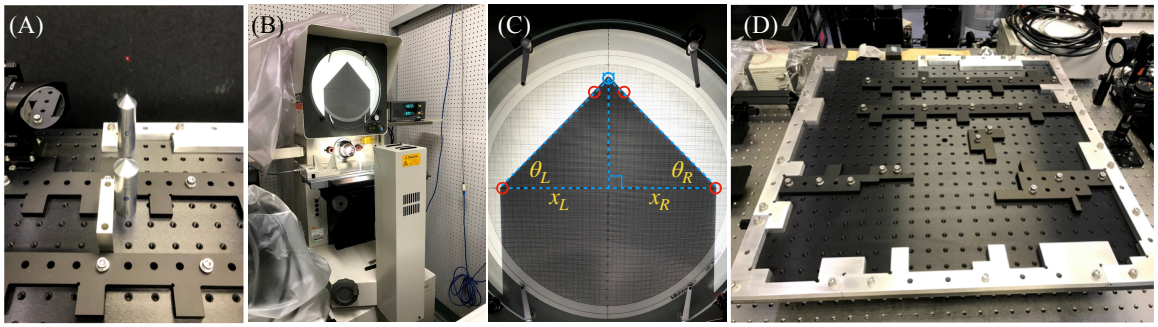

Fig. 2.7 Optical alignment using alignment cones and positioning jigs. (A) Mirrors are aligned so that the simulated laser beam passes through the tip of the two alignment cones. (B) Measurement of alignment cones' shape using a projector. (C) The projected shade of an alignment cone tip. (D) Positioning jigs for placing alignment cones.

is confirmed by inserting a paper edge at the pupil position of the simulation source and checking that an image of the edge is the sharpest on the detector. The pupil relay lens is also finely adjusted so that the pupil of the simulated source images sharply with the correct magnification on the pupil camera.

The focus and pupil cameras are positioned with respect to the mechanical design position determined by the positioning jig. The position of the SH sensor detector is adjusted so that the separation between the spots is 10 pix when the spot images are the sharpest.

As a result, image performances of the focus camera, the pupil camera, and the SH sensor are obtained as shown in figure 2.8 with the simulation source. The cross-shaped shadows seen in the pupil camera and the SH sensor are due to wires placed at the pupil position of the simulated light source to simulate a telescope spider. We confirmed the image sizes are as designed compared to the images expected from the optical simulation.

2.2.6 Installation to the Subaru telescope

The turbulence profiler is installed in the AG-SH module at the optical side Nasmyth focus of the Subaru telescope. The AG-SH module is an instrument placed at the Nasmyth focus on both sides of the Subaru telescope and has the ability to auto-guide the telescope by monitoring stars in the field of view and analyzing the distortion of the primary mirror surface by introducing it into the SH optical system. The AG-SH module is shown in figure 2.9, and the turbulence profiler is installed on the surface of the telescope side of this structure.

First, the base plate, which integrates the two SH optical systems and works as an interface with the AG-SH module, is described. The base plate is an aluminum plate of

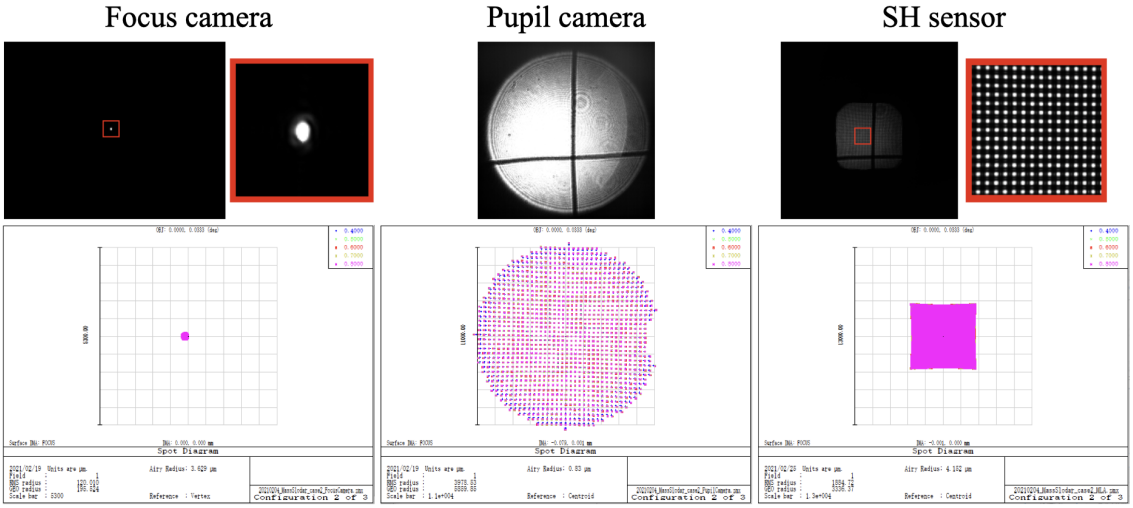

Fig. 2.8 Comparison of images expected in optical simulation and obtained in the laboratory. Left, center, and right panels show a comparison of images of the focus camera, pupil camera, and SH sensor, respectively. The cross-shaped shade on the pupil camera and SH sensor are made by metal wire on the pupil position of the light source for simulating the telescope spider.

$1400 \times 500 \times 15$ mm as shown in figure 2.10, on which the two SH optical systems are attached by three mounting jigs. The position of the two optical benches on the base plate is adjusted by using three clamping screws. Mounting the optical benches on the base plate and adjusting their position on the base plate should be done in advance in the laboratory before installation. In addition, four eye bolts are attached to the base plate. The upper two eye bolts are used for connection to the AG-SH module, and the lower two are for attaching a sling to maintain the inclination of the optics during installation. Four positioning pins, four neodymium magnets, and four clamping screws are mounted on the back side of the base plate. The positioning pins fit into threaded holes on the surface of the AG-SH module to position the turbulence profiler and the AG-SH module. The neodymium magnets are used to attach the entire optical system to the steel AG-SH module and keep it from moving out of position due to vibrations caused by earthquakes and other events. The clamping screw is used to maintain the distance between the neodymium magnet and the surface of the AG-SH module, preventing the magnet from attaching forcefully to the surface, and weakening the magnetic force by pushing the screw in during the optics removal. The total weight of the entire turbulence profiler, including the two SH sensors and the base plate, is approximately 100 kg.

Next, the installation procedure of the turbulence profiler is described. Before installation, two pickoff mirrors are installed and the entire optics are covered. Then, the entire system

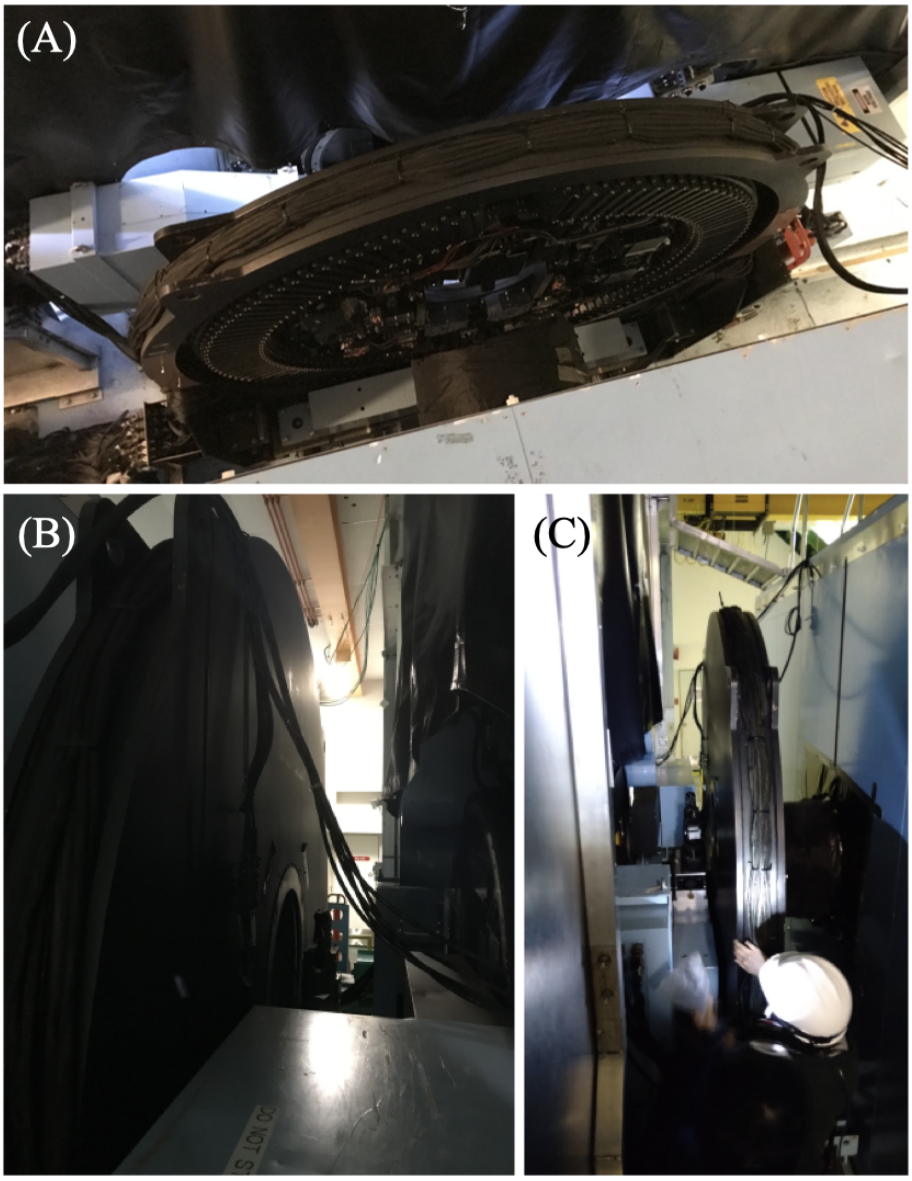

Fig. 2.9 Auto-Guider and Shack-Hartmann (AG-SH) module on the optical Nasmyth platform of the Subaru telescope. (A) Seen from the roof of the High Dispersion Spectrograph (HDS) room. (B) Seen from the front side of the telescope. (C) Seen from the rear side of the telescope.

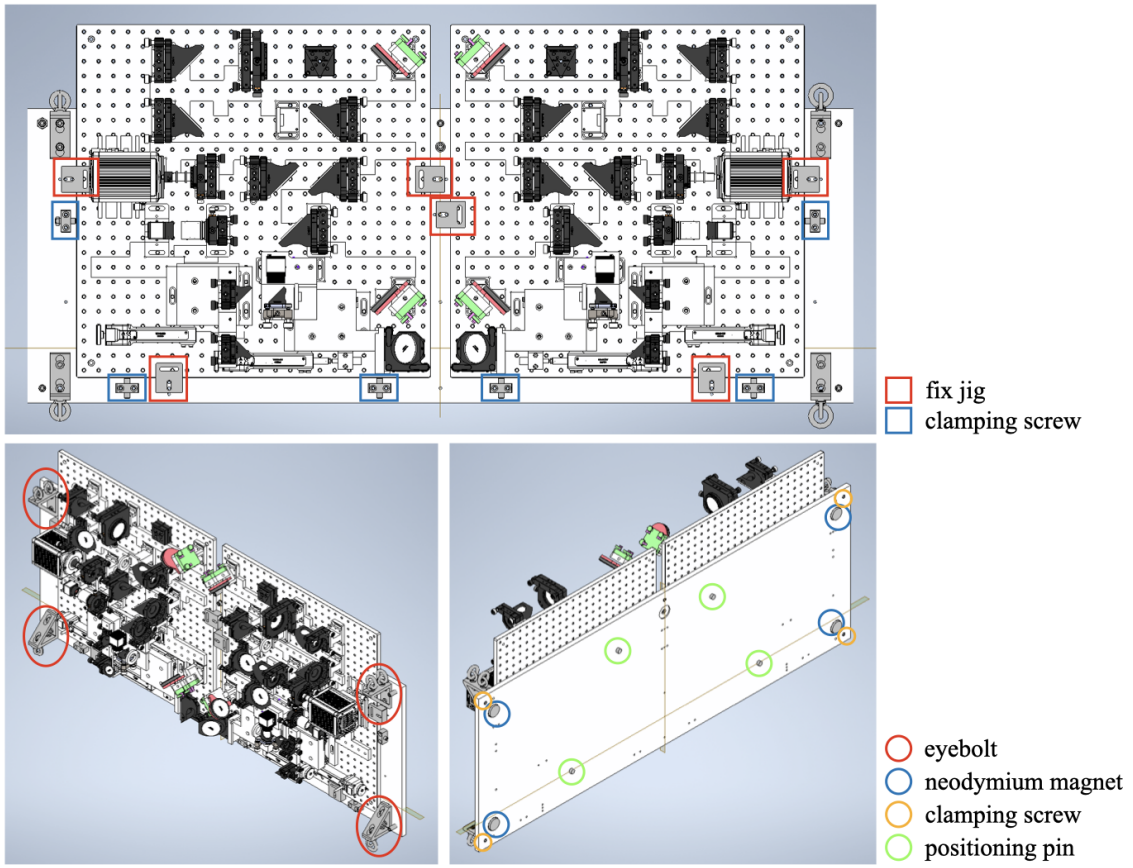

Fig. 2.10 Base plate of the turbulence profiler, which works as an interface between the two SH optical benches and the AG-SH module.

is lifted with a crane in its upright position and carried to the front of the AG-SH module. However, right above the AG-SH module is too close to the telescope to be accessed by a suspended crane on the optical Nasmyth platform. Therefore, a chain block was attached to a fixed point on the end of the crane I-beam, and a turbulence profiler was attached to the chain block so that the optical system could be carried right above the AG-SH module. When moving the optical system while it is suspended, a long sling attached to the eyebolts at the bottom of the base plate is pulled to control its posture and to prevent the optics from colliding with surrounding objects. After carrying the turbulence profiler just above the AG-SH module, the height is gradually lowered by the chain block to a position where the positioning pin on the back of the base plate enters the screw hole on the surface of the AG-SH module. Then, the clamping screw is loosened to the magnets on the back of the base plate attached to the surface of the AG-SH module. Finally, the installation is completed by stretching metal wires to secure the eyebolts on the top of the base plate to the eyebolts pre-installed on the top of the AG-SH module. The installed turbulence profiler is shown in figure 2.11. We should note that the installation method and the fixing method for the AG-SH module had not been done before the turbulence profiler. Therefore, in this study, the safety of the method was confirmed by conducting tests using dummy weights before executing on the real instrument.

After installation, two additional optical alignments are required. The first is the alignment of the pickoff mirrors of the turbulence profiler. Alignments in the laboratory are made with the pickoff mirror removed, so pickoff mirror alignment must be made after installation. On the other hand, the tolerance for the installation angle of the pickoff mirror is strict within ± 0.3 deg based on the condition that the picked-off ray does not leave the detection plane of the focus camera. We therefore developed the following alignment method. First, a laser is placed in the optical path of the turbulence profiler in the opposite direction of the optical path during observation, so that the laser light is emitted outside the optical system through a pick-off mirror. This laser beam returns to the telescope, but when the telescope's tertiary mirror is not inserted, it travels straight to the infrared Nasmyth focus, which is opposite the optical Nasmyth focus where the turbulence profiler is located.

On the other hand, a target is placed on the optical bench of the AO188, which is located at the infrared Nasmyth focus. The center of the target is aligned with the optical axis. On the target, there are concentric circles with a diameter of the distance between the two pickoff mirrors when the observed object is at 3, 4, or 5 arcmin separation. If the telescope image rotator on the optical Nasmyth focus side is rotated one full rotation, the laser beam from the turbulence profiler will make two rotations on the target. Whether the laser beam is parallel to the optical axis, is determined by whether the orbit of the two rotating laser spots is a circle

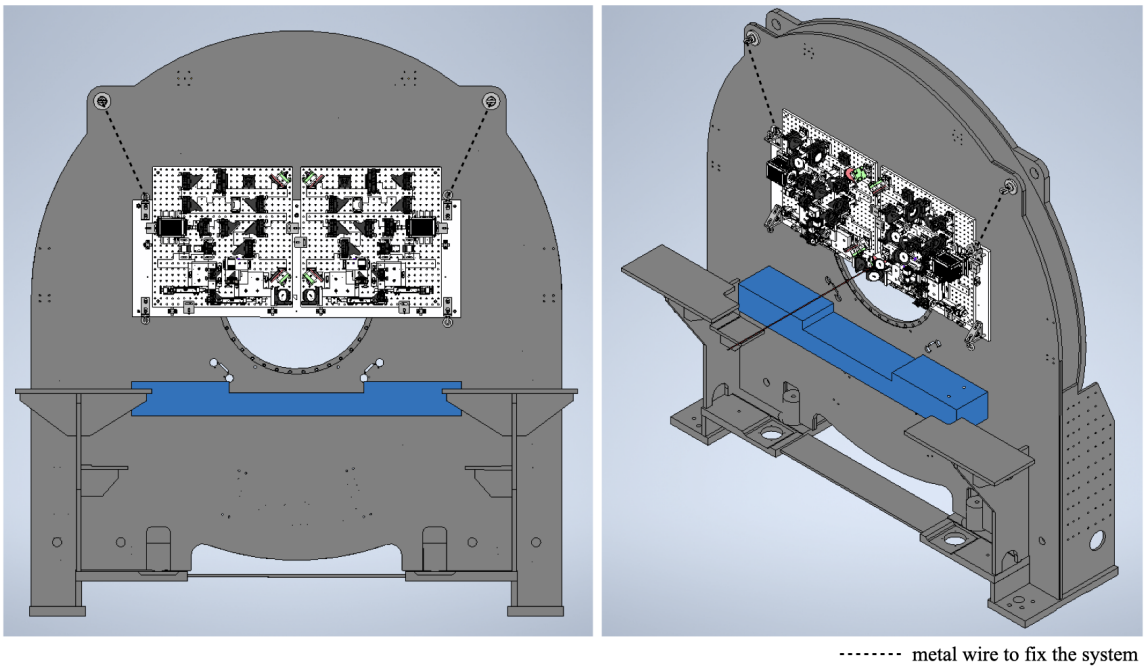

Fig. 2.11 Turbulence profiler installed on the AG-SH module. The weight of the entire system is supported by the two metal wires. To prevent the system from shaking, there are positioning pins and neodymium magnets on the back side of the base plate.

centered on the optical axis. Since the distance between the Nasmyth foci on both sides is approximately 14 m if the accuracy of visually identifying the center of the laser spot with respect to its spread is 5 mm, the accuracy of this alignment method is 0.020 deg. This value is sufficiently small relative to the tolerance that this alignment method is feasible.

The second is an alignment of the pupil positions measured by the two SH optics in the turbulence profiler. Because the two SH optics are independent optics, they may measure different positions on the telescope pupil depending on the alignment accuracy of each internal optics. Therefore, the pupil positions measured by both sensors were aligned by moving the picomotor mirror to match the position of the shadow created by structures such as the spider and secondary mirror when observing the dome flat of the telescope.

In figure 2.12, there are some pictures of the turbulence profiler system which show the entire view of the mechanical components, the upright position of the system with the cover, and the installed and fixed situation to the AG-SH module.

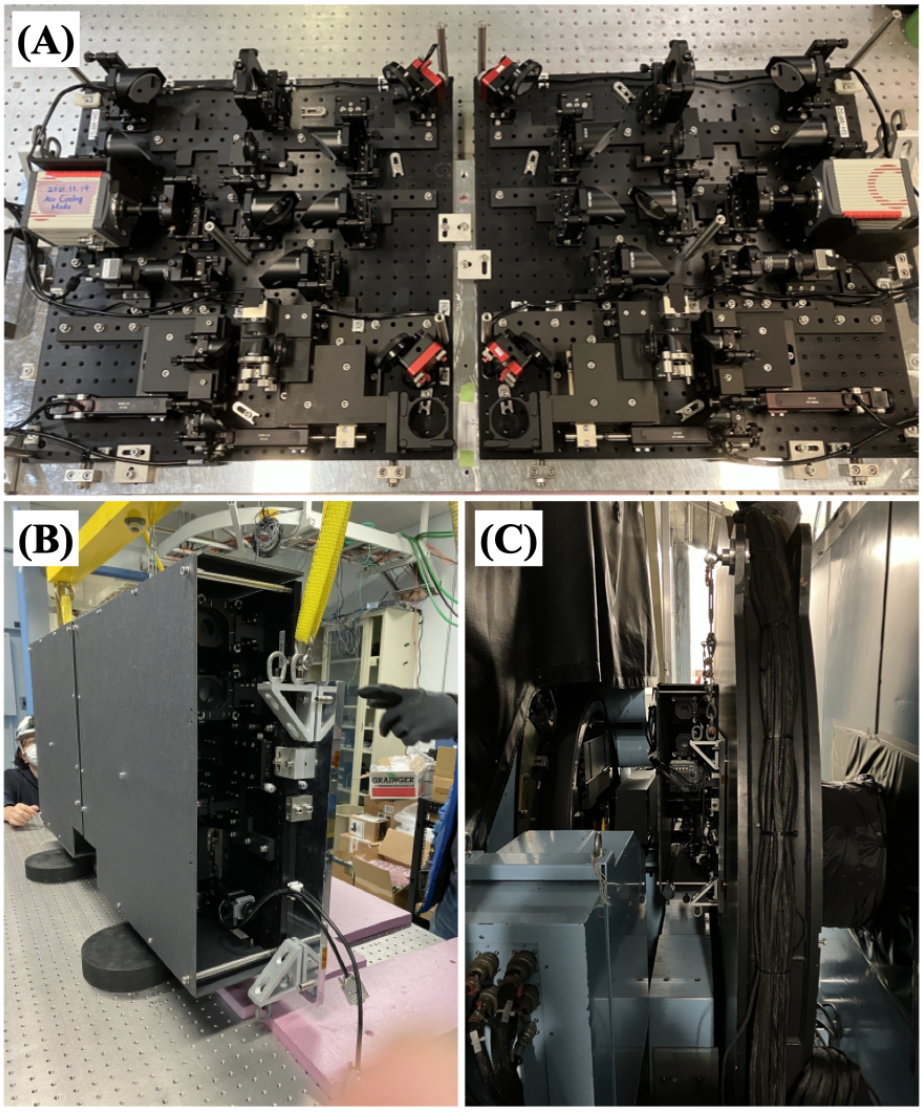

Fig. 2.12 Pictures of the turbulence profiler. (A) The entire view of the turbulence profiler. Two optical benches of the SH sensor are attached to an aluminum base plate. In this picture, two pickoff mirrors are not installed yet. (B) Turbulence profiler with the cover on and suspended by a crane in a vertical position. (C) Turbulence profiler installed at the AG-SH module.

2.3 Observation

2.3.1 Observation target

The observation targets of the turbulence profiler are pairs of natural stars with separation angles of 3-5 arcmin. In addition, each star should be brighter than approximately 6 magnitude in the visible wavelength range. There are only 5 pairs of stars in the sky that are observable from the Subaru telescope, but one or more of the five objects are observable at any time of the year. The five objects that are observable from the Subaru telescope are summarized in table 2.7. To introduce light from a star pair into each SH sensor, the telescope is pointed toward the midpoint of the star pair, and the telescope's image rotator is used to align the separation direction of the star pair and that of the two SH sensors. Pickoff mirror positions of the turbulence profiler are adjusted to match the separation angle, and trombone mirror positions are adjusted to focus the images.

The requirement for a pair of stars comes from the need to perform SLODAR, whereas a single star is sufficient to conduct SH-MASS. Therefore, stars as bright as 1 magnitude are targeted when profiling upper atmospheric turbulence only with SH-MASS.

2.3.2 Engineering observation

Engineering observations with the turbulence profiler on board the Subaru telescope has been made twice so far as of the end of April 2023. The first observation was performed in the first half night of November 12, 2022 in Hawaiian standard time (HST). This was the first observation as a turbulence profiler. We confirmed the procedure of target acquisition and performed data acquisition using the target #1 in Table 2.7. Five time-series data are obtained between 23:00 and 24:00 in local time. Each time series covered 120 seconds continuously, and the exposure time of the SH sensor was varied among the five data acquisitions depending on the size of the images. For each exposure time setting, we also measured the effect of the sky background and readout noise by taking images at an offset position ~ 30 arcsec away from the targets.

The second engineering observation was conducted in the second half night on March 13, 2023 in HST. In addition to data acquisition using target #4, we observed a double star to determine the pixel scale of the SH sensor and acquired data for SH-MASS using a single bright star. It should be noted that the background measurement at an offset position was basically not performed this time. This is because the data analysis of the first engineering observation showed that the readout noise exceeds the Poisson noise of the sky background The effect of readout noise was estimated by conducting data acquisition under

no illumination inside the dome on March 28, 2023, after the test observation and before the optical system removal.

The data for astronomical and non-astronomical objects acquired during each test observation are summarized in Table 2.8 and Table 2.9, respectively.

Table 2.7 Target list of turbulence profiler observation. The coordinates and magnitudes of the targets are taken from the SIMBAD database (http://simbad.cds.unistra.fr/simbad/)

ID	star A					star B			
	Name	RA(J2000) (hms[a])	DEC(J2000) (dms[b])	mag	separation (arcsec)	Name	RA(J2000) (hms)	DEC(J2000) (dms)	mag
1	HD11727	01 55 54.48	+37 16 40.05	5.9(V)	200.742	56And	01 56 09.36	+37 15 06.60	5.0(R)
2	c Ori	05 35 23.16	-04 50 18.09	4.6(V)	252.228	45Ori	05 35 39.48	-04 51 21.84	5.2(V)
3	ksi Pup	07 49 17.66	-24 51 35.23	3.3(V)	287.568	181Pup	07 49 01.67	-24 54 44.09	5.3(V)
4	alf01 Lib	14 50 41.17	-15 59 49.96	4.8(R)	230.532	alf02 Lib	14 50 52.71	-16 02 30.40	2.6(R)
5	eps01 Lyr	18 44 20.34	+39 40 12.45	4.7(V)	208.524	eps02 Lyr	18 44 22.78	+39 36 45.79	5.2(V)

a: hour, minute, second

b: degree, arcmin, arcsec

Table 2.8 Data of astronomical objects obtained by the turbulence profiler

Time (HST)	Obj-1	Obj-2	Mag-1 (mag)	Mag-2 (mag)	Size[a] (pix^2)	Exp.[b] (ms)	Freq.[c] (Hz)	Dur.[d] (sec)	Sync.[e]	Note
Nov.12, 2022										
23:17	HD 11727	56 And	5.9(V)	5.0(R)	800×800	12.99	77	120	yes	
23:37	HD 11727	56 And	5.9(V)	5.0(R)	800×800	12.99	77	120	yes	
23:42	HD 11727	56 And	5.9(V)	5.0(R)	512×512	4.33	231	120	yes	
23:45	HD 11727	56 And	5.9(V)	5.0(R)	256×256	2.89	347	120	yes	
23:49	HD 11727	56 And	5.9(V)	5.0(R)	512×512	4.33	231	120	1.45 ms lag	
Mar.14, 2023										
02:42	Arcturus		-0.05(V)		256×1024	1.43	698	120	no	
02:45	Arcturus		-0.05(V)		256×1024	1.43	698	120	no	
03:30		Arcturus		-0.05(V)	256×1024	1.43	698	120	no	
03:34		Arcturus		-0.05(V)	512×1024	2.87	349	120	no	
03:37		Arcturus		-0.05(V)	800×1024	4.32	231	114	no	
04:16		zet UMa		2.2/3.9(V)	800×1024	500	2	10	no	
04:21	zet UMa		2.2/3.9(V)		800×1024	500	2	10	no	
04:44	Alf02 Lib	Alf01 Lib	2.6(R)	4.8(R)	512×1024	2.88	347	82	yes	
05:07	Alf02 Lib	Alf01 Lib	2.6(R)	4.8(R)	800×1024	12.95	77	124	2.85 ms lag	
05:13	Alf02 Lib	Alf01 Lib	2.6(R)	4.8(R)	800×1024	12.95	77	124	2.85 ms lag	
05:16	Alf02 Lib	Alf01 Lib	2.6(R)	4.8(R)	800×1024	4.32	232	89	yes	cloud
05:20	Alf02 Lib	Alf01 Lib	2.6(R)	4.8(R)	800×1024	12.95	77	57	yes	cloud

a: Size of the Shack-Hartmann detector

b: Exposure time of data acquisition

c: Acquisition frequency

d: Duration of data acquisition

e: Synchronization of the acquisition by the two sensors

Table 2.9 Data of non-astronomical objects obtained by the turbulence profiler

Time (HST)	Obj-1	Obj-2	Size (pix^2)	Exp. (ms)	Freq. (Hz)	# of frames	Sync.	Note
Nov.09, 2022								
15:39		dome flat	800×800	100	10	5	no	
15:39	dome flat		800×800	100	10	5	no	
Nov.13, 2022								
23:24		sky background	800×800	12.98	77	1000	no	
23:24	sky background		800×800	12.98	77	1000	no	
23:48		sky background	256×256	2.88	347	1000	no	
23:48	sky background		256×256	2.88	347	1000	no	
23:51		sky background	512×512	4.32	231	1000	no	
23:52	sky background		512×512	4.32	231	1000	no	
Mar.13-14, 2023								
20:41	dome flat		800×1024	100	10	10	no	
20:42		dome flat	800×1024	100	10	10	no	
Mar.28, 2023								
18:39	bias		256×1024	1.43	698	1000	no	
18:39		bias	256×1024	1.43	698	1000	no	
18:41	bias		512×1024	2.88	349	1000	no	
18:41		bias	512×1024	2.88	349	1000	no	
18:42	bias		800×1024	4.32	232	1000	no	
18:42		bias	800×1024	4.32	232	1000	no	
18:44	bias		800×1024	12.95	77	1000	no	
18:44		bias	800×1024	12.95	77	1000	no	

2.4 Analysis

2.4.1 Timing and synchronicity of data acquisition

Prior to the analysis of the data obtained from the test observations, the timing of data acquisition is checked. The acquisition frequencies and exposure times shown in Table 2.8 are the values obtained by examining the time interval between frames in each dataset. Regarding the synchronicity of the frames acquired in the two SH sensors, it is confirmed that the error is within ±50 μs for more than 97% of the frames in most of the data sets. This means that even when images are taken with the shortest exposure time, they are synchronized strictly within 3.5% of the exposure time. On the other hand, systematic deviations of 1.45 ms or 2.85 ms are found for data acquired at 23:49 on November 12, 2022 and at 05:07 and 05:13 on March 14, 2023, indicating that sufficient synchronization is not achieved. However, since the deviation is not so large as to exceed 50% of the exposure time, they are also included in the analysis.

2.4.2 Shack-Hartmann sensor spot detection

We first define a background frame for each dataset by averaging all the frames obtained without the object. Then, we define a spot reference position by applying center-of-gravity (CoG) measurement for an averaged frame of all the background-subtracted object frames. Since spots are separated by 10 pixels from their neighbors by design, we define a subaperture area on the detector as 9×9 pix region centered at the spot reference position.

Once the subaperture areas are determined for each dataset, spot CoG and brightness measurement are applied for each subaperture in each background-subtracted frame. We simply define spot brightness as the sum of the pixel counts in each subaperture, while we performed the spot CoG measurement with windowing and thresholding to mitigate the noise effect. The window is set to an area of 5×5 pix centered at the spot reference position, considering that the diffraction-limited spot size of the 2 cm subaperture is 3 pix in FWHM and that the typical seeing at Maunakea is sub-pixel on the detector. As thresholding, we set a moderate threshold of 1.3-1.5σ of detector readout noise level depending on the dataset because a higher threshold results in failure of spot detection when the object spot is fainter due to scintillation. Instead of setting the moderate thresholding, we impose a slope-detection condition, in which we only trust CoG measurements for subapertures that have more than three pixels satisfying the threshold in the window region. In the slope analysis using the measured CoG, which is described in section 2.4.3, we only use the CoG of spots that satisfy the condition.

A histogram of the measured CoG of spots satisfying the spot-detection condition in all the frames of each dataset is shown in figure 2.13. The distribution of the CoG position shows a trend that the dispersion increases as the exposure time decreases, indicating that the dispersion is coming from CoG measurement error due to readout noise. However, in CoG correlation analysis, which is described in section 2.4.3, readout noise has little impact on the result because random readout noise shows no correlation.

A histogram of the measured brightness of all the spots in all the frames of each dataset with the object is shown in figure 2.14. For spot brightness, the histogram contains all the spots whether it satisfies the spot-detection condition or not. Due to the readout noise effect, some spot brightness values are negative when the object is relatively faint or the exposure time of the SH sensor is short. In scintillation analysis, the effect of readout noise must be corrected since it is necessary to measure the autocorrelation of spot brightness. The correction method is discussed in detail in section 2.4.4.

2.4.3 Slope auto-covariance

Total seeing of the atmospheric turbulence is estimated by fitting the observed slope auto-covariance map with analytically calculated one assuming a turbulence model (Butterley et al., 2006). "Auto-covariance" here means covariance between slopes in a single SH sensor, while "Cross-covariance" means covariance between slopes in different sensors and is analyzed to obtain turbulence profile as SLODAR method (Wilson, 2002; Butterley et al., 2006).

Let the center position of the i-th subaperture on the pupil and corresponding slope measurement in the x-direction be $\boldsymbol{r}_i$ and s_i^x, respectively. The x-slope auto-covariance map A_x, which shows the x-slope covariance of two spots as a function of their distance vector $\boldsymbol{r}$, is calculated as

$$A_x(\boldsymbol{r}) = \frac{\sum_{\text{valid } i,j} < (s_i^x - \overline{s^x})(s_j^x - \overline{s^x}) >}{\sum_{\text{valid } i,j} 1}, \tag{2.43}$$

where $< \cdot >$ represents the statistical mean of the physical quantity and the sum is performed for valid spot pairs which satisfies $\boldsymbol{r}_j - \boldsymbol{r}_i = \boldsymbol{r}$. When the covariance is computed, the average over all the slopes, $\overline{s^x}$, is subtracted to remove the overall tip-tilt component which might be induced by non-atmospheric effects such as telescope tracking error or vibration of the optical systems.

We calculate the auto-covariance map of the x-slope and y-slope for all the observed data. The top panel of figure 2.15 shows an example of the auto-covariance map. The fitting

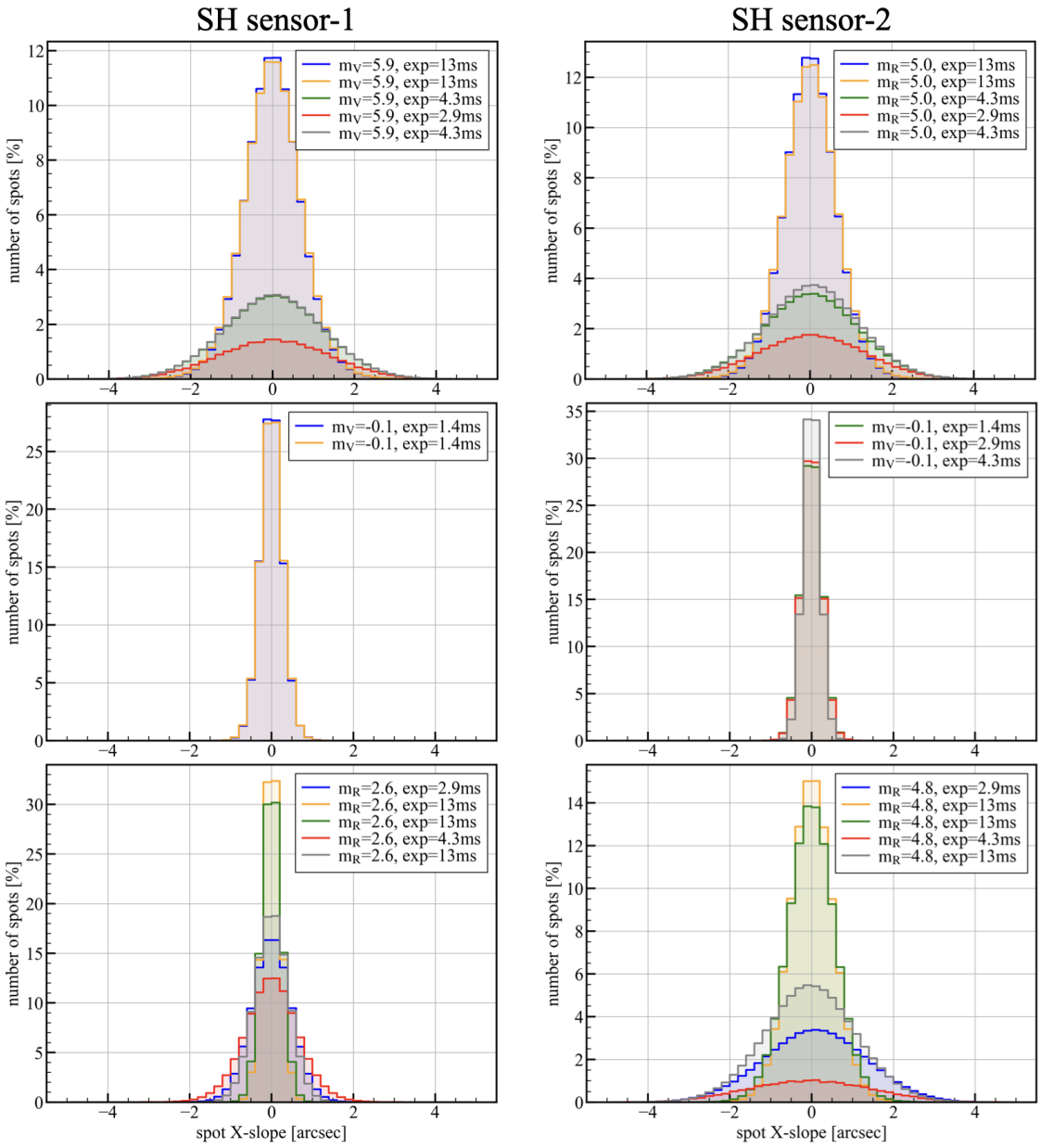

Fig. 2.13 Histogram of detected CoG position of spots in the unit of arcsec. CoG detected by SH-1 (left) and by SH-2 (right) in 23:00-24:00 on Nov.12, 2022 (top), in 2:40-3:40 on Mar.14, 2023 (middle), and in 4:30-5:30 on Mar.14, 2023 (bottom). Only spots that satisfy the detection condition are included. Different colors represent different datasets, i.e. different object brightness and exposure time. Only the CoG in the x-direction is shown as a representative, but similar histograms are obtained for the y-direction.

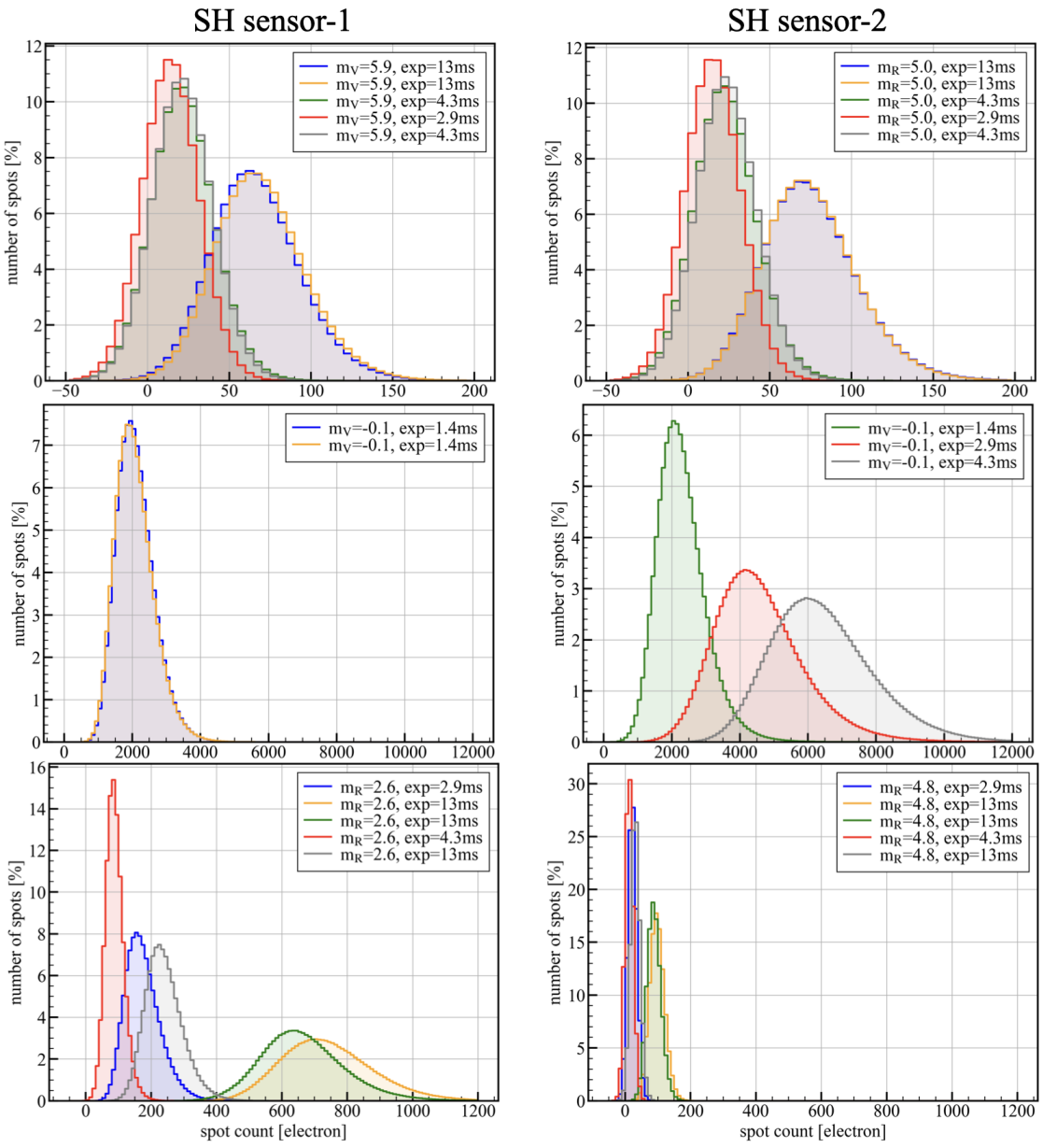

Fig. 2.14 Histogram of detected brightness of spots in the unit of electron. Spot brightness detected by SH-1 (left) and by SH-2 (right) in 23:00-24:00 on Nov.12, 2022 (top), in 2:40-3:40 on Mar.14, 2023 (middle), and in 4:30-5:30 on Mar.14, 2023 (bottom). Only spots that satisfy the detection condition are included. Different colors represent different datasets, i.e. different object brightness and exposure time.

analysis considers only auto-covariance map within ±10 subapertures from the center to remove noisy covariances due to the small number of corresponding subaperture pairs in some datasets.

To calculate the analytical model of slope auto-covariance, we adopt an approximated method for accelerated calculation (Martin et al., 2012; Ono et al., 2016b). Assuming that the measured slope is the phase difference between two points at the edge of the subaperture, the slope s_i^x is modeled as follows,

$$s_i^x = \frac{1}{d}\left[\phi\left(\boldsymbol{r}_i + \frac{d}{2}\boldsymbol{e}_x\right) - \phi\left(\boldsymbol{r}_i - \frac{d}{2}\boldsymbol{e}_x\right)\right]. \tag{2.44}$$

where d is the length of one side of the subaperture, ϕ is the phase, and $\boldsymbol{e}_x$ is the unit vector in the x direction. Then the slope covariance of i-th and j-th spots is written as follows.

$$\begin{aligned} < s_i^x s_j^x > = & \frac{1}{2d^2}[-2D_\phi(\boldsymbol{r}_j - \boldsymbol{r}_i) + D_\phi(\boldsymbol{r}_j - \boldsymbol{r}_i + d\boldsymbol{e}_x) \\ & + D_\phi(\boldsymbol{r}_j - \boldsymbol{r}_i - d\boldsymbol{e}_x)]. \end{aligned} \tag{2.45}$$

where $D_\phi(\boldsymbol{r}) = < [\phi(\boldsymbol{x}) - \phi(\boldsymbol{x}+\boldsymbol{r})]^2 >$ is the structure function of phase. A generalized phase structure function described in Nicholls et al. (1995),

$$D_\phi(\boldsymbol{r}) = \alpha |\boldsymbol{r}|^{\beta-2}, \tag{2.46}$$

is used for the auto-covariance fitting with a normalization coefficient of α and a power coefficient of β, which satisfies $2 < \beta < 4$ (Boreman and Dainty, 1996). It corresponds to Kolmogorov's case when $\beta = 11/3$.

The analytical auto-covariance model is fitted to the measured one with the Nelder-Mead algorithm, which is an iterative solver for non-linear optimization problems, to determine best-fit α and β. We exclude the central pixel of the observed auto-covariance map from fitting since the central value, i.e., slope variance contains noise variance effects. To obtain the seeing values, the center value of the auto-covariance map obtained by the fitting, i.e., slope variance with noise effects removed, is converted to FWHM assuming a Gaussian distribution. The second and third row panels in figure 2.15 show the best-fit auto-covariance map with the generalized model, and residual map from the observed one, respectively. The bottom panels show cross-sections of the maps.

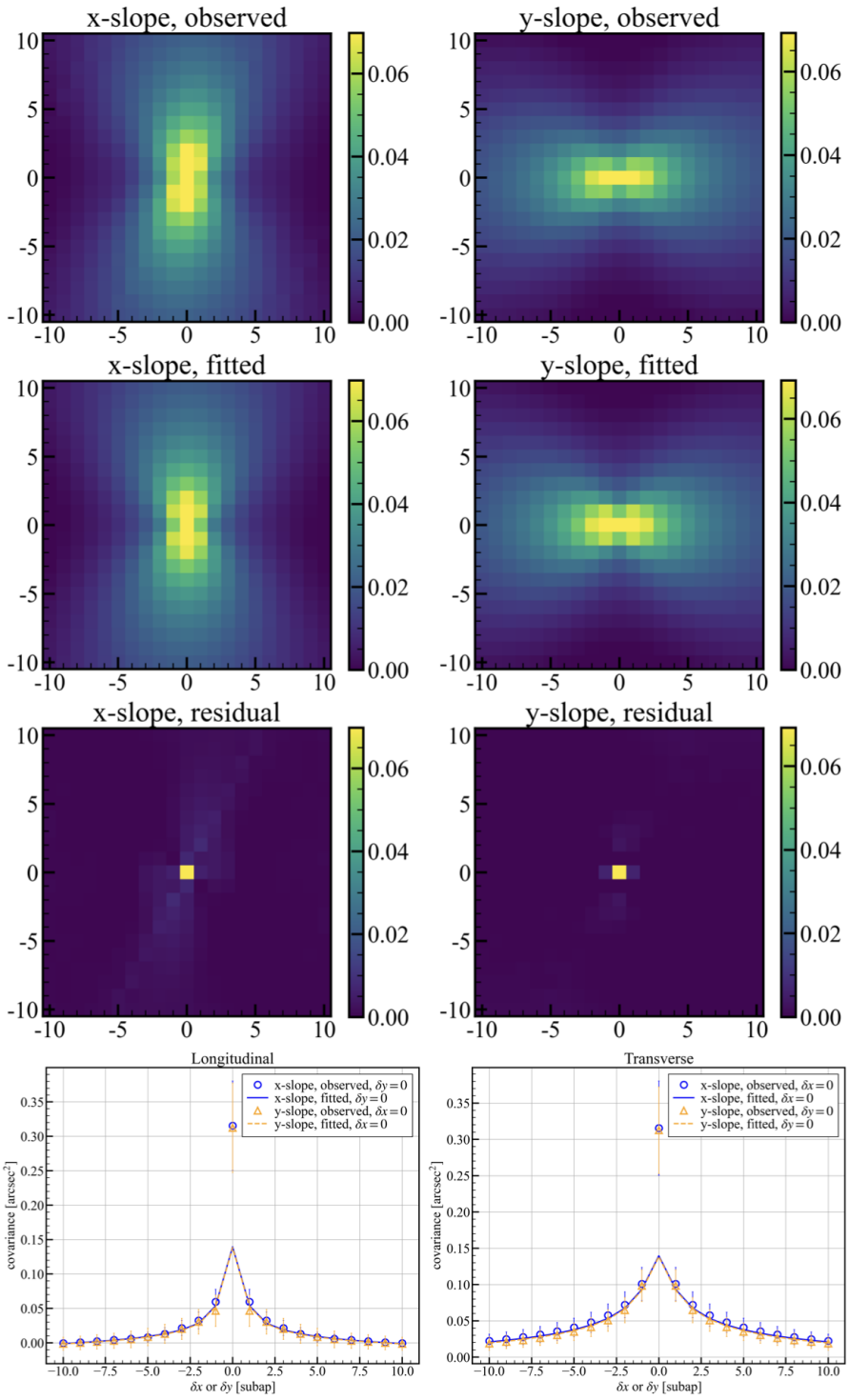

Fig. 2.15 Example of slope auto-covariance analysis. Top: X, Y-slope auto-covariance maps for dataset taken at 04:44, Mar.14, 2023. Middle: fitted X, Y-slope auto-covariance maps. Bottom: residual maps between observed and fitted auto-covariance maps

2.4.4 SH-MASS

The atmospheric turbulence profile is estimated by applying the SH-MASS (Ogane et al., 2021) analysis to the scintillation spatial pattern measured from the intensity fluctuation of the SH spots.

In our analysis, a single atmospheric turbulence profile is obtained from 5×5 spots detected in each dataset. In other words, the apertures for measuring the scintillation indices are limited to combinations of spots separated by 5 subapertures. This implicitly assumes that the scintillation correlation at spatial scales larger than 14 cm, which corresponds to scintillation made by turbulence at a height of $\sim$ 30 km, is not considered. We extract four different spot regions which include 5×5 spots from the acquired dataset and perform four independent SH-MASS at the same time on a single SH sensor. The number of calculated scintillation indices that are defined by the subapertures of 5×5 is 43, including 15 corresponding to the NSI and 28 corresponding to the DSI.

The 43 scintillation indices are calculated from the mean, variance, and covariance of the brightness of each spot based on equations (2.31) and (2.32). Since the variance of spot brightness contains photon noise and readout noise components, we correct these components. The photon noise is corrected by subtracting the mean brightness of each spot from the variance of the spot based on the fact that photon noise follows a Poisson distribution. To estimate the readout noise, we perform the same procedure as spot detection on the background datasets. Because the object is offset in the background datasets, the measured brightness of each subaperture is dominated by readout noise. By subtracting the readout noise from the variance of spot brightness, we correct the readout noise effect. The noise-corrected NSI computed from four different subsets are shown in figure 2.16. Since these eight results are simultaneous and independent measurements, variations in these lines can correspond to errors in measurement. In the following, the standard deviation of the measurement among different subdata is used as the error associated with the scintillation index measurement.

The weighting function matrix corresponding to the 43 aperture patterns is calculated based on equations (2.28) and (2.29). The aperture function $A_X(x, y)$ is expressed for all the 43 aperture patterns with a size of 1024×1024 and a sampling of 2 mm, which is a tenth of the subaperture diameter. By calculating the Fourier transformation of the aperture function, equations (2.28) and (2.29) are numerically computed. The calculation is done for the layer height of every 100 m from 0 km to 50 km high. We set observation wavelength of 550 nm and zenith angle of 0 deg. The computed weighting function matrix is shown in figure 2.17. The two panels show normal and differential weighting function matrices up to 20 km. The weighting function of each aperture pattern is monotonically increasing as a function of

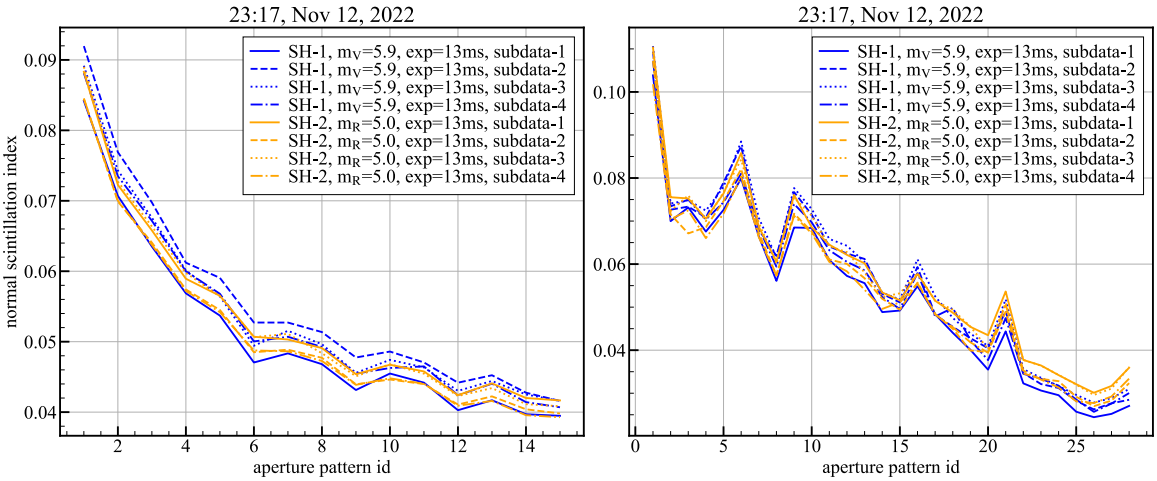

Fig. 2.16 Example of calculated scintillation indices for the data taken at 23:17, Nov.12, 2022. NSI and DSI are shown as a function of aperture pattern ID in the left and right panels, respectively. The IDs are given in the order of the distance between the two spots that constitute the aperture pattern. Differences in colors show differences in sensors that the scintillation index is measured. Differences in line styles correspond to differences in the subdata of each dataset.

height from the ground, meaning that scintillation becomes larger as the propagation distance becomes long. The order of the aperture patterns is sorted by the value of the weighting function at 20 km.

For turbulence profile reconstruction, we set a combination of fixed turbulence layer heights of 1, 2, 4, 8, and 16 km. This is the same situation as MASS-DIMM except for the 0.5 km layer. The 0.5 km layer is removed because the 2 cm subaperture in our SH sensor is too large to constrain turbulence strength at less than $\sim$ 1 km. The smallest aperture of the MASS-DIMM instrument has a 1.3 cm diameter. The combination of heights is converted to propagation distance to the turbulence layer according to the elevation angle of the observation. Columns of the weighting function matrix which corresponds to the propagation distances are extracted from the original weighting function matrix.

By fitting the observed scintillation indices with their analytical expressions, turbulence strengths of each layer $J_i = C_n^2(h_i)\Delta h_i$ are estimated. The reconstruction process is mathematically a linear inverse problem, so it is solved by computing the inverse of the weighting function matrix. However, the weighting function matrix is highly degenerate between rows, and profiles reconstructed by the pseudo-inverse method often have negative turbulence

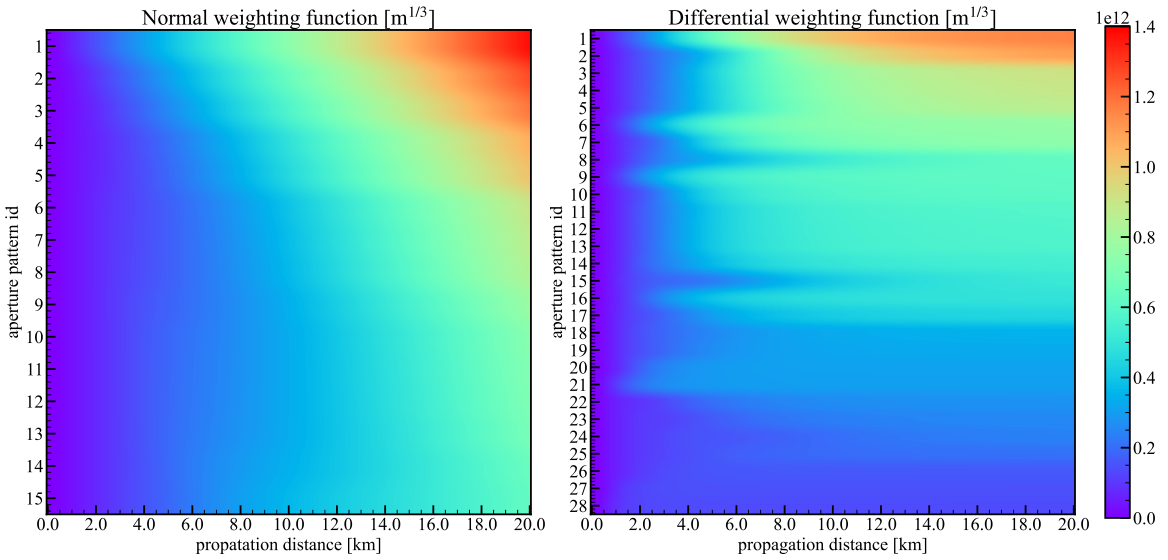

Fig. 2.17 Weighting function matrix for the SH-MASS analysis. The left panel is for normal aperture patterns and the right panel is for differential aperture patterns. The color represents the sensitivity of each aperture pattern to scintillation created by the propagation of each distance.

strength. Therefore, for solving equations (2.26) and (2.27), an optimization problem

$$\begin{aligned} \text{minimize} \quad & \chi^2(\boldsymbol{J}) = \sum_m \frac{\{s_m - (\boldsymbol{W}\boldsymbol{J})_m\}^2}{\sigma_m^2} \\ \text{s.t.} \quad & \sum_i J_i < J_{\text{slope}}, \end{aligned} \tag{2.47}$$

is solved. In this function, s and σ mean the observed scintillation indices and their errors. $\boldsymbol{W}$ is the weighting function matrix and $\boldsymbol{J}$ is turbulence profile, i.e. a vector of $J_i = C_n^2(h_i)\Delta h_i$ for all the layer heights to be profiled. Therefore, modeled scintillation indices based on the turbulence profile, $\boldsymbol{W}\boldsymbol{J}$, are optimized to explain the observed scintillation indices within their measurement errors. As a constraint, we impose sum of turbulence profile should be smaller than the total turbulence strength estimated by the slope auto-covariance analysis. The condition corresponds to a physical requirement that turbulence strength traced by scintillation should be smaller than that traced by slope by ground layer strength, which cannot be traced by scintillation. We solve the problem using the sequential least square programming algorithm, which is one of the iterative solvers for constrained non-linear optimization problems. In the computation, we impose all the components of $\boldsymbol{J}$ to satisfy a condition of $-20 < \log J_i(\mathrm{m}^{1/3}) < -5$. This is an arbitrary condition to prevent the solution

from being negative, but the range is broad enough to include all possible atmospheric turbulence strength considering typical turbulence strength.

2.4.5 Scintillation temporal auto-covariance

We use the temporal auto-covariance maps of scintillation to obtain wind speed and direction profiles. Based on the frozen flow hypothesis, the scintillation pattern moves across the pupil with time following the wind speed and direction at altitudes where turbulence layers exist. Therefore, wind speed and direction are estimated by examining each of the moving peaks on the temporal auto-covariance map of scintillation with a different time lag. The strength of scintillation, which is defined as spot count time series normalized by its time average, depends on the turbulence strength and propagation distance from the turbulence layer, i.e. turbulence altitude. Therefore, the auto-covariance map is more sensitive to turbulence at higher altitudes, but not sensitive to turbulence at ground, similar to the MASS technique.

To calibrate wind direction, a relationship between the direction of the subaperture arrangement on the primary mirror and the direction of the SH sensor field of view is first checked using a ray trace in the optical design. A relationship between the direction of the sensor field of view and the telescope field of view is checked from the telescope image rotator status. Also, the wind direction measured in a plane parallel to the ground surface is obtained by converting the direction on the celestial plane to the horizontal coordinates.

The auto-covariance maps of scintillation obtained with increasing time lags are shown in figure 2.18. The several correlation peaks move toward the left-bottom direction on the map as the time lag increases, indicating that the turbulence in the upper layer is moving with the wind blowing from the northwest direction. The cross-section along the direction of signal movement is examined for each clump in each covariance map to find their peak position. The moving speed of the signal peak is converted to the wind speed. As an example, the cross section of the brightest signal in figure 2.18 is shown in the left panel of figure 2.19. We correct an effect that the apparent wind speed is smaller by the factor of the cosine of observing the zenith angle, assuming that the real wind blows in a plane parallel to the ground.

Also, according to Prieur et al. (2001), the FWHM of the scintillation auto-covariance signal in the Kolmogorov model is approximated as $\sqrt{\lambda z}$, where λ is the observed wavelength and z is the distance from the atmospheric turbulence layer to the ground. Therefore, it is also possible to estimate the height of the turbulence layer by analyzing the width of the auto-covariance signal. We take a cross-section orthogonal to the moving direction at the location of each signal peak, which is shown in the right panel of figure 2.19. The width of the signal is measured by fitting it with the Gaussian function. The procedure of measuring

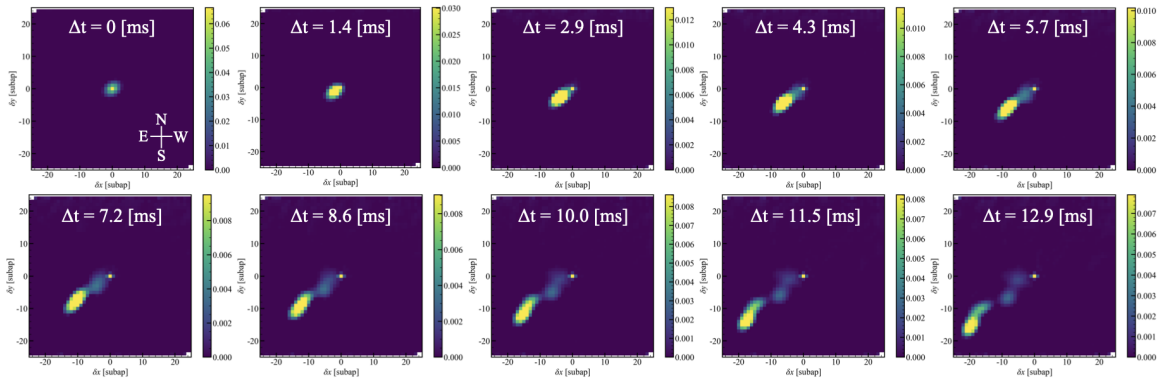

Fig. 2.18 Example of scintillation auto-covariance map for dataset taken at 02:42, Mar.14, 2023. From top-left to bottom-right, an auto-covariance map calculated with a time lag of 0-9 frames is arranged. The peak of the covariance signal moves toward the East-south direction as the time lag increases.

wind speed, direction, and height is performed for several signal clumps found in each auto-covariance map. Clumps to be examined are selected based on that they have enough signal-to-noise ratio on the map and are independent of nearby clamps without overlaps.

Furthermore, similar to the slope auto-covariance analysis, a method for obtaining an atmospheric turbulence profile by fitting the observed scintillation auto-covariance maps with the analytical ones is known as SCO-SLIDAR (Védrenne et al., 2007). In this study, however, atmospheric turbulence based on the scintillation auto-covariance maps is discussed in section 2.6.2.

2.4.6 Pupil matching

Before moving on to the SLODAR analysis, we describe how we identified the pupil positions measured by the two SH sensors. Figure 2.20 shows the time averaged SH image of each dataset. It shows not only many SH spot images but also shaded regions by one of the telescope spiders, which supports the secondary mirror, and the central cone on the secondary mirror, which reflects heat radiation from the center of the primary mirror to outside of the optical path. The location of the measured pupil is identified by examining the shade position of these telescope structures on the respective SH sensor images.

Initially, the size ratio of the central cone shade to the spider shade in the telescope pupil image is examined using pupil images acquired by the AO188 system. Then, the pupil image magnification and rotation angle are identified by examining the width and angle of the spider shade on each SH sensor. Finally, the center position of the telescope pupil is identified to align the edges of the central cone shade. At this time, the spider shade cannot be aligned

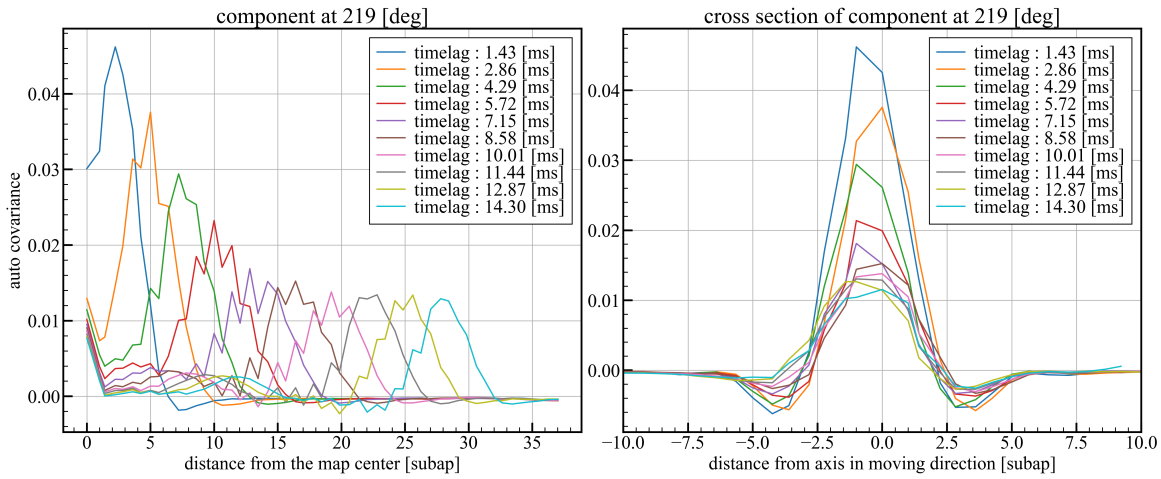

Fig. 2.19 Example of scintillation auto-covariance analysis for the data taken at 02:42 on Mar.14, 2023. Left: Cross section of the covariance map along the direction of signal movement. The wind velocity of the signal component is estimated from the movement of the peak position at a constant speed. Right: Cross-section in the direction perpendicular to the direction of signal movement at the peak position of the signal. Wind height is estimated from the signal width since the width reflects the spatial scale of scintillation.

at the same time. This is because the position of the spider seen from the central cone on the secondary mirror varies with the position of the observed object in the field of view. The results of identifying the position of the pupil image on each SH sensor by this method are shown in figure 2.21 and 2.22.

2.4.7 SLODAR

We calculate the cross-covariance map in the same way as the auto-covariance analysis described in section 2.4.3. Selecting two spots from each of the two different SH sensors, the correlation of the slopes and distance on the pupil between the spots are examined. In order to determine the spot distance on the telescope pupil, we use the information of relative position and angle of the measured pupil by the two SH sensors obtained in section 2.4.6. Because we identify the same position on the two pupil images based on the shade of the central cone on the secondary mirror, the origin of the height direction in SLODAR is the secondary mirror position, which is a conjugate height of -80 m measured from the primary mirror. An example of a measured cross-covariance map of the x-slope and y-slope is shown in the left panels in figure 2.23. The correlation signal in the observed cross-covariance map is located ~ 6 subapertures from the center, indicating that the turbulence distributes at the offset position measured from the secondary mirror position.

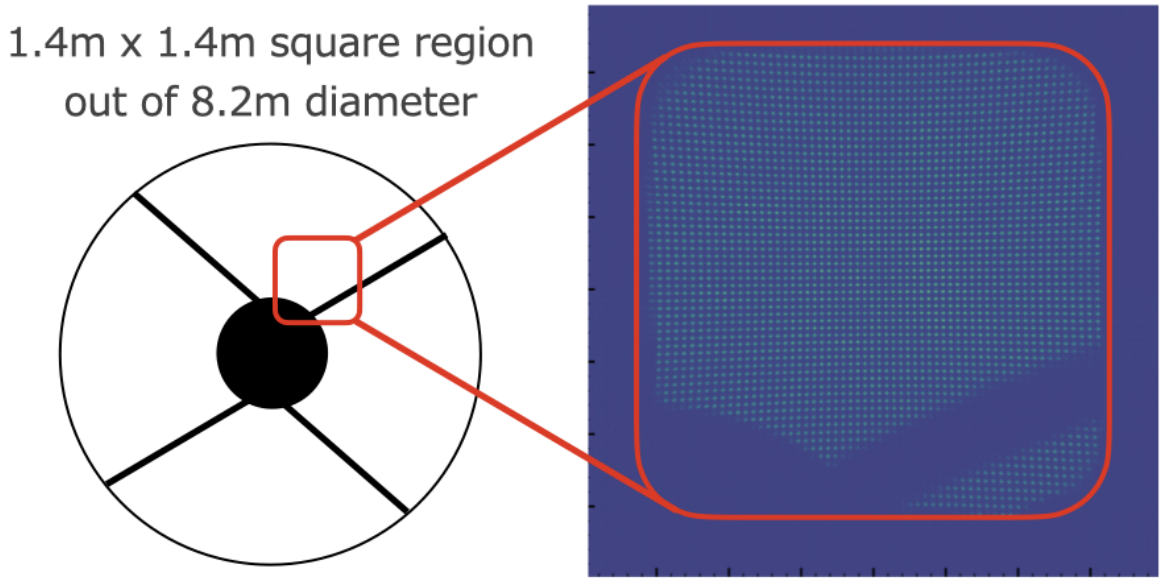

Fig. 2.20 Part of the Subaru telescope pupil measured by the turbulence profiler. A temporally averaged image of a profiler dataset (right) shows the shade of light by telescope spider and central cone on the secondary mirror.

To calculate an analytical cross-covariance map based on equations (2.33) and (2.34), we need information on the measurement geometry, such as angular separation of observed stars and subaperture size of the SH sensor. The separation angles of observed star pair are 200.742 arcsec for the target on November 12, 2022 and 230.532 arcsec for the target on March 14, 2023. Given that the subaperture is 2 cm on the primary mirror, the altitude resolution of SLODAR is 20.6 m and 17.9 m, and the maximum altitude is 411 m and 358 m at each target.

The ground layer turbulence profile is obtained by fitting the analytical cross-covariance maps to the observed one. We conducted minimization of the squared error between the observed map and superposition of the analytical maps of each height as written in equation (2.42). Figure 2.23 shows an example of the fitting results of slope cross-covariance and residual maps.

2.5 Results

2.5.1 Total seeing

The results of the seeing estimation from the slope auto-covariance are shown in the top and middle panels in figure 2.24. The histograms show results of total seeing at each measurement

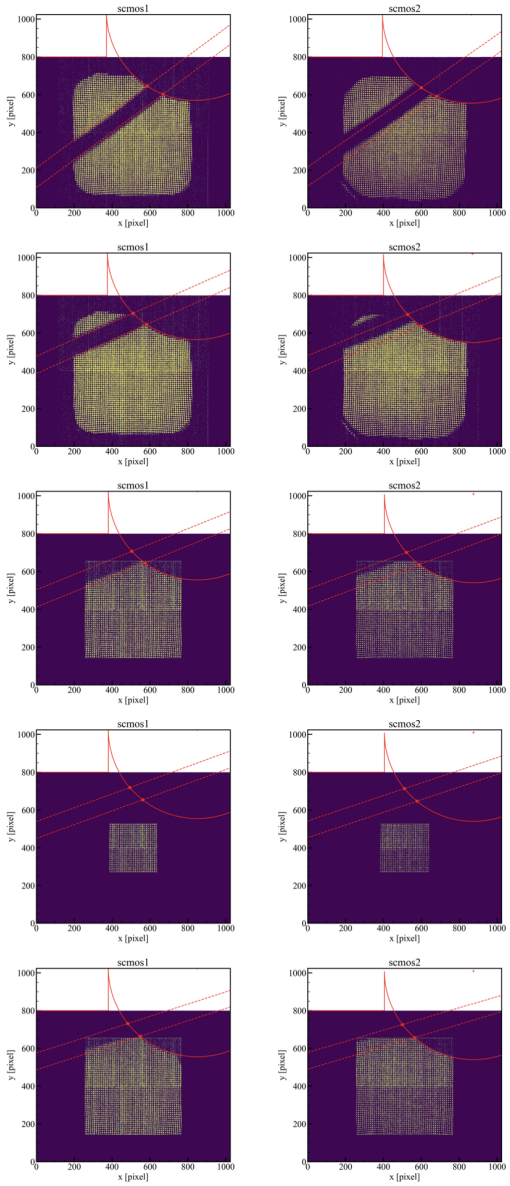

Fig. 2.21 Pupil matching between two SH sensors with datasets taken on Nov.12, 2022. The background is an image of each dataset averaged over time and binarized to 0 or 1 at a certain threshold. The red circle and lines represent shade by the central cone and spider, respectively. The magnification and rotation of the pupil image are determined based on the width and angle of the spider shade, while the position of the pupil image is determined based on the edge of the central cone shade.

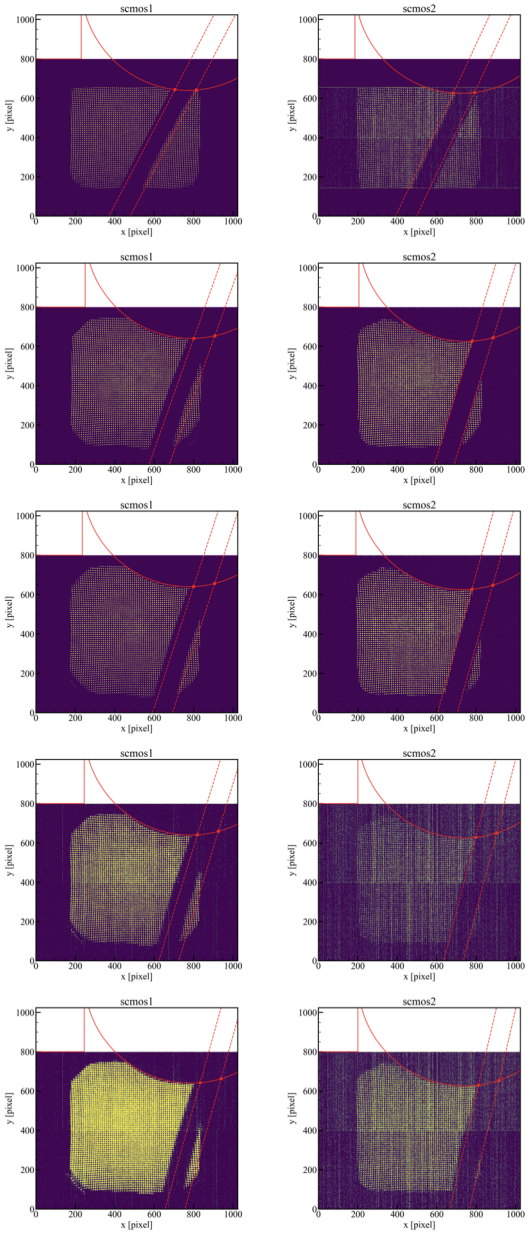

Fig. 2.22 Same figure as 2.21, but for datasets taken on Mar.14, 2023

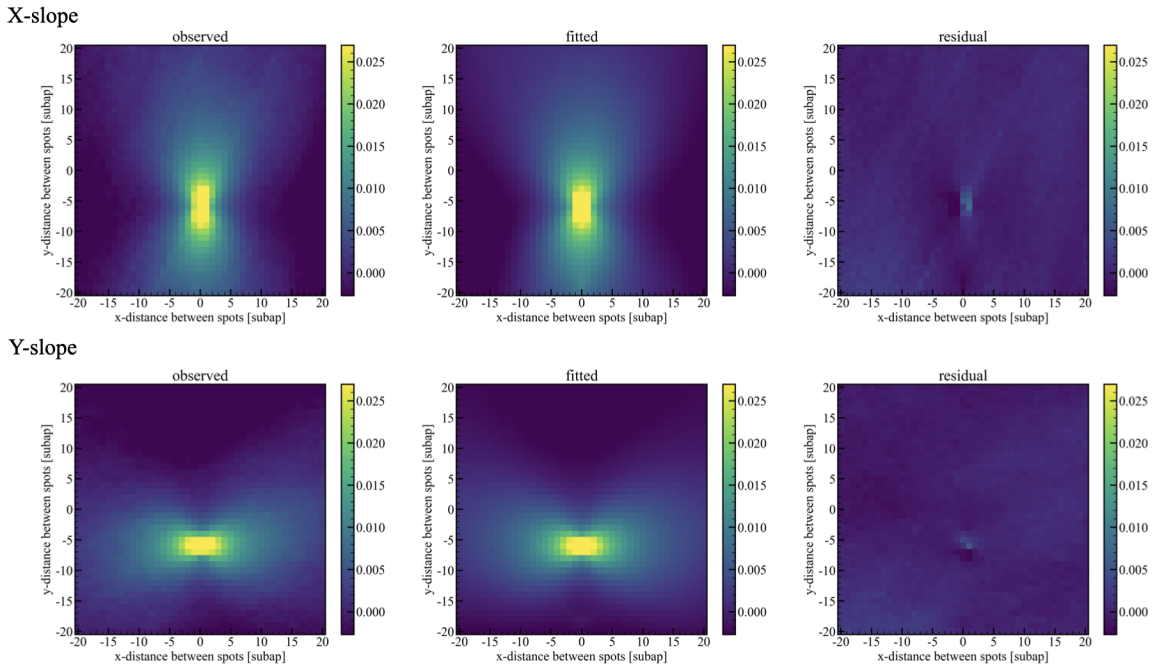

Fig. 2.23 Example of slope cross-covariance analysis. Top-left: Observed X-slope cross-covariance map for dataset taken at 04:44, Mar.14, 2023. bottom-left: Observed Y-slope cross-covariance map. Top-center: Model X-slope cross-covariance map after fitting. bottom-center: Model Y-slope cross-covariance map. Top-right: Residual of the observed and model X-slope cross-covariance map. bottom-right: Residual of the observed and model Y-slope cross-covariance map.

time on Nov.12, 2022, and Mar.14, 2023, respectively. The blue and orange bars indicate that the result is coming from measurement by SH-1 and SH-2, respectively. The estimation error of the total seeing is propagated from the measurement error of the slope auto-covariance map, which is a 1-sigma error reflecting the signal-to-noise ratio of the SH sensor spots. The best signal-to-noise ratio is obtained at 02:42-03:37 on Mar.14, 2023, when Arcturus of the apparent magnitude of ~ 0 is measured. At other times, the measurement error is not as small as the Arcturus measurement due to the faintness of the object and the exposure time of the imaging, but simultaneous measurements by the two SH sensors are achieved.

The total seeing estimated independently from each SH sensor are in good agreement with each other within the estimation error, except for the end of the night, 05:16 and 05:20 on Mar.14, 2023, when the cloud covers part of the sky. Based on the results, medians of total seeing measured in our study are 0.688 arcsec on Nov.12, 2022 and 0.625 arcsec on Mar.14, 2023.

The bottom panel of figure 2.24 shows the measured seeing value as a function of the exposure time of the SH sensor. Seeing on both dates does not show a systematic trend depending on the exposure time, indicating that exposure time difference does not affect the seeing measurements Therefore, in our analysis, we do not correct any effect related to the sensor exposure time.

2.5.2 Free atmospheric turbulence profile

The result of the free atmospheric turbulence profile reconstructed assuming the fixed layers at 1, 2, 4, 8, and 16 km is shown in figure 2.25. Each panel shows an estimated profile at each measurement time. The blue and orange profile is the results of SH-1 and SH-2, respectively. We plot the mean value of all four sub-datasets as symbols and standard deviation as errorbars. The black dotted profile stands for a representative profile obtained at Maunakea by the site testing campaign for the TMT (Els et al., 2009). It shows median turbulence strength individually calculated for each height.

At most measurement times, the blue and orange profiles match and the error sizes are small enough to characterize turbulence strength at each altitude. This indicates that the simultaneous measurements by the two SH sensors and the four sub-datasets show good agreement with one another. As for the large difference between profiles at 23:45, Nov.12, 2022, in which the blue profile shows its peak strength at 8 km while the orange profile has its peak at 4 km above, the orange profile should be more reliable according to the error size. It is possible that some of the sub-datasets in SH-1 show strong turbulence at 8 km instead of 4 km, and the mean of the four sub-datasets is affected. The overall shape of the turbulence profile varies widely from time to time. There is a strong layer at 4 km on Nov.12,

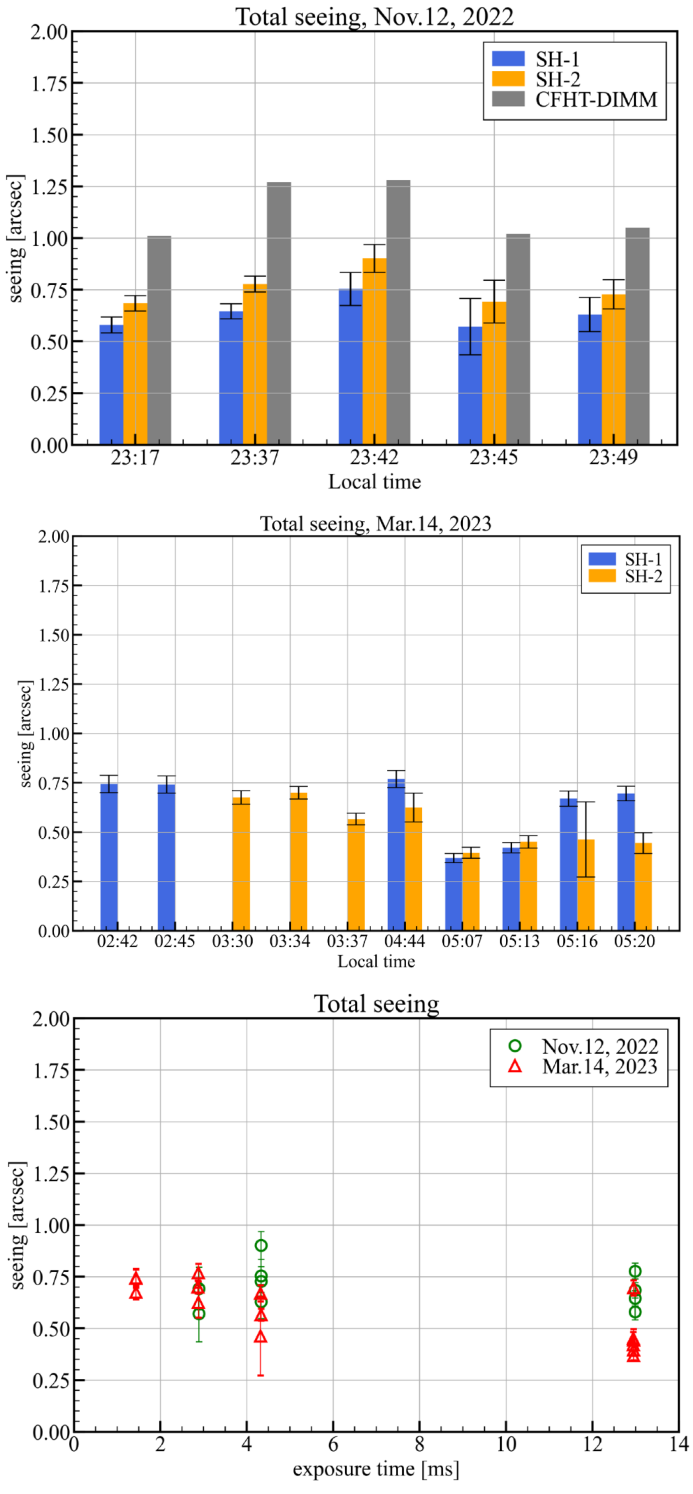

Fig. 2.24 Total seeing measured by slope auto-covariance analysis. Total seeing measured on Nov.12, 2022 and on Mar.14, 2023 is shown in the top and bottom panels, respectively. Blue and orange bars represent results measured by SH sensors 1 and 2, respectively. The errorbar is coming from measurement error of auto-covariance map.

2022 compared to the median profile of site testing. On the other hand, on Mar.14, 2023, turbulence at 1 km and 8 km show intense time variability.

The top and middle panels of figure 2.26 show the integrated strength of the free atmospheric turbulence. The total strength is calculated as the sum of $C_n^2(h)\Delta h$ of turbulence profile at each time shown in figure 2.25. The measurements by SH-1 and SH-2 are consistent within their error range between the two SH sensors. The median of measured free atmospheric seeing is 0.637 arcsec for Nov.12, 2022 and 0.444 arcsec for Mar.14, 2023.

The bottom panel of figure 2.26 shows the free atmospheric seeing as a function of SH sensor exposure time. Here also, measured seeing values do not show any trend depending on the exposure time.

2.5.3 Wind profile

Wind profile, i.e. wind speed and direction as a function of height, is shown in figure 2.27 as a result of the scintillation temporal auto-covariance analysis performed in section 2.4.5. The left and right panels are wind speed and direction profiles, respectively. Results on Nov.12, 2022 are shown in the top panels and Mar.14, 2023 in the bottom. The horizontal axis is the wind speed in the unit of $\mathrm{m} \cdot \mathrm{s}^{-1}$ or wind direction in the unit of deg. The vertical axis means height measured from the altitude of the Subaru telescope (sea level of 4200 m). The colored points correspond to each clump seen in the auto-covariance map of each dataset. Blue and orange colors indicate that the measurement is coming from SH-1 and SH-2, respectively. The result is compared with the wind profile obtained by meteorological measurements, which is available from the Maunakea Weather Center website (http://mkwc.ifa.hawaii.edu/current/). The measurements are conducted using rawinsonde launched at the Hilo airport in Hawaii island twice a day (noon and midnight). The gray points show wind speed and direction by the rawinsonde at the nearest measurement time as our measurements.

The wind profiles measured by the two independent methods are in good agreement in spite of the measurement time variability. While rawinsonde is a direct measurement method at all altitudes by a balloon, the scintillation auto-covariance method is sensitive only to turbulence layers causing strong scintillation intensity. Therefore, the results by scintillation auto-covariance are not continuous in altitude direction and are distributed at different altitudes on the two measurement dates. There are some points of discrepancy seen around the height of 5-10 km in the wind direction profile on Nov.12, 2022 or around the height of 20 km in the wind velocity profile on Mar.14, 2023. Whether this difference is simply due to differences in measurement time or due to systematic measurement errors that occur under certain conditions needs to be investigated in the future.

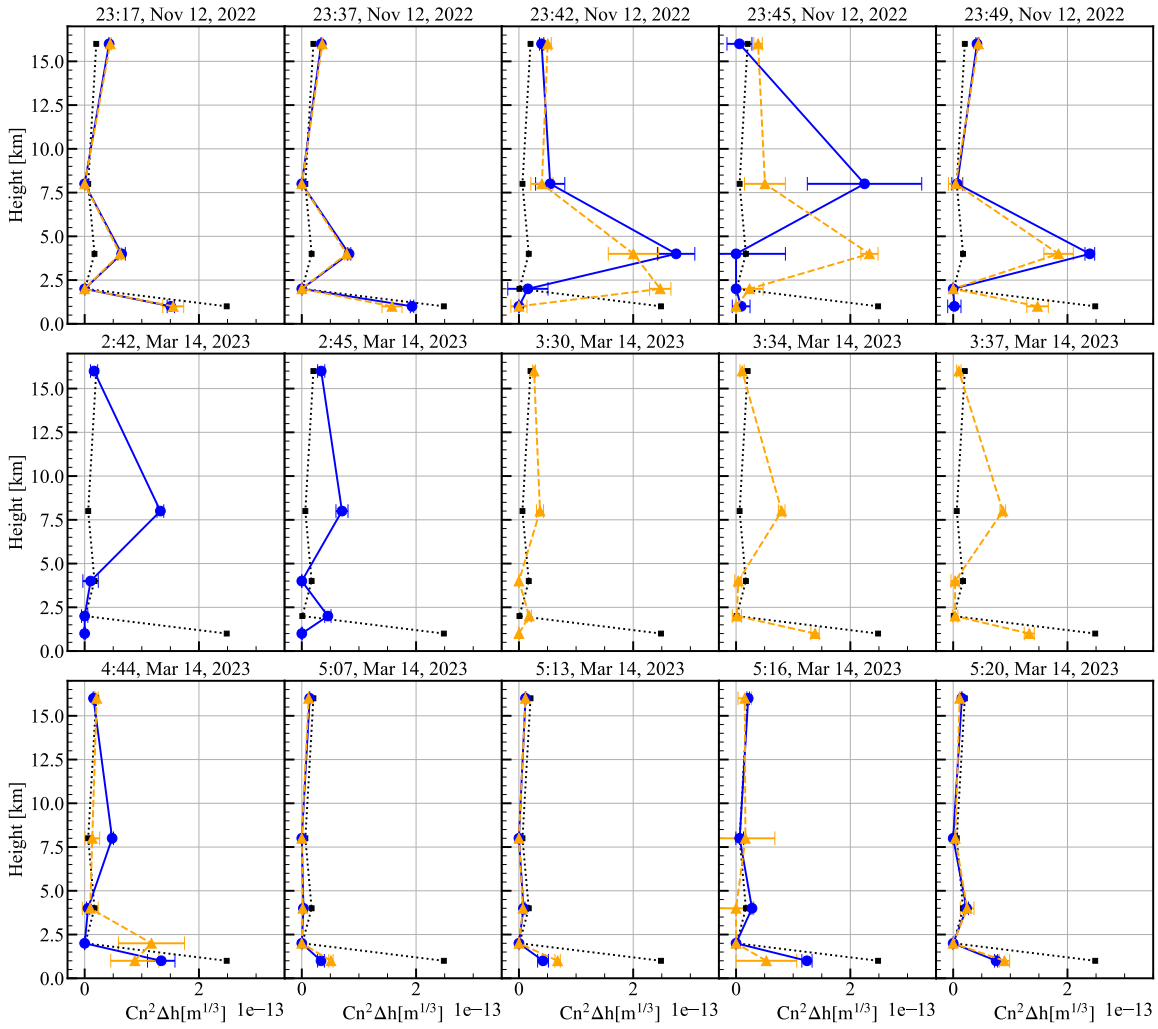

Fig. 2.25 Free atmospheric turbulence profile. The top panels show turbulence profiles on Nov.12, 2022. Middle and bottom panels show turbulence profiles on Mar.14, 2023. In each panel, the colored solid lines are reconstructed profiles at different times, assuming 1, 2, 4, 8, and 16 km fixed height layers. We plot the mean of simultaneous measurement by the four subdata on the two SH sensors. The errorbars represent standard deviation. The black dashed line is a median turbulence profile at Maunakea taken from Els et al. (2009) as a comparison.

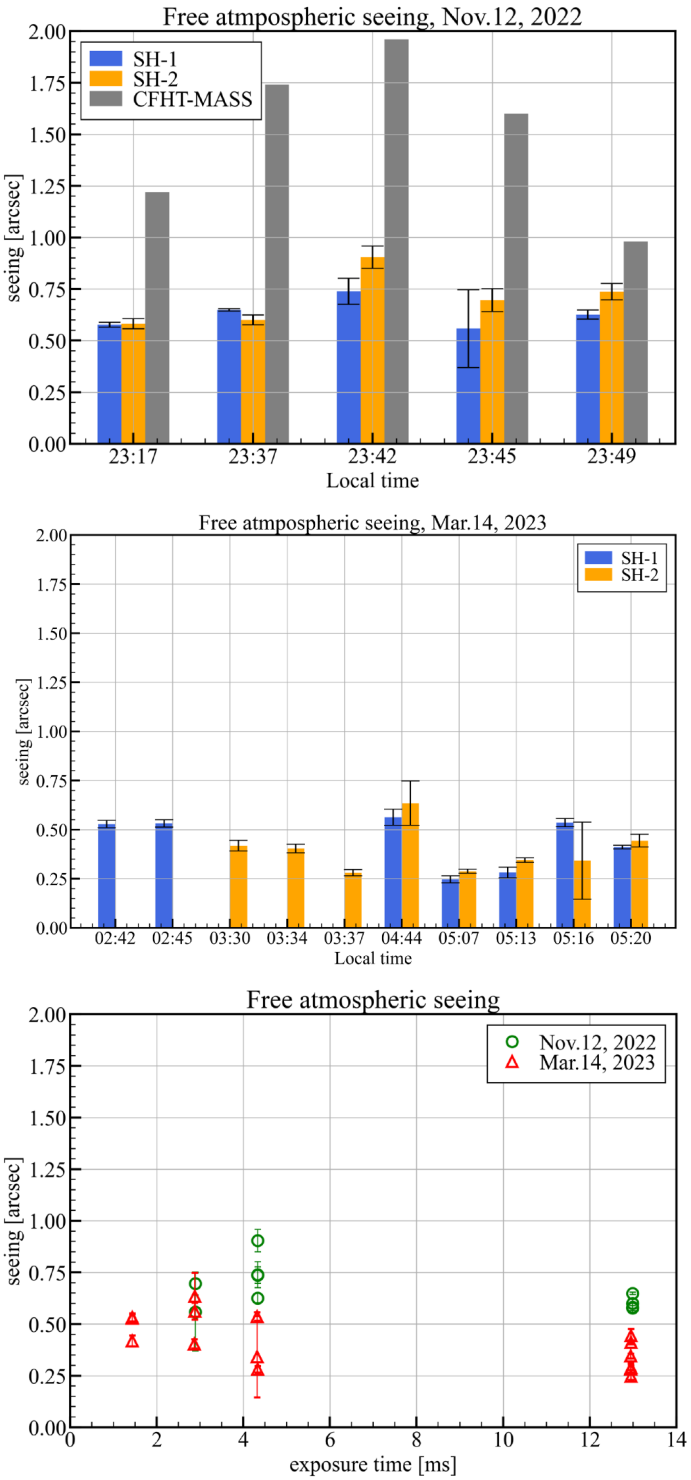

Fig. 2.26 Free atmospheric seeing. The total free atmosphere turbulence is computed as the sum of the free atmospheric turbulence profile shown in figure 2.25. The errorbar of each measurement is the standard deviation of the four profiles reconstructed from four subdata.

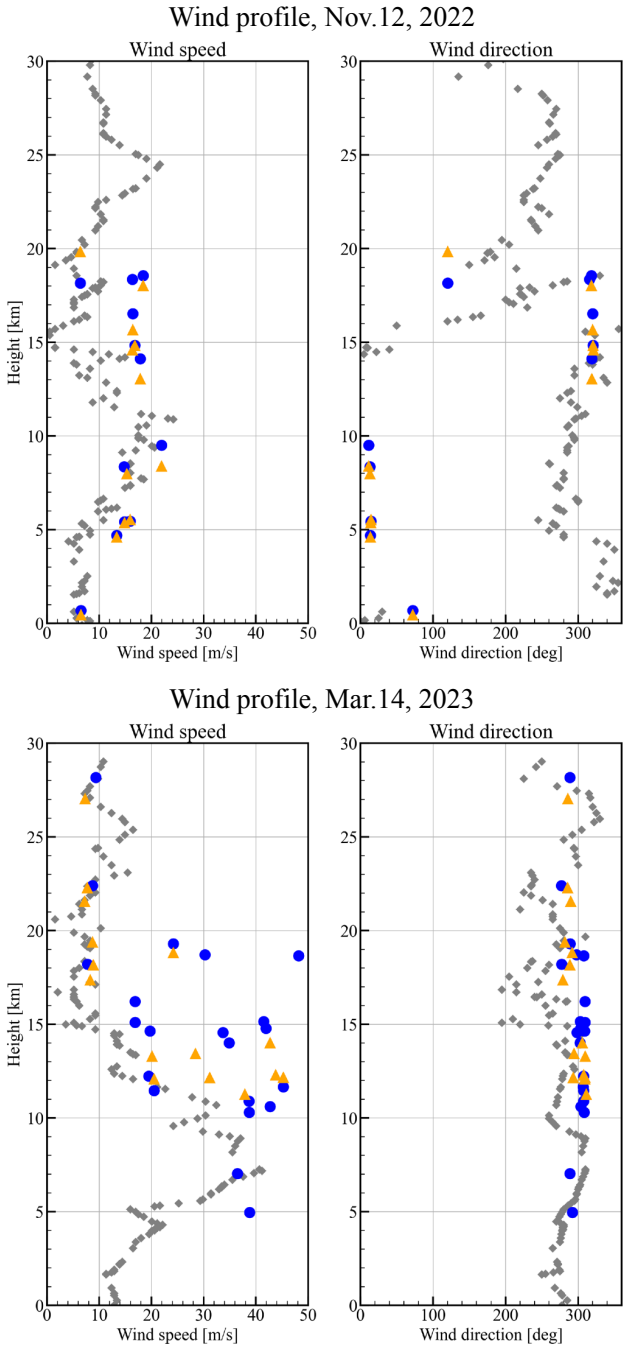

Fig. 2.27 Wind speed/direction profile based on the scintillation auto-covariance analysis. The left panel shows the wind speed profile on Nov.12, 2022. Center and right panels show wind speed at 2:40-2:40 and 4:30-5:30 on Mar.14, 2023, respectively. The blue and orange plots are measured from the scintillation auto-covariance map of SH sensors 1 and 2, respectively. The gray dots are the results of rawinsonde, a balloon measurement, on the same day at the Hilo airport on the Big Island of Hawaii.

2.5.4 Ground layer turbulence profile

Ground layer turbulence profiles estimated by the SLODAR analysis described in section 2.4.7 are shown in the left panel of figure 2.28. All the ground layer profiles obtained from each dataset are shown as different colored lines. The horizontal axis is the logarithm of $C_n^2(h)\Delta h$ and the vertical axis is the height measured from the primary mirror of the Subaru telescope. Because the pupils of the two SH sensors are aligned with respect to the position of the center cone on the secondary mirror, the height reference of SLODAR is the position of the secondary mirror at an optical height of -80 m. By correcting for the effect of the telescope elevation angle of the measurement, the effective altitude range is approximately -75 m to 310 m for Nov.12, 2022 and -60 m to 210 m for Mar.14, 2023. The effective altitude resolution of SLODAR is ~19 m for Nov.12, 2022 and ~13 m for Mar.14, 2023.

The right panel of figure 2.28 shows a cumulative distribution of the turbulence strength. Most of the turbulence power concentrates in the height range of -10 m to 30 m. The negative altitude represents the optically negative altitude, which corresponds to the optical path between the primary and secondary mirrors in the case of the Subaru telescope. Thus, the result means that most of the turbulence up to 300 m is within 30 m height from the telescope primary mirror. Considering that the roof of the dome is located at the height of ~ 20 m from the primary mirror, the dominant component is dome seeing and some components of the ground surface near the dome. The behavior of the green and purple lines is due to noise at the edge of the cross-covariance maps. For the red line, the profile is not reconstructed successfully because the dataset has the lowest signal-to-noise ratio and the entire covariance map is noisy.

The top and middle panels in figure 2.29 show integrated strength of the ground layer turbulence. We converted the sum of the $C_n^2(h)\Delta h$ in all the height ranges of the ground layer profile to the ground layer seeing value. The errorbar of the seeing is estimated from the measurement error of the cross-covariance maps. The result shows that the ground layer seeing is systematically larger on Mar.14, 2023 than the other day, indicating that the ground layer seeing can change with time.

The bottom panel in figure 2.29 is a plot of the ground layer seeing as a function of the exposure time of the SH sensor. Similar to the trend shown in the results of total seeing and free atmospheric seeing, there is no trend that the seeing depends on the exposure time.

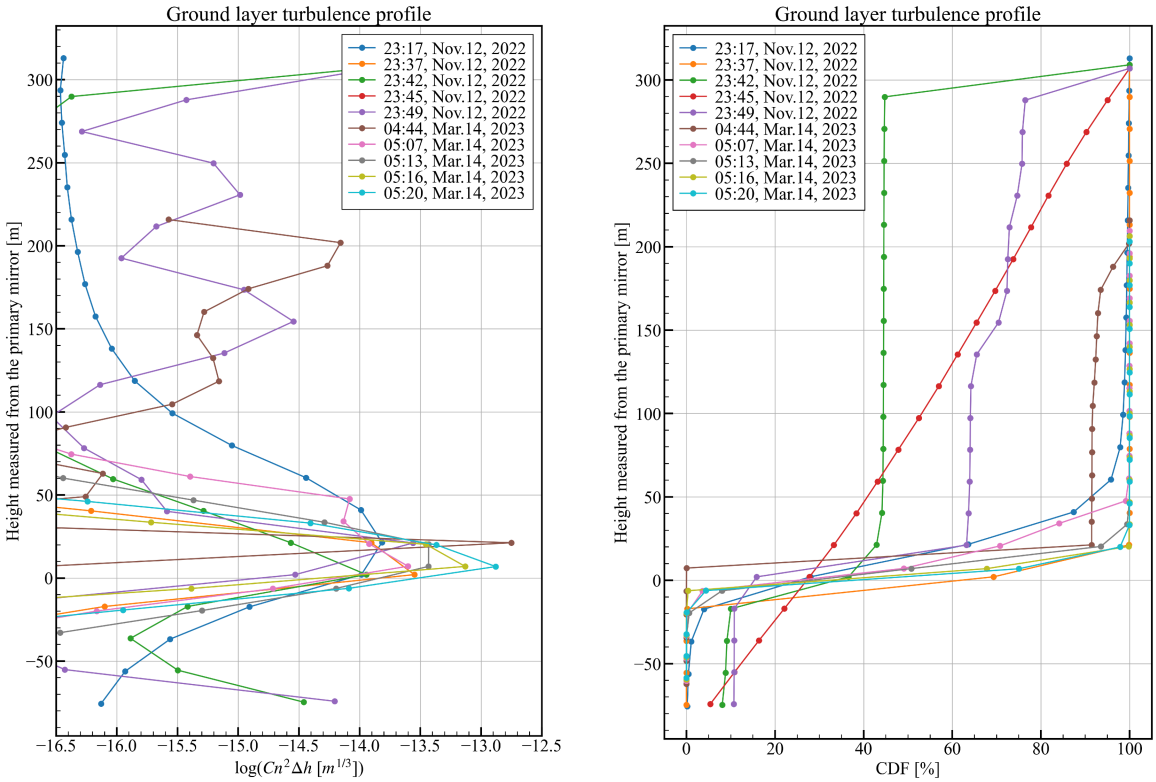

Fig. 2.28 Ground layer turbulence profile. The vertical axis means the height from the primary mirror of the Subaru telescope. Left: The turbulence profile reconstructed from the slope cross-covariance map of each dataset is shown as different colored lines. Right: Cumulative distribution of the ground layer turbulence of each dataset.

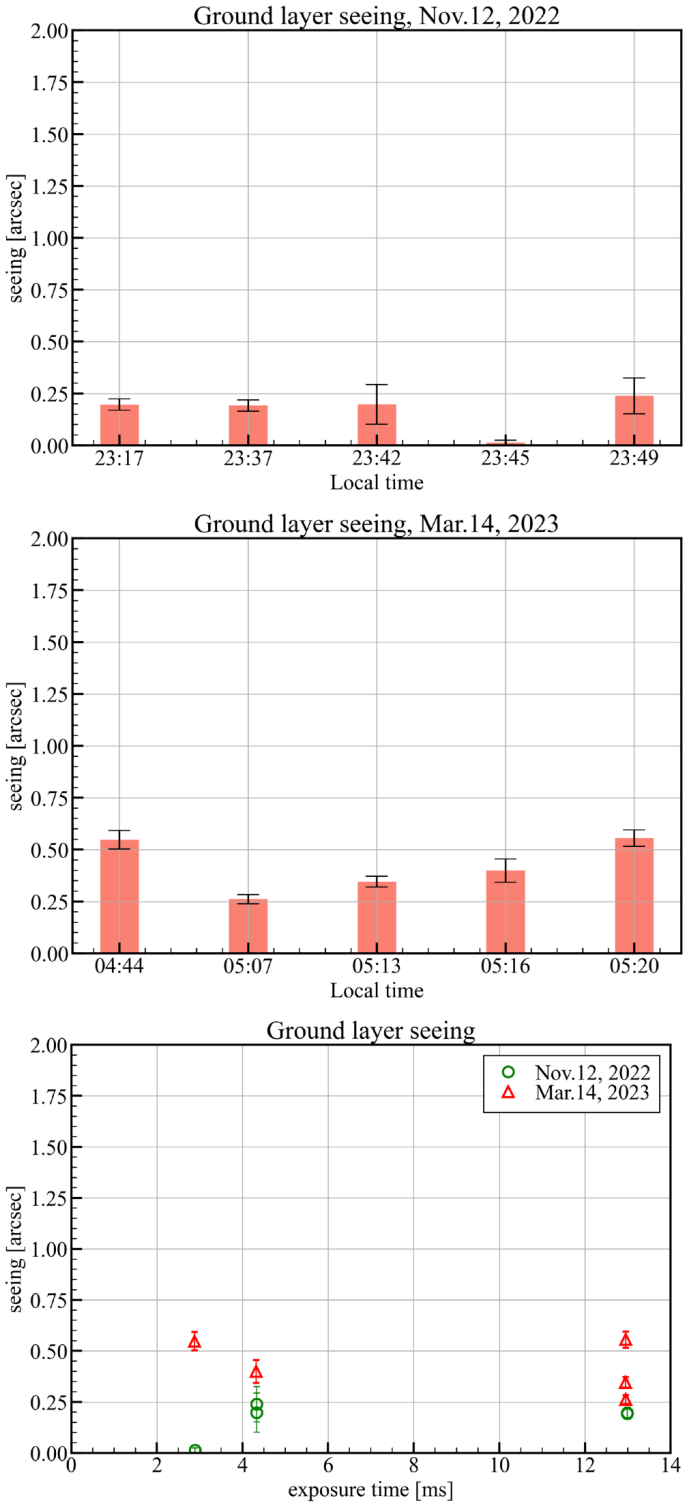

Fig. 2.29 Ground layer seeing. The total ground layer turbulence is computed as the sum of the ground layer turbulence profile shown in figure 2.28. The errorbar of each measurement comes from the measurement error of the cross-covariance map.

2.6 Discussion

2.6.1 Comparison with CFHT MASS-DIMM

As shown in the section 2.5.1 and 2.5.2, our turbulence measurement results are compared with simultaneous measurements performed by the Canada-France-Hawaii telescope (CFHT) MASS-DIMM only for measurements on Nov.12, 2022. Figure 2.30 shows a one-to-one plot of measurement results of CFHT MASS and SH-MASS. Each panel shows turbulence strength of a total, 1 km and below, 2 km, 4 km, 8 km, and 16 km as blue and orange symbols. The sum of 0.5 km and 1 km strength is shown in the 1km-and-below panel for CFHT MASS measurement. Since CFHT MASS has a higher temporal resolution of the measurement, data from the closest time is selected for comparison. The difference in time between the two measurements is less than 1 minute. The distribution of the CFHT MASS 34 measurements between 23:00 and 24:00 is shown in the gray area. The cyan and magenta symbols show the same one-to-one comparison, but the SH-MASS profile is reconstructed without imposing constraints by total seeing measurement.

From the comparison, SH-MASS measurements show good agreement with CFHT MASS at high layers such as 8 km and 16 km. The 4 km turbulence of SH-MASS is slightly smaller than that of CFHT MASS. As for the 2km turbulence, SH-MASS shows systematically much smaller turbulence strength than CFHT MASS. However, according to the gray-shaded distribution, turbulence at the 2 km layer is smaller than in the surrounding layers, and measurements by CFHT MASS are not stable over time. Therefore, both measurements are considered similar in behavior. Regarding the total and 1km-and-below turbulence, the SH-MASS result is consistent without the constraint of seeing measurement using slope information. Based on these results, we can say that SH-MASS and CFHT MASS return consistent results at almost all altitudes when not considering restrictions by seeing determined from the slope.

However, without the seeing constraints, scintillation-based seeing becomes greater than slope-based seeing. It is not a physical case given that the ground layer does not contribute to scintillation. This problem is known as MASS overshoots and common in the traditional MASS-DIMM instrument which estimates ground layer seeing from the difference between MASS seeing ϵ_{MASS} and DIMM seeing ϵ_{DIMM} as $(\epsilon_{\mathrm{DIMM}}^{5/3} - \epsilon_{\mathrm{MASS}}^{5/3})^{3/5}$. The cause of the overshoots is thought to be the actual atmospheric turbulence that does not completely follow weak perturbation theory (Tokovinin and Kornilov, 2007). Some MASS-DIMM instruments have a correcting algorithm empirically determined from numerical simulation, but such a correction is not implemented for the CFHT MASS-DIMM yet. That is the reason why we put the seeing constraints when reproducing turbulence profiles. The cause of the large

discrepancy between the results of SH-MASS and CFHT MASS seen in the top panel of figure 2.26 is possibly overestimation by strong turbulence.

2.6.2 Consistency between scintillation auto-covariance map and SH-MASS

In this study, wind speed and direction profiles are obtained by analyzing the scintillation auto-covariance map, and turbulence profiles are calculated from SH-MASS. However, the information used in both analyses is identical in terms of spatial correlation of scintillation obtained with a single SH sensor. Therefore, we estimate a turbulence profile by obtaining the signal intensity for each component on the scintillation auto-covariance map shown in figure 2.18. In our study, auto-covariance is calculated as a value normalized by the time-averaged value of brightness, i.e., the NSI. Therefore, the relationship with turbulence intensity is a weighting function assuming a single subaperture as the spatial filter. The conversion factor is obtained for the turbulence height estimated from the analysis of the signal width.

The turbulence profiles obtained by the analysis are shown in figure 2.31. In the Nov.12, 2022 profiles, high turbulence intensity of around 1 km and local intensity peaks around 4-5 km are seen. This is in good agreement with the trend seen in figure 2.25. In the Mar. 14, 2023 profile, there is a localized area of strong turbulence around 10-11 km. In figure 2.25, strong turbulence is measured at an altitude equivalent to 8 km in the early hours of 2:40-3:40.

2.7 Conclusion

In this chapter, we report on the atmospheric turbulence profiling experiment for the ULTIMATE: LTAO and GLAO project at the Subaru telescope (mentioned in Chapter 1). The purpose of the project is to obtain (1) free atmospheric turbulence profiles up to $\sim$ 20 km with an altitude resolution of a few km and (2) ground layer turbulence profiles below $\sim$ 1 km with a fine resolution of a few tens of m, as information for LTAO and GLAO projects at Subaru telescope, respectively.

In order to achieve the goal, we develop a turbulence profiler consisting of two SH sensors with a fine subaperture of 2 cm and perform engineering observations of star pairs brighter than a magnitude of $\sim$ 6 in V or R band with a separation angle of 3-5 arcmin at the Subaru telescope.

We apply two analysis methods: SH-MASS, a method for free atmospheric turbulence at higher than 1 km with the same or higher resolution of a few km than classical MASS based on

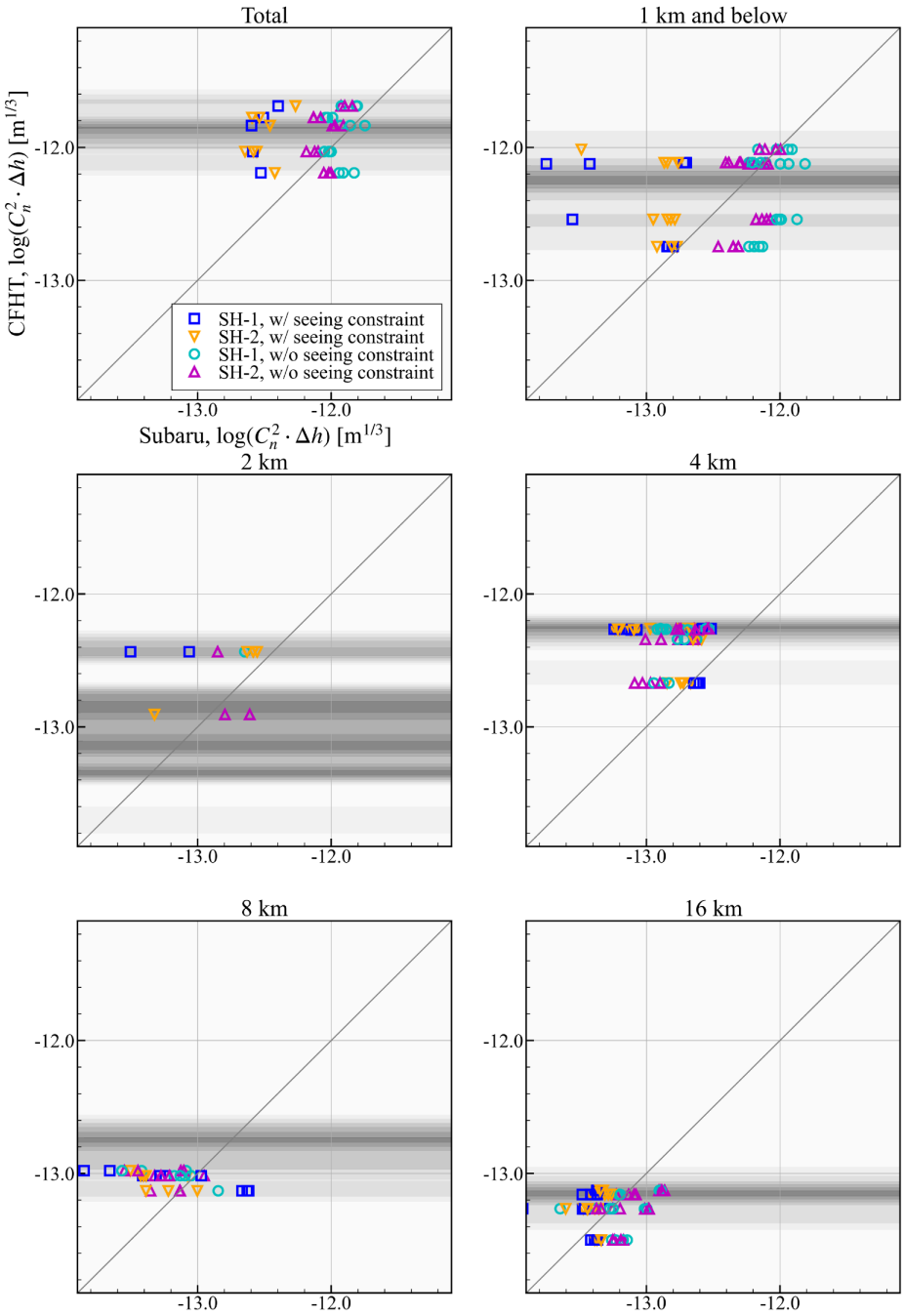

Fig. 2.30 Comparison of free atmospheric turbulence measurement with CFHT MASS. Each panel shows a one-to-one plot of turbulence strength measured by our turbulence profiler and CFHT MASS. The temporal correspondence between the two measurements is less than 1 minute. As for the CFHT MASS measurement, which has higher temporal resolution, the distribution of 34 measurements in 23:00-24:00 on Nov.12, 2022 is shown as gray shade.

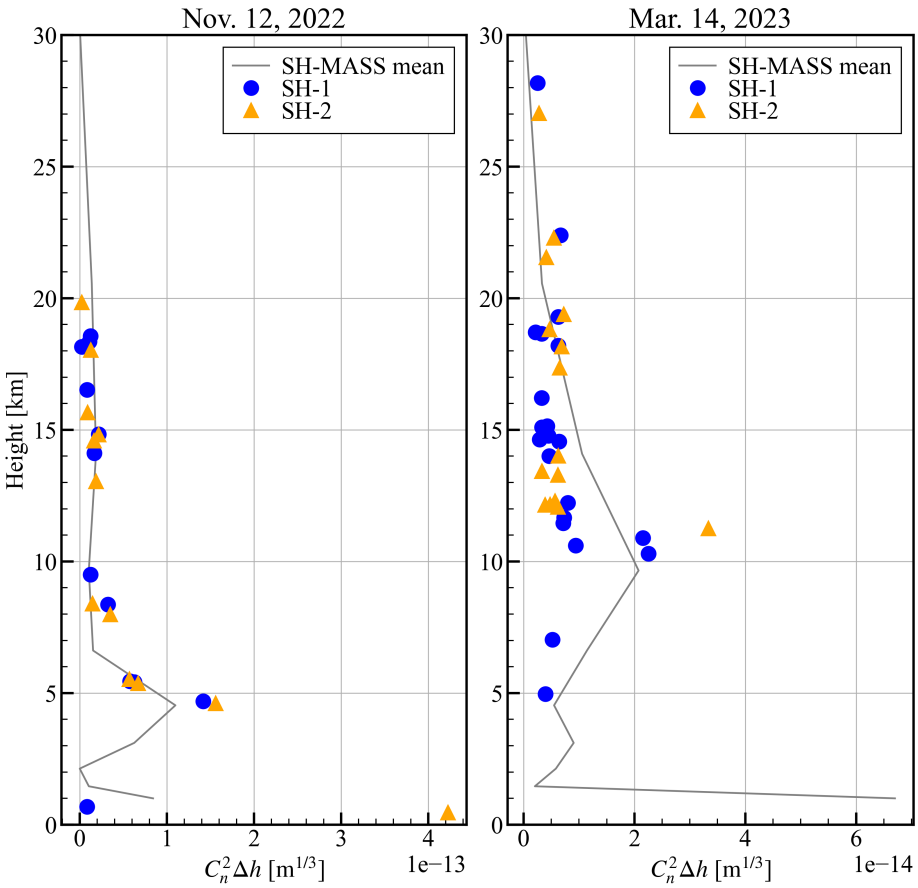

Fig. 2.31 Turbulence strength profile based on the scintillation auto-covariance analysis. The left and right panels show $C_n^2\Delta h$ as a function of height from the telescope measured on Nov.12, 2022 and Mar.14, 2023, respectively. Each colored symbol represents turbulence strength measured with one of the moving peaks in the auto-covariance maps. Blue and orange symbols stand for measurement by SH-1 and SH-2, respectively. Results at all the measurement times are stacked in these figures. As a comparison, the mean of all the SH-MASS profiles is shown as grey lines. The SH-MASS profiles are reconstructed assuming 10 layers at 1.0, 1.5, 2.1, 3.1, 4.5, 6.6, 9.7, 14.1, 20.6, and 30.0 km

spatial correlation of scintillation, and SLODAR, a method for ground layer turbulence below $\sim$ 400 m with high resolution of $\sim$ 20 m from the correlation of wavefront measurements in two different directions. In addition to the profiling of turbulence strength, we measured total seeing from the spatial correlation of wavefront and profiles of moving speed and direction of turbulence from the temporal correlation of scintillation.

As a result, the obtained total seeing shows consistent values between simultaneous measurements by the two SH sensors, but systematically smaller values compared to CFHT DIMM by $\sim$ 35% in median. The reason for the difference might come from the difference in ground layer turbulence including dome seeing between the Subaru and CFHT sites.

The obtained free atmospheric turbulence profiles at 1, 2, 4, 8, and 16 km altitudes are compared with the previous site test campaign for the Thirty Meter Telescope (TMT) and measurement by CFHT MASS. The profiles measured simultaneously by the two independent SH sensors and four sub-datasets show consistent results. The profiles show different shapes between the two observation runs, supporting that the distribution of turbulence is distinguished by SH-MASS. Compared to CFHT MASS, our SH-MASS results show a much smaller total turbulence strength possibly because we impose a physical constraint that the total turbulence strength measured by SH-MASS should be smaller than the total seeing while CFHT MASS does not have such a constraint and suffers from an overshoot problem (total turbulence strength measured by CFHT MASS is larger than that measured by CFHT DIMM). If we perform SH-MASS without physical constraint, the results of SH-MASS and CFHT MASS show good agreement.

The wind speed and direction profile are compared with results from rawinsonde, which are measurements using a balloon. Although our observation and rawinsonde measurement are not simultaneous due to the low temporal frequency of rawinsonde, our measurement of wind speed and direction shows very good agreement with the directly measured results by rawinsonde. With the wind speed and direction, it becomes possible to increase information on wavefront measurement by assuming that each turbulence layer moves toward the wind direction with the wind speed without changing its turbulence structure. This multi-time-step tomographic reconstruction would increase the Strehl ratio by a factor of 1.2-1.5 (Ono et al., 2016a).

The reconstructed ground layer turbulence profiles at below $\sim$ 300 m with a high altitude resolution of 10-20 m suggest that most of the ground layer turbulence is concentrated at below 30 m, which is comparable with or a little higher than the dome of the Subaru telescope, and dominated by dome seeing. The result supports that the GLAO system will effectively work at the Subaru telescope.

Chapter 3

Rolling Shutter Effect on Wavefront Sensing

3.1 Introduction

In many WFS in AO including the SH-WFS, the wavefront distortion is measured as a local wavefront tilt or curvature using an image sensor. This study deals with the effect of shutter modes on wavefront measurements.

Generally, image sensors are divided into two main types. The first is the Charge Coupled Device (CCD). CCD sequentially counts photons received by each of the photodiodes that make up the image sensor by transferring photoelectrons to neighboring pixels. More specifically, by applying a different voltage to the electrode attached to each photodiode than to the adjacent electrode, the photoelectrons are moved vertically and horizontally and are sequentially read out by a single analog-to-digital converter and amplifier. Since the detected charges are temporarily stored by the charge storage area used in interline and frame transfer CCD, it is possible to start and end exposure simultaneously for all pixels. This method is called global shutter mode.

The second is Complementary Metal Oxide Semiconductor (CMOS). CMOS is the same as CCD up to the stage where photoelectrons are received by each photodiode. However, unlike CCD, analog-to-digital conversion and amplification are performed at each pixel. Signals are read out by sequentially switching the connection between each pixel and the signal readout line. In many cases, the switching is performed sequentially pixel row by pixel row. Therefore, the start and end of exposure are also performed at different times for each pixel row. This method is called rolling shutter mode.

In the rolling shutter mode, image distortion becomes a problem when observing fast-moving objects. Since exposure is not simultaneous among pixel rows in a detector, the object image is distorted when the object moves in a short time relative to the difference in exposure timing within a single frame.

For one of the reasons for image distortion caused by rolling shutter mode, many AO WFS have used Electron Multiplying CCD (EM-CCD) with global shutter mode. The EM-CCD is the same as a usual CCD before readout, but the number of photoelectrons is multiplied by applying a higher voltage than usual with a register placed before an analog-to-digital converter. The effective readout noise becomes 1 divided by the multiplication gain, which is typically less than 1 e^-. Another general advantage of CCD is uniformity of image quality. The spatial variation of readout noise is minimal in CCD because they use a single amplifier, while noise performance and gain can vary from pixel to pixel in CMOS.

Nevertheless, it is worth considering the use of CMOS for its many advantages. The first advantage of CMOS is the high-speed readout process. Since CMOS performs digitization and amplification at each pixel, the readout time of the entire image is reduced compared to CCD. The second advantage is the partial readout function by limiting the number of pixel rows to be read. If the entire image area is not needed to detect the target, an even faster readout is achieved instead of reducing the image size. Also, the typical readout noise of CMOS is $\sim$ 1-2 e^-, which is comparable to that of EM-CCD considering that the stochastic multiplication process of EM-CCD introduces multiplicative noise additionally. Another advantage is the absence of smears and blooming. Smear/blooming is a phenomenon in which charge overflows in the direction of charge transfer or in surrounding pixels when strong light is incident. This does not occur in CMOS, which does not perform charge transfer and allows each pixel to be read out independently. CMOS also has the following advantages: it operates at a low voltage without the need for charge transfer, it consumes low power because readout is possible only by switching, and it is easy to make the system smaller and lighter without the need for charge transfer circuits, and it is low in cost.

It should be noted that some recent CMOS have achieved global shutter mode by adopting in-pixel analog memory in each pixel (Oike et al., 2017; Kobayashi et al., 2019). However, the current majority of CMOS still use rolling shutter mode.

From the point of view of WFS in AO, the required performances of the detector are summarized. First is detector size. The target of WFS is basically an LGS. LGS are created by the excitation of natural sodium layer distributed at 90 km above the sky. Since the sodium layer has a thickness of about 10 km (Pfrommer and Hickson, 2014), the LGS has an elongated shape along the direction of laser launch. Therefore, an elongated spot is measured at distant subapertures, while a round laser spot is measured in the subapertures close to

the laser launch telescope. The measured elongation at a distance of telescope diameter away from the laser launch telescope is a few arcsec for an 8-10 m telescope and about 10-20 arcsec for a 30-40 m telescope (Bardou et al., 2021). On the other hand, a pixel scale of about 1.0-1.5 arcsec $\cdot$ pix^{-1} is ideal for measuring positional variations of spots due to atmospheric turbulence. In other words, the number of pixels needed to sample a single spot image may be only a few pixels for an 8-10 m telescope, but more than 10 pixels for a 30-40 m telescope. Furthermore, considering the number of subapertures, a detector size of several hundred pixels is required for an 8-10 m class telescope and several thousand pixels for a 30-40 m class telescope. Next, regarding the frame rate, a speed of 500-1000 Hz is ideal for dealing with temporal variations in atmospheric turbulence. Finally, as for readout noise, a low readout noise of a few electrons is ideal given the fast frame rate and the spot elongation.

Regarding effective readout noise, EM-CCD is superior to CMOS. However, recent CMOS are available with quantum efficiencies as high as 90% or more at 600 nm, making it difficult to determine the better choice in terms of signal-to-noise ratio. With respect to detector size, CMOS tends to have more pixels than EM-CCD. Furthermore, CMOS has a faster readout speed, which may reduce the temporal delay between measurement and correction in the AO loop. Therefore, the most significant concern is the effect of image distortion caused by rolling shutter mode.

With the above background, the purpose of this study is to evaluate the effect of image distortion caused by rolling shutter mode on wavefront measurements in AO.

3.2 Analytical evaluation

3.2.1 Modeling the shutter modes

The first step in evaluating the impact of image distortion due to rolling shutter mode is to model the shutter mode. In this study, we employ two shutter modes that are commonly used in rolling shutter detectors. One is a sequential exposure and readout from the central two rows to the top and bottom rows, which we call the middle-out rolling shutter mode. The other is a sequential exposure and readout mode from the top row to the bottom row, which we call top-bottom rolling shutter mode. Evaluation is performed for three shutter modes, including the usual global shutter mode. A conceptual diagram of each shutter mode is shown in figure 3.1.

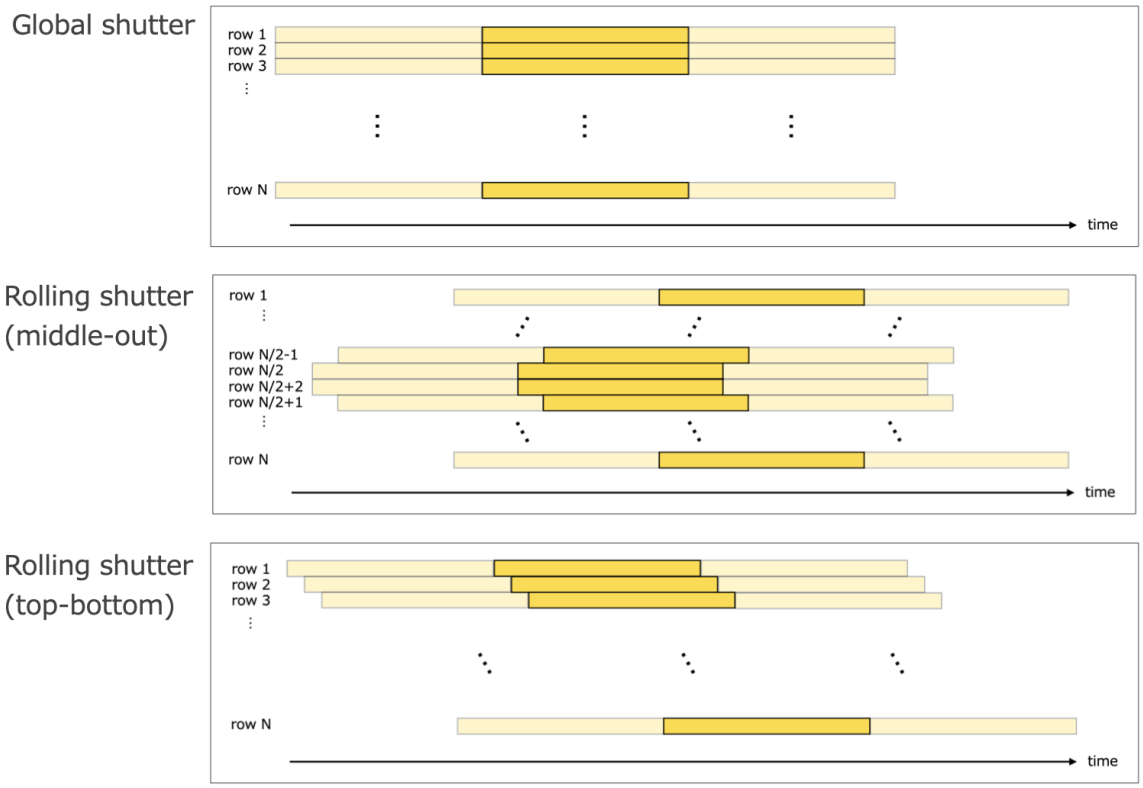

Fig. 3.1 Conceptual diagram of shutter modes for some typical systems considered in this study. In each panel, the horizontal axis is the time axis, and the yellow bars represent the exposure time in each row. The top panel is for global shutter mode and all the rows are exposed simultaneously. The middle and bottom panels are for rolling shutter mode, in which each row is exposed at different times.

3.2.2 Simplified simulation of wavefront measurement

We next describe a simplified simulation conducted to understand how different shutter modes affect wavefront measurements.

In this simulation, we consider a single oscillating Zernike mode as a simplified wavefront. For a single Zernike mode, its coefficient is varied periodically in time as a sine wave. The Zernike mode is represented by a 32×32 grid that matches the number of subapertures in the ULTIMATE-START/Subaru WFS.

The Zernike modes given as input are the 10 lowest-order modes, excluding the piston mode. Because actual atmospheric turbulence has more power on larger spatial scales, i.e., lower-order Zernike modes, we select 10 lowest-order modes, which are tip, tilt, defocus, spherical, and two types of astigmatism, coma, and trefoil. The piston component is not considered here because it cannot be measured by the SH-WFS.

SH-WFS measurement is then simulated according to each shutter mode. The oscillating Zernike mode is sampled at a frame rate of 400 Hz and an integration time of 2.5 ms. Since the SH-WFS measures the wavefront as its tilt, we sample the spatial differential of the time-varying wavefront instead of the wavefront itself. In the case of the global shutter, sampling is done at the same time for the entire 32×32 grid, whereas in the case of the rolling shutter, sampling is done at slightly different timings for each of the 32 rows. For neighboring rows, the sampling is shifted by 2.5/16 = 0.16 ms in the middle-out case and by 2.5/32 = 0.08 ms in the top-bottom case.

For the simulated SH-WFS measurements, we perform Zernike expansion to investigate the shape of the measured wavefront. The Zernike modes themselves are a system of functions that form an orthonormal basis inside the unit circle, but their slopes are not orthonormal. Therefore, the simulated measurements are expanded in orthonormal vector polynomials proposed by Zhao and Burge (2007) and Zhao and Burge (2008), and then converted to Zernike coefficients. We compute the temporal variance of the Zernike coefficients for each measured mode and normalized them by the temporal variance of the input.

Figure 3.2 shows the results when the tip and tilt modes are given as inputs. The vertical axis shows the sum of the temporal variance of all measured mode coefficients, and the horizontal axis shows the oscillation frequency of the input wavefront. Different colors indicate different modes. Since the sampling frequency of the WFS is 400 Hz, the results are shown up to 200 Hz, corresponding to the Nyquist frequency.

The first thing seen from the global shutter results is that the measured mode is consistent with the input mode, i.e., there is no wavefront distortion. Also, the faster the time oscillation of the input wavefront, the smaller the dispersion of the measured mode. This means that

oscillations with time scales shorter than the integration time of the WFS cannot be measured. In this study, we call this effect the attenuation effect.

On the other hand, in the case of rolling shutters, some modes different from the input are measured, and the amount of these modes increases as the oscillation frequency of the input increases. This is the wavefront distortion effect that is the subject of this study and is referred to as the aliasing effect in this research. When tip and tilt modes are given as inputs, the trefoil is dominantly measured for WFS with middle-out rolling shutters, and astigmatism is dominantly measured for WFS with top-bottom rolling shutters. The attenuation effect is also present in the rolling shutter case and is more remarkable than in the global shutter case.

Figure 3.3 shows the results when defocus and spherical aberration modes are given as inputs. Similarly, the results for astigmatism, coma, and trefoil are shown in figure 3.4, figure 3.5, and figure 3.6, respectively. Some combinations of readout system and wavefront mode produce a large aliasing effect, such as a middle-out rolling shutter and vertical coma, or a top-bottom rolling shutter and astigmatism. It should be noted, however, that the composition of each Zernike mode in the actual atmospheric turbulence is not uniform. Tip or tilt aberration is larger than the other aberration components (Noll, 1976).

It is important to mention here the accuracy of the wavefront mode expansion using Zernike polynomials or polynomials in Zhao and Burge (2007). When the number of sub-apertures representing wavefront modes is small, the orthonormality of the modes becomes poor. Therefore, when the wavefront is mode expanded, there is a possibility that components expanded into other modes due to the non-orthonormality may be mistaken for the aliasing effect. Figure 3.7 shows the results of the orthonormality between the wavefront modes expressed by 32×32 segments and tip-tilt mode. In the left panel, the inner products of Zernike modes with tip mode are shown as blue dots, and inner products with tilt mode are shown as orange dots. The right panel is the same as the left panel but for slope modes in Zhao and Burge (2007). From this figure, tip, tilt, and coma, trefoil have a correlation of $\sim 1\%$ as a coefficient. However, the aliasing effect seen in the experiment and simulation is larger than this correlation, suggesting that aliasing due to the rolling shutter is indeed observed.

It is also important to note that the calculations presented in this section are simplified compared to the actual situation. For example, this calculation does not take into account the rolling shutter mode that occurs inside the subaperture. In reality, the rolling shutter mode distorts the shape of the WFS spot, which is expected to cause wavefront measurement errors. Nevertheless, this calculation provides a qualitative understanding of the impact of the rolling shutter mode on wavefront measurement.

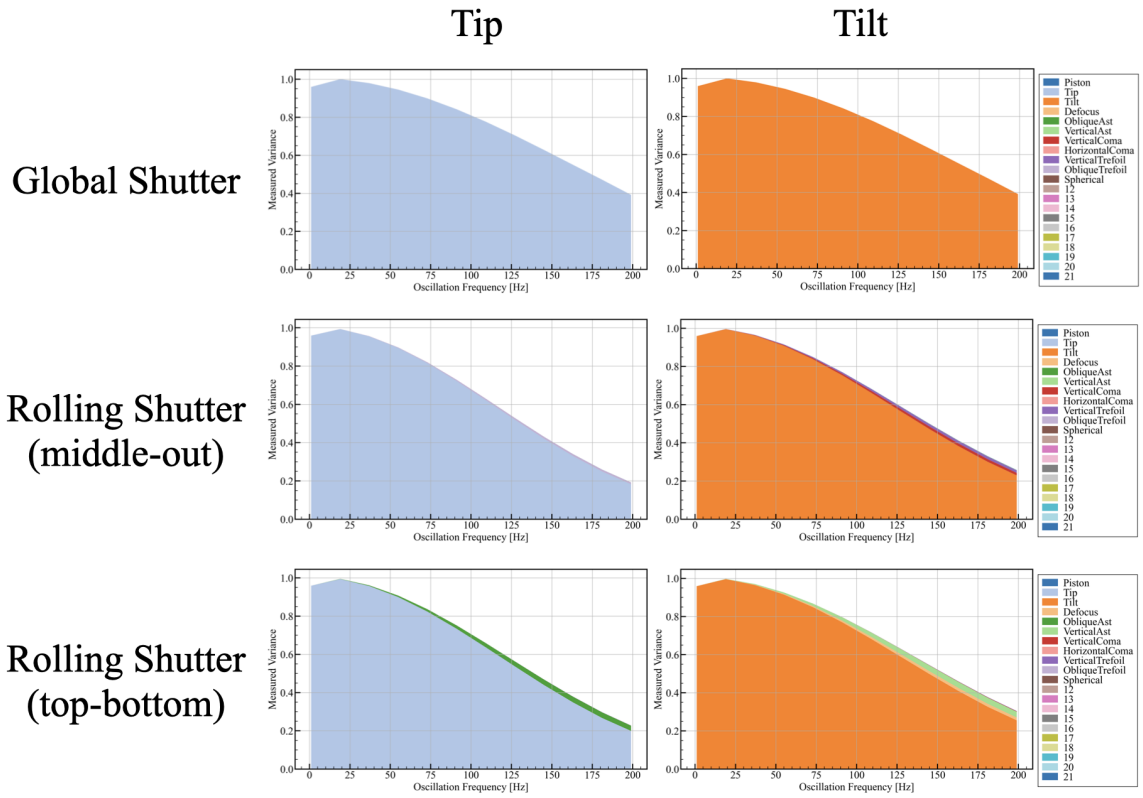

Fig. 3.2 Response of each shutter mode to a simple time-varying wavefront of tip or tilt oscillation. In each panel, the horizontal axis represents the oscillation frequency of the input time-varying Zernike mode while the vertical axis shows a stacked plot of measured variance of Zernike coefficients. Response of global, middle-out rolling and top-bottom rolling shutters are shown from top to bottom. The left column is for tip input and the right column is for tilt input.

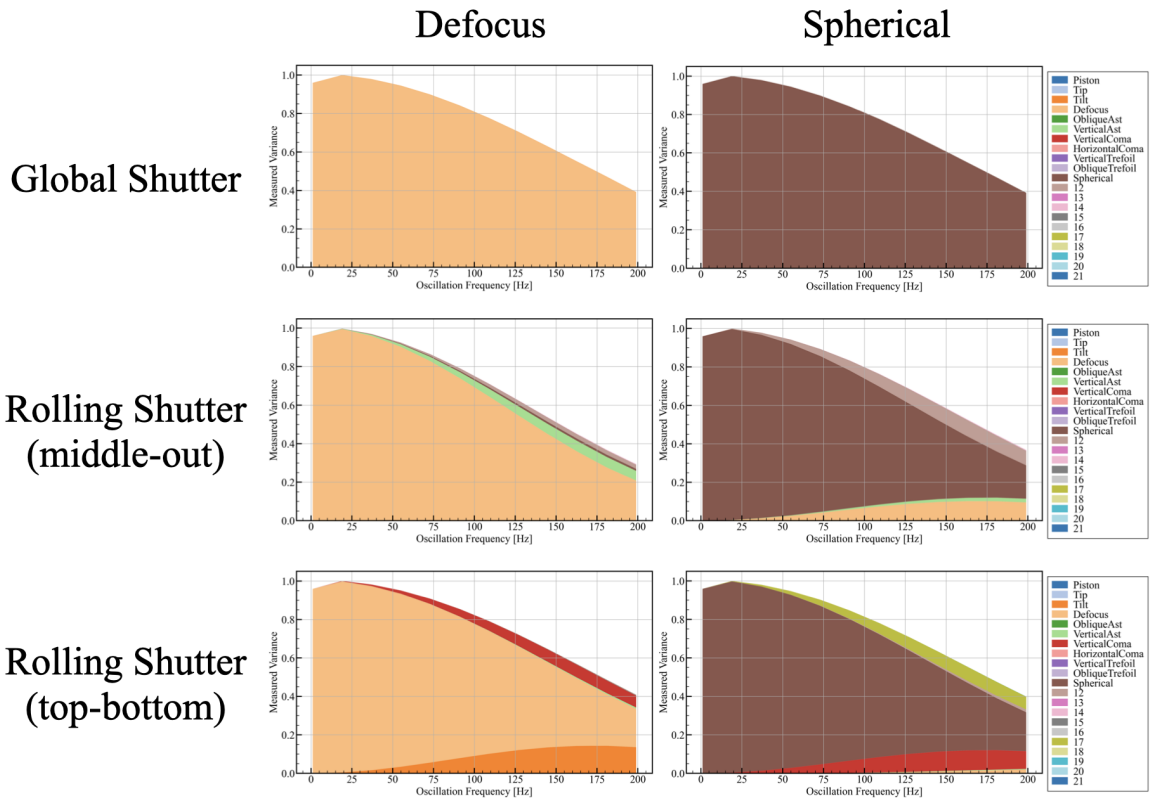

Fig. 3.3 Same figure as figure 3.2, but for input modes of defocus and spherical.

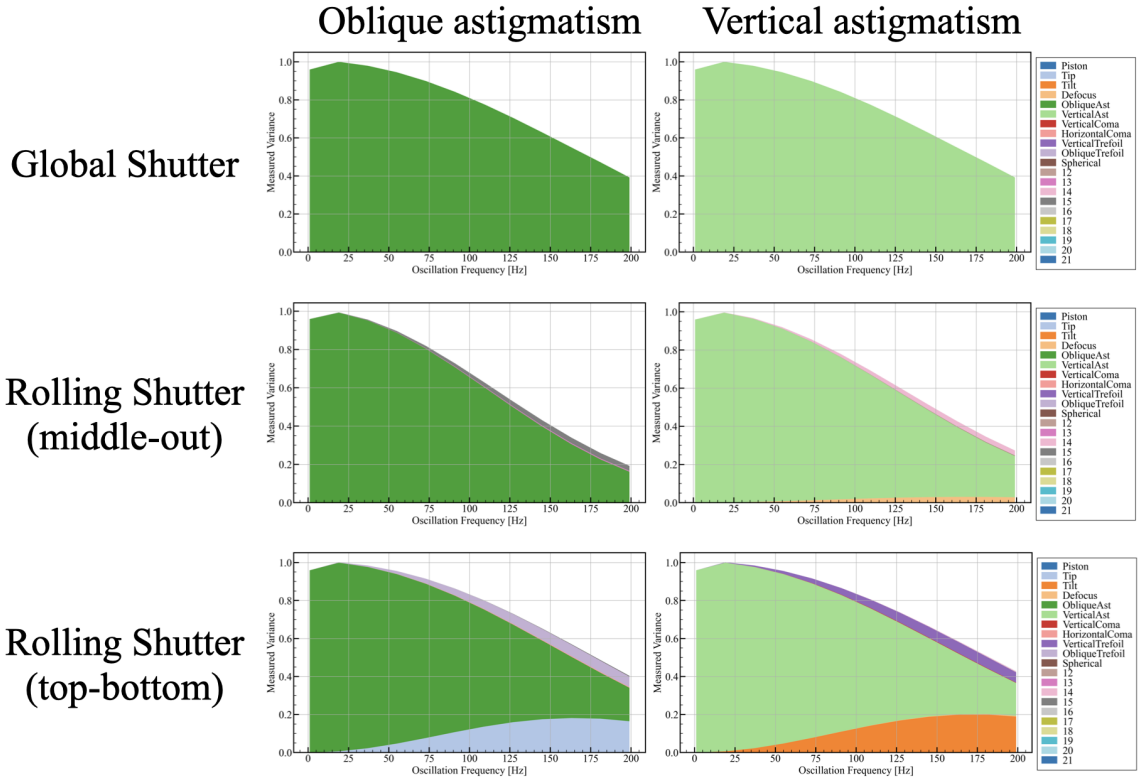

Fig. 3.4 Same figure as figure 3.2, but for input modes of oblique astigmatism and vertical astigmatism.

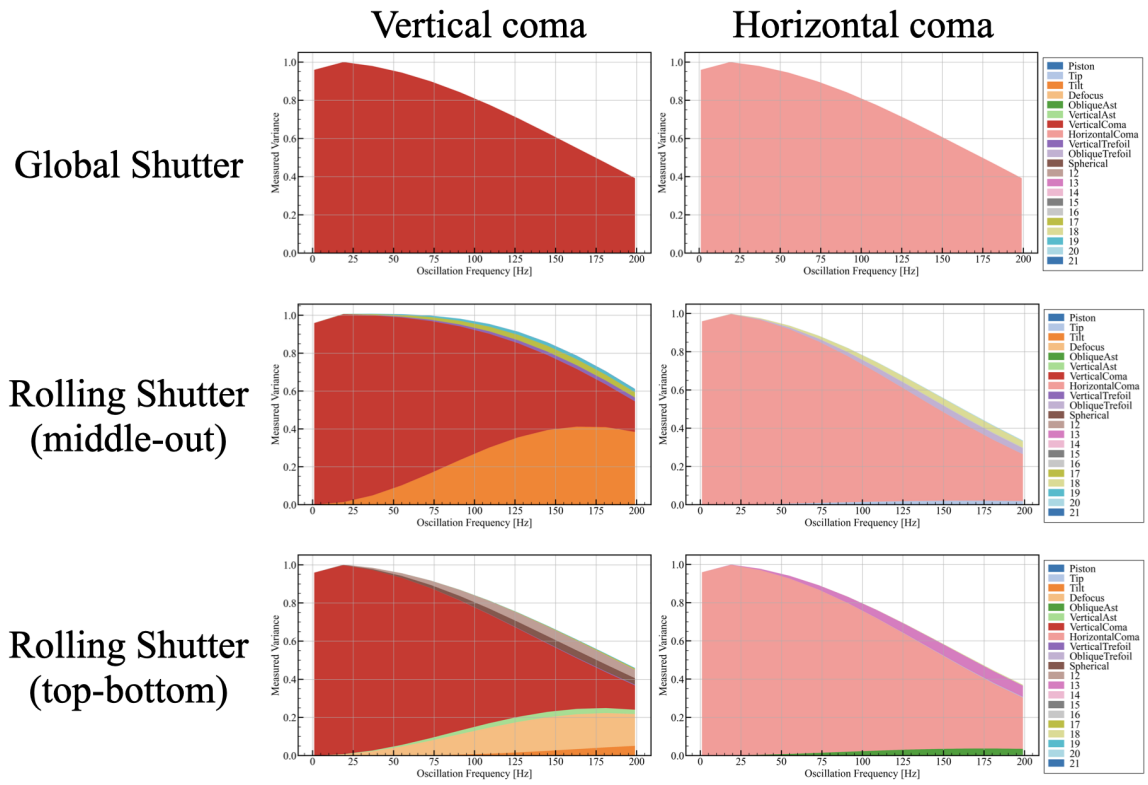

Fig. 3.5 Same figure as figure 3.2, but for input modes of vertical coma and horizontal coma.

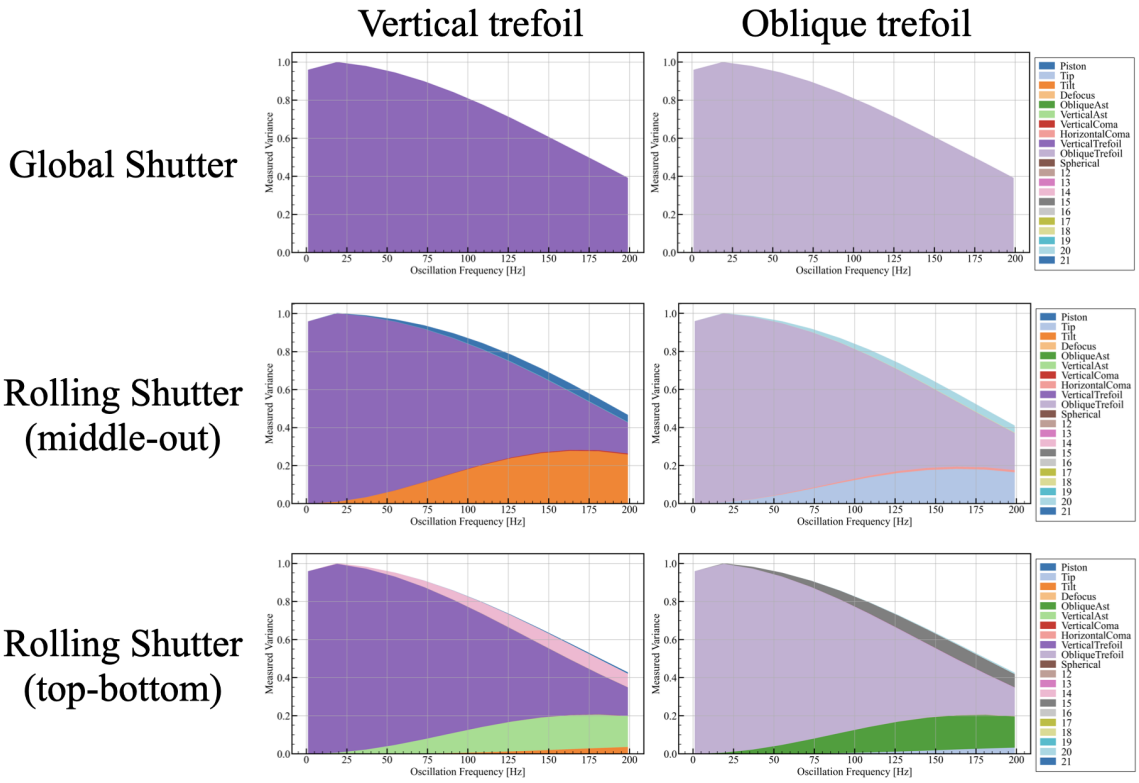

Fig. 3.6 Same figure as figure 3.2, but for input modes of vertical trefoil and oblique trefoil.

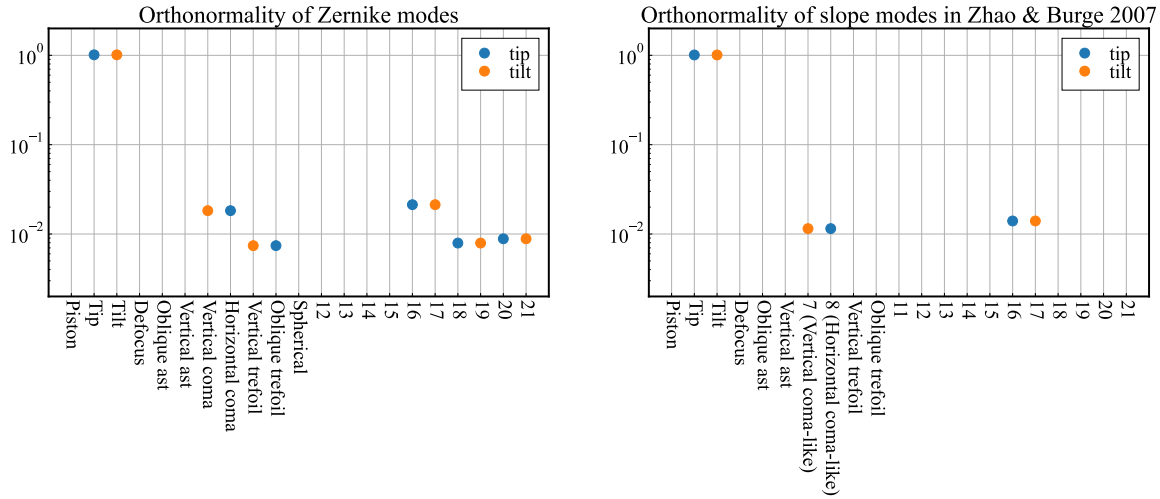

Fig. 3.7 Left: Orthonormality with tip-tilt mode for Zernike modes expressed in 32×32 segments. The inner product of the mode on the horizontal axis with the tip mode is plotted as blue dots, and the inner product with the tilt mode is plotted as orange. Inner products smaller than 2×10^{-3} are not shown in the figure. Right: Same as the left panel but for slope expansion modes in Zhao and Burge (2007).

3.2.3 Laboratory verification

To investigate whether the results of the simple simulation described previously are seen in a real system, we perform an experiment using a rolling shutter WFS. The WFS used in the experiment is a prototype WFS of the ULTIMATE-START project (Akiyama et al., 2020; Terao et al., 2022), which is a demonstration experiment of LTAO at the Subaru telescope. It is a SH type WFS that divides the 8-meter aperture into 32×32 subapertures. The detector is an ORCA-Flash4.0 v2 CMOS detector from Hamamatsu Photonics, which reads out $2\text{k} \times 2\text{k}$ pixels at a frame rate of 100 Hz in the rolling shutter mode from the center row to the top and bottom rows. In this experiment, only the central 512 rows are partially read out, and the frame rate is set to 400 Hz.

The prototype WFS is attached behind AO188 (Minowa et al., 2010), the AO facility of the Subaru telescope, and a laser light source simulating a guide star inside AO188 is injected into the prototype WFS. The tip-tilt mirror inside the prototype WFS is tilted at a constant frequency with an amplitude of 0.5 arcseconds, and the WFS measures the wavefront. In this experiment, the tip-tilt mirror is moved diagonally to give almost equal amounts of tip and tilt components simultaneously. The obtained WFS data is analyzed to perform a mode expansion using the slope modes in Zhao and Burge (2007), which is generated from gradients of the Zernike polynomials and made orthonormal using the Gram-Schmidt technique. After that, we calculate temporal variances of the mode coefficients. This procedure is carried out by changing the oscillation frequency of the tip-tilt mirror, starting from 1 Hz and going up to 10, 30, 50, 70, 100, 150, 205, 305, 505, and 905 Hz. However, due to a malfunction in the behavior of the tip-tilt mirror stage, wavefront data were actually acquired only at 1, 10, 30, 50, and 100 Hz.

The results of the experiment are shown in the top panels in figure 3.8 in comparison with the bottom panels, the results of the simulations described in section 3.2.2. In all panels, the horizontal axis represents the oscillation frequency of the tip-tilt mirror and the vertical axis represents the temporal variance of the expansion coefficient of the measured wavefront. The top panels in figure 3.8 show the experimental results and the bottom panels show the simulation results when equal amounts of tip and tilt are applied. The left panel in each figure shows all expansion modes and the right panel shows modes excluding piston, tip, and tilt. The attenuation effect is stronger in the experiment than in the simulation, with a measured dispersion of $\sim 50\%$ in the experiment and $\sim 75\%$ in the simulation for a 100 Hz vibration. For the aliasing effect, the measured modes are identical to those predicted by the simulation, although quantitatively different between the experiment and the simulation. This experiment provides support for the fact that even the simple simulation described in section 3.2.2 can reproduce the actual behavior qualitatively.

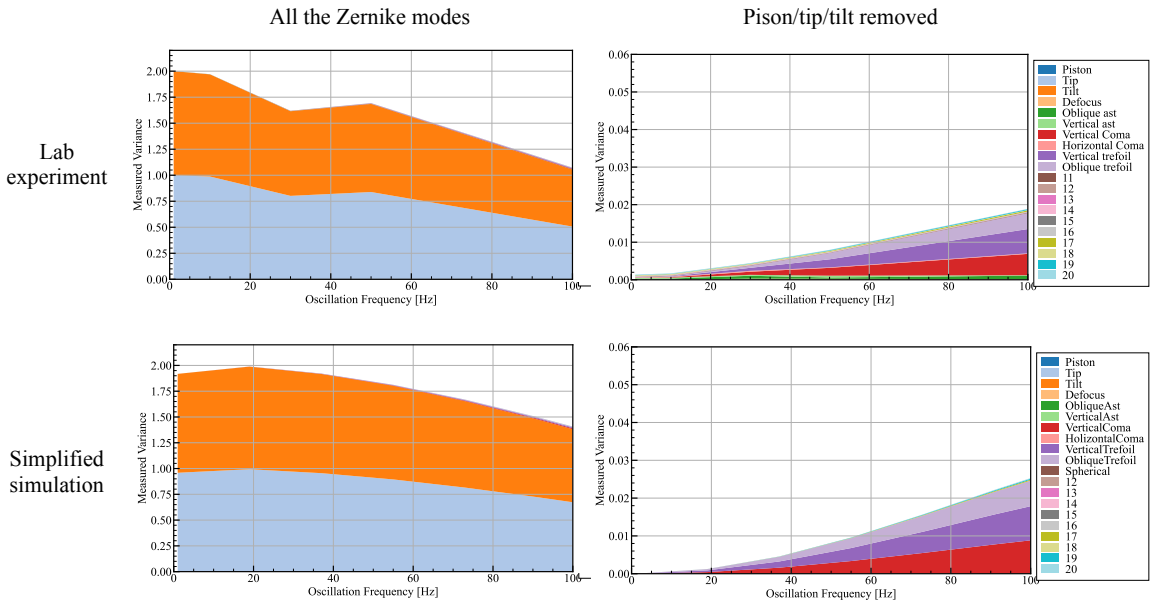

Fig. 3.8 Result of aliasing measurement in a lab experiment. The stacked plot of temporal variances of mode coefficients measured by the laboratory experiment. The mode expansion is done using orthonormal polynomials from Zhao and Burge (2007). The horizontal axis means the oscillation frequency of the tip-tilt mirror. The left panel shows all the modes measured by the WFS, while the right panel shows modes other than piston, tip, and tilt.

3.3 End-to-end simulation

The previous simplified simulation qualitatively explains the effects of rolling shutter modes on several Zernike modes. In this section, we describe an end-to-end simulation performed to quantitatively investigate the effect on AO assuming some realistic sources of wavefront distortion.

3.3.1 Sources of wavefront distortion

Atmospheric turbulence

Wavefront distortion by atmospheric turbulence is a fundamental component in WFS measurement. In our end-to-end simulation, we assume Kolmogorov turbulence. To simulate the turbulence situation at Maunakea, we use a model turbulence profile used in Oya et al. (2014). The model is based on measurements conducted in the TMT site-testing campaign (Els et al., 2009), and is corrected in terms of the following three points; (1) ground layer turbulence is added to match seeing statistics measured by the auto-guider of the Subaru telescope, (2) wind speed profile is taken from the MAOS simulation code, which is used for

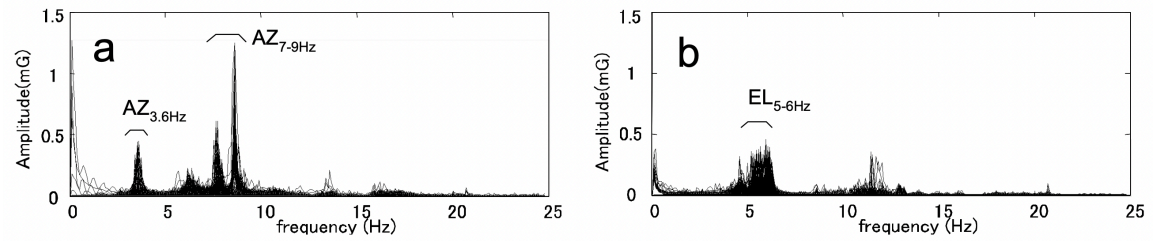

Fig. 3.9 Power spectrum of telescope vibration measured by Kanzawa et al. (2006). The left and right panels show power spectra in telescope azimuth and elevation direction, respectively.

simulating AO system for TMT, NFIRAOS, and (3) wind direction profile is set artificially. We select the "moderate" turbulence model in which seeing at 500 nm is 0.73 arcsec, Fried parameter at 500 nm is 11.8 cm, 7 turbulence layers at 0, 0.5, 1, 2, 4, 8, 16 km are considered, and ground layer (at 0 km) turbulence fraction is 73.2%.

Telescope vibration

Telescope vibration can also be an additional tip-tilt source of wavefront distortion. As the telescope tracks, its inherent vibration created by the movement of the azimuth and elevation drives is measured as a tip-tilt component. The tip-tilt vibration is basically a low-frequency component. For example, in the case of the Subaru telescope, Kanzawa et al. (2006) measured the telescope vibration using an accelerometer, and it has been found that there are intrinsic vibrations at 3.6 Hz and 7-9 Hz in the azimuth axis direction and at 5-6 Hz in the elevation axis direction. Although the magnitude of the vibration is not negligible compared to seeing, the low frequency suggests that the effect of the rolling shutter is small based on the simplified simulation.

Jitter of laser guide star

Another source of concern when measuring the wavefront of LGS is the effect of jitter. LGS jitter is the tip-tilt component caused by changes in the position of the LGS due to atmospheric turbulence during laser launch. Since the tip-tilt effect due to atmospheric fluctuations is larger for upward propagation than for downward propagation, the jitter effect is not negligible. As an example of LGS jitter measurement at the Subaru telescope, measurement results by the ULTIMATE-START prototype WFS are shown in figure 3.10. The aperture diameter of the laser launch telescope of the Subaru telescope is 50 cm, i.e. 16 times smaller than the telescope aperture. The spectrum is continuous in frequency and extends from a few Hz to several hundred Hz. The magnitude of the oscillations has a temporal standard deviation of 0.12 arcsec.

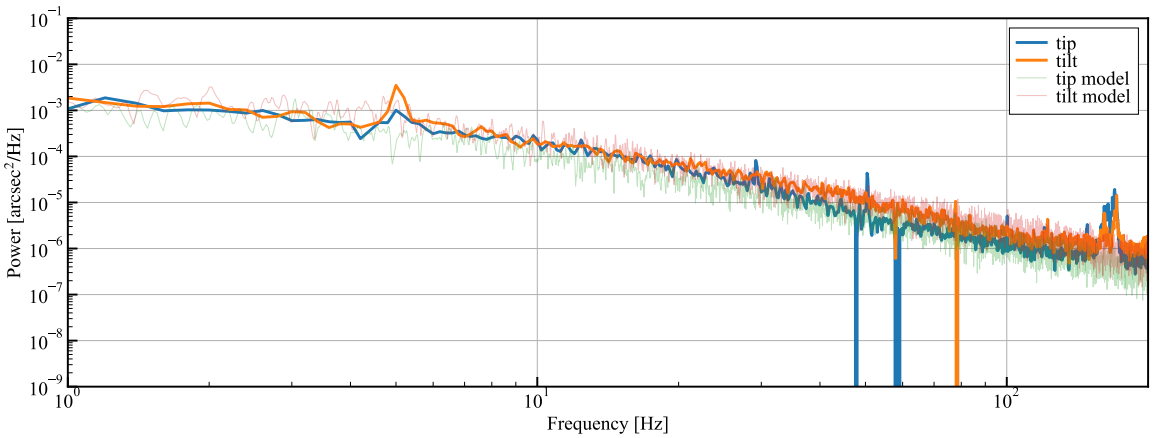

Fig. 3.10 Power spectrum of LGS jitter observed by the ULTIMATE-START prototype WFS. Blue and orange spectra show tip and tilt components, respectively.

3.3.2 Simulation setup

In order to quantitatively evaluate the effect of the aliasing, we conduct end-to-end AO simulations of an AO system with a single LGS using OOMAO, a MATLAB-based AO simulator (Conan and Correia, 2014). A schematic description of the simulation is shown in figure 3.11. Three light sources are set at the center of the field of view in the zenith direction; one for the target object, another for an LGS, and the other for a tip-tilt NGS (TT-NGS). Lights from the three sources propagate the common atmospheric turbulence and enter a telescope with an aperture size of 8 m. Then, the tip-tilt component of telescope vibration is added to their wavefronts while the tip-tilt of LGS jitter is added only to the LGS wavefront. Lights from the target object and tip-tilt NGS are reflected by the DM1, which simulates a DM in a general AO system and enters a science camera and a low-order WFS (LO-WFS), respectively. On the other hand, light from LGS is reflected by the DM2, which simulates a usual DM correction and tip-tilt feedback for the laser launch telescope and enters a high-order WFS (HO-WFS). In the AO loop, tip-tilt measurement by the LO-WFS and high-order wavefront measurement by the HO-WFS are combined and sent to the DM1. All the distortion measurement by the HO-WFS is sent to the DM2 in order to correct the LGS wavefront including the LGS jitter.

We consider the three wavefront aberration sources explained in the previous section. First, for the telescope vibration, we create a random signal by superimposing low-frequency oscillations of 4.6, 6.1, 7.6, and 8.6 Hz in the telescope motion axis, based on the previous measurements at the Subaru telescope. The oscillation in the azimuthal and elevation direction is given as the tip and tilt components of the wavefront, respectively. The jitter of LGS is simulated with the measured power spectrum of the LGS jitter with the ULTIMATE-START

32×32 SH-WFS prototype attached to the Subaru telescope as shown in figure 3.7. The integrated power spectrum of the data corresponds to a jitter with FWHM of 0.3 arcsec, which is 2.5 times smaller than that measured in VLT with a sigma of 0.3 arcsec (Paufique et al., 2016). Because the origin of the difference is not clear now, we multiply the factor 2.5 to simulate the jitter as a worst case. We create a random number that follows the power spectrum (tip model and tilt model in figure 3.10) by filtering white noise. This is added as the tip and tilt component of the wavefront as well as the telescope vibration. The time series and power spectra of telescope vibration and LGS jitter used in the numerical calculations are shown in figure 3.12. The atmospheric turbulence is created by giving OOMAO a median model at Maunakea, in which 7 turbulence layers are considered, the total Fried parameter is 11.8 cm and the maximum layer speed is 19.1 m s^{-1} (Oya et al., 2014).

We assume that 32×32 SH-WFS with 256×256 pixels sample 8 m telescope aperture in 500 Hz loops with a 2 ms integration time of the detector. After the readout of the detector, 2 ms latency is assumed for the reduction of the WFS image. In addition to the usual global shutter mode, rolling shutter modes in which the images are sequentially read out at 10 μs per row following the readout systems in figure 3.1 are implemented. In order to focus on the effect of the shutter mode, we assume no readout and photon noise. The DM has 33×33 grid elements, which is a similar number of elements as the adaptive secondary mirror that will be used in ULTIMATE-Subaru.

Before going to the end-to-end simulation, we conduct a simulation only with a wavefront distortion source of oscillating tip-tilt to check the behavior in the same situation as the simplified simulation. As a result, we confirm the same behavior of detected Zernike modes, indicating that the rolling shutter effect in each subaperture is not significant.

The end-to-end calculations are performed for 1000 loops i.e. 2.5 seconds in closed loop. In each loop, we sample phases map before and after reflection by the DM1 and DM2 to check the open-loop and closed-loop phases in science and HO-WFS paths.

3.3.3 Results

The results of the end-to-end simulation are shown in figure 3.13. In each panel, the RMS histogram of the open-loop phase and closed-loop phase with the three different shutter modes is shown. The panels indicate the total, low-order, and high-order wavefront components from top to bottom. The left column is for the science path and the right column is for the HO-WFS path.

At first, the residual of the high-order mode is 184.7 nm, 196.6 nm, and 203.5 nm for the global, middle-out rolling, and top-bottom rolling shutter mode modes in the science path. If we calculate the squared difference, the corresponding size of the additional noise component

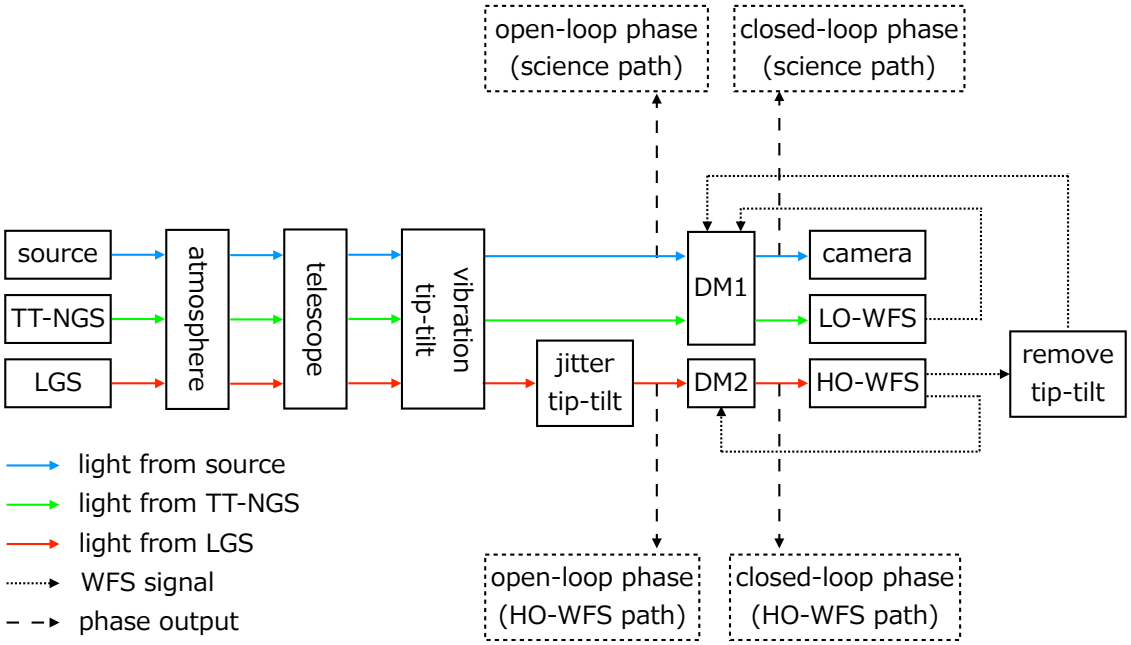

Fig. 3.11 Schematic description of the end-to-end simulation of a single LGS AO system to test the effect of the rolling shutter mode.

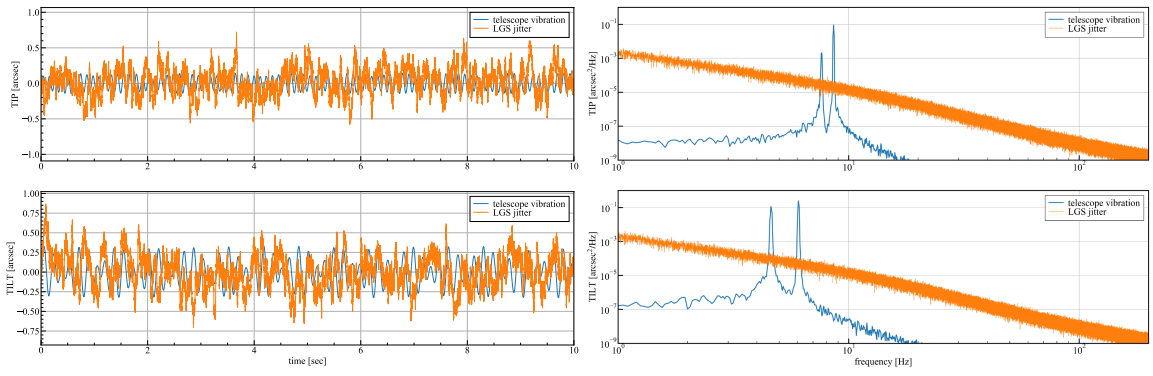

Fig. 3.12 Time series (left) and power spectrum (right) models of telescope vibration (blue) and LGS jitter (orange) used in the end-to-end simulation. The top and bottom panels correspond to the tip and tilt components of the aberration.

due to the rolling shutter mode is 67.4 nm and 85.4 nm for the middle-out and top-bottom modes, respectively. The amount of additional noise is the same level if we evaluate it with the HO-WFS path.

The additional wavefront error of the rolling shutter mode is negligible compared to the wavefront error budget of the GLAO system, which is dominated by the tomographic error caused by the uncorrected high-altitude turbulence ($\sim$ 500 nm under moderate seeing condition). However, it is not negligible in an LTAO system, which targets $\sim$ 100 nm RMS residual in the high-order modes. The residual in the low-order component does not show a difference. We need to note that the current simulation does not include the readout and photon noise effects, therefore the effect of the worse NGS image quality with larger high-order error does not appear in the current simulation. In a real system, such implicit effects on the low-order mode also need to be evaluated.

3.4 Conclusion

In this study, we investigate the effects of image distortion caused by rolling shutters on the wavefront measurements of LGS in the context of AO systems in the ULTIMATE project. We performed a simplified wavefront sensing simulation, in which oscillating Zernike modes are measured by a 32×32 SH-WFS. As a result, we find different Zernike modes from the input mode appear when the oscillation frequency of the input wavefront is more than about half of the Nyquist frequency of WFS. We confirmed the aliasing effect in a laboratory experiment using a prototype WFS of ULTIMATE-START and AO188. We also reproduced the rolling shutter WFS in an end-to-end AO simulation and performed numerical calculations including the effects of atmospheric turbulence, telescope system oscillations, and jitter of the LGS. The results show that the wavefront measurement error associated with the rolling shutter image distortion is 67.4 nm and 85.4 nm in RMS of the wavefront residual for middle-out and top-bottom rolling modes, respectively. This is sufficiently small compared to the typical value of several hundred nm of the overall GLAO error, suggesting that the rolling shutter mode is not a significant problem in the ULTIMATE-Subaru GLAO setting. However, in LTAO, the additional wavefront error is not negligible compared to $\sim$ 100 nm total wavefront error. Techniques such as including time series forecasting may be a solution.

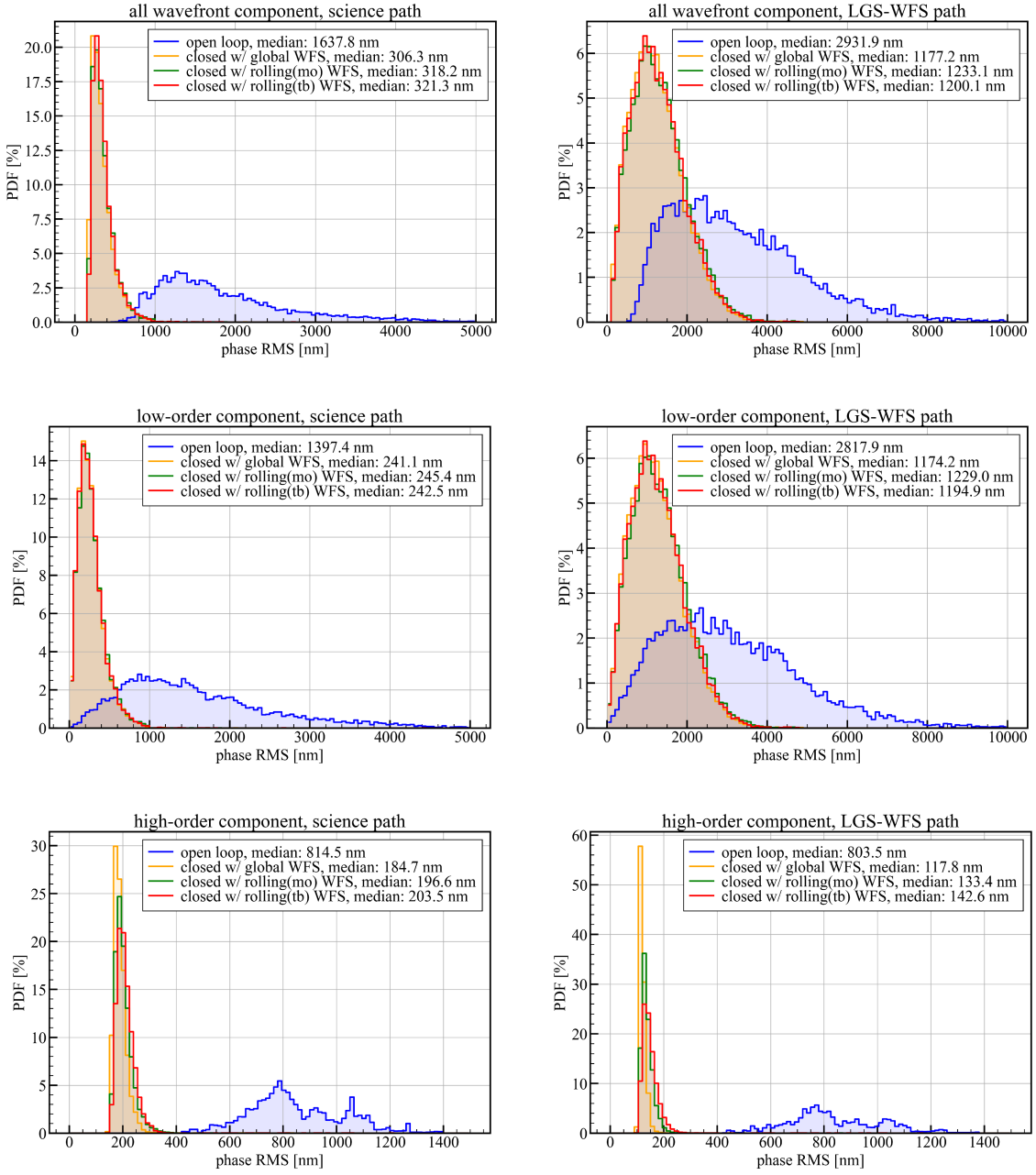

Fig. 3.13 Histogram of wavefront error in end-to-end simulation. The left panels show wavefront error detected in the science path while the right panels are for the HO-WFS path. From top to bottom, overall, low-order, and high-order components are shown.

Chapter 4

Summary and Future Prospects

4.1 Summary of the thesis

In this thesis, we have studied two topics for the development of the next-generation AO system using multiple LGS in the context of ULTIMATE-START (LTAO) and ULTIMATE-Subaru (GLAO) projects at the Subaru telescope.

First, we have developed and demonstrated a new atmospheric turbulence profiler for the LTAO and GLAO. The LTAO estimates and compensates all the atmospheric turbulence in the cylindrical optical path in a narrow field of view and therefore requires the information of atmospheric turbulence profile from the ground to the highest altitude around 20 km for optimizing the tomographic reconstruction matrix. On the other hand, the GLAO system only corrects wavefront distortion caused by turbulence at the ground to provide the seeing improvement uniformly over a wide field of view. Since the GLAO system is sensitive to the turbulence structure of the ground layer up to $\sim$ 1 km, a detailed turbulence profile as fine as a few tens of meters, which resolves turbulence in the telescope dome, is essential to predict the GLAO performance and the design the system. Our approaches to the requirements and obtained conclusions are summarized as follows,

1. We have developed a new atmospheric turbulence profiler, which consists of two SH sensors with a fine pupil sampling of 2 cm, to perform SH-MASS for profiles of free atmospheric turbulence at higher than 1 km with an altitude resolution of a few km, and SLODAR for profiles of ground layer turbulence at lower than a few 100 m with an altitude resolution of a few 10 m, simultaneously.

2. We have conducted two half-night engineering observations of the turbulence profiler attached to the Subaru telescope in November 2022 and March 2023 to demonstrate our profiling method and collect turbulence measurement data at the Subaru telescope.

3. Total seeings have been measured using the information on the spatial correlation between slope measurements by two spots on a single SH sensor. The obtained total seeings are consistent between simultaneous measurements by the two SH sensors, but systematically smaller compared to CFHT DIMM possibly due to the difference in ground layer turbulence between the Subaru and CFHT sites.

4. Free atmospheric turbulence profiles have been reconstructed based on the spatial correlation between scintillation measurements by two spots on a single SH sensor (SH-MASS). The obtained free atmospheric turbulence profiles measured simultaneously by the two independent SH sensors and four sub-datasets show consistent results.

5. Wind speed and direction profiles have been measured using the temporal correlation between scintillation measurements by two spots on a single SH sensor. The results are compared with rawinsonde, balloon-borne measurements. The two independent profiles show very good agreement in spite of the temporal difference of measurements

6. Ground layer turbulence profiles including inside of the Subaru telescope dome have been obtained from spatial correlation between slope measurements by two spots on two different SH sensors (SLODAR). The reconstructed profiles suggest that most of the ground layer turbulence is concentrated at below 30 m, which is comparable with or a little higher than the dome of the Subaru telescope, and dominated by dome seeing.

Second, we have evaluated the effect of the rolling shutter mode of detectors on wavefront sensing in LTAO and GLAO. In the rolling shutter mode, the exposure timing of pixels on a detector is not simultaneous but different for each pixel row, and the image of fast-moving objects is distorted. On the other hand, recent CMOS detectors, many of which adopt the rolling shutter mode, have many attractive features for AO WFS, such as faster readout speed, lower readout noise, higher quantum efficiency, and larger format size, compared to conventionally-used CCD detectors. Therefore evaluating the impact of rolling shutter mode from the perspective of WFS in AO is important. Our approaches to the problem and obtained conclusions are summarized as follows,

1. We have modeled behaviors of WFS in AO using detectors with global shutter, middle-to-out rolling shutter, and top-to-bottom rolling shutter to investigate their responses to the 10 lowest order Zernike modes oscillating in time. As a result, we have found that the aliasing effect, in which different Zernike modes from the input mode are measured, arises in rolling shutter WFS and that the attenuation effect, in which the

measured power of oscillation is smaller than the input power, is stronger in rolling shutter WFS compared to the global shutter WFS.

2. We have confirmed that the aliasing effect expected from the simplified model is actually seen in a laboratory experiment using a prototype WFS of the ULTIMATE-START with a middle-to-out rolling shutter detector.

3. We have performed an end-to-end AO simulation including the effect of rolling shutter WFS to evaluate the amount of additional wavefront error under closed-loop control for compensating typical atmospheric turbulence at Maunakea, the vibration of the telescope, and jitter of LGS. As a result, the additional wavefront error with rolling shutter WFS, calculated as a difference from wavefront error with global shutter WFS, is 67.4 nm and 85.4 nm for middle-to-out and top-to-bottom rolling shutter modes, respectively.

4. We have concluded that the additional wavefront error induced by the rolling shutter effect is sufficiently small compared to the typical total wavefront error of GLAO (~ 500 nm), but not negligible compared to the typical total wavefront error of LTAO (~ 100-150 nm).

4.2 Future prospects

4.2.1 Additional observations with the turbulence profiler

Additional engineering observations with the turbulence profiler will be important to discuss the stochastic behavior of atmospheric turbulence based on a larger amount of measurements or to calibrate the SLODAR measurement, which does not have any simultaneous measurement to be compared with. In fact, we have already conducted the third engineering observation during the second half night on May 4, 2023 (HST). Although analysis of the data is still ongoing as of June 2023, and no results are shown in this thesis, we are going to deepen our understanding of free atmospheric turbulence at Maunakea and the relationship of instrumental behavior between the SH-MASS and CFHT MASS through the data analysis.

Also, we are going to have the fourth engineering observation in November 2023 (HST). The purpose of the engineering run is to conduct a simultaneous measurement of ground layer turbulence between the SLODAR and AIR-FLOW (Airborne Interferometric Recombiner - Fluctuations of Light at Optical Wavelengths), a small portable sensor for local turbulence (Lai et al., 2018). We are planning to put several AIR-FLOWs to different positions on the Subaru telescope or inside the dome to monitor local turbulence at the positions. Through

the experiment, it is expected that sources of strong ground layer turbulence are identified as well as that a portion of the SLODAR profile, which is inside the dome, is calibrated.

4.2.2 Mitigation of the rolling shutter effect for LTAO

Considering total wavefront error as small as ~ 100-150 nm in LTAO, additional wavefront error induced by the rolling shutter mode is not negligible, and mitigation of the additional error will be one of the solutions. To mitigate the effect of rolling shutter mode, one possible method is to read out several pixel rows at a time and update the rows sequentially (Dirnberger et al., 2018; Akiyama et al., 2020). Differences of exposure timing between rows in a frame are reduced and image distortion will be mitigated.

Another possibility is to use a predictive control technique. For each spot of a SH sensor, the time series of the position might be modeled mathematically by training using past measurements of the spot position. By predicting spot position in the next step based on the model, a difference of exposure timing between pixel rows due to the rolling shutter as well as time lag between WFS measurement and DM correction, i.e. temporal error might be mitigated.

Acknowledgements

I had a fulfilling three and a half years in my Ph.D. course with great support from many people. I would like to thank those who gave help to me and contributed to this study.

First of all, I would like to express my greatest appreciation to my supervisor, Dr. Masayuki Akiyama. He has given me plenty of valuable advice, ideas, and opportunities throughout six years of my research life at Tohoku University since I was a fourth-year undergraduate student. He patiently guided and encouraged me in spite of my slow work. Without his support, I would not have been able to complete my doctoral thesis.

I would like to express my special thanks to many staff of the Subaru telescope, who kindly accepted me and supported the profiler development as well as my daily life in Hilo. Since there are too many people who helped me to write about all of them, I mention here three particularly important people. Dr. Yoshito Ono is a large contributor to the profiling project, with respect to the development of the control software and advice on the SLODAR analysis. Dr. Yosuke Minowa gave many important contributions to the mechanical side of the turbulence profiler, especially to optical/mechanical design, installation to the Subaru telesocpe, and engineering observation. Dr. Koki Terao also gave significant help and comments in terms of installation and observation with the Subaru telescope. I am grateful to Dr. Shin Oya of the National Astronomical Observatory of Japan, with whom I discussed much on atmospheric turbulence measurements. He also kindly accepted a reviewer of this thesis. I also would like to thank many staff of Astronomical Instrumentation and Technology Center, Australian National University, with whom I discussed about rolling shutter effect on wavefront sensor. I gratefully acknowledge Dr. Makoto Hattori, Dr. Yoshifusa Ita, and Dr. Jesse Cranney, who gave me constructive comments on this thesis as reviewers. I appreciate much help from Ms. Nozomi Okamoto, Ms. Junko Nagasawa, and Ms. Hiroko Miwa Lane, who assisted in my research activities through administrative work. I received much support from current and former members of the ULTIMATE-START team. Thanks to discussions with Mr. Yuta Iizuka, Mr. Takumi Akasawa, Mr. Riki Homan, and Mr. Masaya Ichinose, I improved my knowledge and skills in adaptive optics. I would also like to thank graduate students and staff at the Astronomical Institute, Tohoku University. I am especially thankful to Dr. Bovornpratch Vijarnwannaluk, Mr. Naoaki Yamamoto, Mr. Kazuki Daikuhara, Mr.

Kenji Amazaki, and Ms. Riho Okazaki. Daily conversations with them made my doctor course enjoyable, despite many limitations caused by COVID-19.

Finally, I would like to express my deep appreciation to my family. My parents, Tadashi and Emiko, understood my interest in astronomy and kindly accepted my going to doctor course. My partner, Kanna, warmly supported me and always encouraged me.

The turbulence profiling project is financially supported by a grant from the Joint Development Research supported by the Research Coordination Committee, National Astronomical Observatory of Japan (NAOJ), National Institutes of Natural Sciences (NINS), and by the FY2021 supplementary budget from the Japanese Ministry of Education, Culture, Sports, Science and Technology (MEXT). The work on turbulence profiler is also supported by the Japan Society for the Promotion of Science (JSPS) KAKENHI Grant Numbers JP17H06129, JP21H05583, and JP22J14095, and by a grant from the Hayakawa Satio Fund awarded by the Astronomical Society of Japan. The work on the rolling shutter effect is supported by the JSPS Core-to-Core Program (grant number: JPJSCCA20210003). The author is supported by the JSPS as a young research fellow and by the Graduate Program on Physics for the Universe (GP-PU), Tohoku University, as a research assistant.

References

Akiyama, M., Minowa, Y., Ono, Y., Terao, K., Ogane, H., Oomoto, K., Iizuka, Y., Oya, S., Mieda, E., and Yamamuro, T. (2020). Ultimate-start: Subaru tomography adaptive optics research experiment project overview. In *Adaptive Optics Systems VII*, volume 11448, pages 385–402. SPIE.

Avila, R., Vernin, J., and Masciadri, E. (1997). Whole atmospheric-turbulence profiling with generalized scidar. *Applied Optics*, 36(30):7898–7905.

Babcock, H. W. (1953). The possibility of compensating astronomical seeing. *Publications of the Astronomical Society of the Pacific*, 65(386):229–236.

Bardou, L., Gendron, É., Rousset, G., Gratadour, D., Basden, A., Calia, D. B., Buey, T., Centrone, M., Chemla, F., Gach, J.-L., et al. (2021). Elt-scale elongated lgs wavefront sensing: on-sky results. *Astronomy & Astrophysics*, 649:A158.

Beckers, J. M. (1988). Increasing the size of the isoplanatic patch with multiconjugate adaptive optics. In *European Southern Observatory Conference and Workshop Proceedings*, volume 30, page 693.

Boreman, G. D. and Dainty, C. (1996). Zernike expansions for non-kolmogorov turbulence. *JOSA A*, 13(3):517–522.

Butterley, T., Wilson, R. W., and Sarazin, M. (2006). Determination of the profile of atmospheric optical turbulence strength from slodar data. *Monthly Notices of the Royal Astronomical Society*, 369(2):835–845.

Cava, A., Schaerer, D., Richard, J., Pérez-González, P. G., Dessauges-Zavadsky, M., Mayer, L., and Tamburello, V. (2018). The nature of giant clumps in distant galaxies probed by the anatomy of the cosmic snake. *Nature Astronomy*, 2(1):76–82.

Conan, R. and Correia, C. (2014). Object-oriented matlab adaptive optics toolbox. In *Adaptive optics systems IV*, volume 9148, pages 2066–2082. SPIE.

Coulman, C., Vernin, J., and Fuchs, A. (1995). Optical seeing‘Ă‘Ťmechanism of formation of thin turbulent laminae in the atmosphere. *Applied optics*, 34(24):5461–5474.

Dirnberger, M., Rigaut, F., Minowa, Y., Conan, R., Guyon, O., Gratadour, D., and Korkiakoski, V. (2018). Rolling shutter detector data flow strategies to push the limits of ao performance. In *Adaptive Optics Systems VI*, volume 10703, pages 1218–1227. SPIE.

References

Ellerbroek, B. L. (2002). Efficient computation of minimum-variance wave-front reconstructors with sparse matrix techniques. *JOSA A*, 19(9):1803–1816.

Els, S., Travouillon, T., Schöck, M., Riddle, R., Skidmore, W., Seguel, J., Bustos, E., and Walker, D. (2009). Thirty meter telescope site testing vi: turbulence profiles. *Publications of the Astronomical Society of the Pacific*, 121(879):527.

Farley, O., Osborn, J., Morris, T., Fusco, T., Neichel, B., Correia, C., and Wilson, R. (2020). Limitations imposed by optical turbulence profile structure and evolution on tomographic reconstruction for the elt. *Monthly Notices of the Royal Astronomical Society*, 494(2):2773–2784.

Foy, R. and Labeyrie, A. (1985). Feasibility of adaptive telescope with laser probe. *Astronomy and Astrophysics (ISSN 0004-6361), vol. 152, no. 2, Nov. 1985, p. L29-L31.*, 152:L29–L31.

Fried, D. L. (1965). Statistics of a geometric representation of wavefront distortion. *JoSA*, 55(11):1427–1435.

Gendron, E., Morel, C., Osborn, J., Martin, O., Gratadour, D., Vidal, F., Le Louarn, M., and Rousset, G. (2014). Robustness of tomographic reconstructors versus real atmospheric profiles in the elt perspective. In *Adaptive Optics Systems IV*, volume 9148, page 91484N. International Society for Optics and Photonics.

Greenwood, D. P. (1977). Bandwidth specification for adaptive optics systems. *JOSA*, 67(3):390–393.

Guesalaga, A., Ayancán, B., Sarazin, M., Wilson, R., Perera, S., and Le Louarn, M. (2020). Fass: a turbulence profiler based on a fast, low-noise camera. *Monthly Notices of the Royal Astronomical Society*.

Guesalaga, A., Ayancán, B., Sarazin, M., Wilson, R., Perera, S., and Le Louarn, M. (2021). Fass: a turbulence profiler based on a fast, low-noise camera. *Monthly Notices of the Royal Astronomical Society*, 501(2):3030–3045.

Guo, Y., Ferguson, H. C., Bell, E. F., Koo, D. C., Conselice, C. J., Giavalisco, M., Kassin, S., Lu, Y., Lucas, R., Mandelker, N., et al. (2015). Clumpy galaxies in candels. i. the definition of uv clumps and the fraction of clumpy galaxies at 0.5< z< 3. *The Astrophysical Journal*, 800(1):39.

Guo, Y., Rafelski, M., Bell, E. F., Conselice, C. J., Dekel, A., Faber, S., Giavalisco, M., Koekemoer, A. M., Koo, D. C., Lu, Y., et al. (2018). Clumpy galaxies in candels. ii. physical properties of uv-bright clumps at 0.5‘L‘d’ z< 3. *The Astrophysical Journal*, 853(2):108.

Habib, A., Vernin, J., Benkhaldoun, Z., and Lanteri, H. (2006). Single star scidar: atmospheric parameters profiling using the simulated annealing algorithm. *Monthly Notices of the Royal Astronomical Society*, 368(3):1456–1462.

Hammer, F., Puech, M., Assemat, F. F., Gendron, E., Sayede, F., Laporte, P., Marteaud, M., Liotard, A., and Zamkotsian, F. (2004). Falcon: a concept to extend adaptive optics corrections to cosmological fields. In *Second backaskog workshop on extremely large telescopes*, volume 5382, pages 727–736. International Society for Optics and Photonics.

Hardy, J. W. (1998). *Adaptive optics for astronomical telescopes*, volume 16. Oxford University Press on Demand.

Hartmann, J. (1900). Bermerkungen über den bau und die justierung von spektrographen. *Zeitschrift für Instrumentenkunde*, 20:47.

Hayano, Y., Akiyama, M., Hattori, T., Iwata, I., Kodama, T., Lai, O., Minowa, Y., Ono, Y., Oya, S., Takiura, K., et al. (2014). Ultimate-subaru: project status. In *Adaptive Optics Systems IV*, volume 9148, pages 965–972. SPIE.

Hudgin, R. (1977). Wave-front compensation error due to finite corrector-element size. *JOSA*, 67(3):393–395.

Kanzawa, T., Tomono, D., Usuda, T., Takato, N., Negishi, S., Sugahara, S., and Itoh, N. (2006). Improvement of the pointing accuracy of the subaru telescope by suppressing vibrations. In *Ground-based and Airborne Telescopes*, volume 6267, pages 1237–1246. SPIE.

Kern, P., Lena, P., Gigan, P., Fontanella, J.-C., Rousset, G., Merkle, F., and Gaffard, J.-P. (1989). Come-on: an adaptive optics prototype dedicated to infrared astronomy. In *New Technologies for Astronomy*, volume 1130, pages 17–28. SPIE.

Kobayashi, M., Sekine, H., Miki, T., Muto, T., Tsuboi, T., Onuki, Y., Matsuno, Y., Takahashi, H., Ichikawa, T., and Inoue, S. (2019). A 3.4 μm pixel pitch global shutter cmos image sensor with dual in-pixel charge domain memory. *Japanese Journal of Applied Physics*, 58(SB):SBBL02.

Kolmogorov, A. N. (1941). Local turbulence structure in incompressible fluids at very high reynolds numbers. In *Dokl. Akad. Nauk SSSR*, volume 30.

Lai, O., Chun, M., Abdurrahman, F., Lu, J., Fohring, D., Toomey, D., et al. (2018). Deconstructing turbulence and optimizing glao using imaka telemetry. In *Adaptive Optics Systems VI*, volume 10703, pages 1441–1454. SPIE.

Martin, O., Gendron, É., Rousset, G., and Vidal, F. (2012). Temporal convergence of phase spatial covariance matrix measurements in tomographic adaptive optics. In *Adaptive Optics Systems III*, volume 8447, pages 855–868. SPIE.

Minowa, Y., Clergeon, C., Akiyama, M., Rigaut, F., d'Ă'ŹOrgeville, C., Price, I., Herrald, N., Koyama, Y., Iwata, I., Hattori, T., et al. (2017). Ultimate-subaru: Wide-field near-infrared surveyor with glao at subaru telescope. *Adaptive Optics for Extremely Large Telescopes V (AO4ELT5)],(Jun 2017)*.

Minowa, Y., Hayano, Y., Oya, S., Watanabe, M., Hattori, M., Guyon, O., Egner, S., Saito, Y., Ito, M., Takami, H., et al. (2010). Performance of subaru adaptive optics system ao188. In *Adaptive Optics Systems II*, volume 7736, page 77363N. International Society for Optics and Photonics.

Minowa, Y., Ono, Y., Tanaka, Y., Yoshida, H., Terao, K., Koyama, Y., Ali, S., Tanaka, I., Hattori, T., Okita, H., et al. (2022). Ultimate-subaru: Glao preliminary design overview. In *Adaptive Optics Systems VIII*, volume 12185, pages 635–646. SPIE.

Nicholls, T., Boreman, G., and Dainty, J. (1995). Use of a shack–hartmann wave-front sensor to measure deviations from a kolmogorov phase spectrum. *Optics letters*, 20(24):2460–2462.

Noll, R. J. (1976). Zernike polynomials and atmospheric turbulence. *JOsA*, 66(3):207–211.

Obukhov, A. (1949). Pressure fluctuations in turbulent flow. *CR Acad. Sci. URSS*, 66:17–20.

Obukhov, A. M. (1970). Structure of temperature field in turbulent flow. Technical report, AIR FORCE SYSTEMS COMMAND WRIGHT-PATTERSON AFB OH FOREIGN TECHNOLOGY DIVISION.

Ogane, H., Akiyama, M., Oya, S., and Ono, Y. (2021). Atmospheric turbulence profiling with multi-aperture scintillation of a shack–hartmann sensor. *Monthly Notices of the Royal Astronomical Society*, 503(4):5778–5788.

Oike, Y., Akiyama, K., Hung, L. D., Niitsuma, W., Kato, A., Sato, M., Kato, Y., Nakamura, W., Shiroshita, H., Sakano, Y., et al. (2017). 8.3 m-pixel 480-fps global-shutter cmos image sensor with gain-adaptive column adcs and chip-on-chip stacked integration. *IEEE Journal of Solid-State Circuits*, 52(4):985–993.

Ono, Y. H., Akiyama, M., Oya, S., Lardiére, O., Andersen, D. R., Correia, C., Jackson, K., and Bradley, C. (2016a). Multi time-step wavefront reconstruction for tomographic adaptive-optics systems. *JOSA A*, 33(4):726–740.

Ono, Y. H., Correia, C. M., Andersen, D. R., Lardière, O., Oya, S., Akiyama, M., Jackson, K., and Bradley, C. (2016b). Statistics of turbulence parameters at maunakea using the multiple wavefront sensor data of raven. *Monthly Notices of the Royal Astronomical Society*, 465(4):4931–4941.

Osborn, J., Wilson, R., Butterley, T., Shepherd, H., and Sarazin, M. (2010). Profiling the surface layer of optical turbulence with slodar. *Monthly Notices of the Royal Astronomical Society*, 406(2):1405–1408.

Oya, S., Hayano, Y., Lai, O., Iwata, I., Kodama, T., Arimoto, N., Minowa, Y., Akiyama, M., Ono, Y. H., Terada, H., et al. (2014). Ultimate-subaru: simulation update. In *Adaptive Optics Systems IV*, volume 9148, pages 2097–2104. SPIE.

Paufique, J., Madec, P.-Y., Kolb, J., Kuntschner, H., Argomedo, J., Kiekebusch, M. J., Donaldson, R. H., Arsenault, R., Siebenmorgen, R., Soenke, C., et al. (2016). Graal on the mountaintop. In *Adaptive Optics Systems V*, volume 9909, pages 806–820. SPIE.

Perera, S., Wilson, R. W., Butterley, T., Osborn, J., Farley, O. J., and Laidlaw, D. J. (2023). Shimm: a versatile seeing monitor for astronomy. *Monthly Notices of the Royal Astronomical Society*, 520(4):5475–5486.

Pfrommer, T. and Hickson, P. (2014). High resolution mesospheric sodium properties for adaptive optics applications. *Astronomy & Astrophysics*, 565:A102.

Platt, B. and Shack, R. V. (1971). Lenticular hartmann screen. *Newsletter*, 5:15.

Prieur, J.-L., Daigne, G., and Avila, R. (2001). Scidar measurements at pic du midi. *Astronomy & Astrophysics*, 371(1):366–377.

Ragazzoni, R. (1996). Pupil plane wavefront sensing with an oscillating prism. *Journal of modern optics*, 43(2):289–293.

Rigaut, F. (2002). Ground conjugate wide field adaptive optics for the elts. In *European Southern Observatory Conference and Workshop Proceedings*, volume 58, page 11.

Rocca, A., Roddier, F., and Vernin, J. (1974). Detection of atmospheric turbulent layers by spatiotemporal and spatioangular correlation measurements of stellar-light scintillation. *JOSA*, 64(7):1000–1004.

Roddier, F. (1981). V the effects of atmospheric turbulence in optical astronomy. In *Progress in optics*, volume 19, pages 281–376. Elsevier.

Roddier, F., Roddier, C., and Roddier, N. (1988). Curvature sensing: a new wavefront sensing method. In *Statistical Optics*, volume 976, pages 203–209. SPIE.

Sarazin, M. and Roddier, F. (1990). The eso differential image motion monitor. *Astronomy and Astrophysics*, 227:294–300.

Shepherd, H., Osborn, J., Wilson, R., Butterley, T., Avila, R., Dhillon, V., and Morris, T. (2014). Stereo-scidar: optical turbulence profiling with high sensitivity using a modified scidar instrument. *Monthly Notices of the Royal Astronomical Society*, 437(4):3568–3577.

Tallon, M. and Foy, R. (1990). Adaptive telescope with laser probe-isoplanatism and cone effect. *Astronomy and Astrophysics*, 235:549–557.

Tatarski, V. (1971). The effects of the turbulent atmosphere on wave propagation. *US Department of Commerce*.

Terao, K., Akiyama, M., Minowa, Y., Ono, Y., Ogane, H., Akasawa, T., Oya, S., and Yamamuro, T. (2022). Ultimate-start: current status of the subaru tomography adaptive optics research experiment. In *Adaptive Optics Systems VIII*, volume 12185, pages 2057–2064. SPIE.

Terao, K., Akiyama, M., and Oya, S. (2020). Measurements of image quality and surface shape of microlens arrays for shack-hartmann wavefront sensors. In *Adaptive Optics Systems VII*, volume 11448, pages 1242–1248. SPIE.

Thompson, L. A. and Gardner, C. S. (1987). Experiments on laser guide stars at mauna kea observatory for adaptive imaging in astronomy. *Nature*, 328(6127):229–231.

Tokovinin, A. (2004). Seeing improvement with ground-layer adaptive optics. *Publications of the Astronomical Society of the Pacific*, 116(824):941.

Tokovinin, A. (2021). Measurement of turbulence profile from defocused ring images. *Monthly Notices of the Royal Astronomical Society*, 502(1):794–808.

Tokovinin, A. and Kornilov, V. (2007). Accurate seeing measurements with mass and dimm. *Monthly Notices of the Royal Astronomical Society*, 381(3):1179–1189.

Tyson, R. K. and Frazier, B. W. (2022). *Principles of adaptive optics*. CRC press.

Védrenne, N., Michau, V., Robert, C., and Conan, J.-M. (2007). C n 2 profile measurement from shack-hartmann data. *Optics letters*, 32(18):2659–2661.

Vidal, F., Gendron, E., and Rousset, G. (2010). Tomography approach for multi-object adaptive optics. *JOSA A*, 27(11):A253–A264.

Wilson, R. W. (2002). Slodar: measuring optical turbulence altitude with a shack–hartmann wavefront sensor. *Monthly Notices of the Royal Astronomical Society*, 337(1):103–108.

Yaglom, A. (1949). On the acceleration field in a turbulent flow. *CR Akad. USSR*, 67:795–798.

Young, A. (1970). Aperture filtering and saturation of scintillation. *JOSA*, 60(2):248–250.

Zhao, C. and Burge, J. H. (2007). Orthonormal vector polynomials in a unit circle, part i: basis set derived from gradients of zernike polynomials. *Optics Express*, 15(26):18014–18024.

Zhao, C. and Burge, J. H. (2008). Orthonormal vector polynomials in a unit circle, part ii: completing the basis set. *Optics Express*, 16(9):6586–6591.

Appendix A

Correlation function, structure function, and power spectrum of wavefront distortion by a thin turbulent layer

First, the derivation of the correlation function of wavefront distortion in equation (1.16) is shown. By substituting equation (1.14) into equation (1.15),

$$\begin{aligned} B_\phi(\boldsymbol{x}) &= k^2 \int_{h_0}^{h_0+\Delta h_0} dh \int_{h_0}^{h_0+\Delta h_0} dh' < n(\boldsymbol{r},h)n(\boldsymbol{r}+\boldsymbol{x},h') > \\ &= k^2 \int_{h_0}^{h_0+\Delta h_0} dh \int_{h_0-h}^{h_0+\Delta h_0-h} d\eta < n(\boldsymbol{r},h)n(\boldsymbol{r}+\boldsymbol{x},h+\eta) > \\ &= k^2 \int_{h_0}^{h_0+\Delta h_0} dh \int_{h_0-h}^{h_0+\Delta h_0-h} d\eta B_n(\boldsymbol{x},\eta). \end{aligned} \tag{A.1}$$

Since Δh_0 is large enough compared to the typical correlation length of refractive index, one can extend the integration range of $[h_0-h, h_0+\Delta h_0-h]$ to $(-\infty,\infty)$ and

$$\begin{aligned} B_\phi(\boldsymbol{x}) &\sim k^2 \int_{h_0}^{h_0+\Delta h_0} dh \int_{-\infty}^{\infty} d\eta B_n(\boldsymbol{x},\eta) \\ &= k^2 \Delta h_0 \int_{-\infty}^{\infty} d\eta B_n(\boldsymbol{x},\eta). \end{aligned} \tag{A.2}$$

Correlation function, structure function, and power spectrum of wavefront distortion by a thin turbulent layer

Then, structure function of wavefront distortion in equation (1.18) is, using equations (1.17) and (1.10),

$$\begin{aligned} D_\phi(\boldsymbol{x}) &= 2k^2\Delta h_0 \int_{-\infty}^{\infty} d\eta \left[B_n(\boldsymbol{0},\eta) - B_n(\boldsymbol{x},\eta)\right] \\ &= k^2\Delta h_0 \int_{-\infty}^{\infty} d\eta \left[D_n(\boldsymbol{x},\eta) - D_n(\boldsymbol{0},\eta)\right] \\ &= k^2\Delta h_0 \int_{-\infty}^{\infty} d\eta C_n^2(\eta) \left[(|\boldsymbol{x}|^2+\eta^2)^{1/3} - \eta^{2/3})\right] \end{aligned} \tag{A.3}$$

Because the $C_n^2(\eta)$ is valid when $\eta \sim h_0$,

$$\begin{aligned} D_\phi(\boldsymbol{x}) &\sim k^2 C_n^2(h_0)\Delta h_0 \int_{-\infty}^{\infty} d\eta \left[(|\boldsymbol{x}|^2+\eta^2)^{1/3} - \eta^{2/3})\right] \\ &= 2.91 k^2 C_n^2(h_0)\Delta h_0 |\boldsymbol{x}|^{5/3} \end{aligned} \tag{A.4}$$

By taking two-dimensional Fourier transform of equation (A.2), power spectrum of wavefront distortion in equation (1.19) is written as follows,

$$\begin{aligned} \Phi_\phi(\boldsymbol{f}) &= k^2\Delta h_0 \int_{-\infty}^{\infty} d\eta \mathcal{F}\left[B_n(\boldsymbol{x},\eta)\right] \\ &= k^2\Delta h_0 \Phi_n(\boldsymbol{f}, h_0) \\ &= 9.7\times 10^{-3} k^2 |\boldsymbol{f}|^{-11/3} C_n^2(h_0)\Delta h_0, \end{aligned} \tag{A.5}$$

where $\mathcal{F}[\cdot]$ means two-dimensional Fourier transform.

Appendix B

Power spectrum of amplitude fluctuation and wavefront distortion after Fresnel propagation

Based on equations (2.3) and (2.4), power spectrum of amplitude fluctuation $\Phi_\chi(\boldsymbol{f})$ and that of wavefront distortion $\Phi_\psi(\boldsymbol{f})$ are

$$\Phi_\chi(\boldsymbol{f}) = \Phi_\phi(\boldsymbol{f}) \times \left| \mathcal{F}\left[\frac{1}{\lambda z} \cos\left(\pi \frac{|\boldsymbol{x}|^2}{\lambda z} \right) \right] \right|^2, \tag{B.1}$$

$$\Phi_\psi(\boldsymbol{f}) = \Phi_\phi(\boldsymbol{f}) \times \left| \mathcal{F}\left[\frac{1}{\lambda z} \sin\left(\pi \frac{|\boldsymbol{x}|^2}{\lambda z} \right) \right] \right|^2, \tag{B.2}$$

where $\mathcal{F}[\cdot]$ is two-dimensional Fourier transform.

The Fourier transform parts in equations (B.1) and (B.2) are real part and imaginary part of $\mathcal{F}\left[\frac{1}{\lambda z} \exp\left(i\pi \frac{|\boldsymbol{x}|^2}{\lambda z} \right) \right]$, as

$$\mathcal{F}\left[\frac{1}{\lambda z} \exp\left(i\pi \frac{|\boldsymbol{x}|^2}{\lambda z} \right) \right] = \mathcal{F}\left[\frac{1}{\lambda z} \cos\left(\pi \frac{|\boldsymbol{x}|^2}{\lambda z} \right) \right] + i\mathcal{F}\left[\frac{1}{\lambda z} \sin\left(i\pi \frac{|\boldsymbol{x}|^2}{\lambda z} \right) \right], \tag{B.3}$$

where i is the imaginary unit.

And $\mathcal{F}\left[\frac{1}{\lambda z}\exp\left(i\pi\frac{|\boldsymbol{x}|^2}{\lambda z}\right)\right]$ is calculated, as follows,

$$\begin{aligned}
\mathcal{F}\left[\frac{1}{\lambda z}\exp\left(i\pi\frac{|\boldsymbol{x}|^2}{\lambda z}\right)\right] &= \int dx \int dy \frac{1}{\lambda z}\exp\left(i\pi\frac{x^2+y^2}{\lambda z}\right)\exp\left(-2\pi i(f_x x + f_y y)\right) \\
&= \frac{1}{\lambda z}\left(\int dx \exp\left(\frac{i\pi}{\lambda z}x^2 - 2\pi i f_x x\right)\right)^2 \\
&= \frac{1}{\lambda z}\left(\int dx \exp\left(\frac{i\pi}{\lambda z}(x-\lambda z f_x)^2 - i\pi\lambda z f_x^2\right)\right)^2 \\
&= \frac{1}{\lambda z}\exp\left(-i\pi\lambda z(f_x^2+f_y^2)\right)\left(\int dx \exp\left(\frac{i\pi}{\lambda z}(x-\lambda z f_x)^2\right)\right)^2 \\
&= i\exp\left(-i\pi\lambda z(f_x^2+f_y^2)\right) \\
&= \sin\left(\pi\lambda z(f_x^2+f_y^2)\right) + i\cos\left(\pi\lambda z(f_x^2+f_y^2)\right) \qquad \text{(B.4)}
\end{aligned}$$

Therefore, we obtain equations (2.5) and (2.6), i.e.

$$\Phi_\chi(\boldsymbol{f}) = \Phi_\phi(\boldsymbol{f})\sin^2(\pi\lambda z|\boldsymbol{f}|^2), \qquad \text{(B.5)}$$

$$\Phi_\psi(\boldsymbol{f}) = \Phi_\phi(\boldsymbol{f})\cos^2(\pi\lambda z|\boldsymbol{f}|^2). \qquad \text{(B.6)}$$

Appendix C

Slope auto-covariance analysis

We show the same figures as 2.15 but for all the datasets.

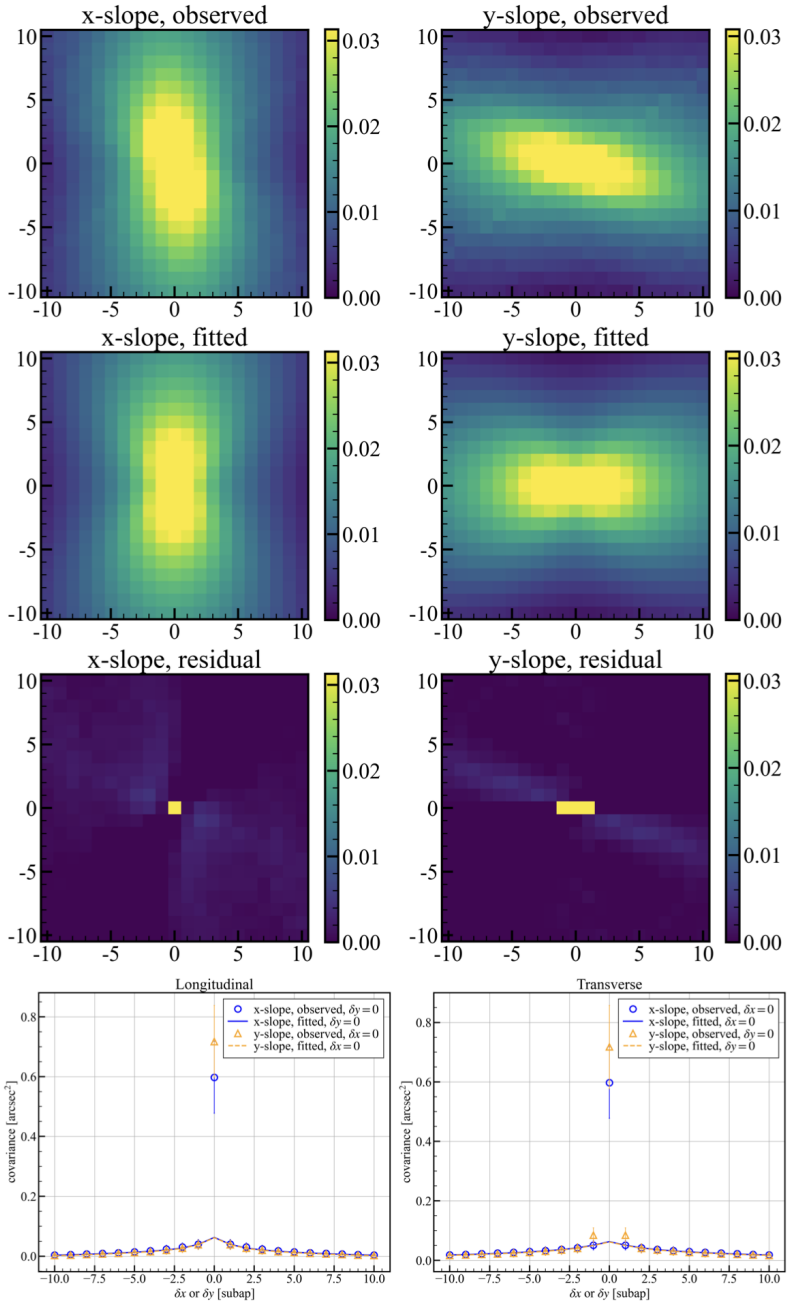

Fig. C.1 Top: X, Y-slope auto-covariance maps for dataset taken at 23:17, Nov.12, 2022 by SH-1. Second row: fitted X, Y-slope auto-covariance maps. Third row: residual maps between observed and fitted auto-covariance maps. Bottom: Cross-section of the auto-covariance maps at $\delta x = 0$ or $\delta y = 0$

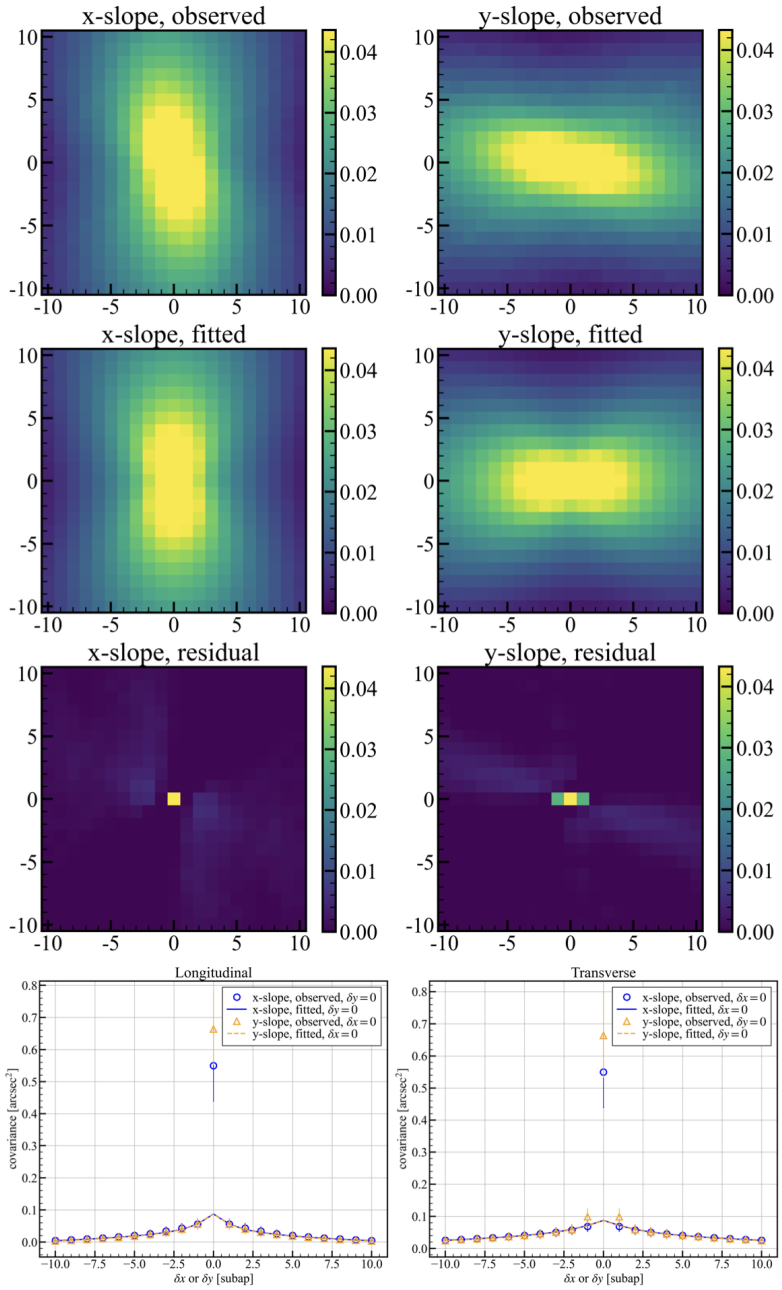

Fig. C.2 Same as figure C.1 but for dataset obtained at 23:17, Nov.12, 2022 by SH-2.

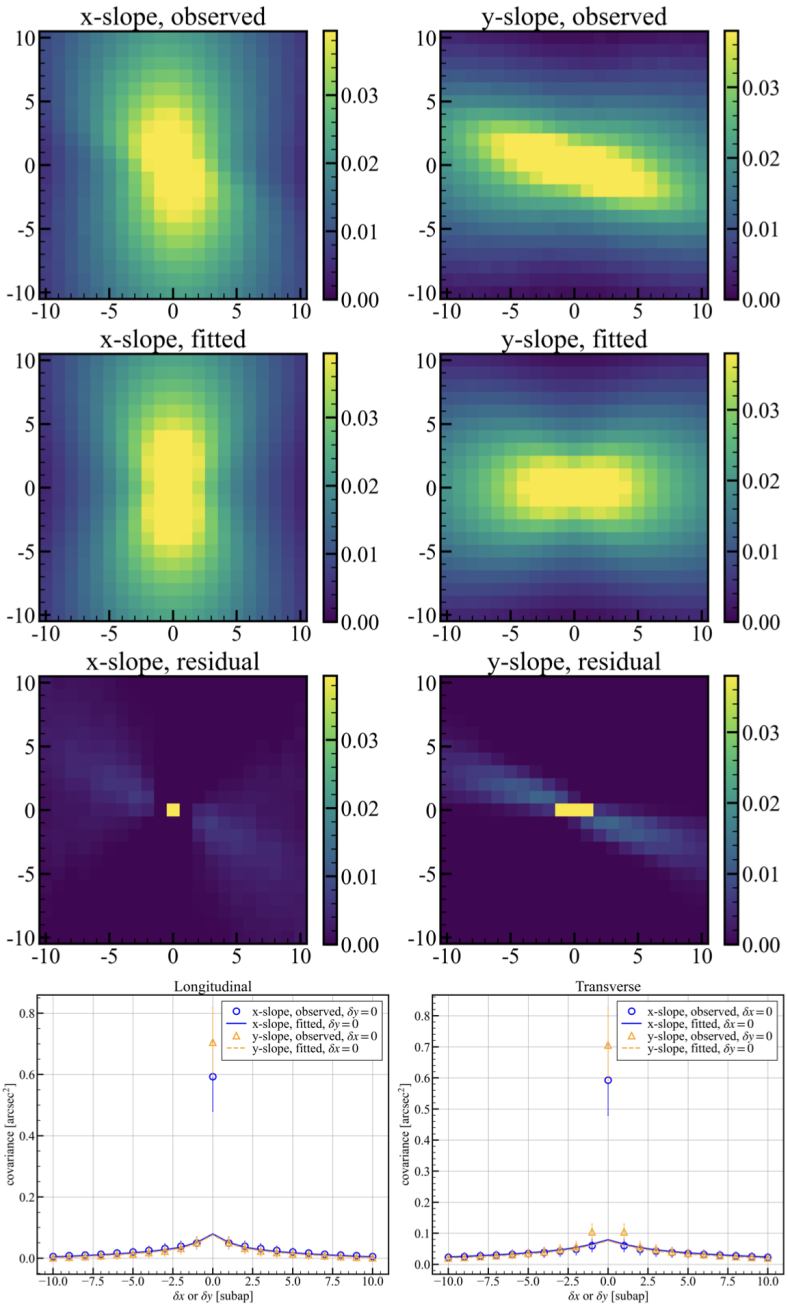

Fig. C.3 Same as figure C.1 but for dataset obtained at 23:37, Nov.12, 2022 by SH-1.

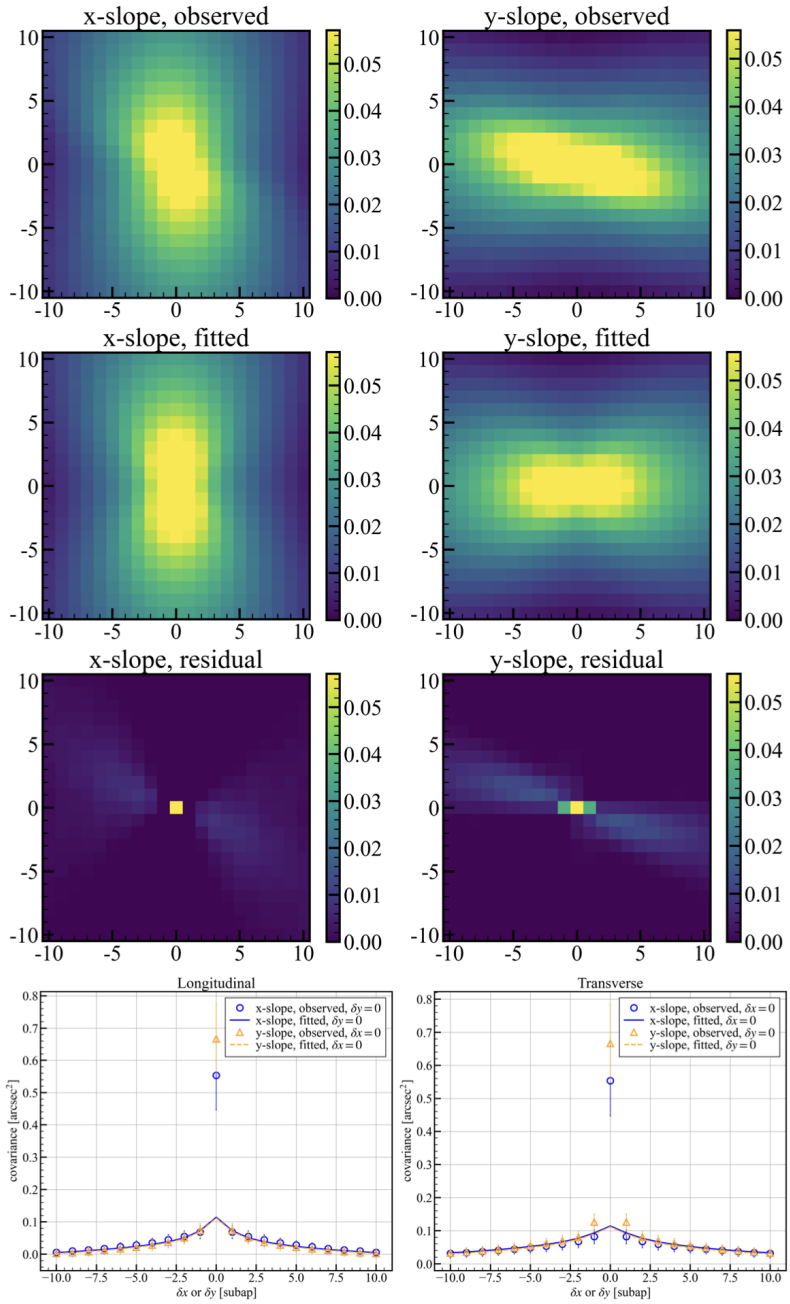

Fig. C.4 Same as figure C.1 but for dataset obtained at 23:37, Nov.12, 2022 by SH-2.

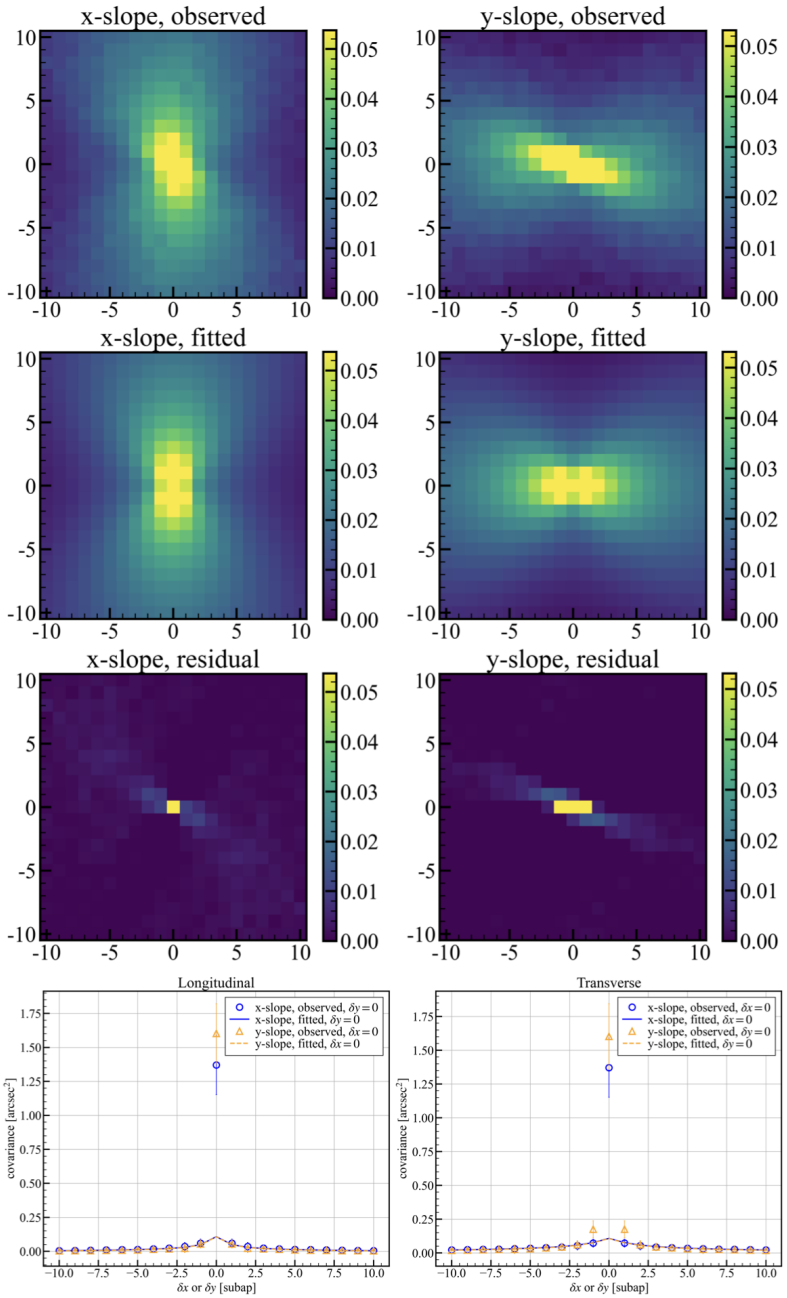

Fig. C.5 Same as figure C.1 but for dataset obtained at 23:42 Nov.12, 2022 by SH-1.

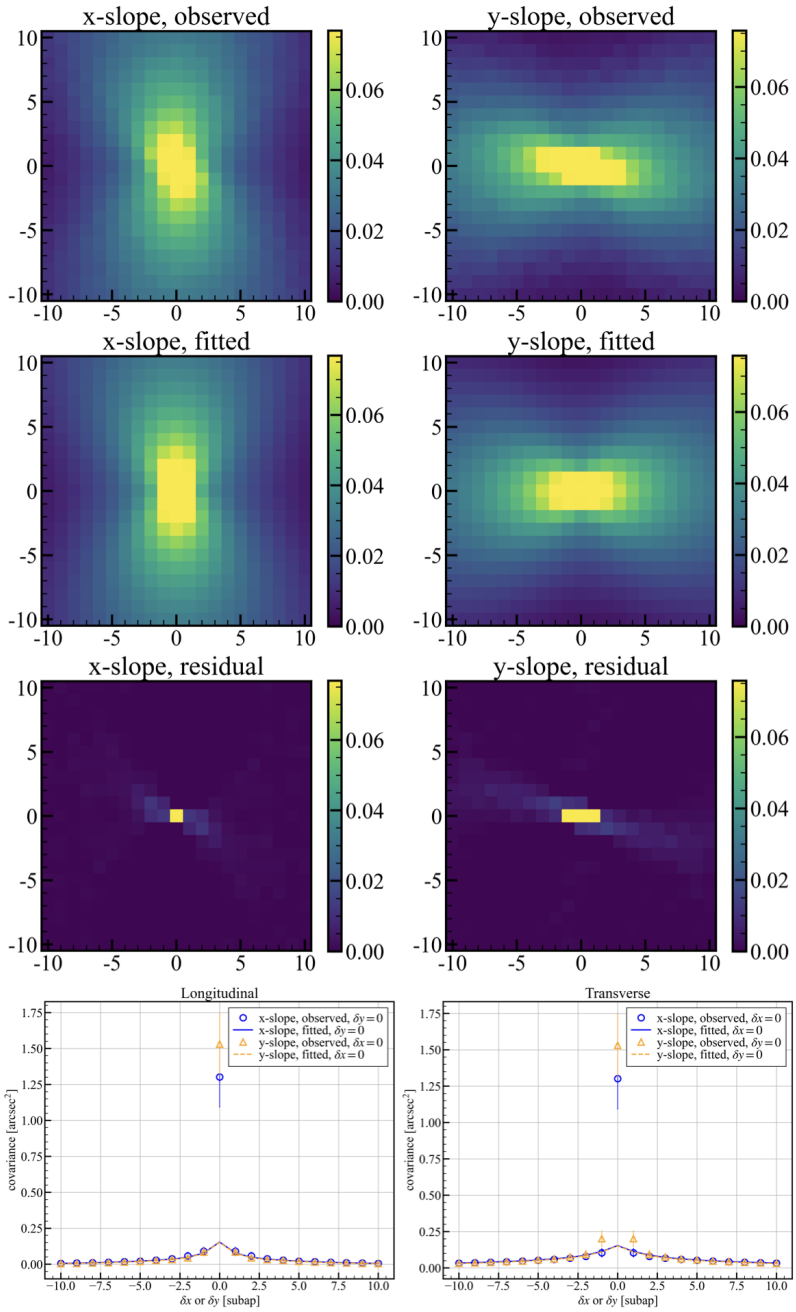

Fig. C.6 Same as figure C.1 but for dataset obtained at 23:42 Nov.12, 2022 by SH-2.

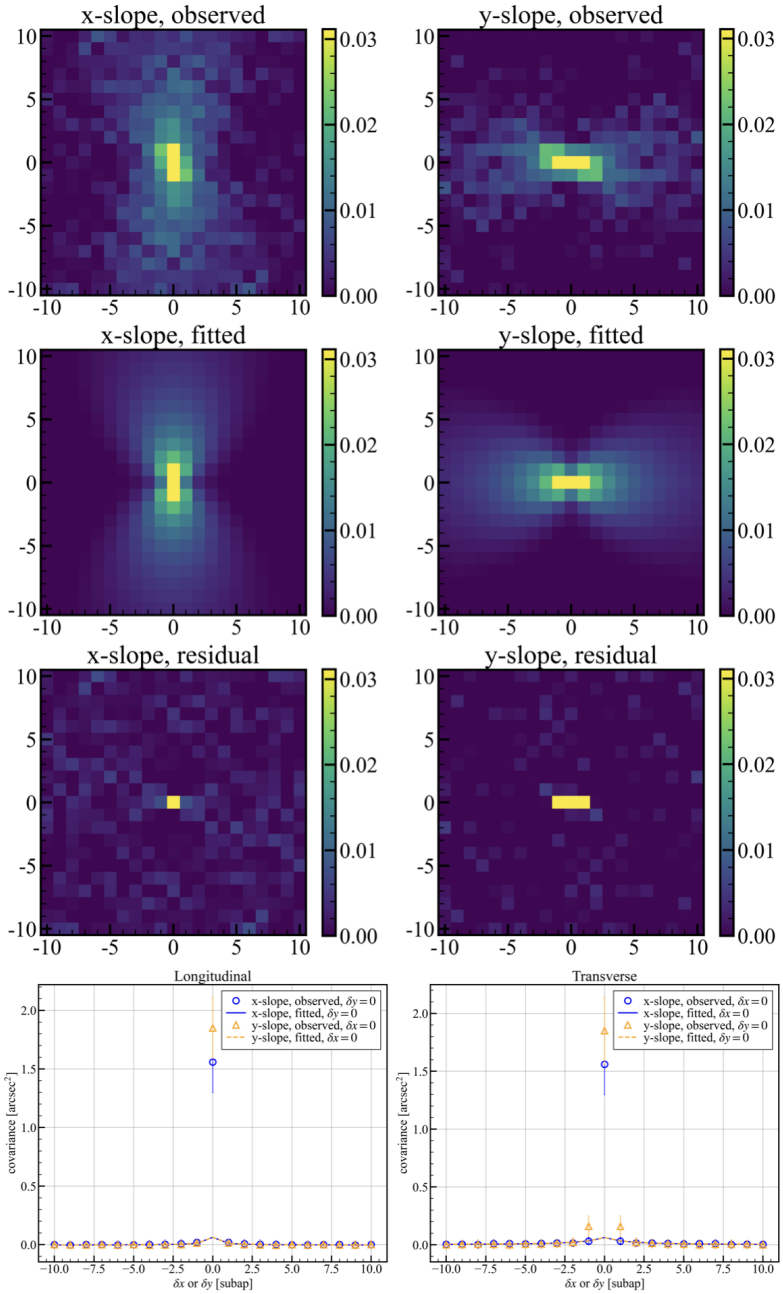

Fig. C.7 Same as figure C.1 but for dataset obtained at 23:45, Nov.12, 2022 by SH-1.

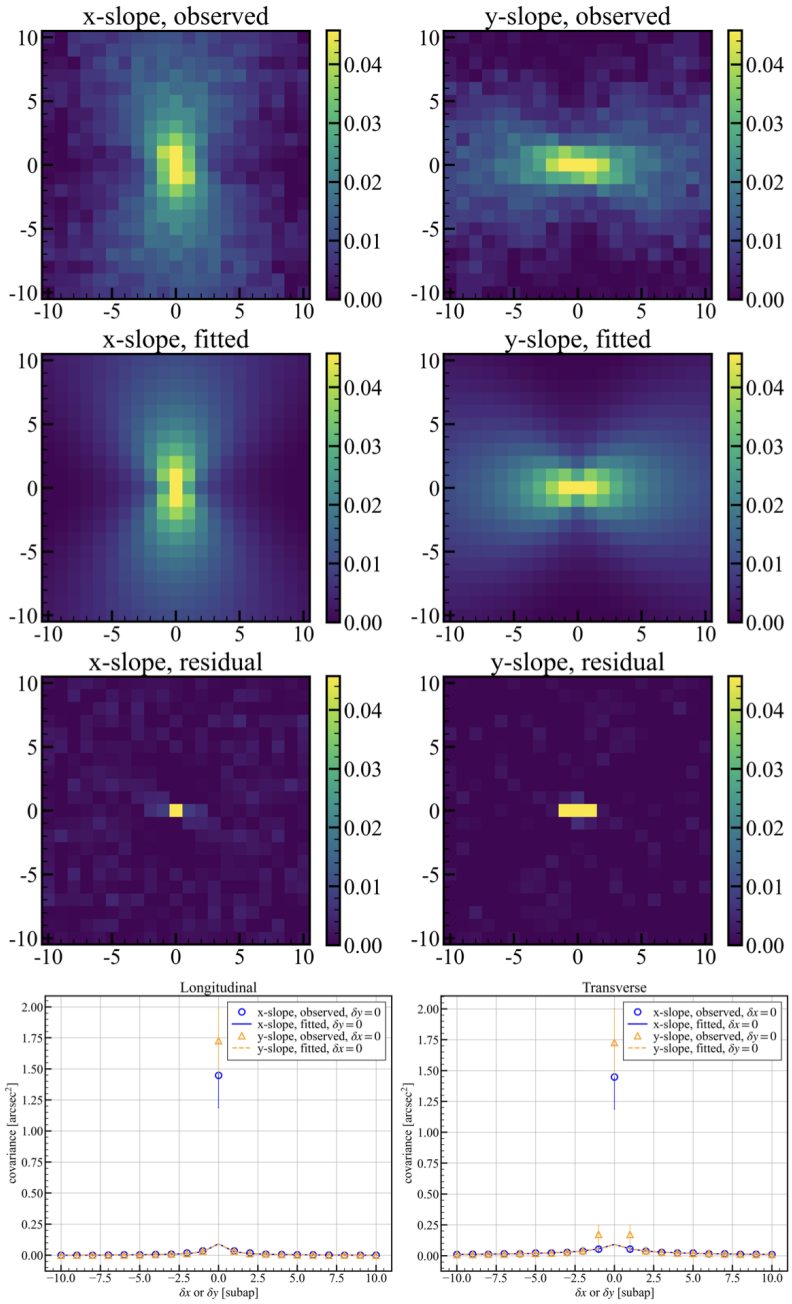

Fig. C.8 Same as figure C.1 but for dataset obtained at 23:45, Nov.12, 2022 by SH-2.

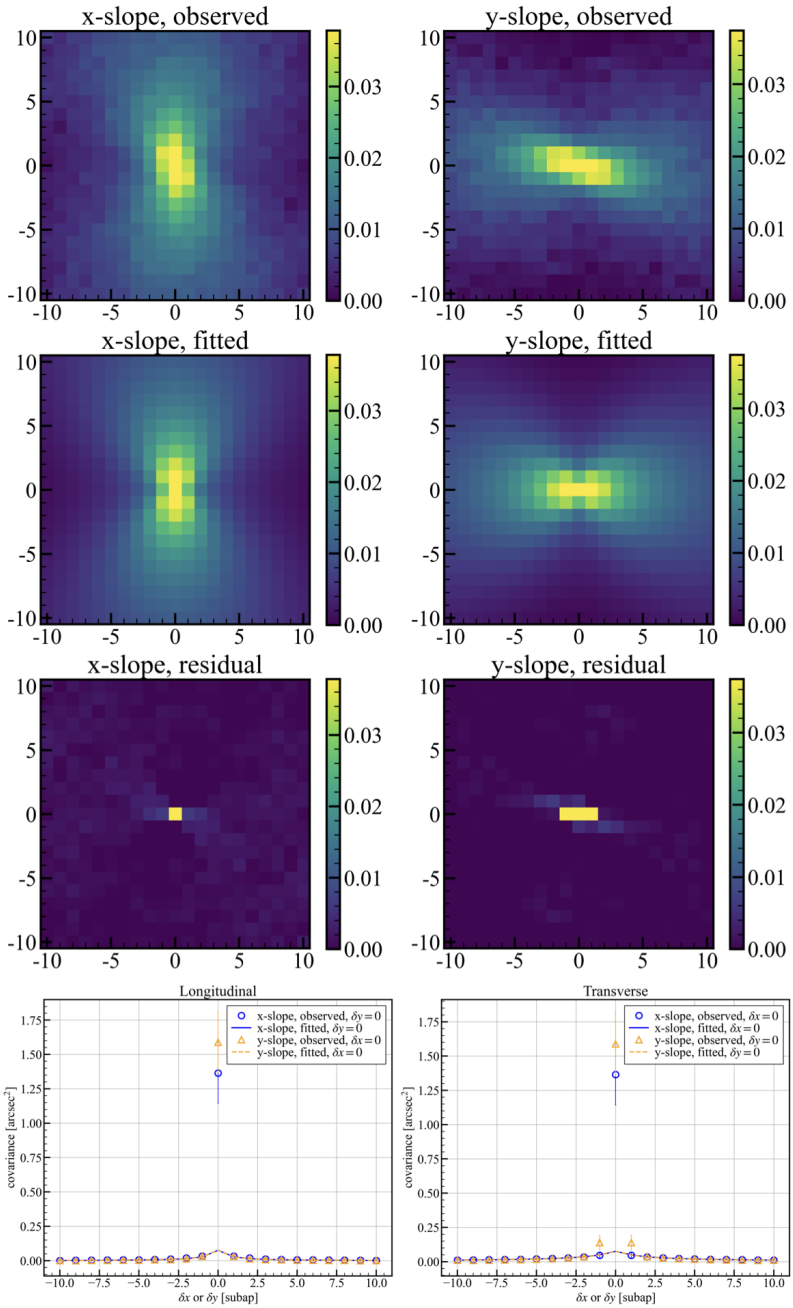

Fig. C.9 Same as figure C.1 but for dataset obtained at 23:49, Nov.12, 2022 by SH-1.

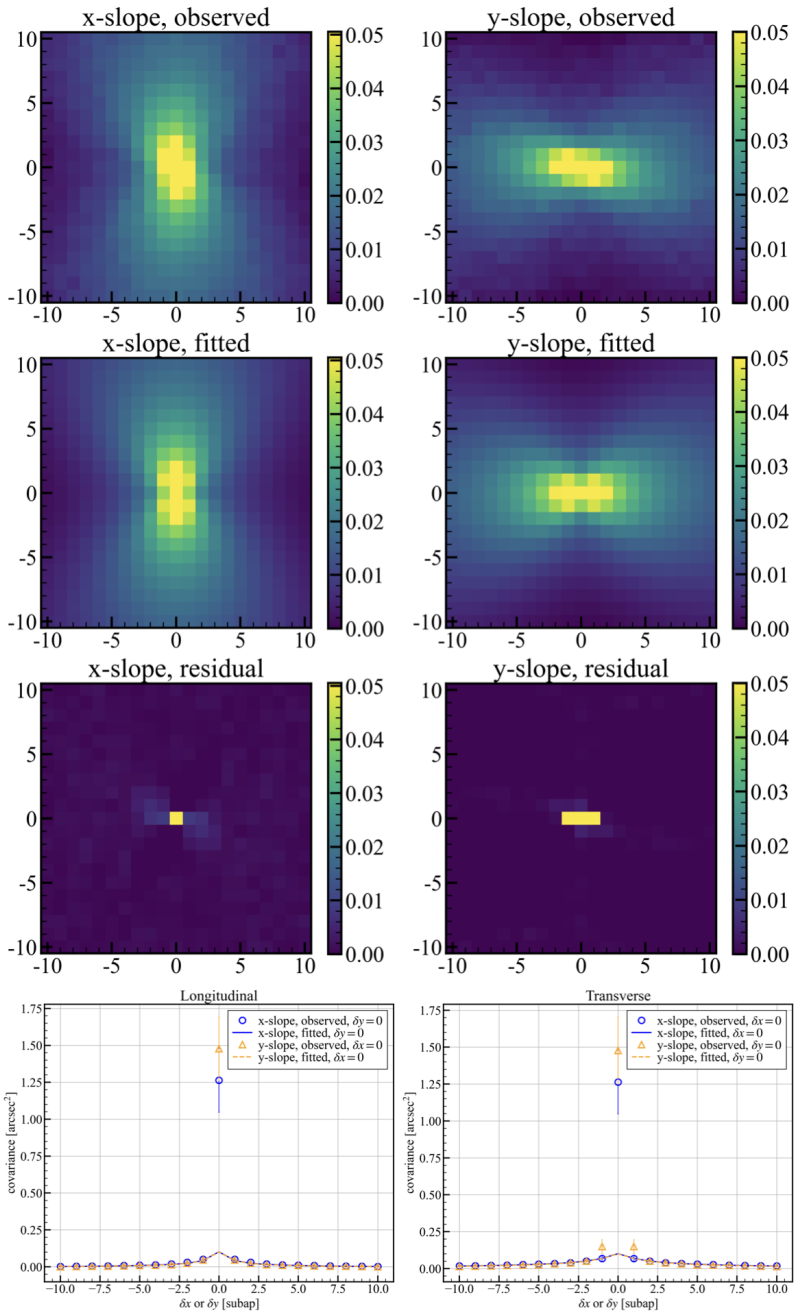

Fig. C.10 Same as figure C.1 but for dataset obtained at 23:49, Nov.12, 2022 by SH-2.

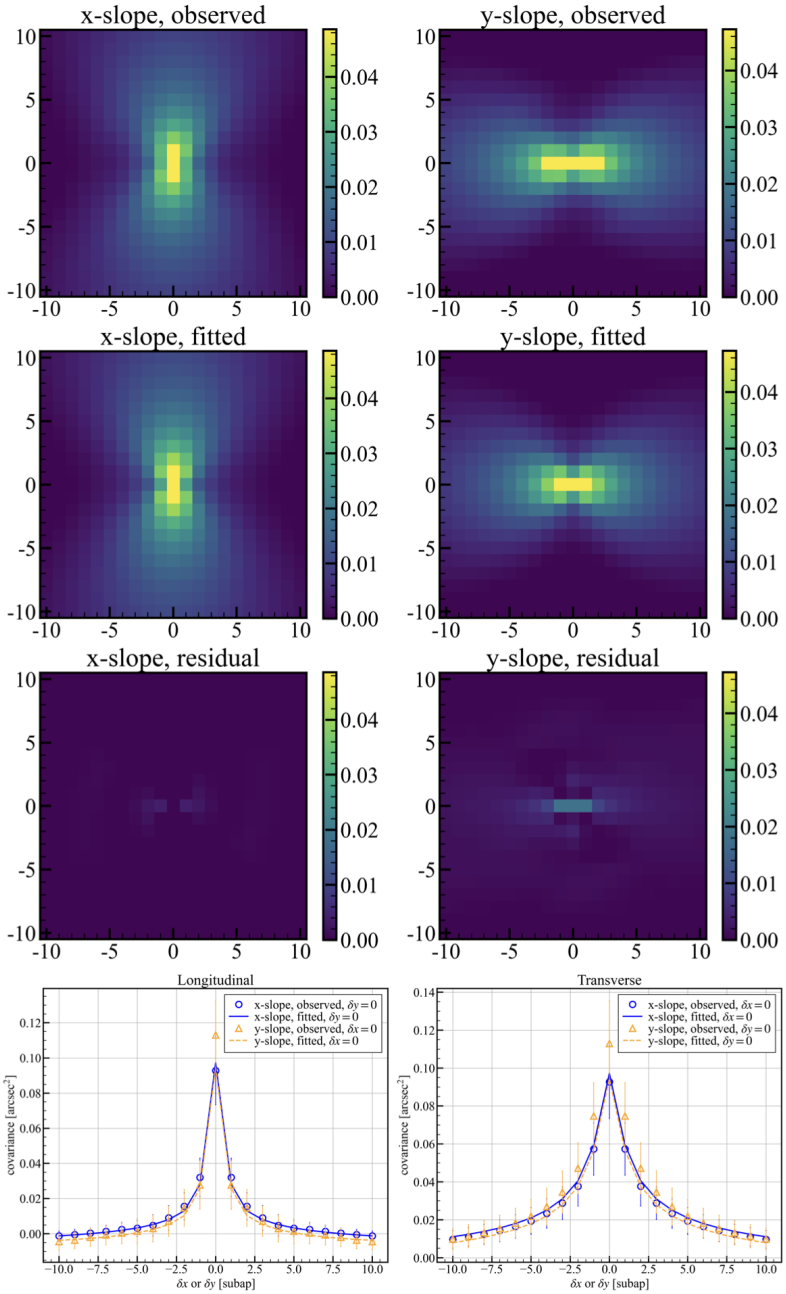

Fig. C.11 Same as figure C.1 but for dataset obtained at 2:42, Mar.14, 2023 by SH-1.

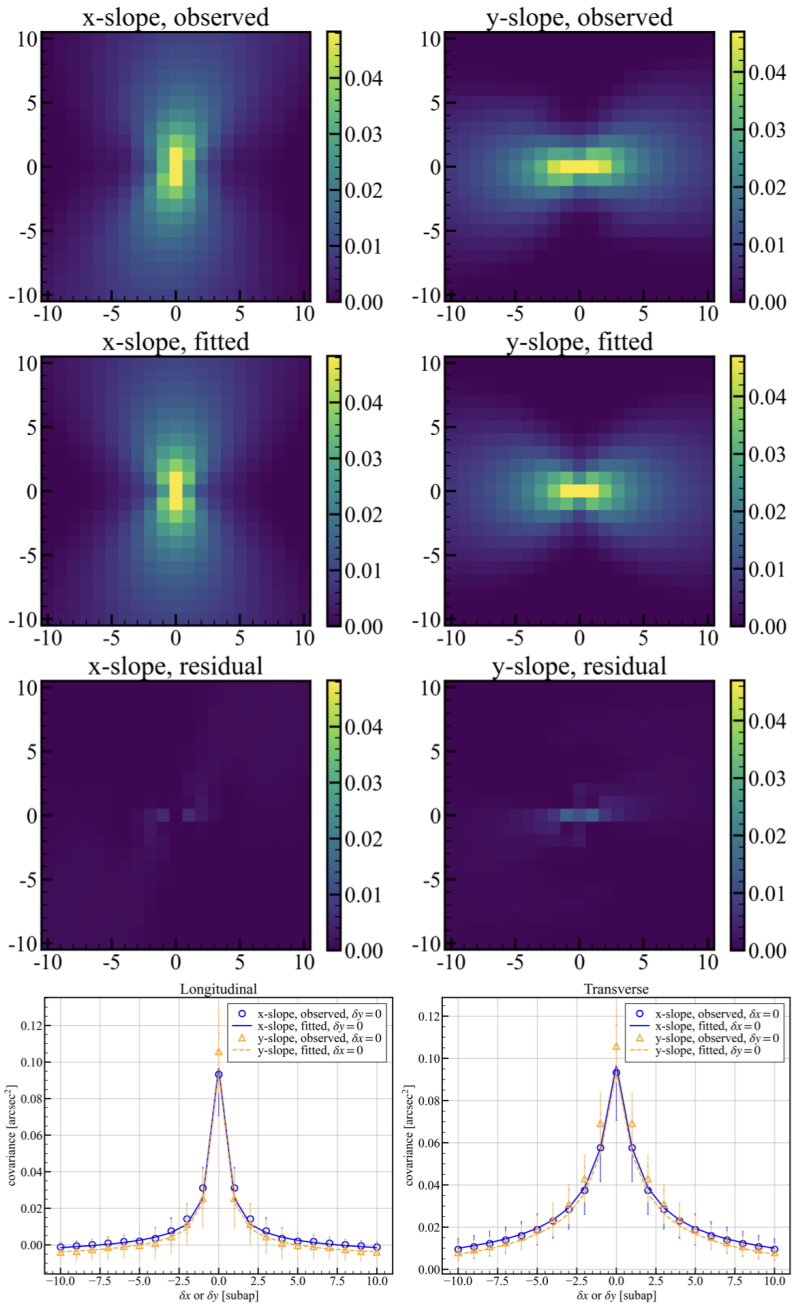

Fig. C.12 Same as figure C.1 but for dataset obtained at 2:45, Mar.14, 2023 by SH-1.

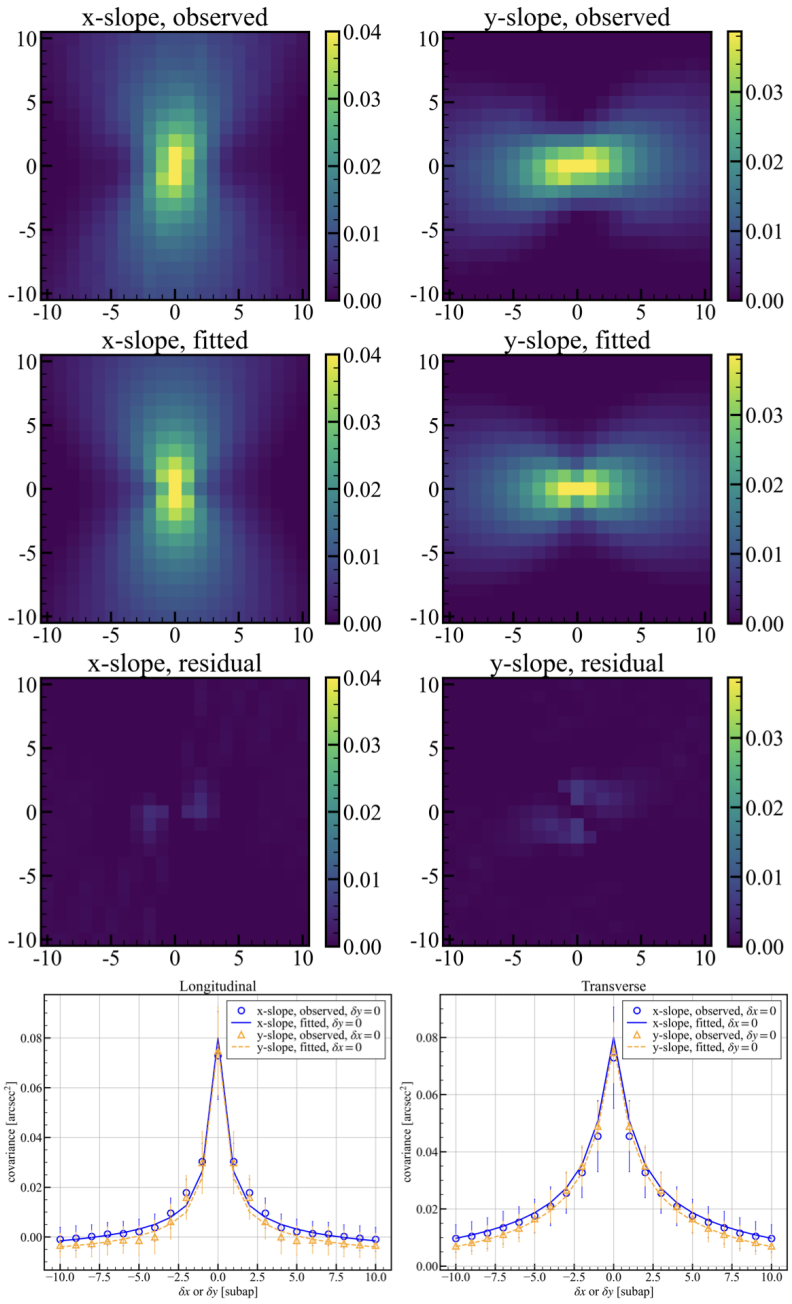

Fig. C.13 Same as figure C.1 but for dataset obtained at 3:30, Mar.14, 2023 by SH-2.

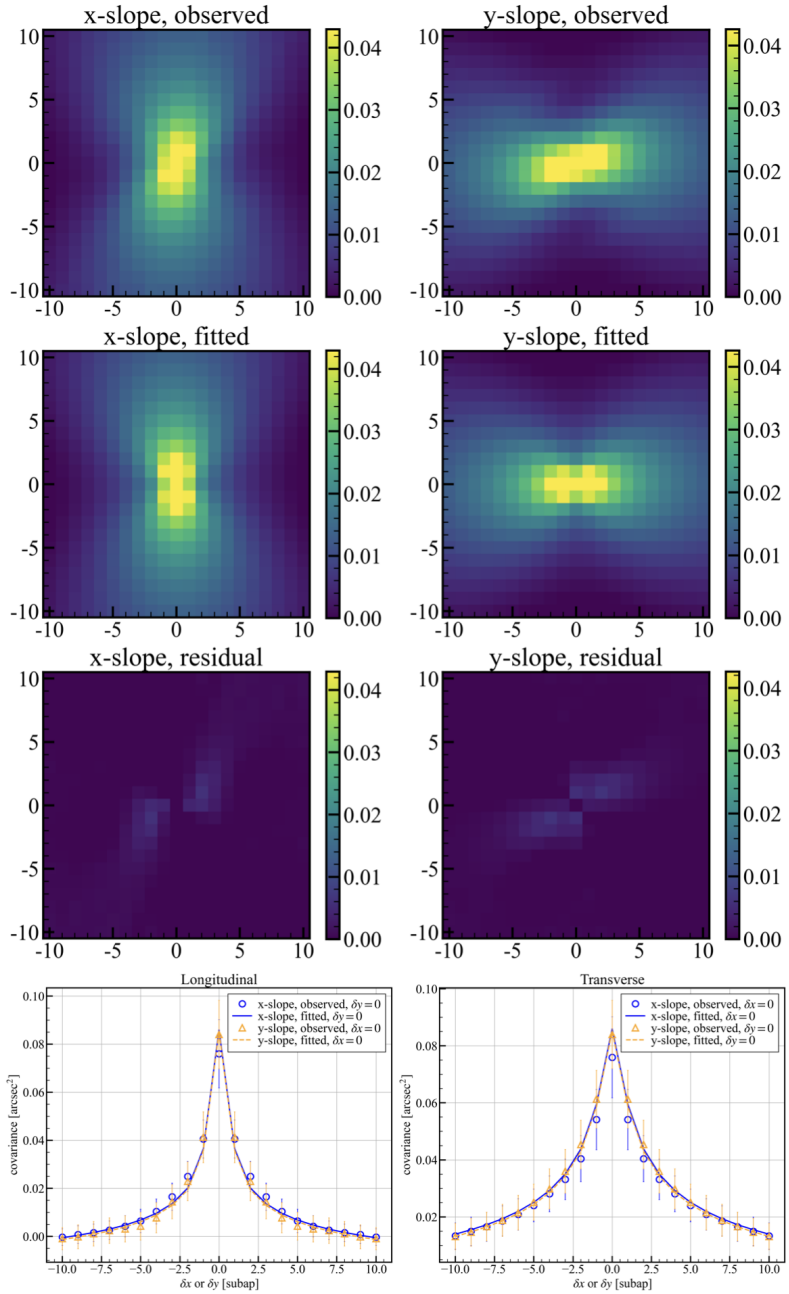

Fig. C.14 Same as figure C.1 but for dataset obtained at 3:34, Mar.14, 2023 by SH-2.

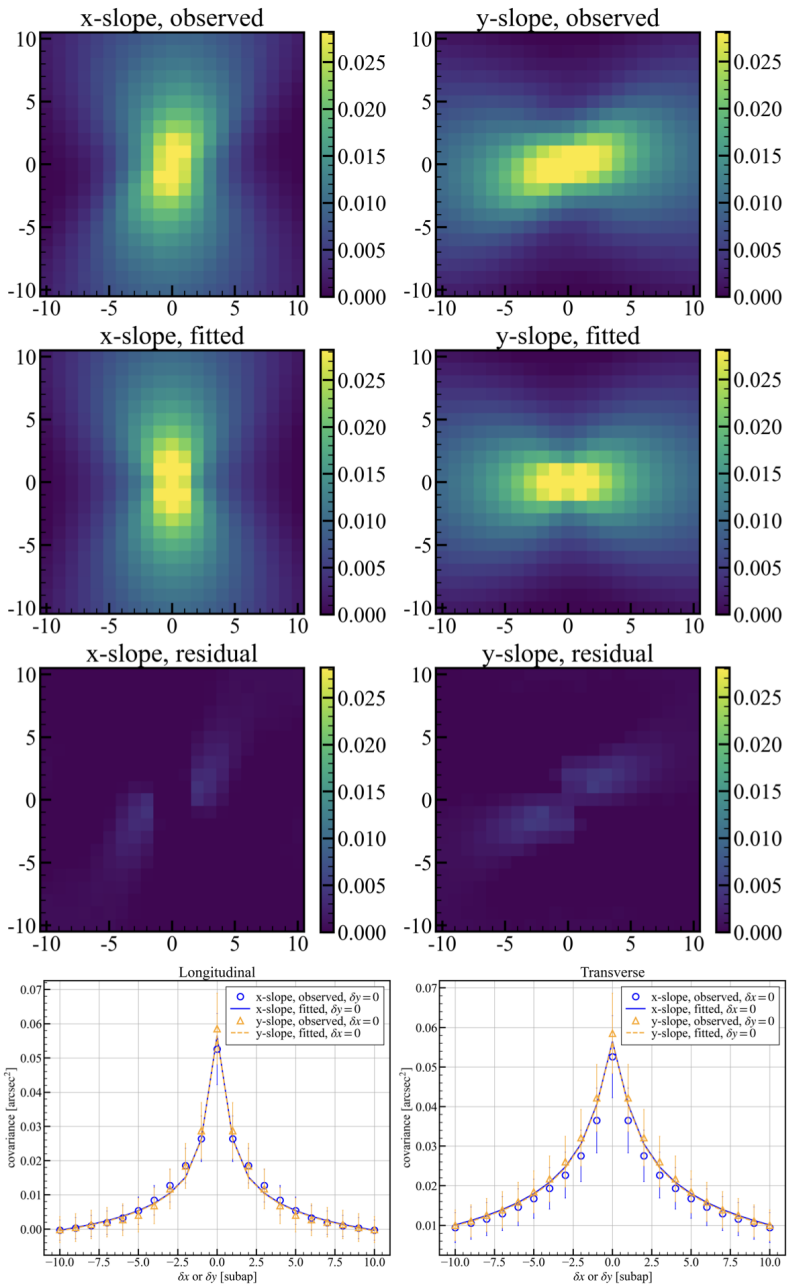

Fig. C.15 Same as figure C.1 but for dataset obtained at 3:37, Mar.14, 2023 by SH-2.

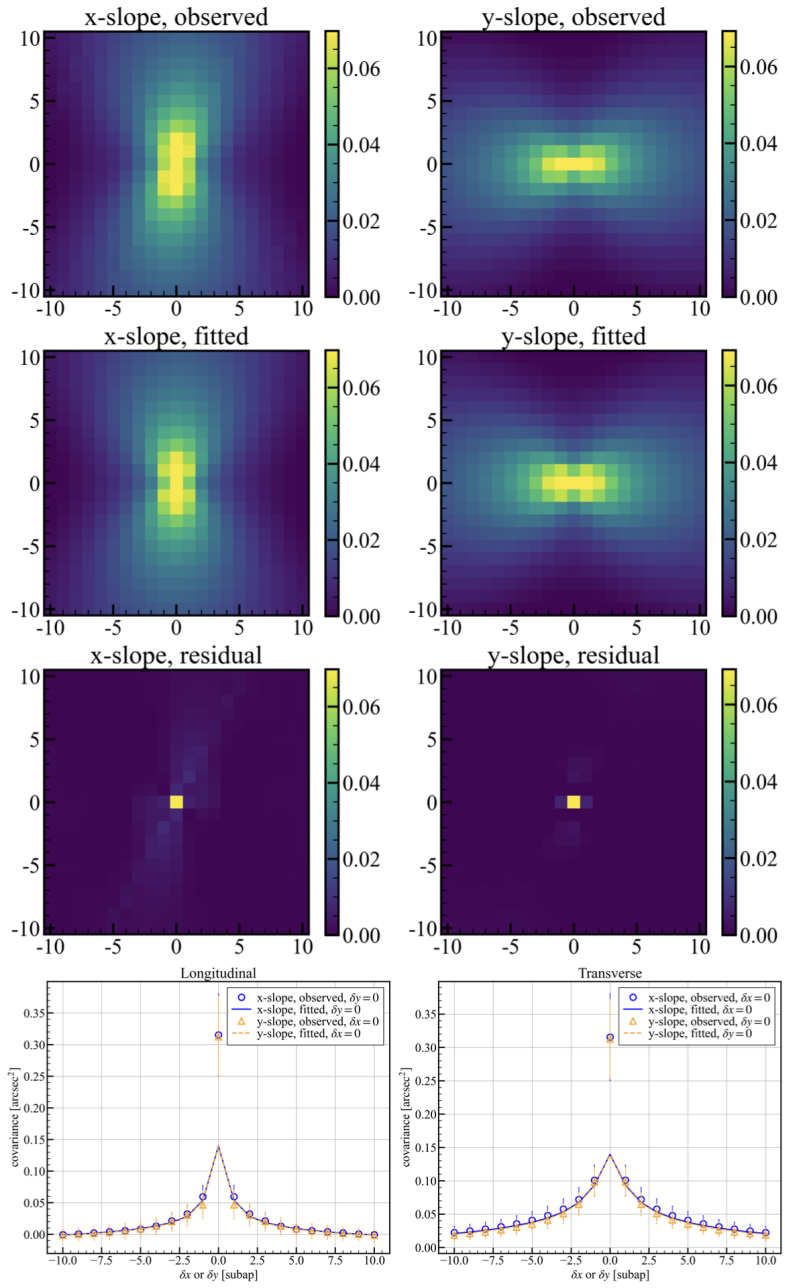

Fig. C.16 Same as figure C.1 but for dataset obtained at 4:44, Mar.14, 2023 by SH-1.

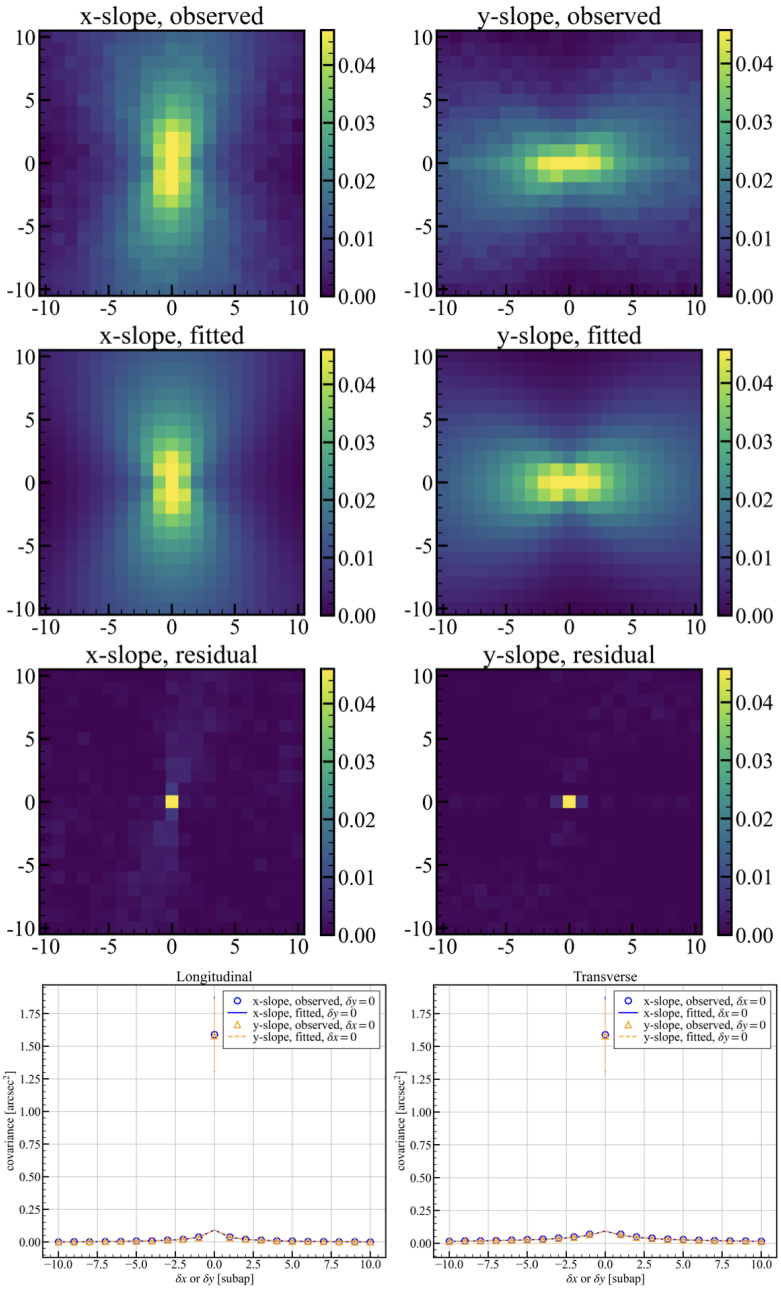

Fig. C.17 Same as figure C.1 but for dataset obtained at 4:44, Mar.14, 2023 by SH-2.

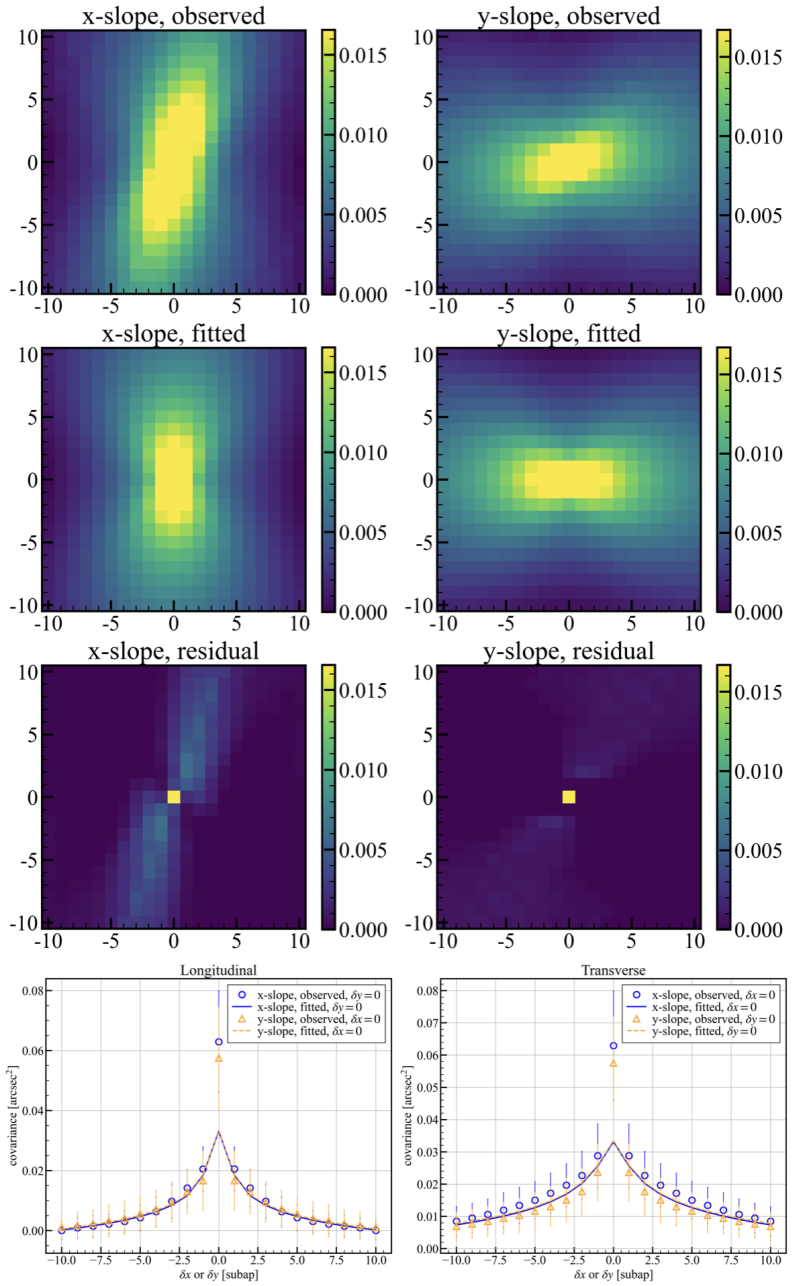

Fig. C.18 Same as figure C.1 but for dataset obtained at 5:07, Mar.14, 2023 by SH-1.

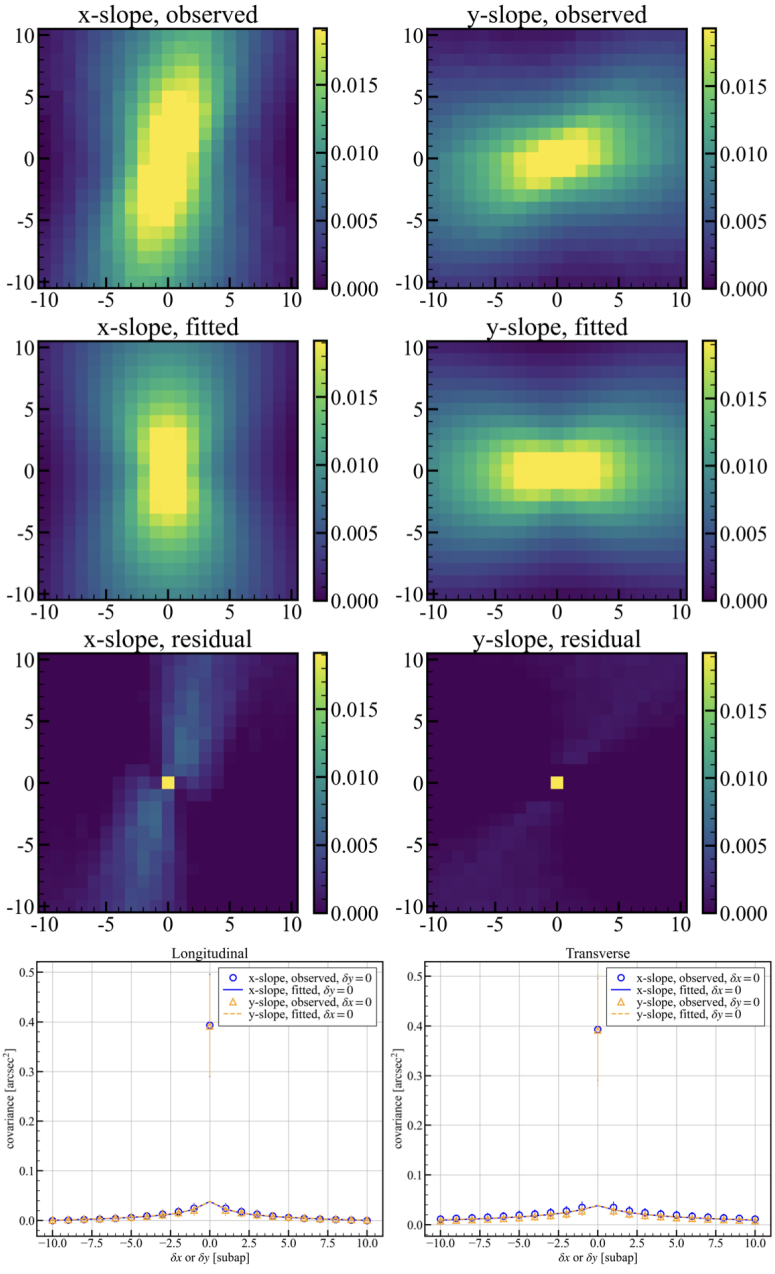

Fig. C.19 Same as figure C.1 but for dataset obtained at 5:07, Mar.14, 2023 by SH-2.

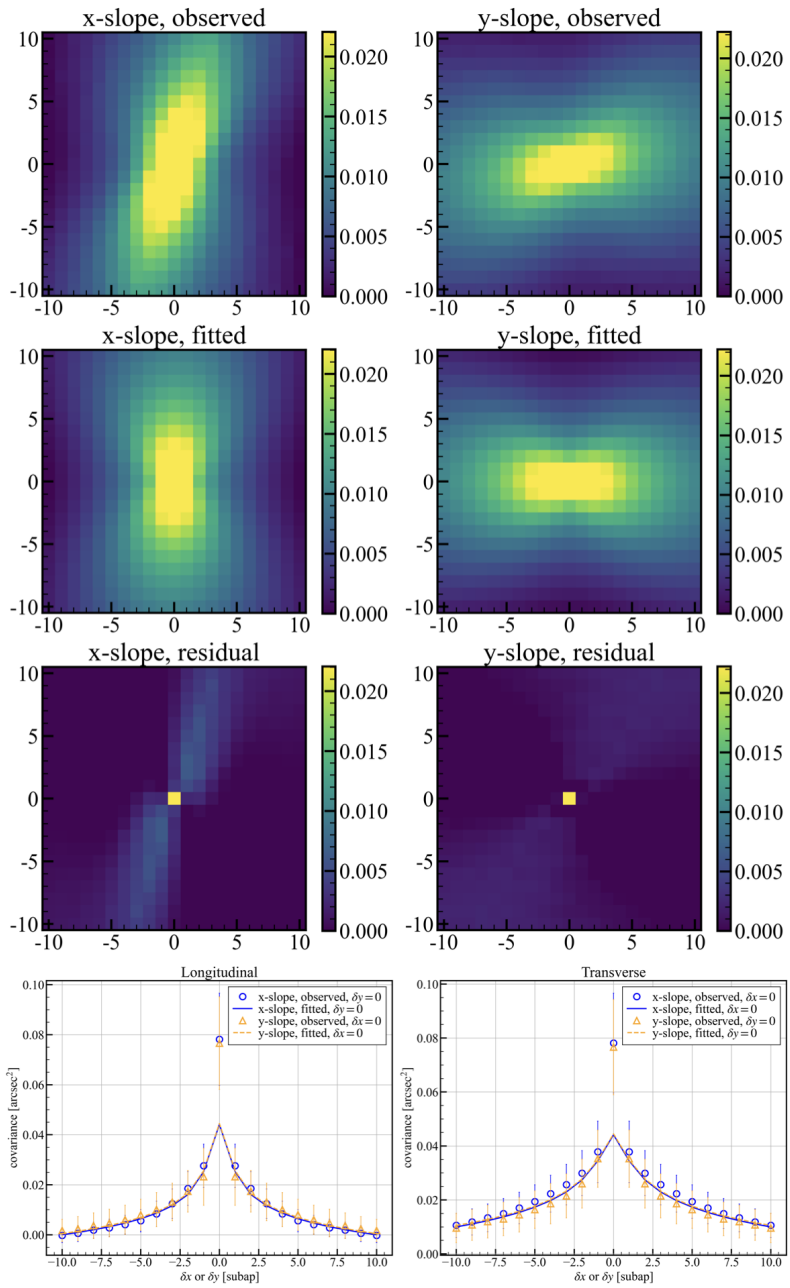

Fig. C.20 Same as figure C.1 but for dataset obtained at 5:13, Mar.14, 2023 by SH-1.

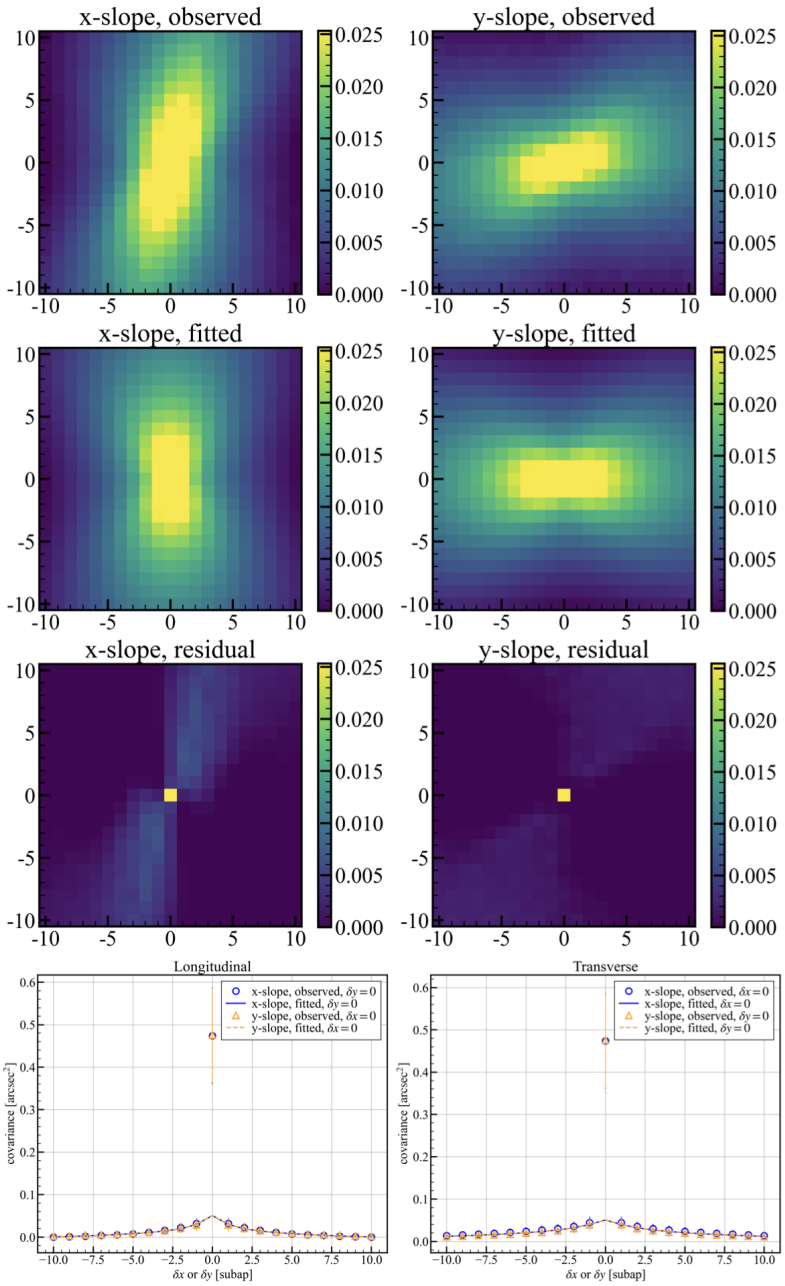

Fig. C.21 Fitting slope auto-covariance map obtained at 5:13, Mar.14, 2023 by SH-2.

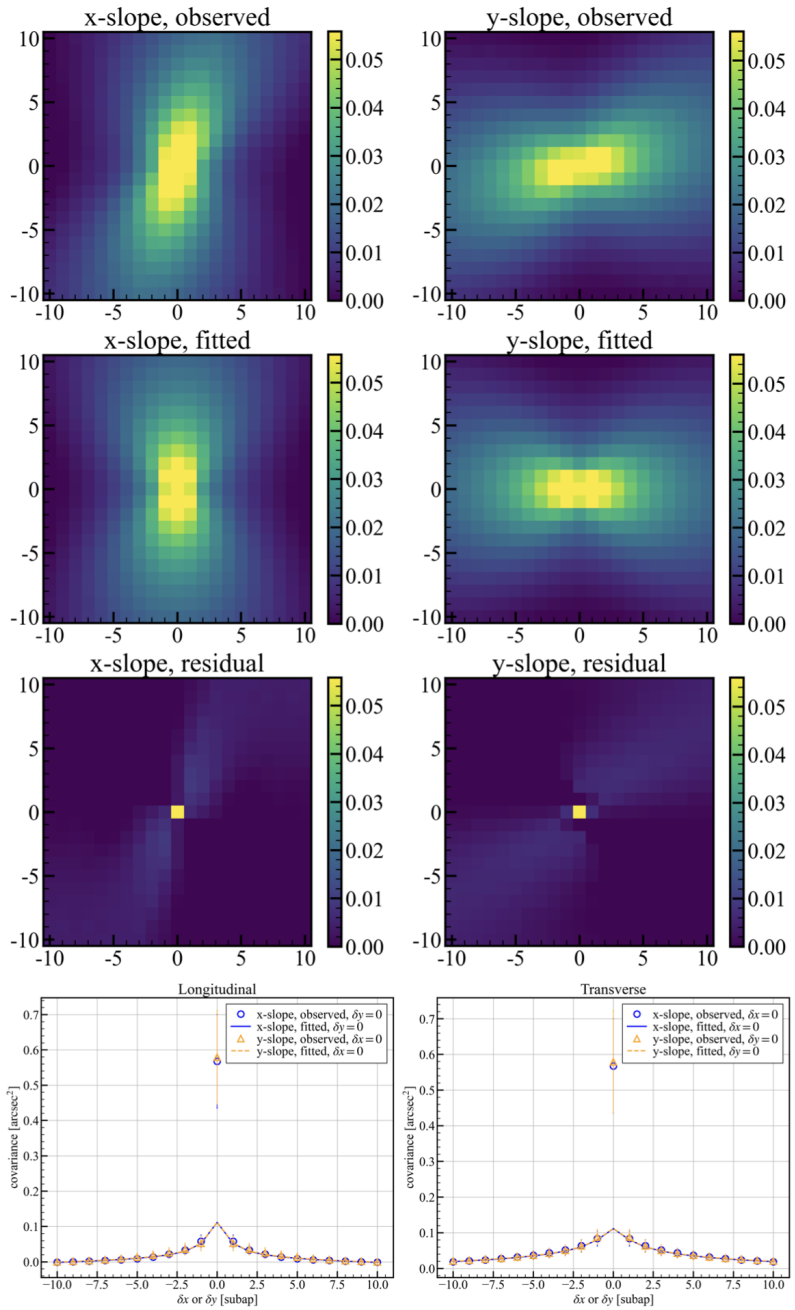

Fig. C.22 Same as figure C.1 but for dataset obtained at 5:16, Mar.14, 2023 by SH-1.

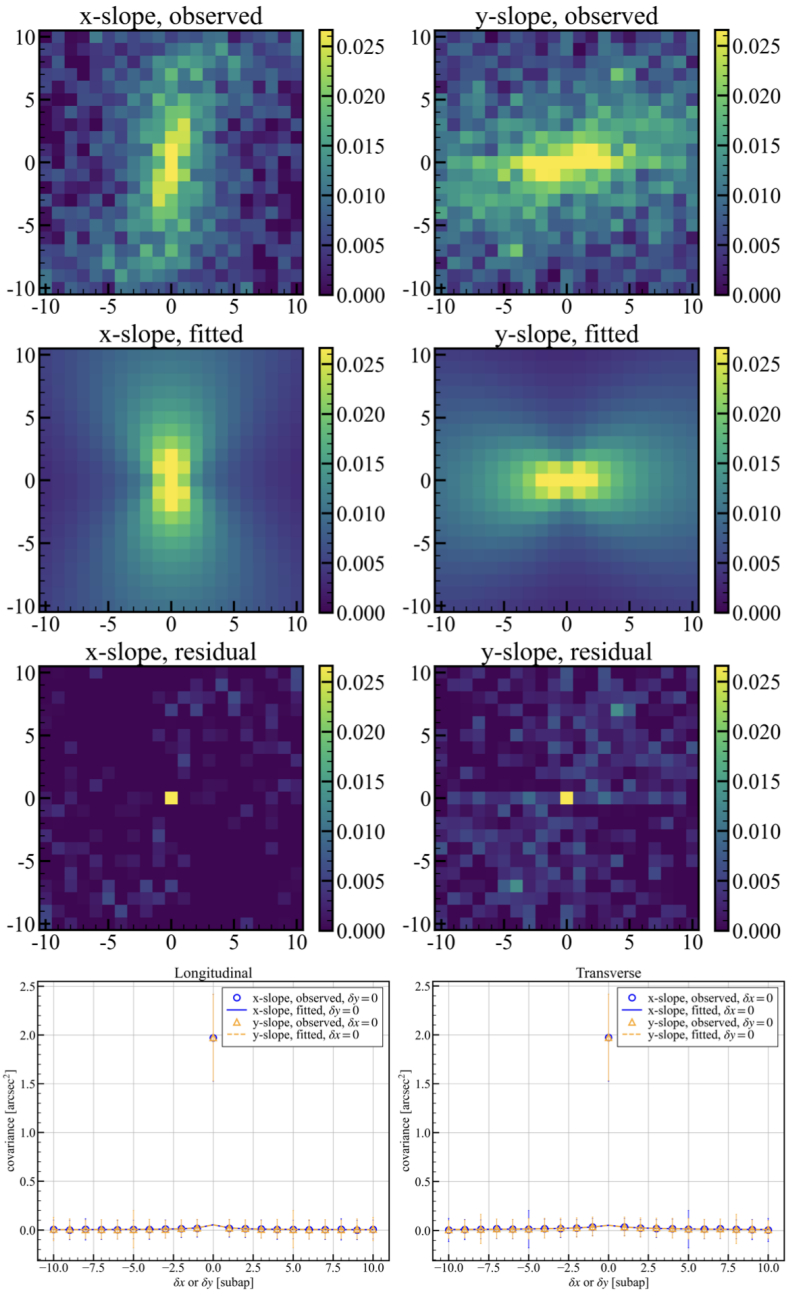

Fig. C.23 Same as figure C.1 but for dataset obtained at 5:16, Mar.14, 2023 by SH-2.

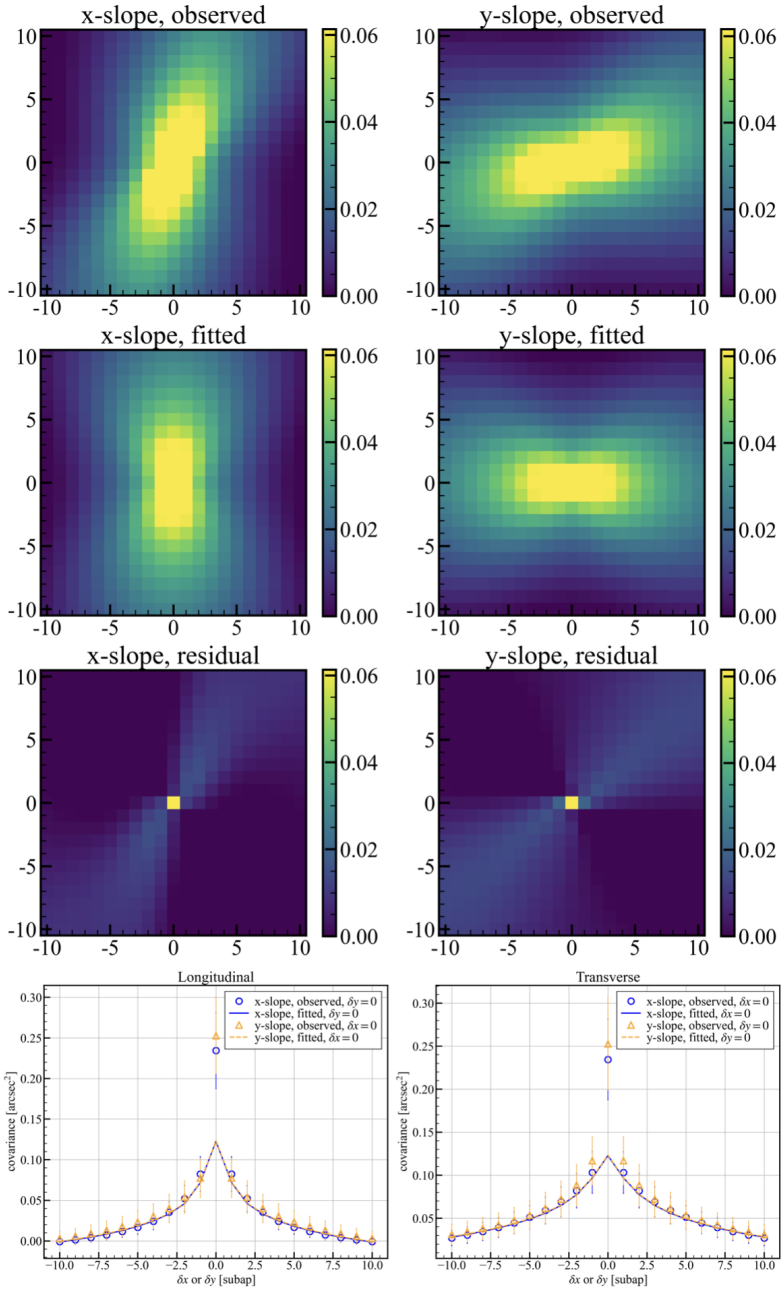

Fig. C.24 Same as figure C.1 but for dataset obtained at 5:20, Mar.14, 2023 by SH-1.

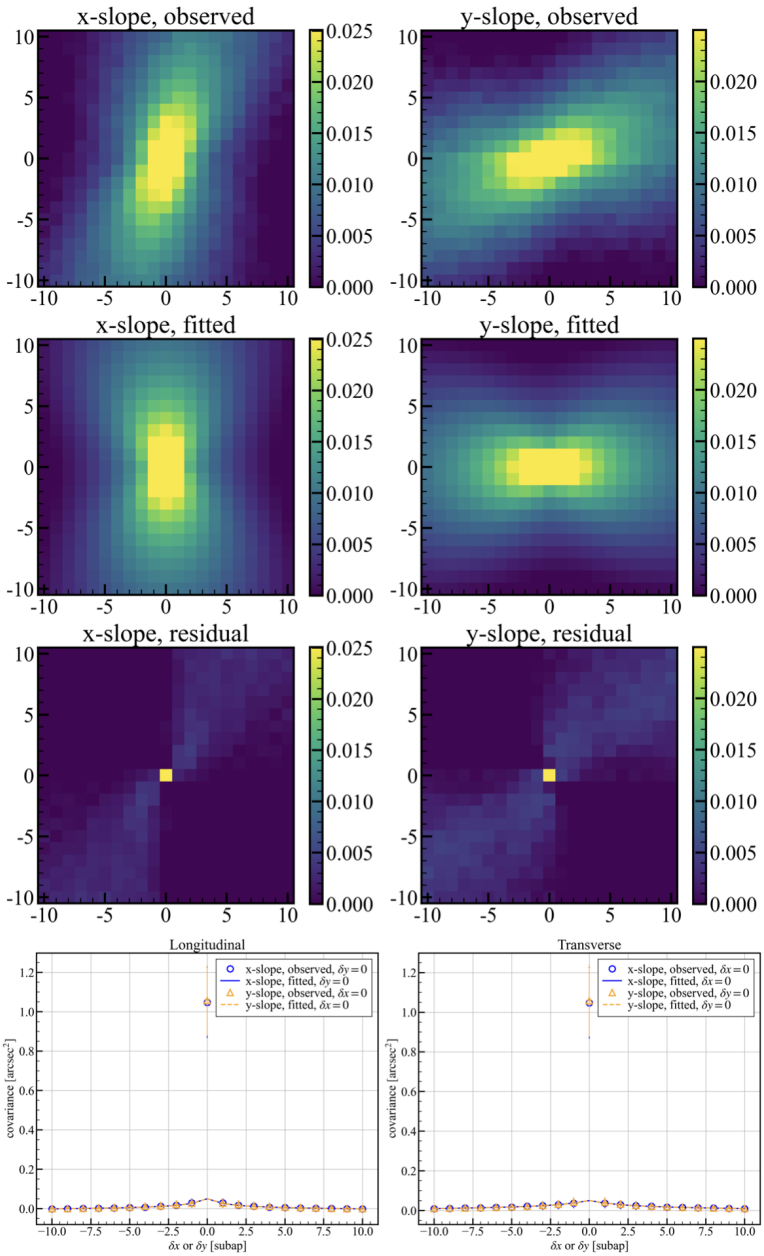

Fig. C.25 Same as figure C.1 but for dataset obtained at 5:20, Mar.14, 2023 by SH-2.

Appendix D

SH-MASS analysis

We show the same figures as 2.16 but for all the datasets.

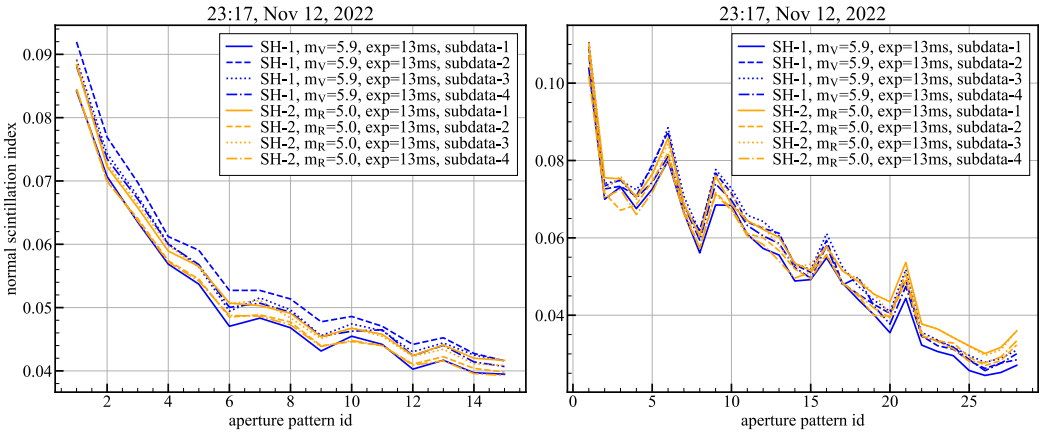

Fig. D.1 Scintillation indices obtained at 23:17, Nov.12, 2022. Left and right panels show normal and differential scintillation indices, respectively.

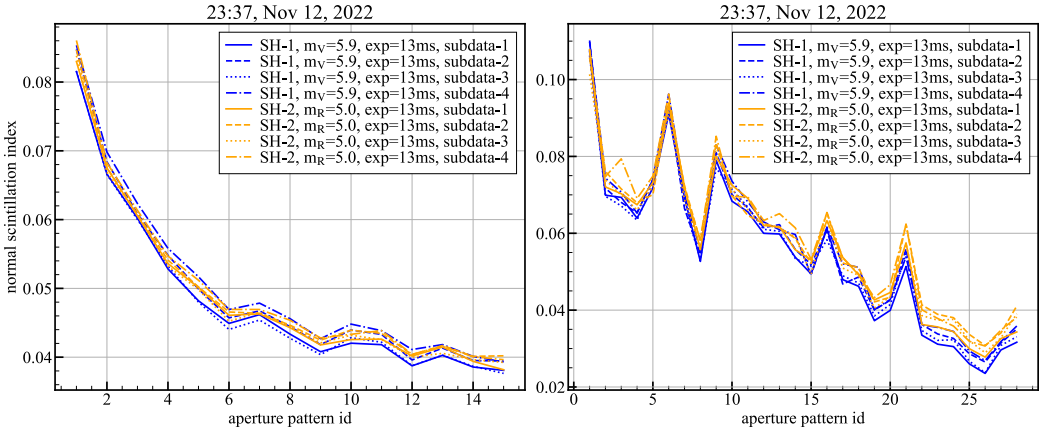

Fig. D.2 Same as figure D.1 but for dataset obtained at 23:37, Nov.12, 2022.

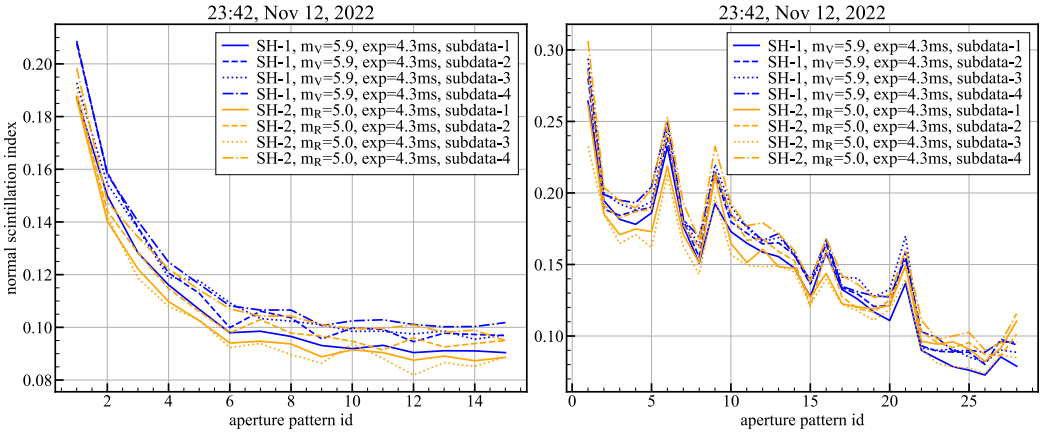

Fig. D.3 Same as figure D.1 but for dataset obtained at 23:42, Nov.12, 2022.

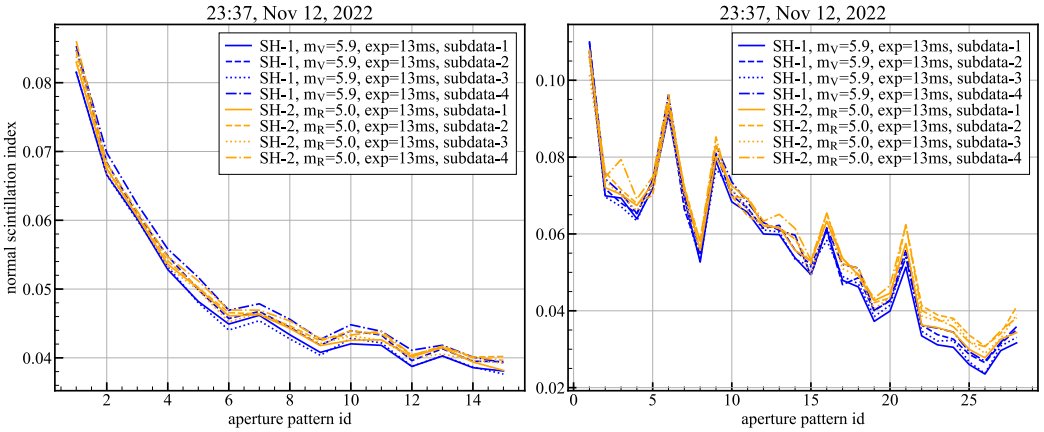

Fig. D.4 Same as figure D.1 but for dataset obtained at 23:45, Nov.12, 2022.

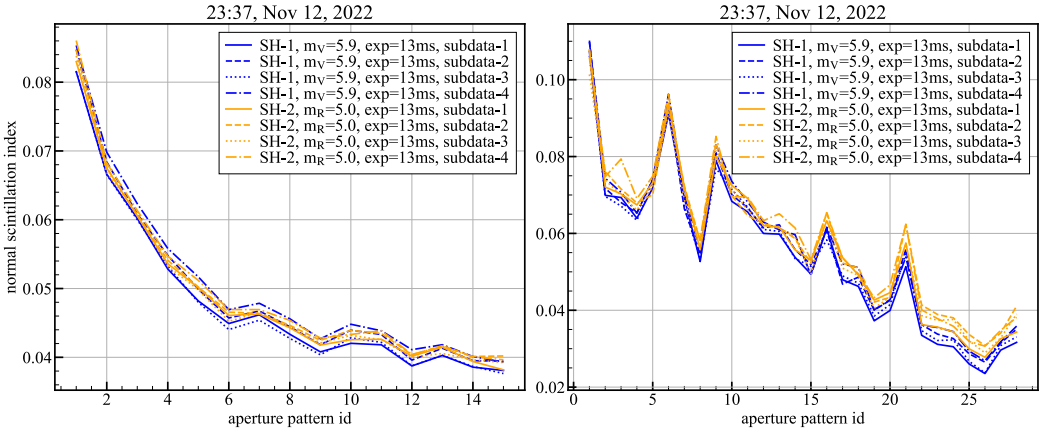

Fig. D.5 Same as figure D.1 but for dataset obtained at 23:49, Nov.12, 2022.

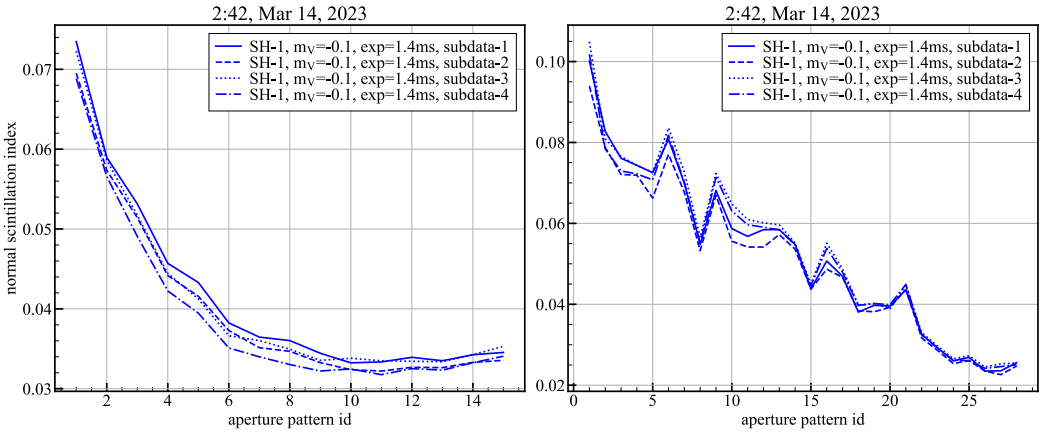

Fig. D.6 Same as figure D.1 but for dataset obtained at 2:42, Mar.14, 2023.

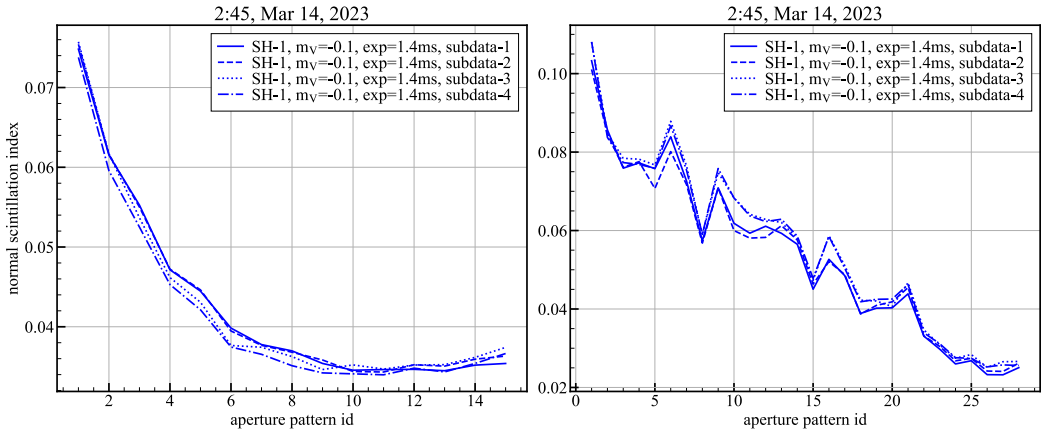

Fig. D.7 Same as figure D.1 but for dataset obtained at 2:45, Mar.14, 2023.

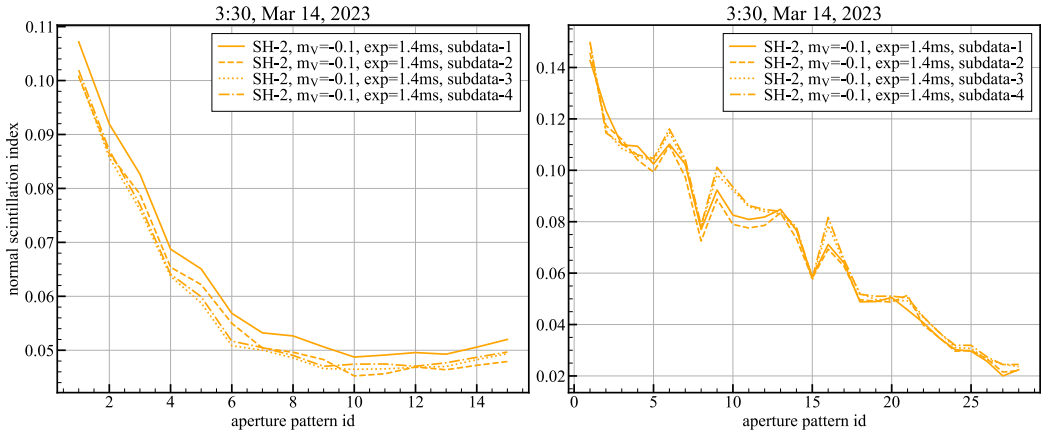

Fig. D.8 Same as figure D.1 but for dataset obtained at 3:30, Mar.14, 2023.

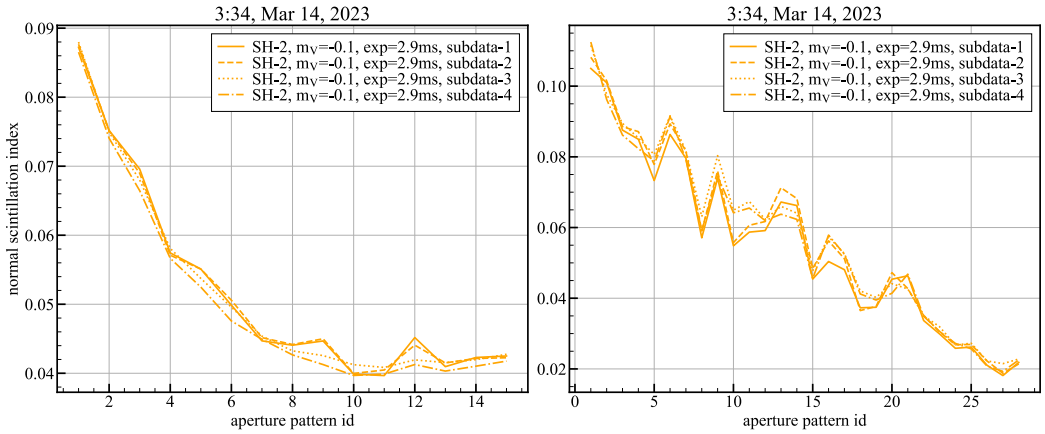

Fig. D.9 Same as figure D.1 but for dataset obtained at 3:34, Mar.14, 2023.

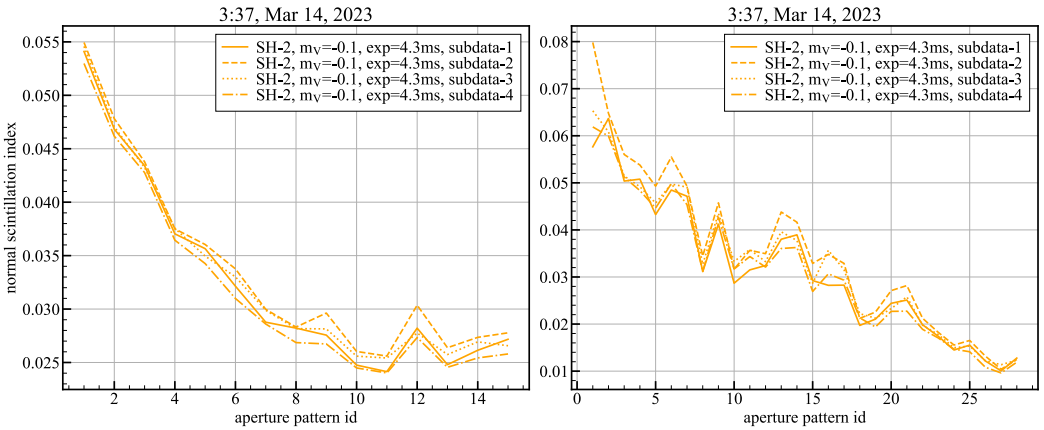

Fig. D.10 Same as figure D.1 but for dataset obtained at 3:37, Mar.14, 2023.

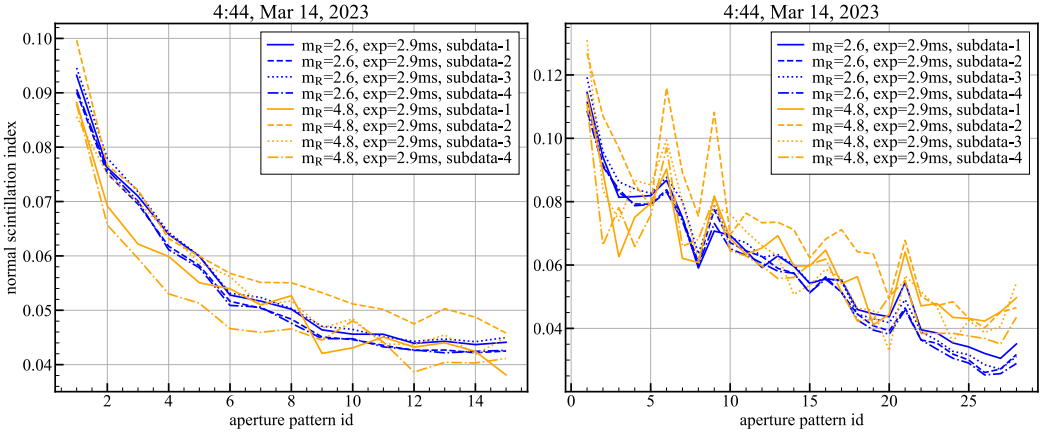

Fig. D.11 Same as figure D.1 but for dataset obtained at 4:44, Mar.14, 2023.

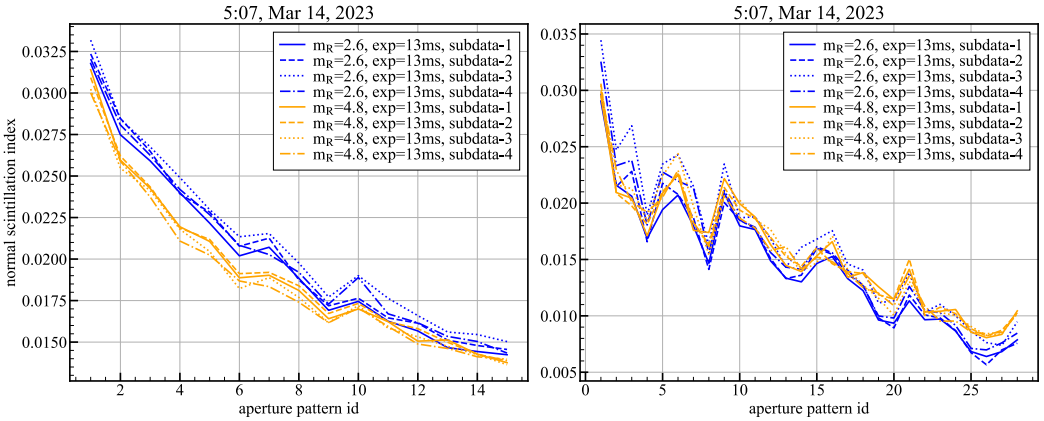

Fig. D.12 Same as figure D.1 but for dataset obtained at 5:07, Mar.14, 2023.

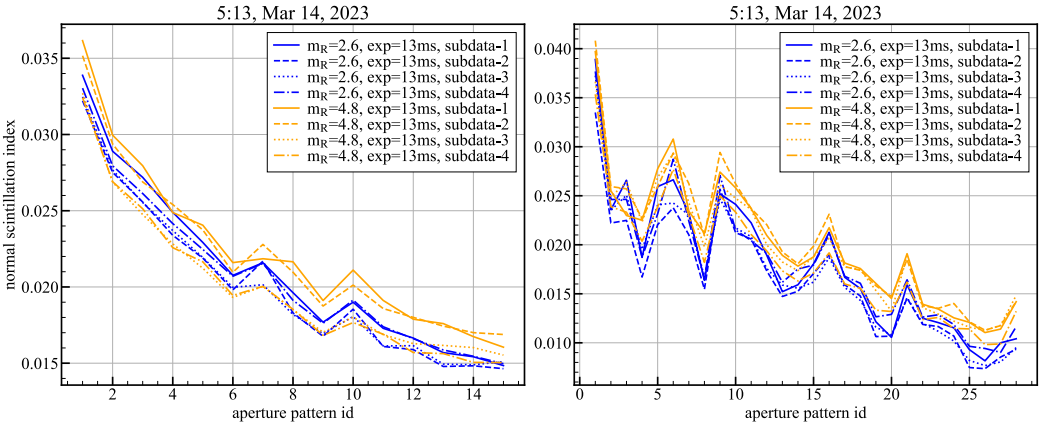

Fig. D.13 Same as figure D.1 but for dataset obtained at 5:13, Mar.14, 2023.

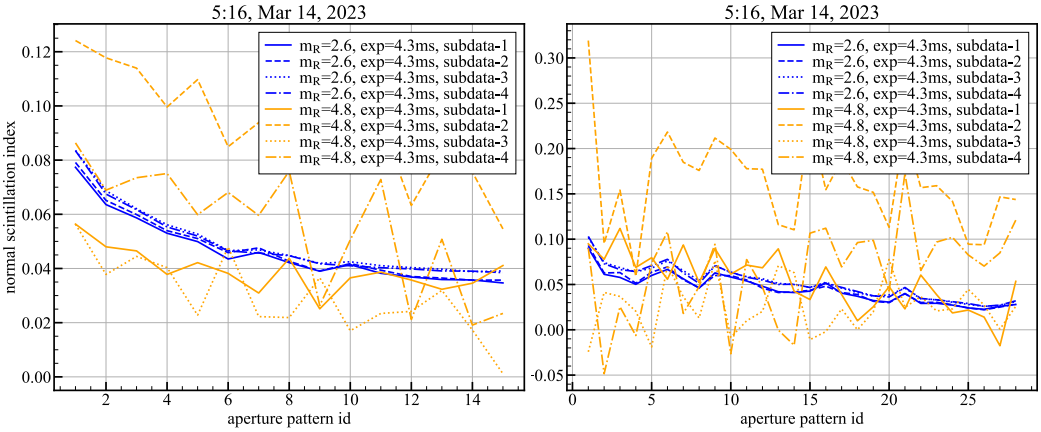

Fig. D.14 Same as figure D.1 but for dataset obtained at 5:16, Mar.14, 2023.

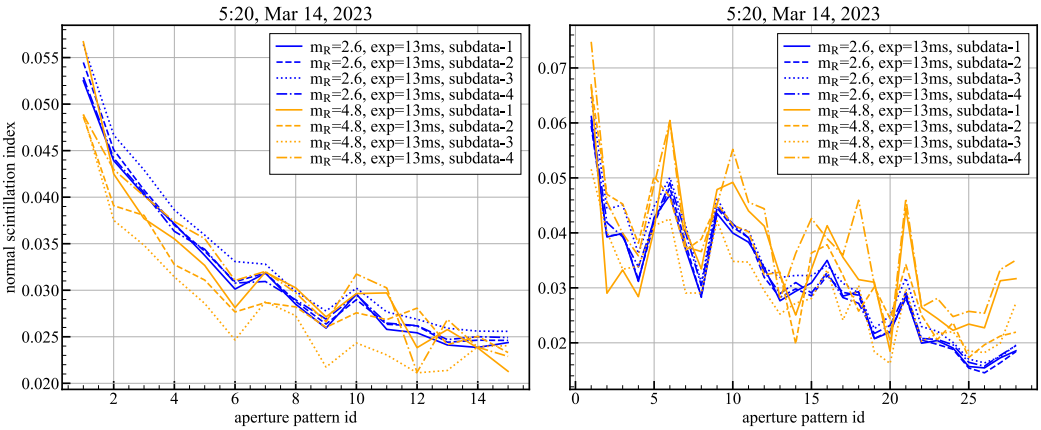

Fig. D.15 Same as figure D.1 but for dataset obtained at 5:20, Mar.14, 2023.

Appendix E

Scintillation auto-covariance analysis

We show the same figures as figure 2.18 but for all the datasets.

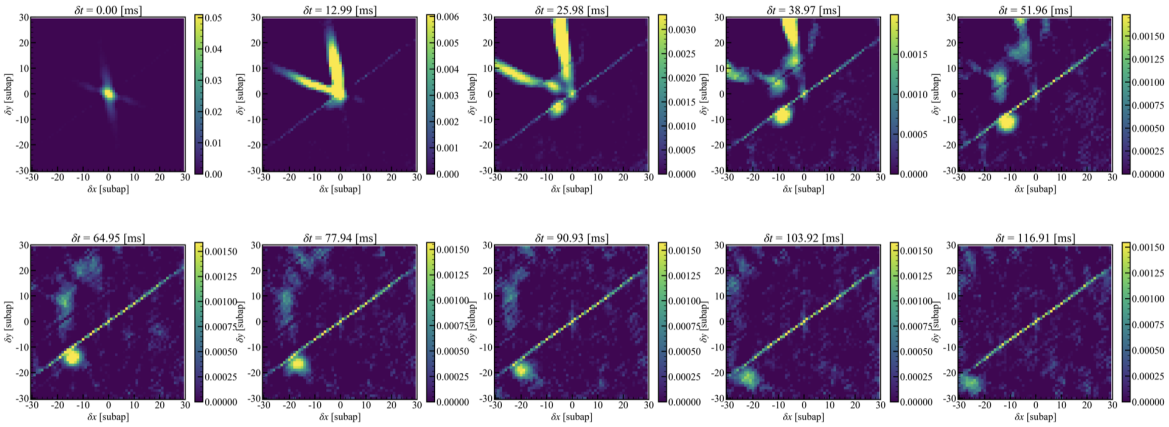

Fig. E.1 Scintillation auto-covariance map for dataset taken by SH-1 at 23:17, Nov.12, 2022. From top-left to bottom-right, an auto-covariance map calculated with a time lag of 0-9 frames is arranged.

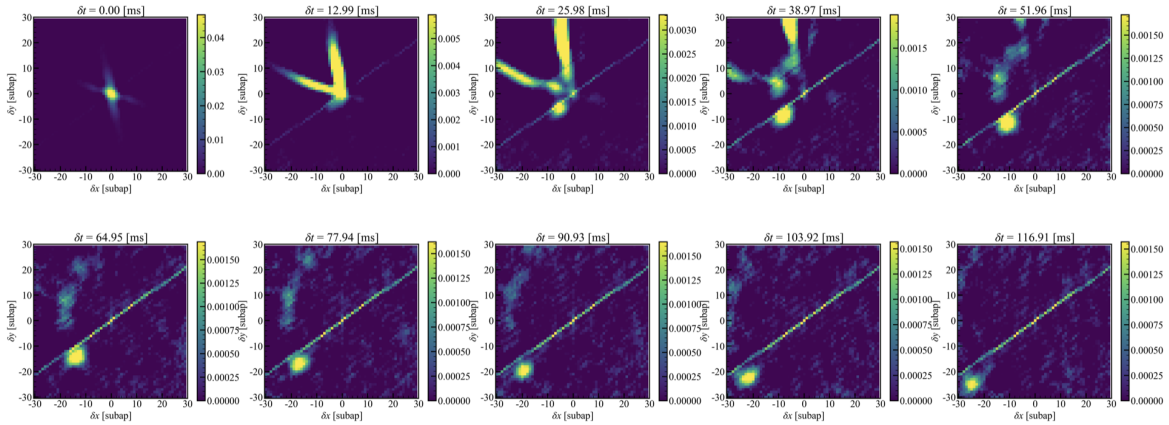

Fig. E.2 Same as figure E.1 but for dataset taken by SH-2 at 23:17, Nov.12, 2022.

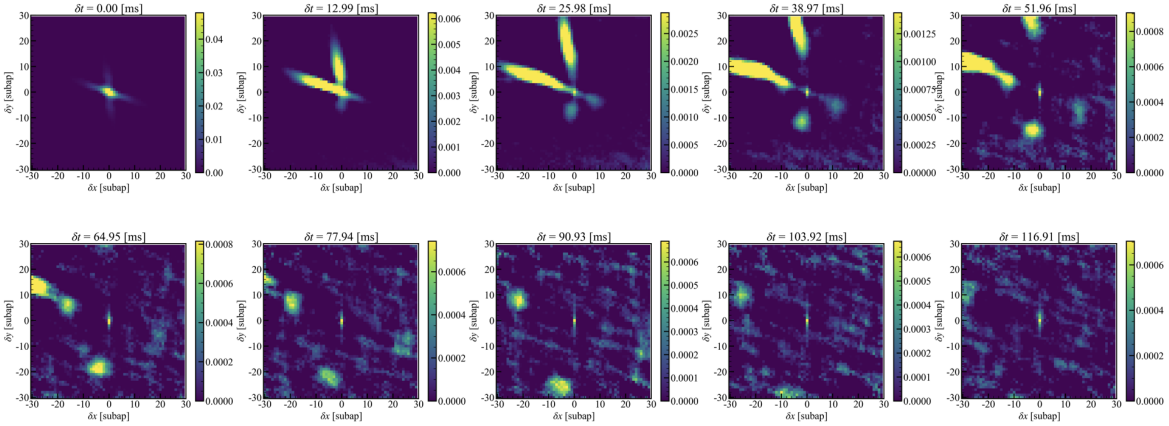

Fig. E.3 Same as figure E.1 but for dataset taken by SH-1 at 23:37, Nov.12, 2022.

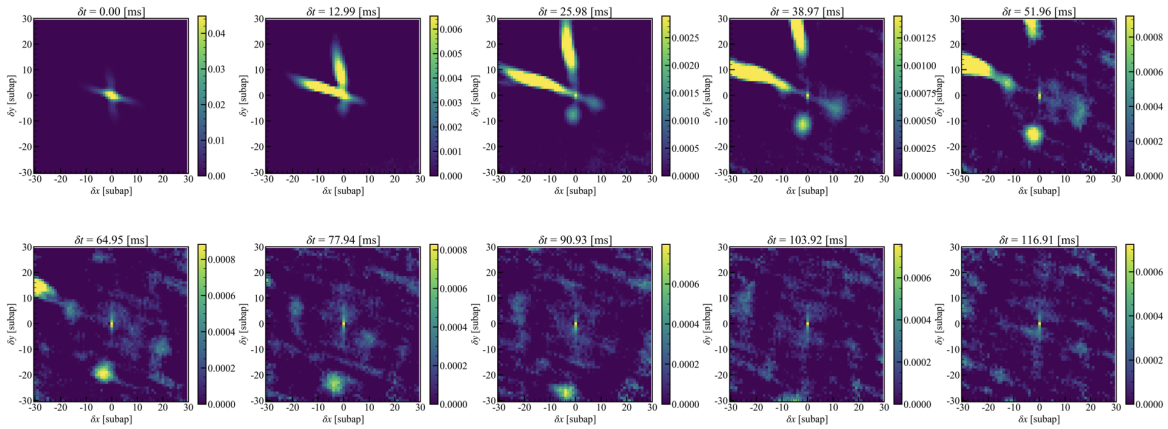

Fig. E.4 Same as figure E.1 but for dataset taken by SH-2 at 23:37, Nov.12, 2022.

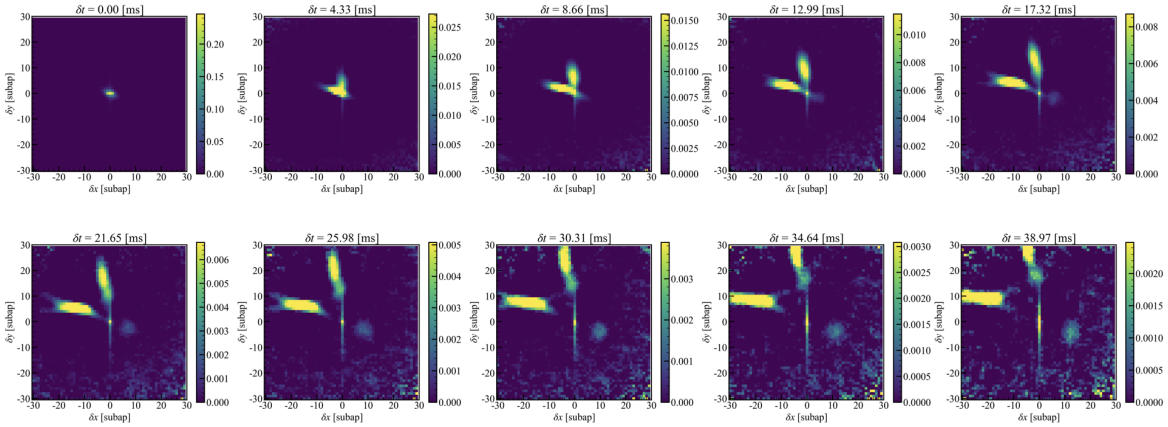

Fig. E.5 Same as figure E.1 but for dataset taken by SH-1 at 23:42, Nov.12, 2022.

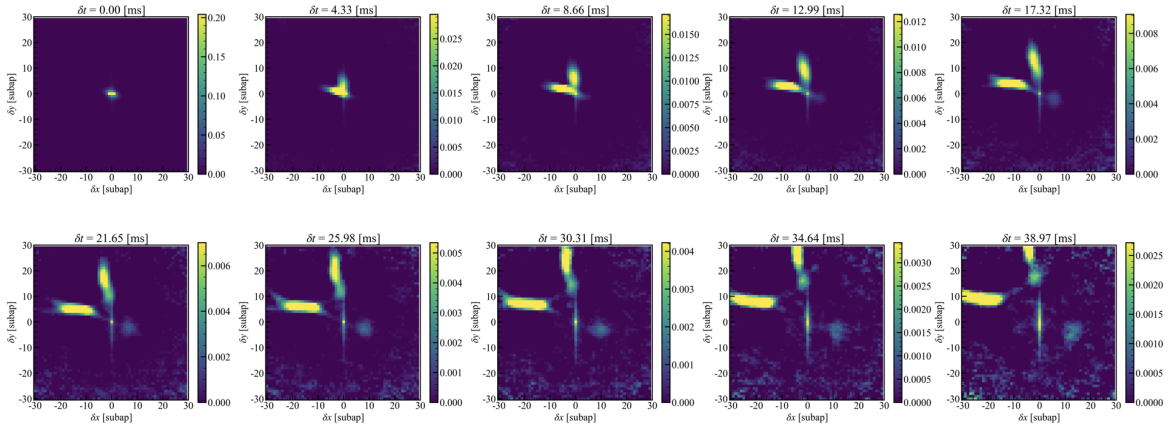

Fig. E.6 Same as figure E.1 but for dataset taken by SH-2 at 23:42, Nov.12, 2022.

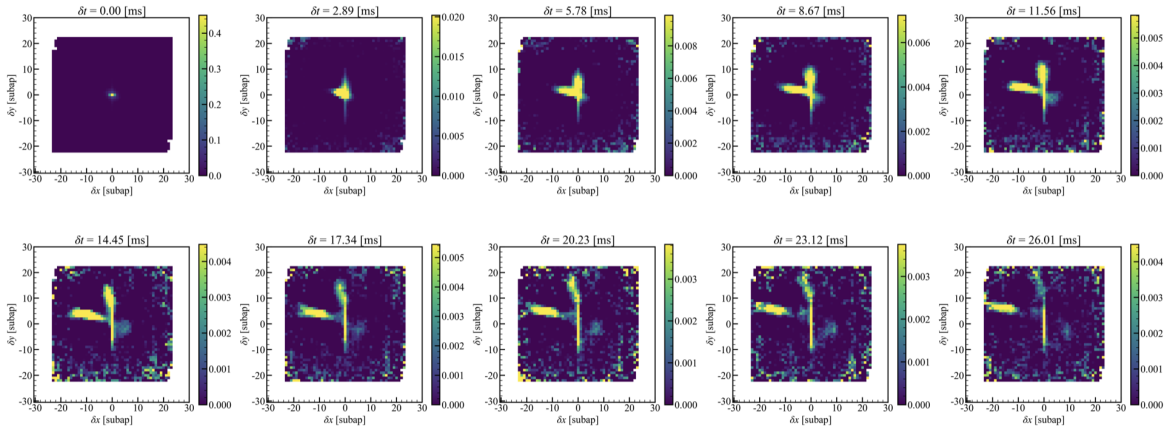

Fig. E.7 Same as figure E.1 but for dataset taken by SH-1 at 23:45, Nov.12, 2022.

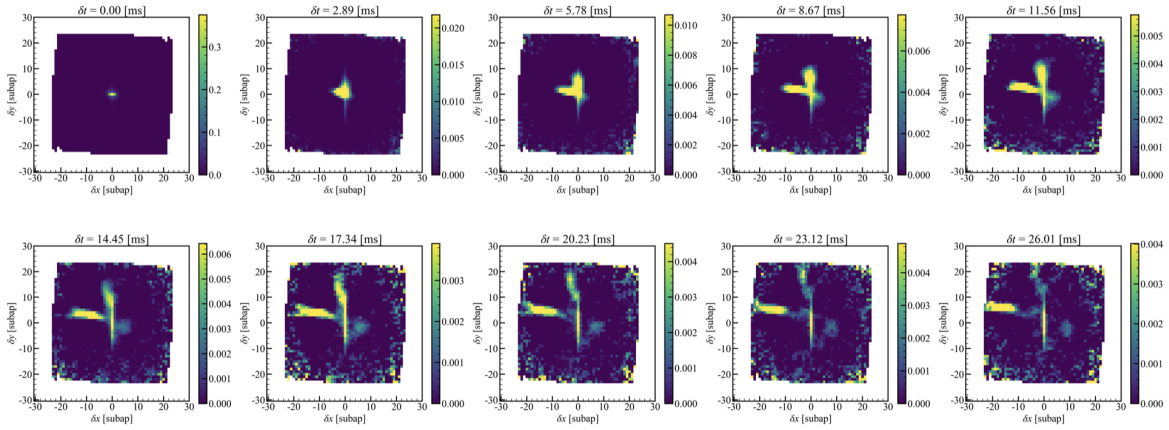

Fig. E.8 Same as figure E.1 but for dataset taken by SH-2 at 23:45, Nov.12, 2022.

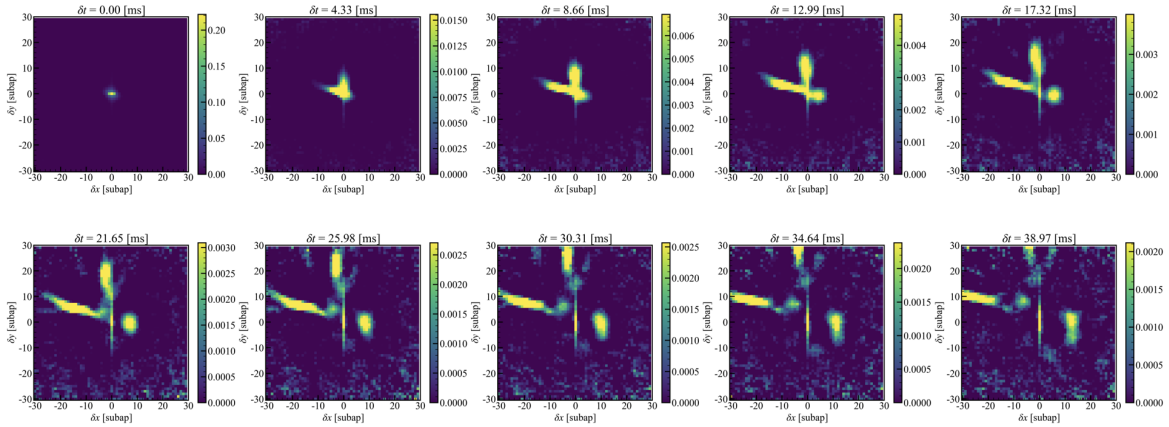

Fig. E.9 Same as figure E.1 but for dataset taken by SH-1 at 23:49, Nov.12, 2022.

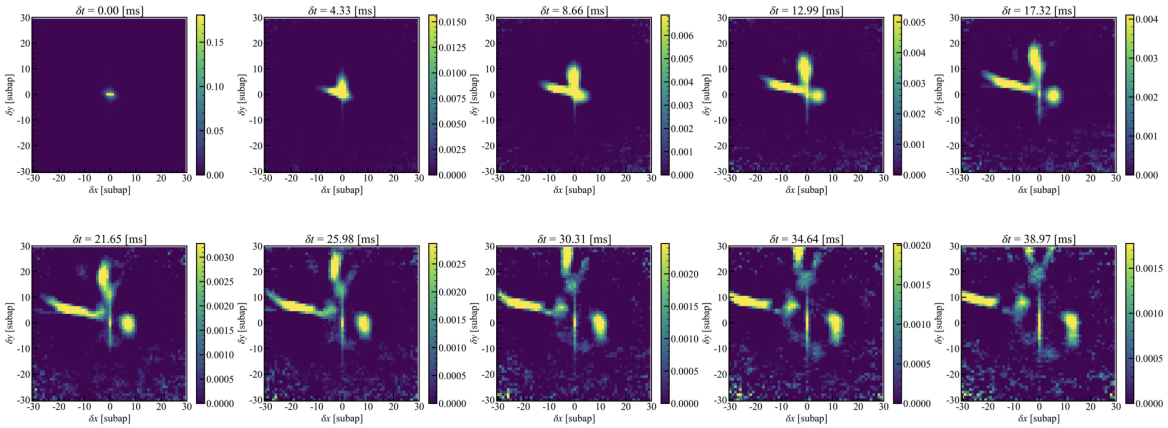

Fig. E.10 Same as figure E.1 but for dataset taken by SH-2 at 23:49, Nov.12, 2022.

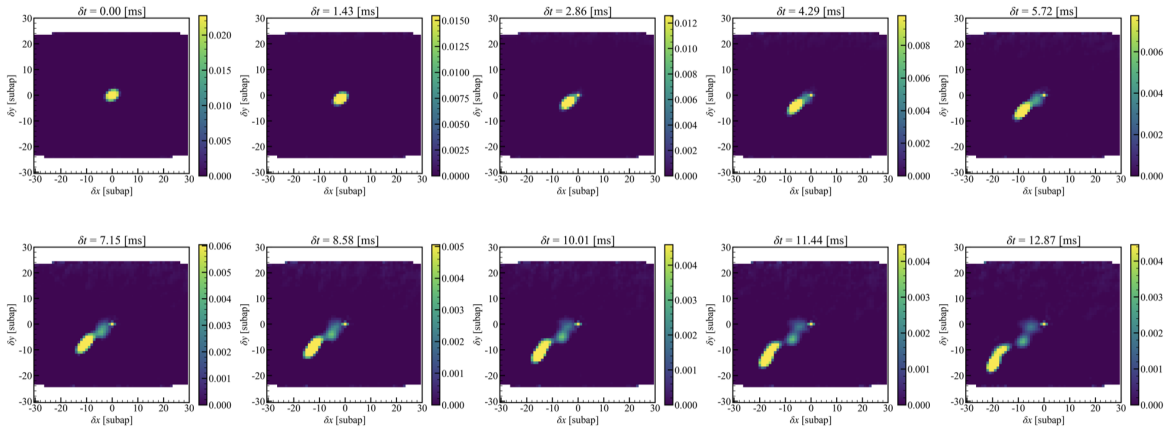

Fig. E.11 Same as figure E.1 but for dataset taken by SH-1 at 2:42, Mar.14, 2023.

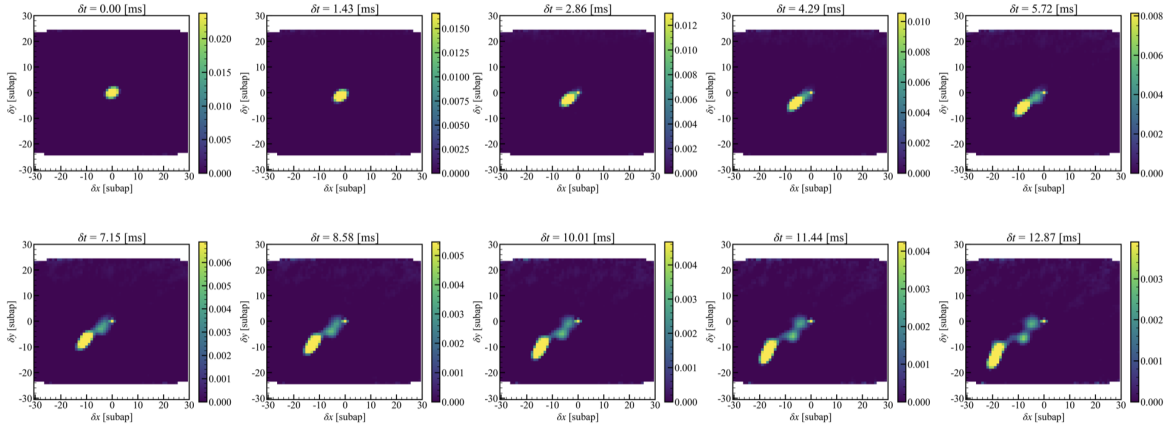

Fig. E.12 Same as figure E.1 but for dataset taken by SH-1 at 2:45, Mar.14, 2023.

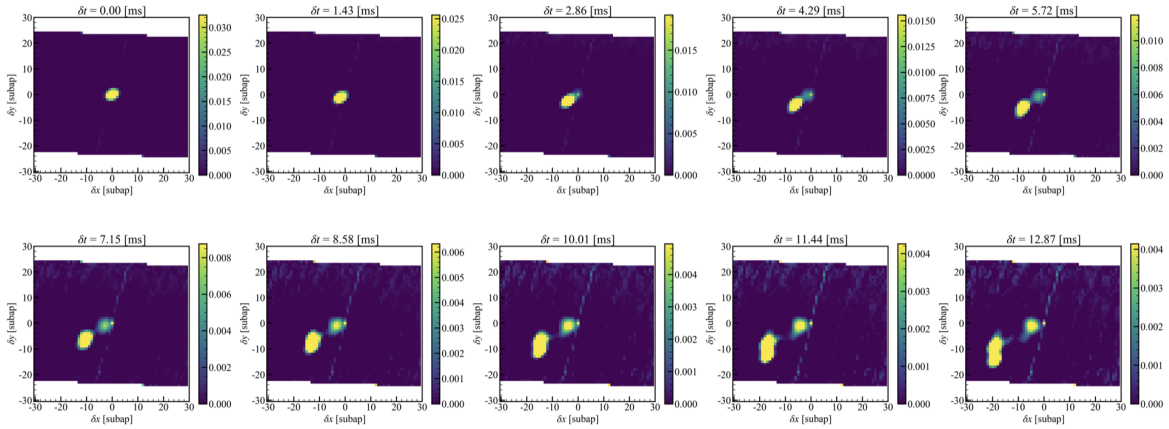

Fig. E.13 Same as figure E.1 but for dataset taken by SH-2 at 3:30, Mar.14, 2023.

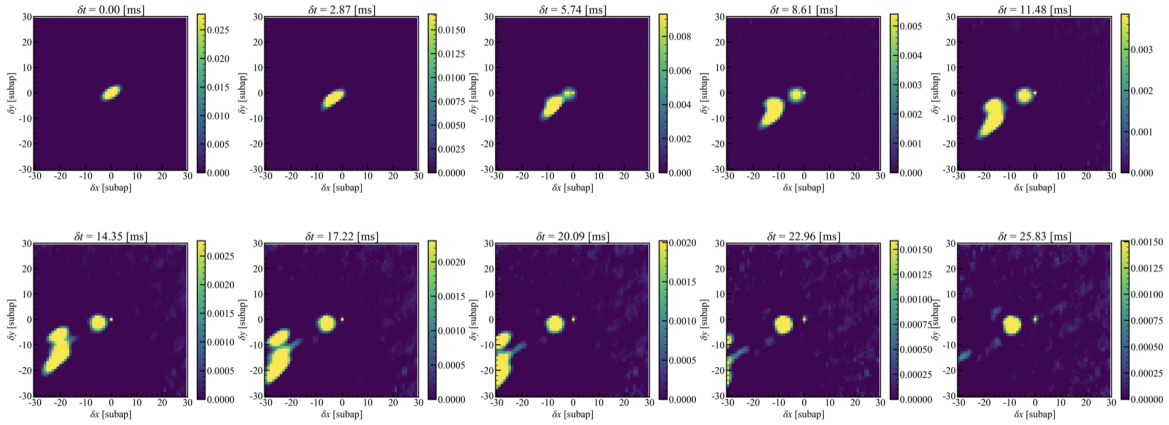

Fig. E.14 Same as figure E.1 but for dataset taken by SH-2 at 3:34, Mar.14, 2023.

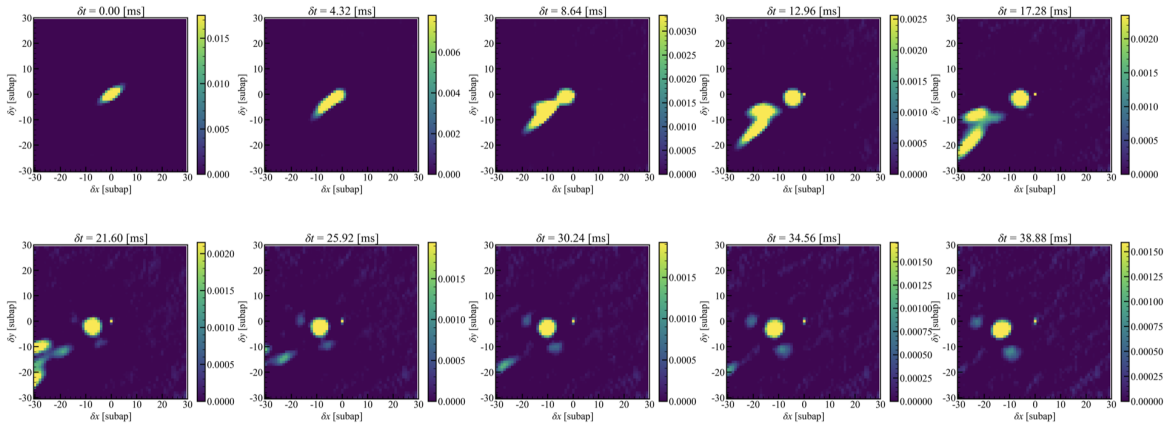

Fig. E.15 Same as figure E.1 but for dataset taken by SH-2 at 3:37, Mar.14, 2023.

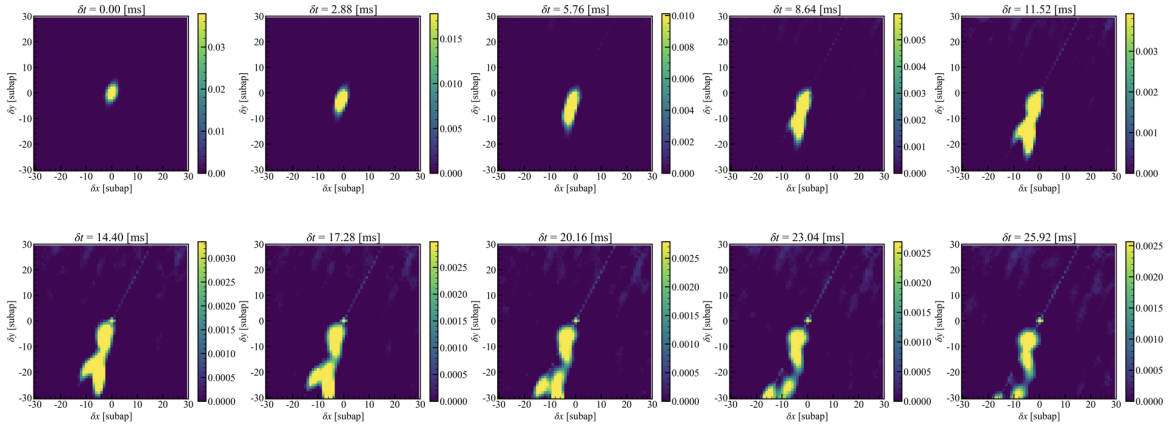

Fig. E.16 Same as figure E.1 but for dataset taken by SH-1 at 4:44, Mar.14, 2023.

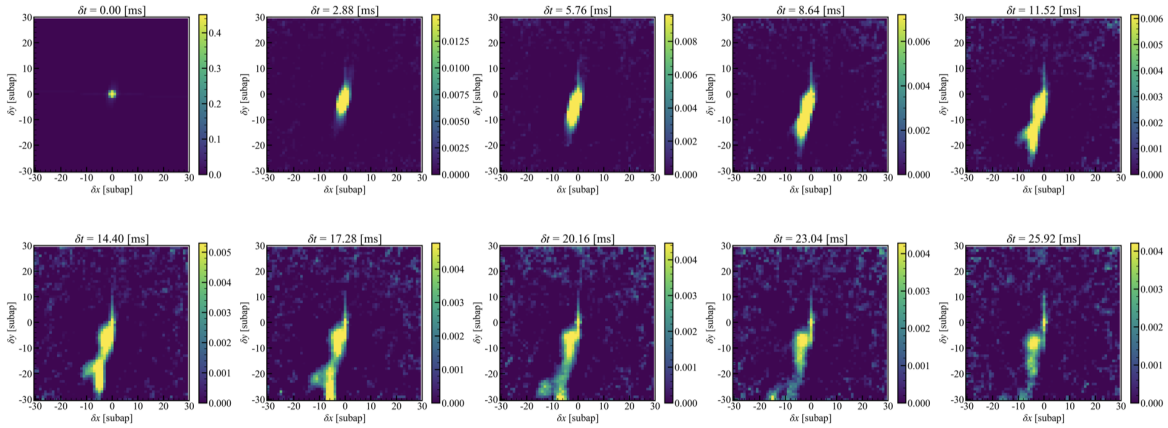

Fig. E.17 Same as figure E.1 but for dataset taken by SH-2 at 4:44, Mar.14, 2023.

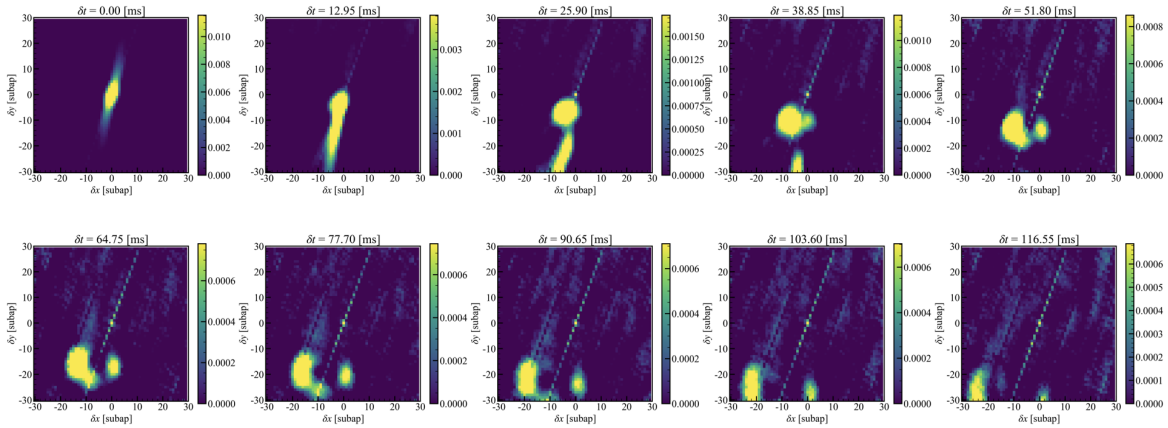

Fig. E.18 Same as figure E.1 but for dataset taken by SH-1 at 5:07, Mar.14, 2023.

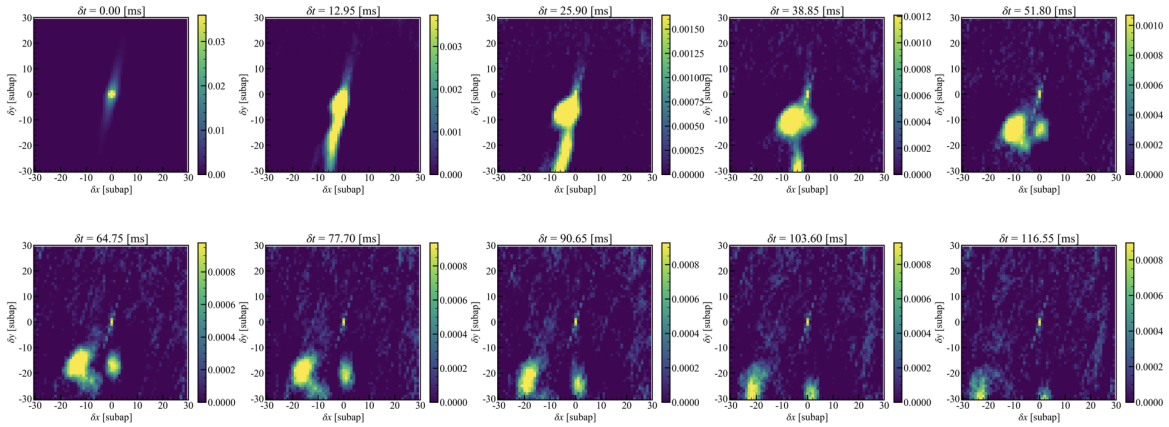

Fig. E.19 Same as figure E.1 but for dataset taken by SH-2 at 5:07, Mar.14, 2023.

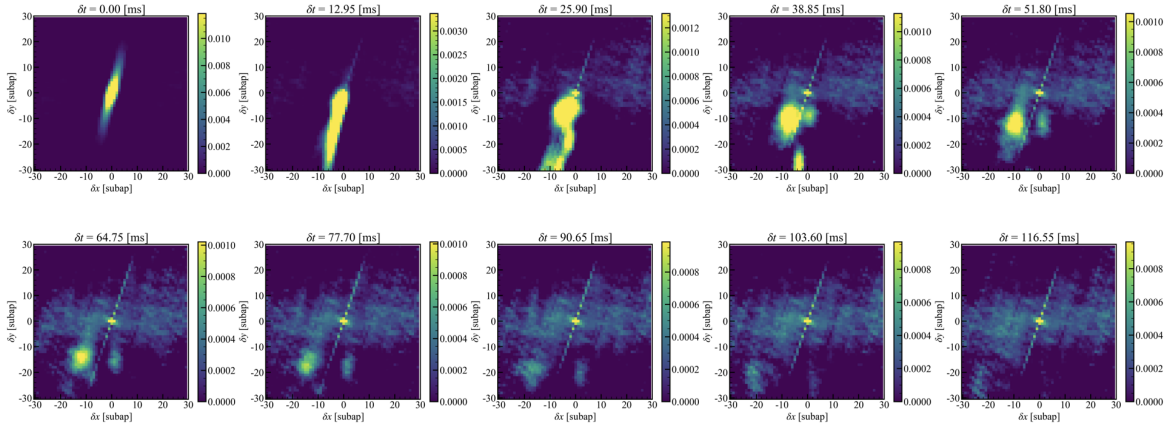

Fig. E.20 Same as figure E.1 but for dataset taken by SH-1 at 5:13, Mar.14, 2023.

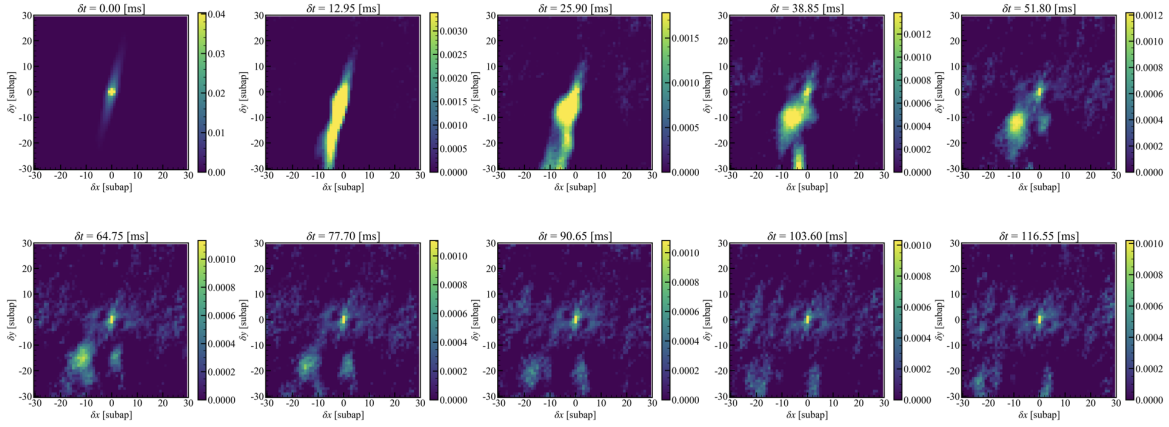

Fig. E.21 Same as figure E.1 but for dataset taken by SH-2 at 5:13, Mar.14, 2023.

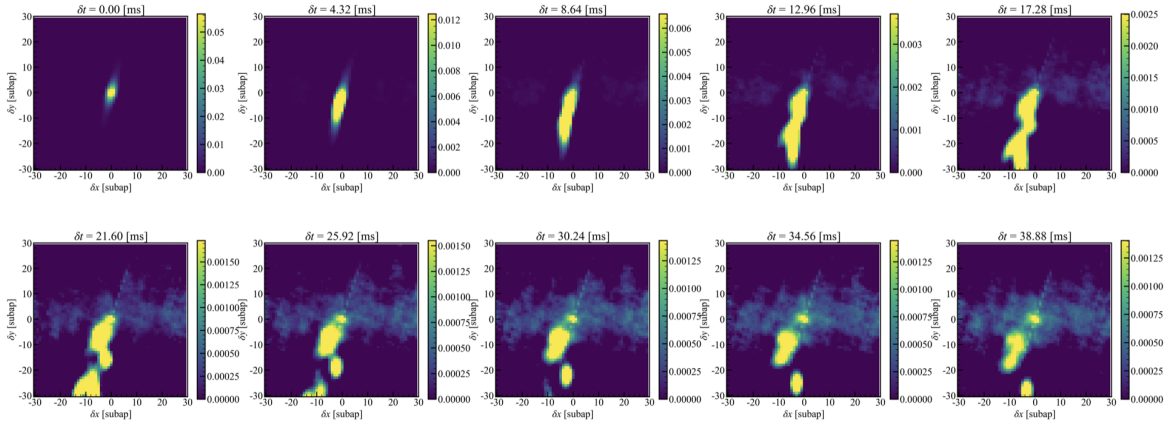

Fig. E.22 Same as figure E.1 but for dataset taken by SH-1 at 5:16, Mar.14, 2023.

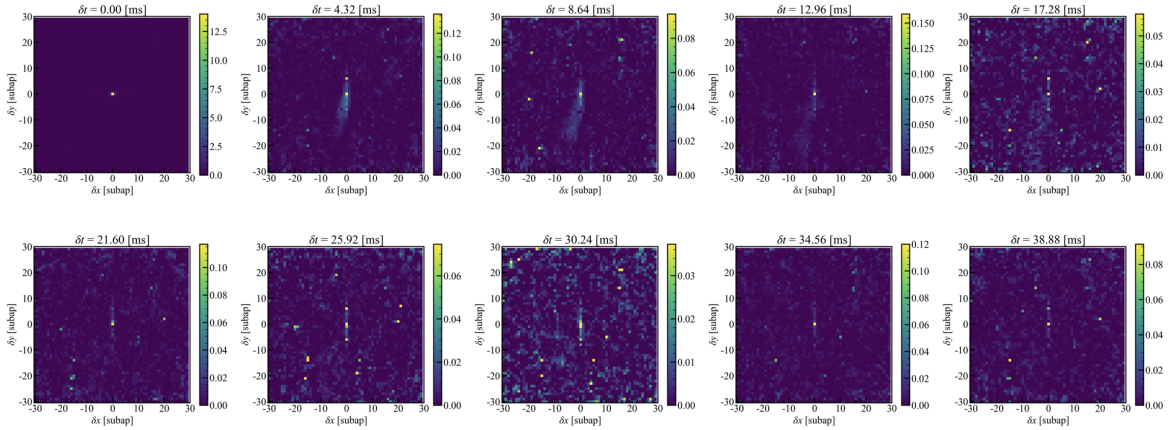

Fig. E.23 Same as figure E.1 but for dataset taken by SH-2 at 5:16, Mar.14, 2023.

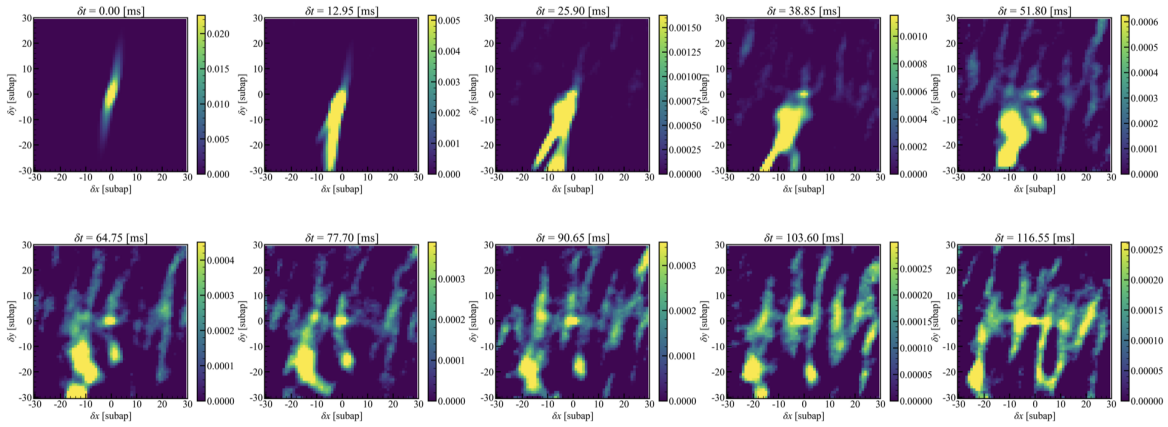

Fig. E.24 Same as figure E.1 but for dataset taken by SH-1 at 5:20, Mar.14, 2023.

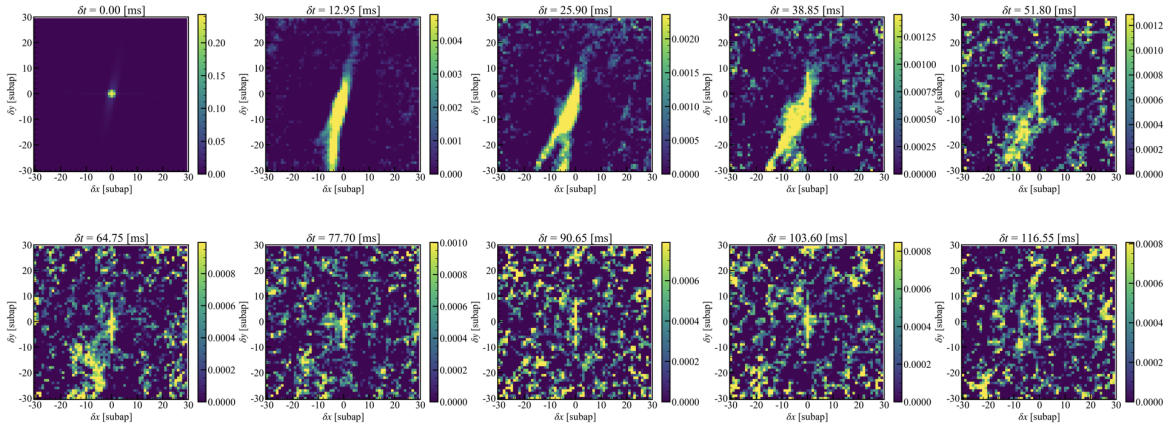

Fig. E.25 Same as figure E.1 but for dataset taken by SH-2 at 5:20, Mar.14, 2023.

Appendix F

SLODAR analysis

We show the same figures as figure 2.23 but for all the datasets.

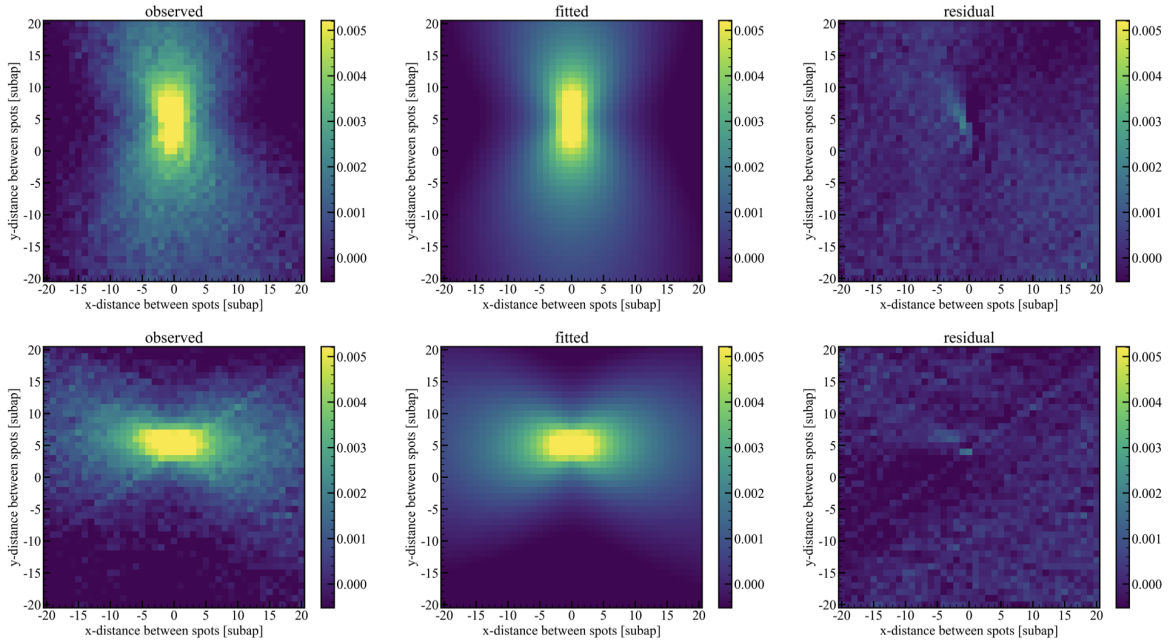

Fig. F.1 Top-left: Observed X-slope cross-covariance map for dataset taken at 23:17, Nov.12, 2022. bottom-left: Observed Y-slope cross-covariance map. Top-center: Model X-slope cross-covariance map after fitting. bottom-center: Model Y-slope cross-covariance map. Top-right: Residual of the observed and model X-slope cross-covariance map. bottom-right: Residual of the observed and model Y-slope cross-covariance map.

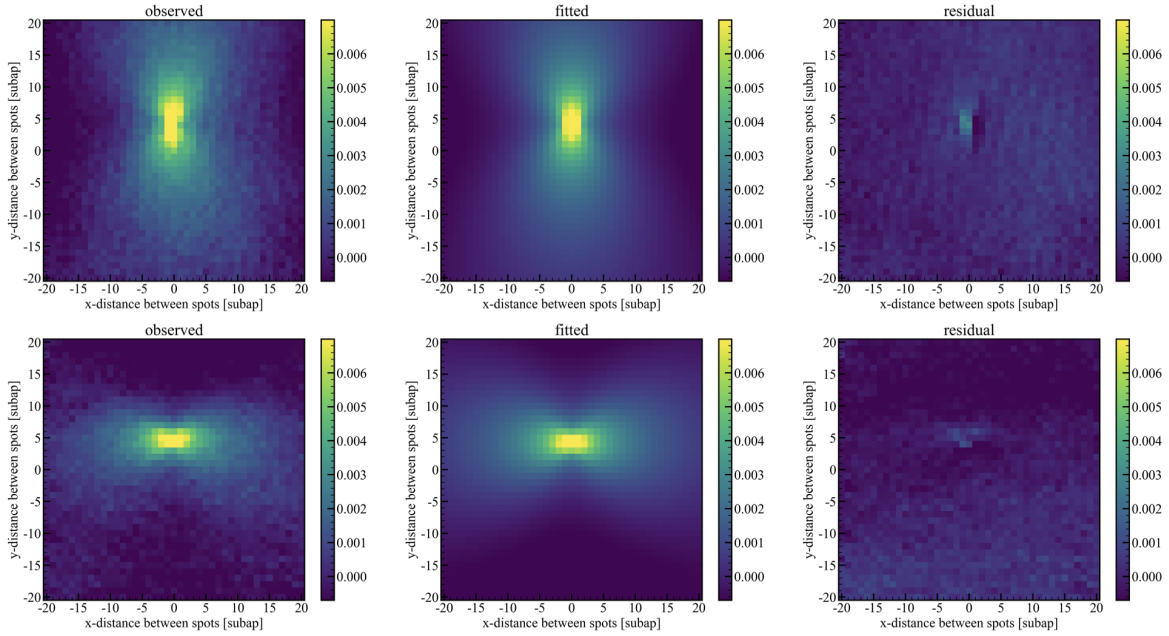

Fig. F.2 Same as figure F.1 but for dataset taken at 23:37, Nov.12, 2022.

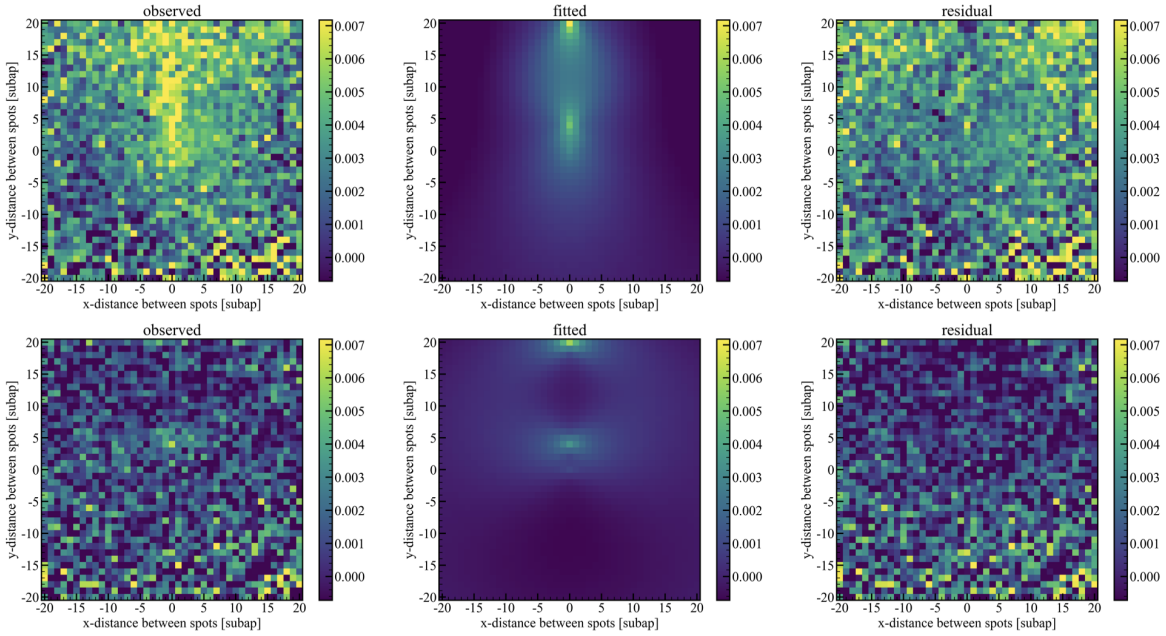

Fig. F.3 Same as figure F.1 but for dataset taken at 23:42, Nov.12, 2022.

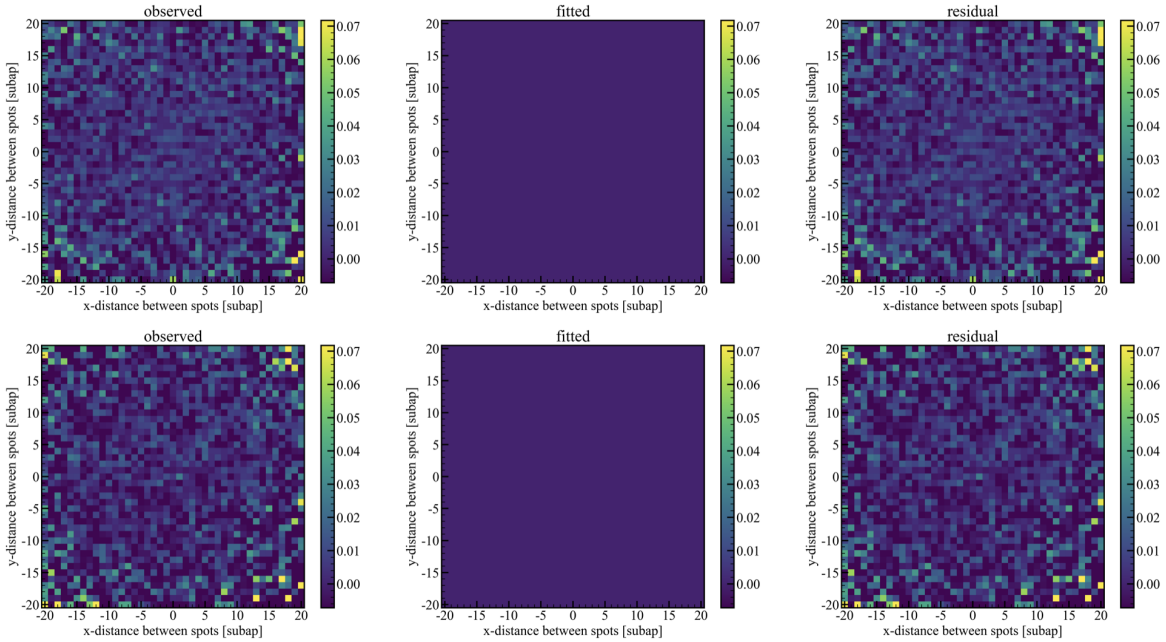

Fig. F.4 Same as figure F.1 but for dataset taken at 23:45, Nov.12, 2022.

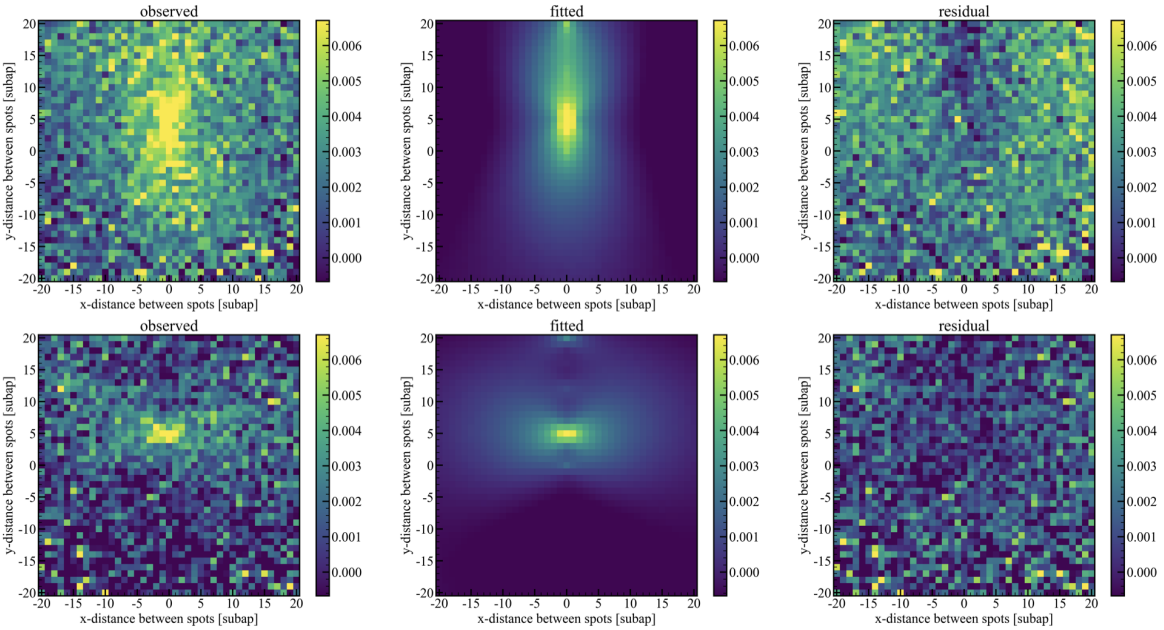

Fig. F.5 Same as figure F.1 but for dataset taken at 23:49, Nov.12, 2022.

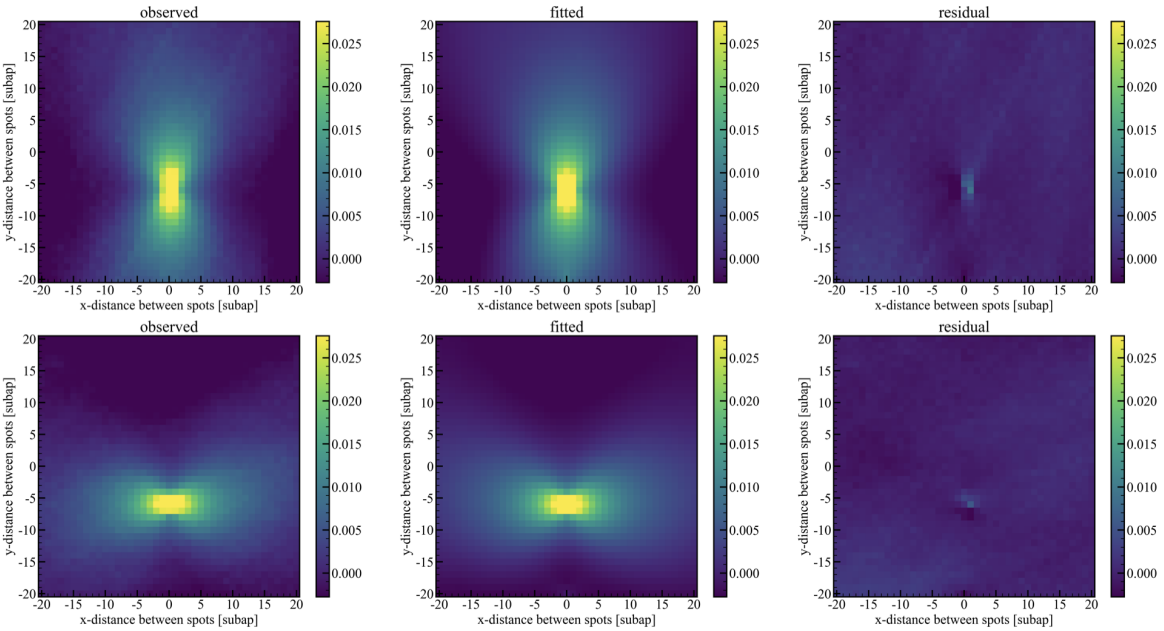

Fig. F.6 Same as figure F.1 but for dataset taken at 4:44, Mar.14, 2023.

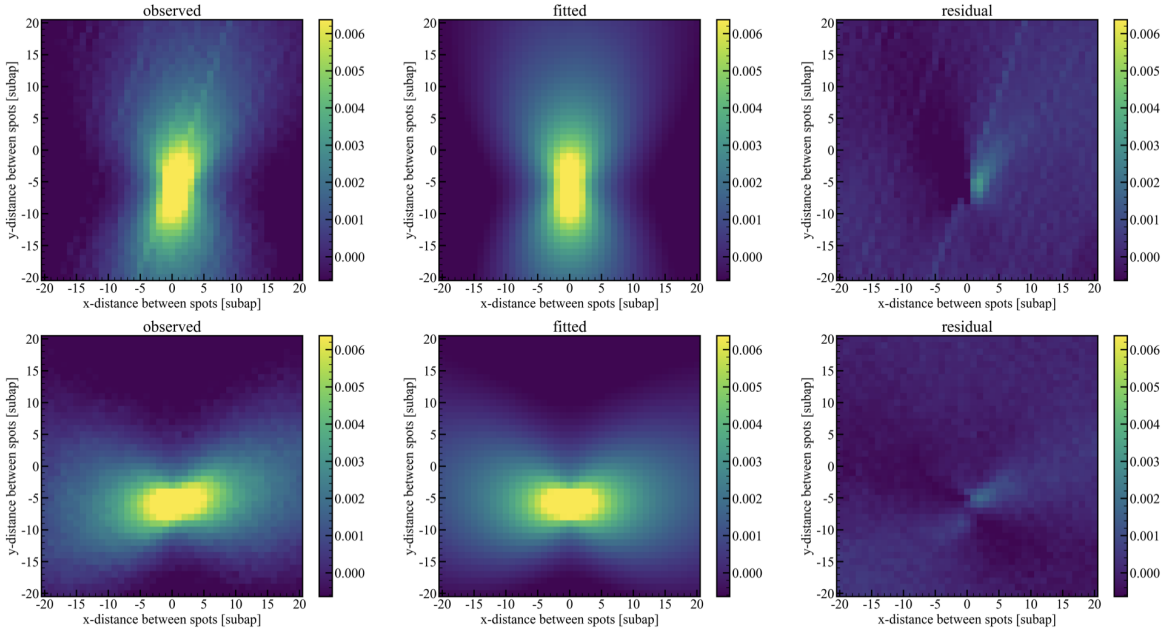

Fig. F.7 Same as figure F.1 but for dataset taken at 5:07, Mar.14, 2023.

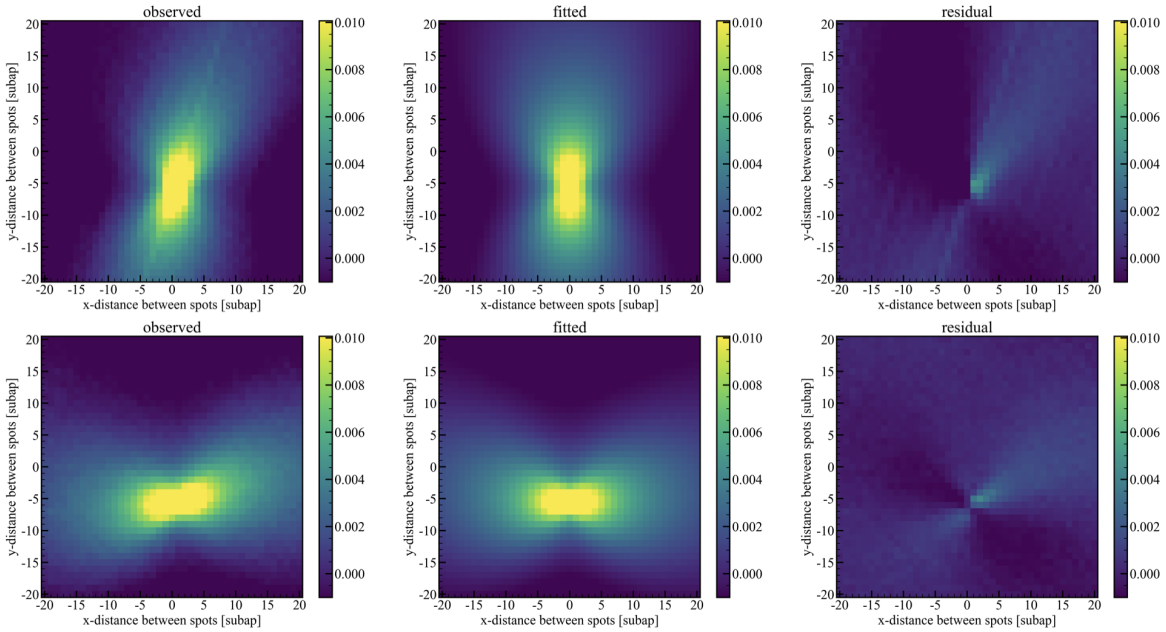

Fig. F.8 Same as figure F.1 but for dataset taken at 5:13, Mar.14, 2023.

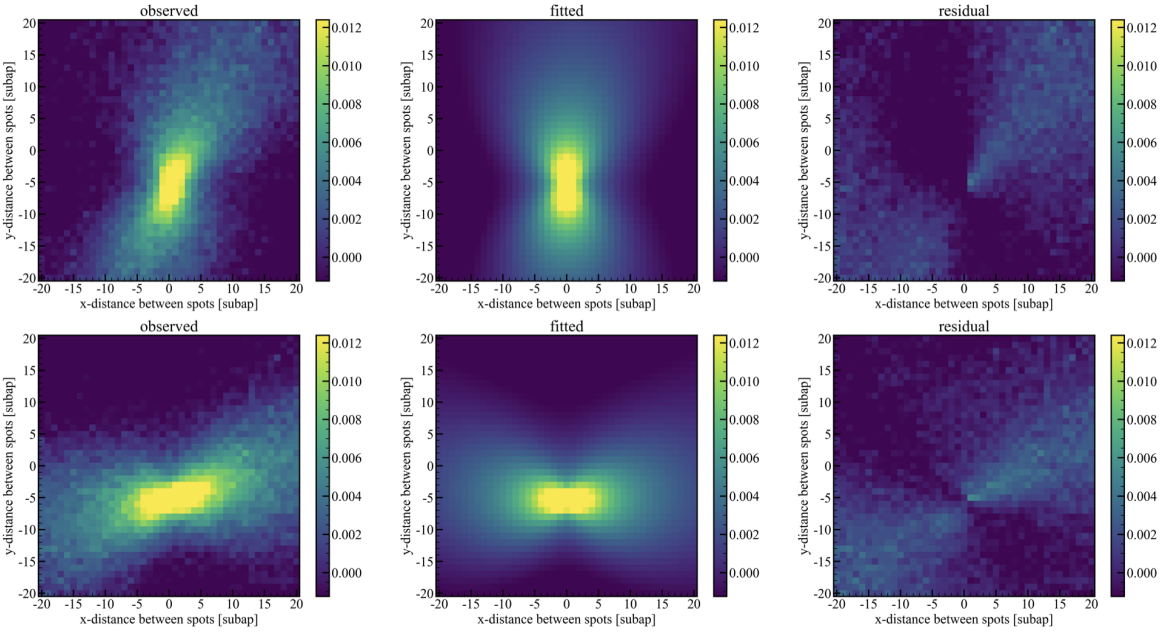

Fig. F.9 Same as figure F.1 but for dataset taken at 5:16, Mar.14, 2023.

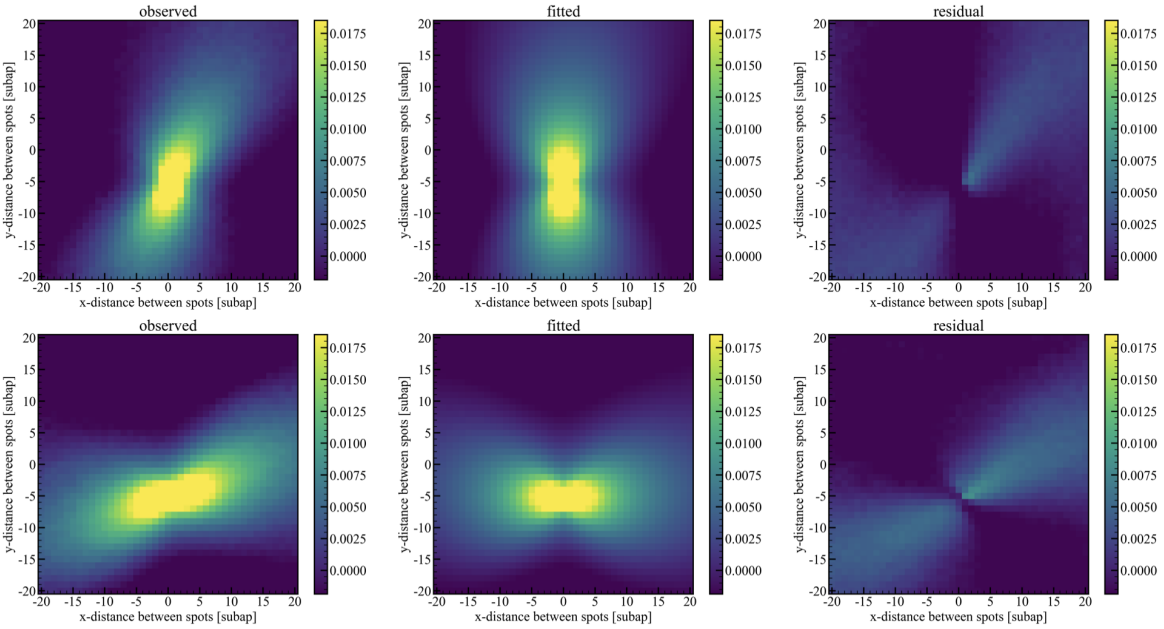

Fig. F.10 Same as figure F.1 but for dataset taken at 5:20, Mar.14, 2023.